WWU

Institut für Materialphysik

The Interstitialcy Diffusion Mechanism in Alkali Feldspar: Self-Diffusion Measurements and Monte Carlo Simulations

Inaugural-Dissertation zur Erlangung des Doktorgrades der Naturwissenschaften im Fachbereich Physik der Mathematisch-Naturwissenschaftlichen Fakultät der Westfälischen Wilhelms-Universität Münster

vorgelegt von

Fabian Hergemöller, geb. Wilangowski

aus Soest

– 2017 –

Dekan:	Prof. Dr. Michael Klasen
Erster Gutachter:	Prof. Dr. Gerhard Wilde
Zweiter Gutachter:	Priv.-Doz. Dr. Sergiy Divinski
Tag(e) der mündlichen Prüfung(en):	23.03.2018
Tag der Promotion:	23.03.2018

In Gedenken an

Nico Stolwijk

Abstract

The rock-forming alkali feldspars belong to the most abundant minerals in the Earth's crust and are formed as a solid solution between the sodium ($NaAlSi_3O_8$, albite) and potassium ($KAlSi_3O_8$, orthoclase) end-member compositions. Well-founded knowledge of self-diffusion data in alkali feldspar is a prerequisite for interpreting existing interdiffusion data that, in turn control re-equilibration features in alkali feldspar that pertain to evolution and dynamics of the crust. Sodium diffusivities in potassium-rich alkali feldspar single crystals originating from the Eifel, Germany and Madagascar were measured with the radiotracer technique using the ^{22}Na isotope. It was found that the diffusion coefficients follow linear Arrhenius relations with activation energies between 1.2 eV and 1.3 eV (Eifel feldspars) and 2.0 eV (Madagascar feldspar) and with pre-exponential factors between $2 \times 10^{-8}\,m^2/s$ and $8 \times 10^{-8}\,m^2/s$ (Eifel feldspars) and $2 \times 10^{-6}\,m^2/s$ (Madagascar feldspar). The same Eifel feldspar was implanted with ^{43}K at the ISOLDE/CERN radioactive ion-beam facility normal to the (001) crystallographic plane. Potassium diffusion coefficients are described by an activation energy of 2.4 eV and a pre-exponential factor of $5 \times 10^{-6}\,m^2/s$, which is more than three orders of magnitude lower than the ^{22}Na diffusivity and rules out a vacancy-controlled diffusion mechanism for alkali diffusion in alkali feldspar. Over the past decades, there have been numerous Monte Carlo (MC) studies on diffusion by the vacancy mechanism. These were motivated by the importance of vacancies for atomic transport in many materials, particularly in metallic systems, and further inspired by Manning's random alloy model. However, MC investigations on diffusion involving interstitialcy defects have remained extremely sparse, although self-interstitials may play a crucial role in ionic crystals and semiconductor alloys. In this work, some basic features of atomic (or ionic) movement mediated by interstitialcies in binary random alloys AB with a simple cubic structure are explored by MC simulations. The concepts and methods were also applied to the monoclinic alkali feldspar in consideration of clustering on the Na-K sublattice, revealing a predominance of indirect interstitial jumps over vacancy jumps. When results for the Haven ratio are discussed, which relates the tracer diffusion coefficients to the charge diffusivity as may be deduced from the ion conductivity through the Nernst-Einstein equation, the findings give strong evidence for a correlated motion of Na and K through the interstitialcy mechanism.

Zusammenfassung

Die gesteinsbildenden Alkalifeldspate gehören zu den häufigsten Mineralien der Erdkruste und bilden ein Mischkristallsystem mit einem natriumreichen ($NaAlSi_3O_8$, Albit) und einem kaliumreichen Endglied ($KAlSi_3O_8$, Orthoklas). Die fundierte Kenntnis von Selbstdiffusionsdaten ist Voraussetzung für die Interpretation der Interdiffusion in Alkalifeldspat, die wiederum die Austauschrate mit der Umgebung sowie die Kinetik der Entmischung und damit verbunden die Mikrostruktur bestimmt. Die Na-Diffusion in kaliumreichen Feldspateinkristallen aus der Eifel und aus Madagaskar wurde mit der Radiotracermethode und dem Isotop ^{22}Na gemessen. Die Diffusionskoeffizienten folgen linearen Arrheniusbeziehungen mit Aktivierungsenergien zwischen 1.2 eV und 1.3 eV (Eifel-Feldspate) und 2.0 eV (Madagaskar-Feldspat) und mit exponentiellen Vorfaktoren zwischen $2 \times 10^{-8}\,\mathrm{m^2/s}$ und $8 \times 10^{-8}\,\mathrm{m^2/s}$ (Eifel-Feldspate) und $2 \times 10^{-6}\,\mathrm{m^2/s}$ (Madagaskar-Feldspat). Der selbe Eifel-Feldspat wurde mit ^{43}K senkrecht zur kristallografischen (001)-Ebene am ISOLDE Experiment am CERN implantiert. Die Kaliumdiffusionskoeffizienten sind durch eine Aktivierungsenergie von 2.4 eV und einen exponentiellen Vorfaktor von $5 \times 10^{-6}\,\mathrm{m^2/s}$ charakterisiert, was über drei Größenordnungen unterhalb der ^{22}Na-Diffusion liegt und einen gemeinsamen leerstellenbasierten Mechanismus der Alkalidiffusion ausschließt. Unzählige Monte-Carlo-Studien (MC-Studien) zur Diffusion über den Leerstellenmechanismus sind motiviert von der Relevanz der Leerstellen für den atomaren Transport in vielen Materialien, speziell in metallischen Systemen, und basieren auf Mannings 'random alloy' Modell. MC-Studien zur Analyse der Diffusion von Eigenzwischengitteratomen sind hingegen selten, obwohl diese Defekte eine entscheidende Rolle bei der Diffusion in ionischen Kristallen und halbleitenden Legierungen spielen können. In dieser Arbeit sind einige grundlegende Eigenschaften des atomaren (und ionischen) Transports über Eigenzwischengitteratome in binären Legierungen AB mit regelloser Ordnung in einem einfach kubischen Gitter durch MC-Simulationen untersucht. Die Methoden wurden weiterhin auf die monokline Struktur des Alkalifeldspats angewandt, wobei Cluster auf dem Na-K Untergitter berücksichtigt wurden. Aus den Ergebnissen kann auf eine überwiegende Beteiligung von interstitiellen Sprüngen gegenüber Leerstellensprüngen geschlossen werden. Messdaten für das Haven-Verhältnis, das einen Zusammenhang zwischen der Tracer- und Ladungsträgerdiffusion herstellt, geben deutliche Hinweise für die korrelierte Diffusion von Na und K über den indirekt-interstitiellen Diffusionsmechanismus.

Contents

1. Introduction

Alkali feldspar is among the most abundant rock-forming minerals in the Earth's crust. The alkali feldspars form a solid-solution series along the binary join between the sodium ($NaAlSi_3O_8$, albite) and potassium ($KAlSi_3O_8$, orthoclase) end members. The crystal structure is comprised of a 3D framework of corner-sharing $[SiO_4]^{4-}$ and $[AlO_4]^{5-}$ tetrahedra, and the alkali cations occupy large, irregularly coordinated cavities (cf. Chapter 2, Fig. 2.3). As compared to Al and Si in the tetrahedral framework, the alkali cations are relatively mobile. The interdiffusion of Na^+ and K^+ in alkali feldspar plays a pivotal role in the reequilibration of Na-K partitioning between alkali feldspar and other Na- and K-bearing minerals and thus, for the reconstruction of formation conditions from phase equilibria [1]. Moreover Na-K interdiffusion controls microstructure and composition evolution during cooling-induced exsolution of alkali or ternary feldspar leading to perthite formation [2, 3, 4].

Diffusion of alkali cations in alkali feldspar has been investigated over several decades now. Major contributions to this field date back to the 1970s comprising the tracer diffusion measurements from Bailey [5], Lin and Yund [6], Petrović [7], Foland [8] and Kasper [9]. In many of the previous studies grains from the mechanically crushed starting material were exchanged with salt or salt solutions and the diffusivities were analysed from the bulk exchange. Although these techniques were state of the art at that time, the measurement of diffusional anisotropy is, a priori, limited which may complicate the interpretation of the results. For a comprehensive discussion of the previous studies the reader is referred to the review by Cherniak [10].

In the last few years, much more information on the Na-K interdiffusion has become available. Cation exchange experiments were carried out by the Vienna group [11, 12, 13] using K-rich gem-quality sanidine and KCl salt melt. A field-emission gun electron microprobe was employed to analyse the composition variation along different directions. An example for the obtained interdiffusion coefficients at 850 °C

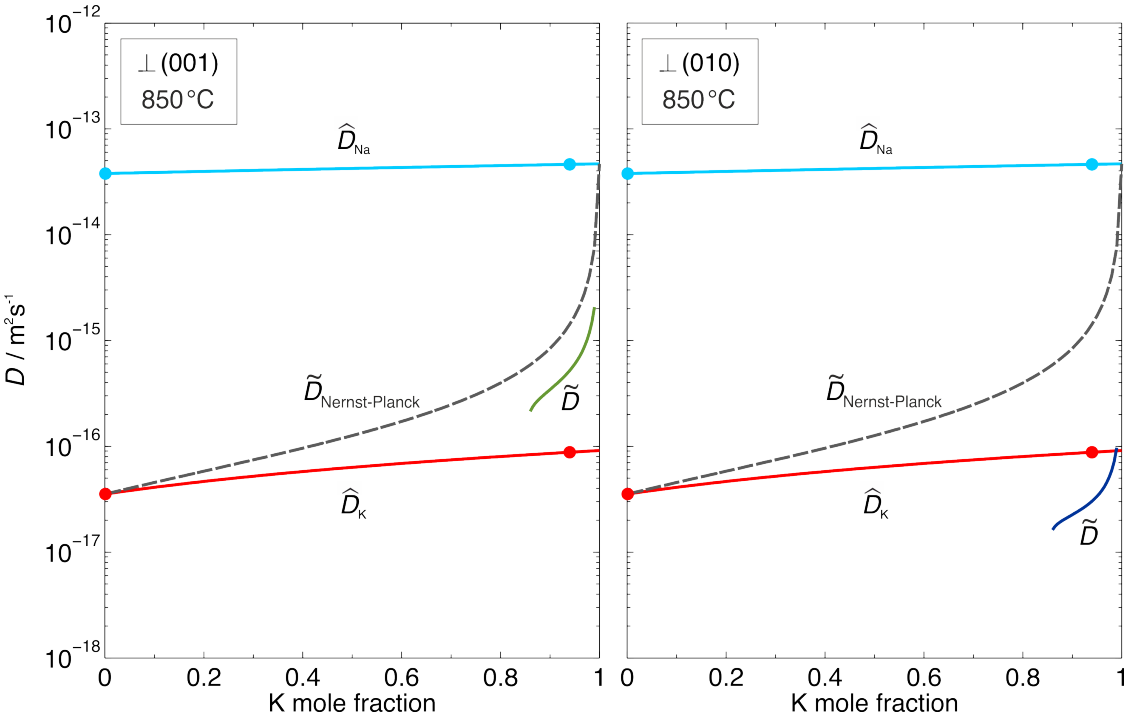

Figure 1.1.: Comparison of measurements of the Na-K interdiffusion coefficient $\tilde{D}$ by Schaeffer [13] and predicted interdiffusion coefficients (dashed lines) based on the Nernst-Planck equation for an ideal solid solution and using experimentally determined Na and K tracer diffusion coefficients, $\widehat{D}_{\mathrm{Na}}$[1]and $\widehat{D}_{\mathrm{K}}$, respectively. The tracer diffusion coefficients were estimated over a wide composition range by interpolation (solid lines) of the bulk-exchange data (solid circles) by Kasper [9] for albite and by Foland [8] for orthoclase; edited after Petrishcheva et al. [11].

is given in Fig. 1.1 for the directions normal to (001) and normal to (010). The findings from this study reveal systematic differences between the experimentally determined Na-K interdiffusion coefficients and those calculated from inserting published Na and K self-diffusion coefficients in theoretical interdiffusion models [14, 15]. In particular, the experimentally determined composition dependence of the interdiffusion coefficient deviates systematically from theoretical predictions. Furthermore, Na-K interdiffusion is markedly direction dependent, whereas no information on the direction dependence of Na and K tracer diffusion is available. A comparison of the measured composition-distance data for the two investigated directions showed that the concentration fronts are sharp along profiles normal to (010) and comparatively broad in profiles measured normal to (001). It was

[1]To reduce the number of indices, the common asterisk for labelling tracer diffusivity (D^*) has been replaced by the 'hat' symbol ($\widehat{D}$) throughout this work.

later concluded from electron back-scatter diffraction measurements that diffusion induced lattice strain may be the reason for the exceptionally sharp concentration fronts normal to (010) that may act as self-induced diffusion barrier [16].
Based on the systematic of the available composition-distance data, it may be assumed that a fast diffusing Na species becomes important at close to potassium end-member compositions. In this composition domain, Na-K interdiffusion is primarily controlled by the tracer diffusion of Na. At close to potassium-end-member compositions, the total Na concentration in the crystal is low, and a significant fraction of Na may be present on interstitial sites with high mobility. Because the high Si-O bonding energies make Schottky defect formation extremely unfavourable it was concluded by Behrens et al. [17] that likely Frenkel pairs are the major point defects. It may therefore be concluded that diffusion via vacancies or via self-interstitials is the rate determining process.
For better modelling of the Na-K interdiffusion process and thus for a proper interpretation of composition patterns found in natural feldspar, the transport properties on the alkali sublattice should be characterised comprehensively. One necessary route to this goal involves determining accurate tracer diffusion coefficients for Na and K. Another route focuses on measuring the dc ionic conductivity σ, which comprises the joint contributions of Na^+ and K^+ ions to overall charge transport. A combination of reliable data on mass and charge transport obtained for the identical feldspar mineral gives access to the Haven ratio that is inherently connected to the correlation effects of the microscopic diffusion mechanism. Based on this approach, a consistent physical picture has been obtained, e.g., for some alkali halide crystals [18, 19]. Alkali feldspar bears, however, much more structural complexity and the concomitant diffusion of Na and K sharing the same sublattice must be considered. In particular, the Na tracer diffusion may experience percolation problems – expressed through extremely small correlation factors f – if the pathways for long-range diffusion are occupied by the slower moving K atoms. There is a considerable amount of literature on diffusion correlation effects in solids, mainly dealing with cubic crystals or other systems of high symmetry. For example, correlation effects pertaining to diffusion via vacancies in binary alloys were investigated with the aid of Monte Carlo simulations for a random bcc alloy [20, 21, 22] and for a random fcc alloy [20, 22, 23, 24]. A comprehensive overview of previous studies was given by LeClaire [25] and Murch [26]. The existing concepts and methods have to be adapted to the monoclinic alkali sublattice of alkali

feldspar to analyse the percolation behaviour which is inherently related to the diffusion mechanism and structural properties such as the coordination number. The combination of predicted percolation threshold values and Haven ratios with measurements from tracer diffusion and ionic conductivity may prove as a powerful method to elucidate the microscopic mechanism of diffusion which is the aim of this thesis. In order to do so the following studies are presented:

(i) In Chapter 3 the tracer diffusion of ^{22}Na is analysed using gem-quality single crystal feldspar of different K-rich compositions to obtain information of the composition-dependent Na self-diffusion.

(ii) Chapter 4 examines the ^{43}K diffusion that was measured at the ISOLDE[2] experiment at CERN using a gem-quality K-rich feldspar mineral. This information is used to determine the diffusivity ratio $\widehat{D}_{\mathrm{Na}}/\widehat{D}_{\mathrm{K}}$.

(iii) Measurements of the ionic conductivity using the same feldspar mineral as above are presented in Chapter 5 and results for the Haven ratio are reported.

(iv) A vacancy diffusion model of Na and K in alkali feldspar is presented in Chapter 6 and tracer and vacancy correlation factors are analysed with Monte Carlo simulations. In a similar way, the interstitialcy diffusion mechanism is comprehensively investigated throughout the Chapters 7, 8 and 9.

The findings for both diffusion mechanisms can be compared with the measured data which provides strong evidence that the interstitialcy diffusion mechanism is the major mechanism of the Na diffusion in alkali feldspar.

[2]ISOLDE: Isotope Separator On Line DEvice.

2. Fundamentals

2.1. Alkali feldspar

Most feldspars belong to a solid-solution series within a ternary join between the calcium ($CaAl_2Si_2O_8$, anorthite), sodium ($NaAlSi_3O_8$, albite) and potassium ($KAlSi_3O_8$, orthoclase) end members (see Fig. 2.1). The binary join between the albite (Ab) and orthoclase (Or) end members is denoted as alkali feldspar. The phase diagram of alkali feldspar is displayed in Fig. 2.2 and it can be seen from the figure that it is completely miscible at high temperatures. For temperatures below $\sim 600\,^{\circ}\mathrm{C}$ a miscibility gap can be observed and hence, feldspar separates into a Na-rich and a K-rich phase. Stable phases of feldspar are, e.g., albite and microcline which show a triclinic structure (C-1) and sanidine and orthoclase with a monoclinic structure (C2/m).
The crystal structure of alkali feldspar is comprised of a 3D framework of corner-sharing $[SiO_4]^{4-}$ and $[AlO_4]^{5-}$ tetrahedra. As illustrated in Fig. 2.3, it can be seen that crankshaft-like chains are formed by the silicate framework. One unit cell comprises 16 tetrahedra sites and four types of these sites can be distinguished, i.e., $T_{1(0)}$, $T_{1(m)}$, $T_{2(0)}$ and $T_{2(m)}$. In the monoclinic case, only two types of sites exist and the relations $T_{1(0)} \equiv T_{1(m)} \equiv T_1$ and $T_{2(0)} \equiv T_{2(m)} \equiv T_2$ hold. Each T-site is occupied by either Si^{4+} or by Al^{3+} and the ordering degree for the monoclinic structure is given by

$$\frac{t_1 - t_2}{t_1 + t_2}\,, \tag{2.1}$$

where t_1 and t_2 are site-occupancy probabilities for T_1 and T_2 sites, respectively. Irregularly coordinated cavities in the framework structure are occupied by K^+ and Na^+ cations with an ionic radius of 1.33 Å and 0.98 Å [30], respectively. K^+ and Na^+ can be substituted, e.g., by Rb^+, Ca^{2+} or Ba^{2+} [31], whereas the Ba end member $BaAl_2Si_2O_8$, that is uncommon in nature, is denoted as celsian (Cs). As compared to Al and Si in the tetrahedral framework, the alkali cations are relatively mobile.

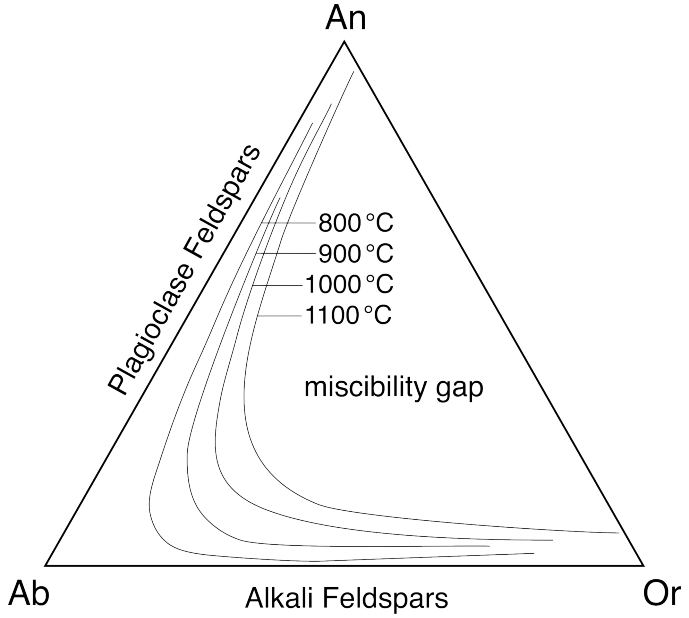

Figure 2.1.: Ternary phase diagram anorthite (An) - albite (Ab) - orthoclase (Or). The miscibility gap is calculated for a pressure of 8 kbar after Elkins and Grove [27, 28].

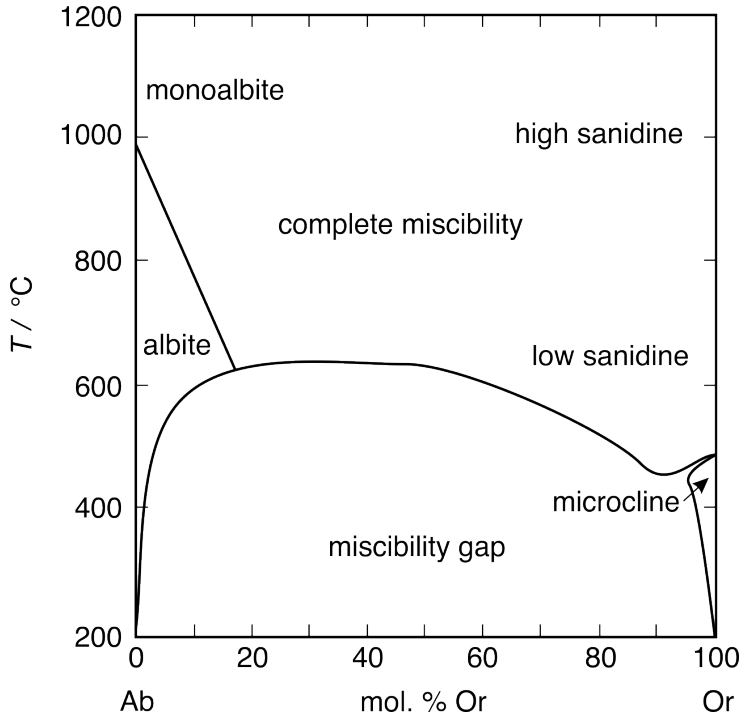

Figure 2.2.: Subsolidus phase diagram for binary alkali feldspars. The alkali feldspars are completely miscible for temperatures T above $\sim 600\,°C$. A large miscibility gab can be observed for lower temperatures and accordingly, feldspars separate into a Na-rich and a K-rich phase; edited after Okrusch [29].

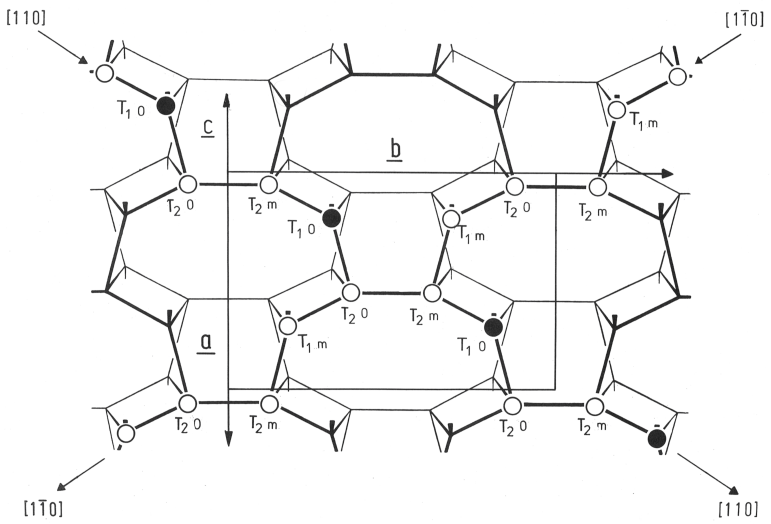

Figure 2.3.: Idealised illustration of the monoclinic feldspar structure projected onto the (001) plane. Central tetrahedra sites (T) are occupied by Si^{4+} (open circles) and Al^{3+} (full circles) atoms. All Al^{3+} atoms are located on $T_{1(0)}$ sites which implies a complete Al-Si ordering; illustrated by H. Kroll.

Sample material

In this thesis, three natural K-rich alkali feldspars from different localities are considered, i.e., a sanidine from the Eifel region Rockeskyll, Germany (RK), a sanidine from the Eifel region Volkesfeld (VF) and an orthoclase originating from Madagascar (MO). The VF sanidine shows two colour variants, i.e., colourless and smoky brown whereas the RK sanidine is colourless and the MO feldspar shows a yellowish colour. All crystals show perfect (010) and (001) cleavage planes and only the MO feldspar is cleavable along several further planes. The employed feldspars are homogeneous down to the nanometre scale and detailed chemical analyses have been reported earlier [32, 33, 12]. Table 2.1 compiles the averages of several analysed MO, VF and RK crystals in numbers or fractions per formula unit, which is based on normalisation to 8.00 oxygen atoms. The compositions of the MO orthoclase is $Or_{95}Ab_5$ and the sanidines VF and RK are given by $Or_{83}Ab_{15}Cs_1$ and $Or_{71}Ab_{26}Cs_2$, respectively. Minor elements are Fe in all three feldspars and Ba which was only found in the Eifel sanidines (see Tab. 2.1). All feldspars have a monoclinic structure characterised by the space group C2/m. On the tetrahedral sites, Al and Si are highly disordered with $2t_1 = 0.61$ (VF) [32] and $2t_1 = 0.58-0.62$ (RK) [33] whereas the MO feldspar shows a slightly higher degree of ordering, i.e.,

Table 2.1.: Mean stoichiometric composition of gem-quality single-crystal feldspar from Madagascar (MO), Volkesfeld/East Eifel (VF) and Rockeskyller Kopf/West Eifel (RK) normalised to 8.00 oxygen atoms per formula unit. The data refer to averages taken from previous studies on samples of the same or similar large crystals [32, 33, 12]. Σ_{cat} denotes the sum of the cation values. The general uncertainty of ± 0.01 applies to every entry.

Element	MO	VF	RK
Si	3.02	2.98	2.97
Al	0.93	1.02	1.02
Ti	0.00	0.00	0.00
Fe	0.04	0.01	0.01
Mg	0.00	0.00	0.00
Ca	0.00	0.00	0.00
Na	0.05	0.15	0.26
K	0.96	0.83	0.71
Rb	n/a	0.00	n/a
Ba	0.00	0.01	0.02
Sr	n/a	0.00	0.01
O	8.00	8.00	8.00
Σ_{cat}	5.00	5.00	5.00

$2t_1 = 0.70$ [32]. Here $2t_1 = 2t_2 = 0.5$ means according to Eq. 2.1 total disorder and $2t_1 = 1$ reflects rigorous order. In the latter case all Al ions are uniformly accommodated on T_1 tetragonal sites, whereas the other half of the T_1 tetrahedrons and all T_2 sites are occupied by Si (see Fig. 2.3). The mass density determined by the Archimedes method was obtained as $2.54\,\mathrm{gcm}^{-3}$ for single-crystal VF which is only slightly below the calculated value of $2.57\,\mathrm{gcm}^{-3}$. The mass density of RK and MO feldspar was in both cases determined to $2.56\,\mathrm{gcm}^{-3}$, in good agreement with the literature [32].

2.2. Diffusion in single-crystalline solids

Diffusion in the solid state comprises the random thermally activated movement of atoms that results in the net displacement of atoms. In ionic conductors the transport of matter is linked with charge transport which implies a close relation between diffusion and ionic conduction. In contrast to diffusion in gasses or liquids, diffusion in (single-crystalline) solids often involves point defects such as vacancies or self-interstitials which may act as diffusion vehicle. The mobility of atoms strongly depends on the atomic radius and on the diffusion mechanisms that are involved. In the present section, a phenomenological description of the diffusion process is given and models for the elementary microscopic displacements are presented.

2.2.1. Fick's laws and solutions of the diffusion equation

It was Fick (1855) who first recognised that diffusion is – in analogy to the transfer of heat – mediated through random molecular motion. By adopting Fouriers (1822) mathematical theory of heat conduction Fick derived a theory of diffusion in isotropic media based on the hypothesis that the transfer rate of diffusing substance through the unit area of a section (flux) is proportional to the concentration gradient normal to the section. Ficks first law of diffusion is therefore given by

$$\vec{j}(\vec{x},t) = -\mathbf{D}\cdot\nabla\vec{c}(\vec{x},t)\,, \tag{2.2}$$

where $\vec{j}$ is a flux, $\vec{c}$ is a volume concentration, $\vec{x}$ is the space coordinate normal to the section and $\mathbf{D}$ is a proportionality factor with an SI unit of $\mathrm{m^2 s^{-1}}$ denoted as diffusion coefficient. In three dimensions the relation $\nabla\vec{c}(\vec{x},t) \equiv \frac{\partial c_x}{\partial x}+\frac{\partial c_y}{\partial y}+\frac{\partial c_z}{\partial z}$ holds. Under the assumption that sinks or sources for diffusing particles can be neglected the number of diffusing particles is conserved and the continuity equation

$$\frac{\partial\vec{c}(\vec{x},t)}{\partial t} + \nabla\vec{j}(\vec{x},t) = 0 \tag{2.3}$$

holds true. It is straightforward to show that combination of Eq. 2.2 and Eq. 2.3 gives Fick's second law, i.e.,

$$\frac{\partial\vec{c}(\vec{x},t)}{\partial t} = \nabla\cdot(\mathbf{D}\cdot\nabla\vec{c}(\vec{x},t))\ . \tag{2.4}$$

The above equation is a second-order partial differential equation involving space and time that requires some initial and boundary conditions for the solution. A common approach is the consideration of homogeneous and isotropic media that implies for the diffusion coefficient

$$\mathbf{D}(\vec{c}, \vec{x}, t) = D\,. \tag{2.5}$$

Using the above relation, Fick's second law of diffusion in any space direction x is given by

$$\frac{\partial c(x,t)}{\partial t} = D\frac{\partial^2 c(x,t)}{\partial x^2}\,. \tag{2.6}$$

Three relevant boundary conditions are discussed in the following.

Thin-film source conditions

For certain initial and boundary conditions exact formal solutions for Fick's second law of diffusion can be derived. For several one-dimensional diffusion processes the initial condition may be given by

$$c(x, t=0) = M\delta\left(x\right)\,, \tag{2.7}$$

where M is the total amount of diffusing substance and $\delta\left(x\right)$ describes an infinitely thin film on the surface ($x = 0$) of a medium. Under the assumption of a semi-infinite extension of the medium the boundary conditions are given by

$$\begin{aligned} c(x,t) &= 0 \quad \text{for} \quad x < 0 \\ \lim_{x\to\infty} c(x,t) &= 0\,. \end{aligned} \tag{2.8}$$

For $t > 0$ the diffusing particles spread from the source into one half-space of the medium and Ficks second law is described by a Gaussian behaviour, i.e., [34]:

$$c(x,t) = \frac{M}{\sqrt{\pi D t}}\exp\left(-\frac{x^2}{4Dt}\right)\,. \tag{2.9}$$

From the above relation $2\sqrt{Dt}$ can be interpreted as a characteristic diffusion length which often occurs in diffusion problems.

Constant source conditions

In contrast to the previously discussed initial condition of an infinitely thin film the source can be otherwise significantly extended. This may imply a constant surface concentration for $t > 0$ if the source is not consumed by the medium during the diffusion process and hence, the initial conditions are

$$c(x, t = 0) = \begin{cases} c_0 & \text{for} \quad x = 0 \\ 0 & \text{for} \quad x > 0 \end{cases} \tag{2.10}$$

and the boundary conditions can be expressed as

$$\begin{aligned} c(x = 0, t) &= c_0 \\ \lim_{x \to \infty} c(x, t) &= 0\,. \end{aligned} \tag{2.11}$$

The ansatz for solving Fick's second law in Eq. 2.4 is based on an infinite number of infinitely thin sources $c_0 \mathrm{d}\xi$ which spread into a semi-infinite medium. According to Eq. 2.9 the concentration for one infinitely thin source at a time t is given by

$$c(\xi, t) = \frac{M}{\sqrt{\pi D t}} \exp\left(-\frac{\xi^2}{4Dt}\right)\,. \tag{2.12}$$

From the summation over all elements $\mathrm{d}\xi$ together with the initial and boundary conditions Eqs. 2.10 and 2.11, respectively, it follows for the solution [34]

$$c(x, t) = \frac{c_0}{2\sqrt{\pi D t}} \int_x^\infty \exp\left(-\xi^2/4Dt\right) \mathrm{d}\xi\,. \tag{2.13}$$

By introducing the complementary error function, i.e., $\mathrm{erfc}\; x = 1 - \mathrm{erf} x$, Eq. 2.13 may be expressed as

$$c(x, t) = \frac{1}{2} c_0\; \mathrm{erfc}\left(\frac{x}{2\sqrt{Dt}}\right)\,, \tag{2.14}$$

and the amount of diffusing particles per unit area is given by

$$M(t) = c_0 \sqrt{\frac{Dt}{\pi}}\,. \tag{2.15}$$

Exchange of the diffusant with the ambience

A variation from the thin-film solution is given if the diffusant exchanges with the ambience which is, e.g., given if the source evaporates during the diffusion process. Under the assumption that the initial condition is given in analogy to the thin-film problem, i.e., $c(x, t = 0) = 0$ for $x > 0$, the boundary condition can be expressed as [35]

$$\frac{\partial c}{\partial x}(x = 0, t) = H \left[c(x = 0, t) - c_0 \right] , \tag{2.16}$$

where c_0 is a constant concentration of the diffusant in the ambience of the medium and H quantifies the exchange between the source and the ambience with the SI unit m^{-1}. For $c_0 = 0$ the solution of Fick's second law is given by [35]

$$c(x, t) = M \left[\frac{1}{\sqrt{\pi D t}} e^{-\frac{x^2}{4Dt}} - H e^{DtH^2 + Hx} \operatorname{erfc}\left(\frac{x}{2\sqrt{Dt}} + H\sqrt{Dt} \right) \right] . \tag{2.17}$$

At the surface of the medium the projection of the flux j_x to the x-direction is

$$j_x = -D \underbrace{\frac{\partial c}{\partial x}}_{>0} , \tag{2.18}$$

which implies a characteristic peak concentration within the medium. In the limiting case of $H = 0$ Eq. 2.17 is fully equivalent to the thin-film solution (see Eq. 2.9).

2.2.2. Diffusion in anisotropic media

In anisotropic media, the diffusion coefficient is generally direction dependent and given by a second-order tensor, i.e.,

$$\mathbf{D} = \begin{pmatrix} D_{11} & D_{12} & D_{13} \\ D_{21} & D_{22} & D_{23} \\ D_{31} & D_{32} & D_{33} \end{pmatrix} . \tag{2.19}$$

However, only four independent matrix elements have to be considered if the medium shows a monoclinic symmetry. The matrix form of the diffusion tensor is then given by

$$\mathbf{D} = \begin{pmatrix} D_{11} & 0 & D_{13} \\ 0 & D_{22} & 0 \\ D_{31} & 0 & D_{33} \end{pmatrix} , \tag{2.20}$$

where $D_{13} = D_{31}$ holds. The latter relation stays without proof here because it has been discussed in detail by Nye [36]. It is easy to find the corresponding polynomial form, i.e.,

$$D_{11}x_1^2 + D_{22}x_2^2 + D_{33}x_3^2 + 2D_{13}x_1x_3 = 1\,. \tag{2.21}$$

Equation 2.21 describes a quadric surface which can be an ellipsoid or an hyberboloid that is tilted around the x_2-axis with the angle of rotation ϕ given by

$$\phi = \frac{1}{2}\arctan\frac{2D_{13}}{D_{11} - D_{33}}\,. \tag{2.22}$$

A rotation of the coordinate system around the diad-axis (in monoclinic systems this is always the x_2-axis) by the angle ϕ leads to the normal form of the diffusion tensor

$$\mathbf{D} = \begin{pmatrix} D_1 & 0 & 0 \\ 0 & D_2 & 0 \\ 0 & 0 & D_3 \end{pmatrix} . \tag{2.23}$$

The elements D_i are called the *principal diffusivities* and can be identified as the eigenvalues of the Matrix in Eq. 2.20. Along the direction x_2 the obvious relation $D_2 = D_{22}$ holds true. The remaining two principal diffusivities are related to the matrix elements of the non-linearised form in Eqs. 2.20 and 2.21 by [36]

$$D_1 = \frac{D_{11} + D_{33}}{2} + \sqrt{\left(\frac{D_{33} - D_{11}}{2}\right)^2 + D_{13}^2}\,, \tag{2.24}$$

$$D_3 = \frac{D_{11} + D_{33}}{2} - \sqrt{\left(\frac{D_{33} - D_{11}}{2}\right)^2 + D_{13}^2}\,. \tag{2.25}$$

The coordinate system given by the principal axes of diffusion is shown in Fig. 2.4 together with a radius vector $\vec{r}$. The projection of any radius vector onto the axis x_1, x_2 and x_3, respectively is given by

$$\vec{r} = \frac{1}{\sqrt{D}}\left(\cos\theta_1, \cos\theta_2, \cos\theta_3\right)\,, \tag{2.26}$$

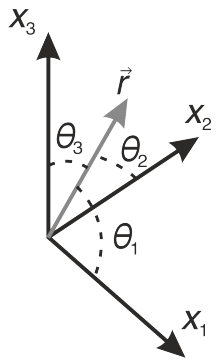

Figure 2.4.: Orthonormal system x_1, x_2 and x_3 representing the principal axes of diffusion with an arbitrary vector $\vec{r}$ representing a considered diffusion direction.

where θ_1, θ_2 and θ_3 is an angel between $\vec{r}$ and the principal axis, respectively, as indicated in Fig. 2.4. The diffusion along an arbitrary direction is then given by

$$D_r = D_1 \cos^2 \theta_1 + D_2 \cos^2 \theta_2 + D_3 \cos^2 \theta_3 \,. \tag{2.27}$$

2.2.3. Basic atomic diffusion mechanisms and correlation effects

The macroscopic diffusion of a tracer atom comprises a long sequence of elementary microscopic jumps between local minima in the energy landscape of the host lattice. Depending on the type of diffusant and on the host lattice crucial local minima can be at substitutional (S) or interstitial (I) sites. The displacements of a single tracer atom can be idealised by a random walk. However, Bardeen and Herring [37] recognised that for certain types of mechanisms tracer diffusion deviates from a purely random walk. In particular, if the jumps are mediated by diffusion vehicles (e.g., vacancies and self-interstitials) a correlation between the directions of successive jumps of a single tracer atom is predicted. This can be understood as follows: A diffusion vehicle enters a nearest-neighbour site of a tracer atom from a random direction. Assuming that a first reaction between the tracer atom and the diffusion vehicle takes place the diffusion vehicle is still at a nearest-neighbour position. A subsequent jump of the tracer atom therefore occurs with a higher than statistical probability along a reversed direction. Only if the diffusion vehicle escapes from the tracer atom and a new diffusion vehicle approaches from a random direction the first and the second jump of the tracer atom are uncorrelated.

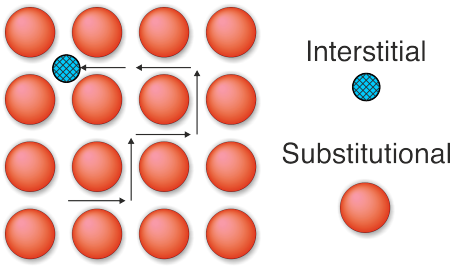

Figure 2.5.: Schematic two-dimensional representation of the direct interstitial diffusion mechanism via subsequent I-I jumps of an atom.

Consequently, a so-called correlation factor f has to be taken into account that depends on the available diffusion pathways and thus on the crystal structure and diffusion mechanism. Three examples are discussed in the following.

Direct interstitial diffusion

If the diffusing atoms are small compared to the substitutional atoms, e.g, if the diffusion of small foreign atoms is considered the mechanism may comprise a sequence of direct steps from one interstitial site to another (direct interstitial mechanism) [38, 39]. The distortion of the lattice during migration is influenced by the atom radius and hence, small atoms diffuse more readily than larger atoms. As illustrated in Fig. 2.5, no intrinsic point defects are involved in the direct interstitial mechanism which implies that the jumps of an atom will not, in general, depend on the preceding jumps. The jump of a tracer atom is therefore described by a random walk and the value of the correlation factor equals unity ($f = 1$). Beyond that, the diffusion coefficient is independent of the concentration of intrinsic point defects.

Vacancy diffusion

A vacancy is a point defect in crystals that comprises an unoccupied substitutional lattice site. Crystals inherently possess imperfections such as intrinsic vacancies and in thermal equilibrium the vacancy concentration is a constant that depends on temperature (cf. Eq. 2.34). The vacancy diffusion mechanism takes place if a substitutional atom jumps into a neighbouring vacant lattice site. This process is displayed in Fig. 2.6 and it can be seen that the atom and the vacancy migrate in opposite directions. In the limit of low vacancy concentrations and for a high

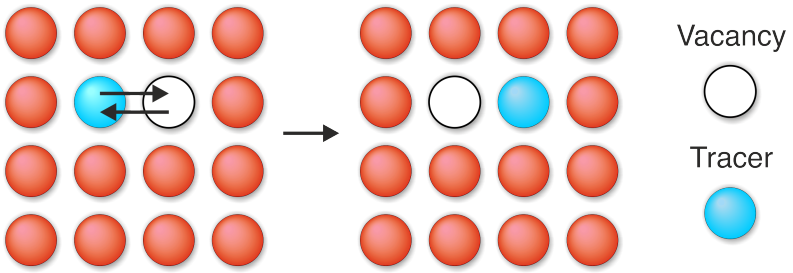

Figure 2.6.: Exchange of a substitutional tracer atom with a vacancy located at a nearest-neighbour site in a two-dimensional square lattice.

symmetry the displacement of the vacancy can be described as a random-walk if the substitutional atoms are indistinguishable and all lattice sites are equivalent. In contrast, the subsequent jumps of a tracer atom are generally correlated ($f < 1$). Some examples for tracer correlation factors in simple three-dimensional structures were reported by Montet [40], i.e., $f = 0.6531$ for a simple cubic lattice, $f = 0.7272$ for a body centred cubic lattice and $f = 0.7815$ for a face centred cubic lattice.

Interstitialcy diffusion

Interstitial atoms are point defects in crystals which can be seen as counterpart of vacancy defects. Although substitutional lattice sites are energetically more favourable self-interstitials occur in thermal equilibrium with a constant concentration, e.g., through the production of Frenkel pairs. If the lattice distortion for direct jumps between interstitial sites is too large self-interstitials may migrate via interstitial-substitutional exchange (I-S) as illustrated in Fig. 2.7. In the so called interstitialcy (or indirect interstitial) diffusion mechanism an interstitial atom pushes one of its nearest-neighbour substitutional atoms into another interstitial site and, in turn, occupies the lattice site of the displaced atom. In general, two types of interstitialcy jumps can be distinguished, i.e., *collinear* and *non-collinear* jumps. If the jump vector of the interstitial atom has the same direction as the jump vector of the substitutional atom the mechanism is denoted as *collinear* (see Fig. 2.7) and it is termed *non-collinear* if the directions differ. Although two atoms are involved in an elementary interstitialcy step a generalised interstitial defect I can be defined that is represented by the atom which is located at an interstitial site. If all substitutional atoms are indistinguishable and the symmetry is high the diffusion of I is uncorrelated in the limit of low defect concentrations. Subsequent

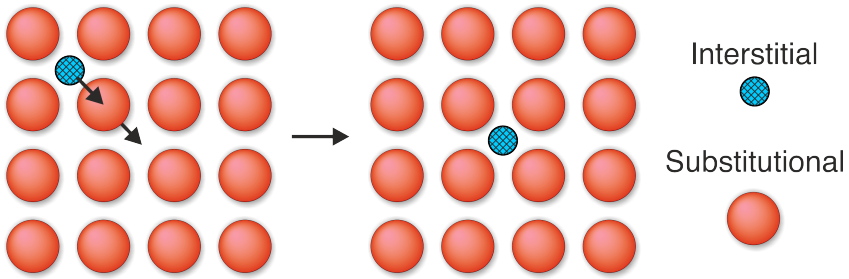

Figure 2.7.: A self-interstitial atom (crosshatched circle) jumps via I-S exchange to a substitutional site. The substitutional atom moves in a collinear jump to an empty interstitial site.

jumps of a tracer atom are, however, dependent on the preceding jumps and the correlation factor is smaller than unity. For example, the collinear interstitialcy diffusion mechanism is related to a correlation factor of $f = \frac{6}{7}$ for diffusion in a simple cubic lattice and $f = \frac{4}{5}$ for a face centred cubic lattice [41].

2.2.4. Microscopic migration energy

According to the above diffusion mechanisms thermally activated migration of atoms in a crystal occurs in a sequence of subsequent discrete jumps from one equilibrium position (lattice site or interstitial site) to the next. For example, the energy for a single jump of a substitutional atom (S) to a neighbouring interstitial site (I) is schematically illustrated in Fig. 2.8 as a function of distance. During the migration from the substitutional site (energy E_{S}) to the interstitial site (energy E_{I}) the jumping atom provokes a distortion of the surrounding lattice which can be expressed as a saddle point energy, E_{SP}. Accordingly, the energy required for this elementary step is given by the migration barrier, i.e., $E^m = E_{\mathrm{SP}} - E_{\mathrm{S}}$ (see Fig. 2.8). This energy is usually large compared to the thermal energy given by $k_{\mathrm{B}}T$, where k_{B} is the Boltzmann constant and T is a temperature. A thermal oscillation of the atoms around their equilibrium positions is therefore much more frequent than successful jumps between sites. The rate at which atoms migrate between sites was described by Vineyard [42], i.e.,

$$w = \nu^0 \exp\left(\frac{S^m}{k_{\mathrm{B}}}\right) \exp\left(-\frac{E^m}{k_{\mathrm{B}}T}\right), \tag{2.28}$$

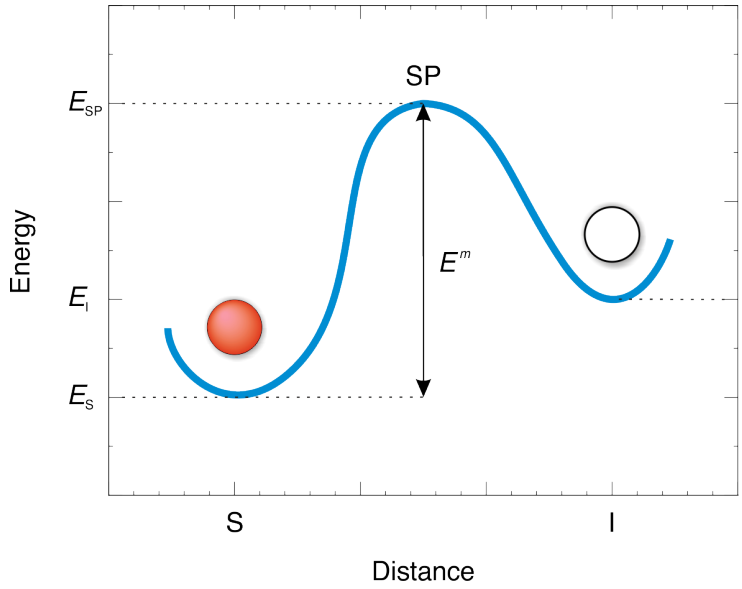

Figure 2.8.: Schematic representation of an energy profile during migration of a substitutional atom (S) via a saddle-point (SP) to an empty interstitial site (I).

where ν^0 is an attempt frequency on the order of the Debye frequency that characterises the lattice vibrations. At high enough temperatures $T \gg h\nu_{\max}/2k_B$, where h is the Planck constant and $\nu_{\max}$ is the maximum phonon frequency, the temperature dependence of ν^0 can be neglected [43, 44]. The entropy of migration S^m relates to the change in lattice vibrations associated with the displacement of the jumping atom from its initial equilibrium configuration to the saddle point configuration.

2.3. Diffusion in binary alloys

In alkali feldspar, the location of substitutional K^+ and Na^+ atoms is restricted to cation sites within the anionic framework structure. It seems therefore attractive to consider the alkali sublattice in feldspar as a binary alloy with negligible interactions with the surrounding framework. Under this assumption well-established methods and conceptions for binary alloys may be transferred to the present diffusion problem.

2.3.1. Random alloy model

An important model to describe disordered multicomponent alloys was introduced by Manning [14, 45] which is called the random alloy model. For a binary alloy of the components $i = \mathrm{A}, \mathrm{B}$ the atoms are randomly mixed and the probability to find an atom of species i on any lattice site is given under the assumption of negligibly low defect concentrations by its site fraction C_i, where $C_\mathrm{A} + C_\mathrm{B} = 1$ holds true. The random alloy model assumes that the rate at which an atom of species i exchanges with a vacancy is given by w_i, whereas this rate only depends on the identity of i and not on the identity of other neighbouring atoms nor on the lattice site. The total vacancy jump frequency is then given by

$$w_\mathrm{V} = z\left(C_\mathrm{A} w_\mathrm{A} + C_\mathrm{B} w_\mathrm{B}\right) , \tag{2.29}$$

where z is the number of nearest-neighbour atoms to a vacancy (coordination number). The diffusion of each species is related to a correlation factor, i.e., f_i. In crystals having sufficient symmetry, the general expression for f_i can be given by [14, 45]

$$f_i = H_i / \left(2w_i + H_i\right) , \tag{2.30}$$

where H_i is the frequency for an effective escape of the vacancy after it has exchanged with an atom of type i. Assuming the general case that $w_\mathrm{A} \neq w_\mathrm{B}$ holds, also the subsequent jumps of the vacancy depend on the preceding jumps and hence, a correlation factor for the vacancy, $f_\mathrm{V} \neq 1$, can be introduced.
Based on this physical model Manning was able to derive mathematical expressions for the correlation factors f_A, f_B and f_V that only hold to a fair approximation. For example, an estimate for the threshold composition for site-percolation ($w_\mathrm{A}/w_\mathrm{B} \to \infty$) is given by $1 - f_0$ where f_0 is the geometrical correlation factor of tracer atoms in the corresponding pure crystal. Moreover, the tracer correlation factors are related to the vacancy correlation factors according to $f_i = f_0 f_\mathrm{V}^i$, where f_V^i is a partial vacancy correlation factor of the species i. Only in the dilute extremes this relation holds and it is violated in the domain of concentrated alloys. In general, the vacancy correlation factors are therefore predicted with a higher accuracy and the Manning model overestimates the tracer correlation factors. In contrast to Manning's analytical framework tracer correlation factors can be computed for the random alloy model, e.g., by Monte Carlo simulations to any desired degree of accuracy.

2.3.2. Frenkel Pair formation

The production of Frenkel defects introduces both vacancies and self-interstitials in a crystal. In terms of quasi-chemical reactions, the Frenkel pair production for a binary alloy AB is given by the reactions

$$\mathrm{E_I} + \mathrm{A_S} \rightleftharpoons \mathrm{A_I} + \mathrm{V} \tag{2.31}$$

$$\mathrm{E_I} + \mathrm{B_S} \rightleftharpoons \mathrm{B_I} + \mathrm{V}\,, \tag{2.32}$$

where $\mathrm{E_I}$ denotes an empty interstitial site, V is a randomised alkali vacancy, $\mathrm{A_S}$ and $\mathrm{B_S}$ are sublattice ions, and $\mathrm{A_I}$ and $\mathrm{B_I}$ are interstitial ions. Assuming that extrinsic defects and similar effects on charge balance can be neglected the charge neutrality condition causes the concentrations of vacancies and interstitials to be equal, so that

$$C_\mathrm{V} = C_\mathrm{I} = C_\mathrm{A,I} + C_\mathrm{B,I} \tag{2.33}$$

holds true. Here, $C_\mathrm{A,I}$ and $C_\mathrm{B,I}$ are the concentrations of self-interstitial $\mathrm{A_I}$ and $\mathrm{B_I}$ atoms, respectively and their concentrations may considerably differ, i.e., $C_\mathrm{A,I} \neq C_\mathrm{B,I}$. Applying the mass action law to Eq. 2.31 yields

$$C_\mathrm{A,I} C_\mathrm{V} = k_\mathrm{F1} = C_\mathrm{A,S} \exp\left(-G_\mathrm{F1}/k_\mathrm{B}T\right), \tag{2.34}$$

where k_F1 is a reaction constant, G_F1 is a free enthalpy of Frenkel pair production and $C_\mathrm{A,S}$ is a site fraction of substitutional $\mathrm{A_S}$ atoms. For simplicity, equal numbers of interstitial and substitutional sites are assumed. For Eq. 2.32, mass action law predicts in a similar way

$$C_\mathrm{B,I} C_\mathrm{V} = k_\mathrm{F2} = C_\mathrm{B,S} \exp\left(-G_\mathrm{F2}/k_\mathrm{B}T\right). \tag{2.35}$$

With the aid of the charge neutrality condition in Eq. 2.33, summation of Eqs. 2.34 and 2.35 gives

$$C_\mathrm{V} C_\mathrm{I} = C_\mathrm{A,S} \exp\left(-G_\mathrm{F1}/k_\mathrm{B}T\right) + C_\mathrm{B,S} \exp\left(-G_\mathrm{F2}/k_\mathrm{B}T\right), \tag{2.36}$$

$$C_\mathrm{I} = C_\mathrm{V} = \left[C_\mathrm{A,S} \exp\left(-G_\mathrm{F1}/k_\mathrm{B}T\right) + C_\mathrm{B,S} \exp\left(-G_\mathrm{F2}/k_\mathrm{B}T\right)\right]^{\frac{1}{2}}. \tag{2.37}$$

By substituting Eq. 2.37 into Eq. 2.34 follows an expression for the concentration of self-interstitials A_I, i.e.,

$$C_{A,I} = \frac{k_{F1}}{C_V} = \frac{C_{A,S} \exp\left(-G_{F1}/k_B T\right)}{\left[C_{A,S} \exp\left(-G_{F1}/k_B T\right) + C_{B,S} \exp\left(-G_{F2}/k_B T\right)\right]^{\frac{1}{2}}}, \tag{2.38}$$

and in a similar way by substituting Eq. 2.37 into Eq. 2.35 gives

$$C_{B,I} = \frac{k_{F2}}{C_V} = \frac{C_{B,S} \exp\left(-G_{F2}/k_B T\right)}{\left[C_{A,S} \exp\left(-G_{F1}/k_B T\right) + C_{B,S} \exp\left(-G_{F2}/k_B T\right)\right]^{\frac{1}{2}}}. \tag{2.39}$$

Finally, the ratio of self-interstitial A_I and B_I is then given by

$$\frac{C_{A,I}}{C_{B,I}} = \frac{C_A}{C_B} \exp\left[-\left(G_{F1} - G_{F2}\right)/k_B T\right]. \tag{2.40}$$

3. Sodium self-diffusion in single-crystal alkali feldspar

Diffusion of alkali cations in alkali feldspar has been investigated over several decades now, but still bears several unresolved problems. Fundamental questions have arisen in the course of recent work by the Vienna group [11, 12, 13] which reveals systematic differences between the experimentally determined Na–K interdiffusion coefficients and those calculated from inserting published Na and K self-diffusion coefficients in theoretical interdiffusion models [14, 15]. In particular, the experimentally determined composition dependence of the interdiffusion coefficient disagrees with the theoretical predictions (cf. Fig. 1.1). In addition, the Na–K interdiffusion is markedly direction dependent, whereas the respective Na tracer diffusion coefficient has so far mainly been investigated by means of bulk diffusion methods applied to grained natural feldspar that do not discriminate between crystal orientations. These discrepancies may indicate that the models in use do not fully account for the complexity of Na–K interdiffusion in alkali feldspar and furthermore, motivate the need for additional direction-dependent self-diffusion data.

Frenkel pairs are likely to be the major point defects in the feldspar structure because the high Si-O bonding energies make Schottky defect formation extremely unfavourable [17]. In general, the vacancy mechanism and the interstitialcy mechanism should therefore be considered as predominant in alkali diffusion processes. Based on the systematic of the available interdiffusion data, it may be hypothesised that the fast tracer diffusion of Na becomes important at close to potassium end-member compositions. In this composition domain, the total Na concentration in the crystal is low and a significant fraction of Na may be present on interstitial sites with high mobility. To enhance modelling of the Na-K interdiffusion process the transport properties on the alkali sublattice should be characterised comprehensively. This involves accurate measurements of the tracer

diffusion coefficients, which will be presented in the present chapter for Na diffusion and in the following chapter for K diffusion.
In this study of Na diffusion in alkali feldspar the radiotracer technique was applied with benefit from ^{22}Na to three natural single-crystal feldspars of different close to potassium end-member compositions, i.e., in the range from 71 % to 95 % K on the alkali sublattice. Data were obtained in the temperature range from 603 K to 1173 K and for three orientations ($\perp$ (001), $\perp$ (010) and $\parallel$ [100]). It will be shown that the results reveal a consistent picture in terms of temperature, orientation, and composition dependence. In particular, a distinctly higher self-diffusion coefficient is observed in the $\perp$ (001) and $\perp$ (010) directions when compared to the direction [100]. The composition dependence suggests that considerable correlation effects diminish Na diffusion when the Na concentration is below a percolation threshold.

3.1. Experimental procedures

3.1.1. Radiotracer diffusion method

The method of radiotracer diffusion has been established over decades and has been widely used in materials physics to investigate diffusion in various solid materials. The technique is dependent on the availability of suitable radionuclides of the relevant element that offer a reasonable long half-life time of typically a few days and longer. Radionuclides are primarily produced in high energy reactions in cyclotron or reactor facilities and to some extend commercially or non-commercially offered and shipped to other institutes. This study of self-diffusion in alkali feldspar via radiotracer diffusion was performed using the isotope ^{22}Na $\left(t_{1/2} = 950\,\mathrm{d}\right)$ that was commercially obtained from Perkin Elmer with an initial specific activity of 830 mCi/mg. A liquid solution of the NaCl salt was further diluted in bi-distilled water to an activity of several kBq/µl to make it readily consumable. A key benefit of radiotracer diffusion is that only extremely small amounts of the tracer are required and that low concentrations (on the order of ppm) of the tracer can reliably be detected quantitatively after a diffusion experiment. The sample material may therefore be considered as chemically unchanged which considerably simplifies the evaluation of a self-diffusion experiment when compared to chemical diffusion. The steps of the radiotracer diffusion technique are consecutively (cf. Fig. 3.1): (i) Deposition of the radiotracer on the polished sample surface normal to the

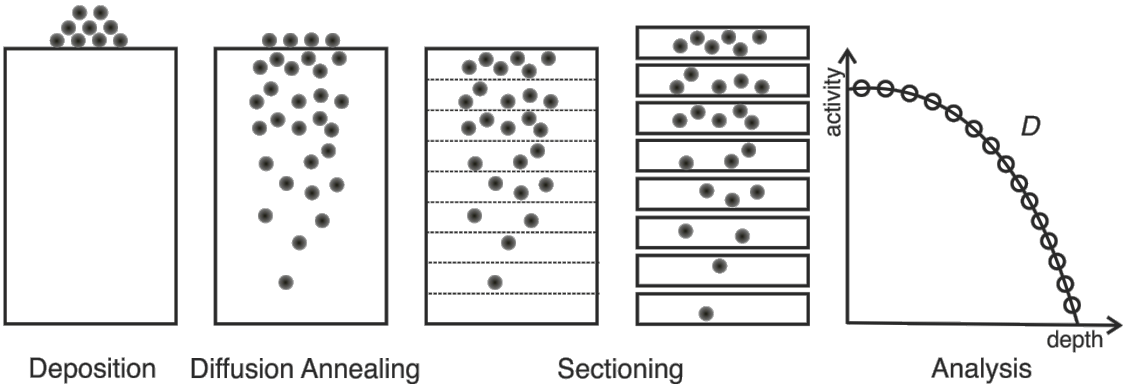

Figure 3.1.: Schematic presentation of the radiotracer diffusion method that comprises the following steps: (a) Deposition of the radiotracer diluted in water with a pipette on the sample surface. (b) Temperature treatment for activation of diffusion processes in a tube or mirror furnace. (c) Serial sectioning of the sample by mechanical grinding or ion beam sputtering. (d) Analysis of the sections activity and evaluation of the depth profile to determine the diffusion coefficient D.

(virtually one dimensional) diffusion direction. (ii) Isothermal diffusion treatment at an annealing temperature T for a suitable length of time t. (iii) Serial sectioning of the sample parallel to the front surface accompanied by a determination of the mass loss after each repetition. (iv) Analysis of the individual sections in a gamma radiation detector. The thereby determined activity of each section can directly be related to the relative tracer concentration within this section. This relative tracer concentration as a function of penetration depth is referred to as the diffusion profile and can be evaluated by a suitable solution of the diffusion equation, that is in most cases either a Gaussian or a complimentary error function depending on the boundary conditions. Least-square fitting of either of these functions to the measured diffusion profile yields the diffusion coefficient D. Most consistent results are commonly obtained by using the logarithmic form of the diffusion equation for fitting procedures.

Diffusion Annealing

The isothermal treatment applied in this study is divided into two methods. For long-time temperature treatments $\geq 3\,\mathrm{h}$ annealing in a commercially available tube furnace was preferred. Prior to the annealing the sample material was encapsuled in a quartz ampule under Ar atmosphere to protect the sample from oxidation and the furnace from evaporation of the radioactive substances. At the end of the annealing

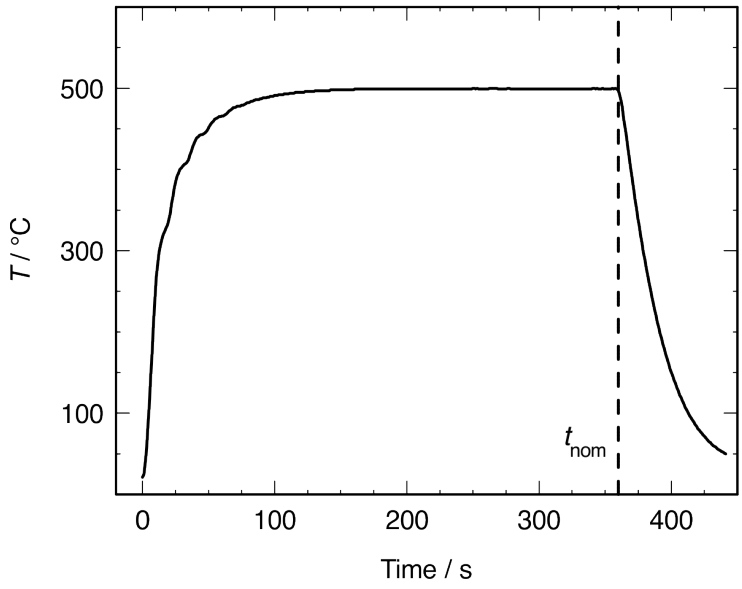

Figure 3.2.: Temperature-time profile of a thermal treatment performed with an alkali feldspar sample at 500 °C and a diffusion time of 5 minutes in a custom-built mirror furnace. The nominal annealing time of $t_{\mathrm{nom}} = 6$ minutes is marked with a dashed line.

the ampule was quenched in water for rapid abortion of the diffusion process. Although the heating-up procedure may take several minutes by this method, the experimental error in diffusion time only amounts to a few percent for the shortest annealing duration.

For a short annealing duration of down to 5 min a custom-built mirror furnace that offers rapid heating and cooling properties was used. The samples were contained in custom boron-nitride crucibles and placed on top of a Pt-PtRd thermocouple in a vertically mounted quartz ampule. During the isothermal treatment, the quartz ampule was evacuated to medium vacuum conditions of $p < 10^{-1}$ mbar. Four industrial 2 kW lamps are each mounted in the focal point of a paraboloid and operated by a PID controller to obtain a rapid heating. The quartz ampule is flushed with LN_2 to stop the diffusion process. Figure 3.2 shows a typical temperature-time profile that was recorded with the time interval Δt by the internal Pt-PtRd thermocouple. It is representative for a diffusion annealing at 500 °C for 5 minutes. Based on a well-known temperature activation of the diffusivity $D(T)$, the effective annealing time may be given by [46]

$$D\left(T_{\mathrm{nom}}\right) t_{\mathrm{diff}} = \sum_{t=0}^{\infty} D(T(t))\Delta t \tag{3.1}$$
$$\rightarrow t_{\mathrm{diff}} = \left(\sum_{t=0}^{\infty} \exp\left(-\frac{\Delta H}{k_{\mathrm{B}} T(t)}\right)\Delta t\right) / \exp\left(-\frac{\Delta H}{k_{\mathrm{B}} T_{\mathrm{nom}}}\right),$$

where ΔH denotes an activation energy and k_{B} is the Boltzmann constant. According to Eq. 3.1 a rule of thumb for the effective diffusion time was found to be $t_{\mathrm{diff}} = t_{\mathrm{nom}} - 1\,\mathrm{min}$ for diffusion runs on the order of 5 minutes. For longer run times of $t_{\mathrm{diff}} \geq 10\,\mathrm{min}$ the relation $t_{\mathrm{diff}} = t_{\mathrm{nom}} - 30\,\mathrm{s}$ holds.

Serial Sectioning

Depending on the estimated volume penetration depth $\sqrt{Dt}$ (D is the bulk diffusion coefficient and t is the annealing time) of a diffusion experiment one of two different serial sectioning techniques was applied to achieve depth profiling. For diffusion coefficients of roughly $D \geq 10^{-15}\,\mathrm{m}^2/\mathrm{s}$ the penetration depth ranged from approximately 10 µm to 100 µm and the precision grinding technique was employed. Small sections of a few µm thickness were cut in parallel to the front surface by machine-support and collected on the lapping film. The residual mass of the sample material was measured with a micro balance (Sartorius, readability of 0.1 µg) to determine the thickness pertaining to each section via the sample's surface area and its density.

For smaller penetration depths of 1 µm to 4 µm that are usually connected to diffusion coefficients of $D \leq 10^{-15}\,\mathrm{m}^2/\mathrm{s}$ a high-resolution depth profiling was achieved by ion beam sputtering of the sample material. A unique apparatus was designed and built at the Institut für Materialphysik for this purpose [47] that comprises the following features: (i) A commercially available 3 cm dc ion beam source operated at beam voltages of up to 1.2 kV. (ii) A chilled Cu sample holder that is constantly rotated during depth profiling that improves uniform removal of the sample surface. (iii) A Mylar film is used as substrate for the removed sample material. It is automatically transported by an electronic tape station to achieve discrete sample sections. (iv) A dedicated slow control to operate the depth profiling with a minimum of user interaction.

In contrast to mechanical serial sectioning the sample material is continuously removed during this procedure which does not allow for mass measurements of

each single section. The ion beam is therefore operated for 30 min prior to the actual depth profiling while the sample is covered by a shutter in order to maintain stable beam conditions. The sample's complete mass loss is then determined by measurements before and after sputtering. Calibration of the length axis is achieved by considering all sections equal in mass and with the knowledge of the material density. A steel capsule with a fixed aperture that is mounted on top of the sample during depth profiling determines the sample area. To avoid any influences from the residual tracer source on the diffusion profile the source was removed from the sample surface by wiping with a cotton stick and ethanol.

Gamma Analysis

After depth profiling each section was put in a vial for further analysis in a $3'' \times 3''$ well-type (4π) NaI-detector. A gamma energy spectrum that is representative for the decay of ^{22}Na measured by this detector is shown in Fig. 3.3a. Three isotope specific peaks at energies of 511 keV, 1022 keV and 1275 keV are observed which can be attributed to the decay scheme (cf. Fig. 3.3b) of ^{22}Na as follows: The 511 keV peak results from positron annihilation due to the 90 % probability [48] of an β^+ decay of ^{22}Na into ^{22}Ne* which produces two events related to the mass of one electron and one positron, respectively. In the case of a simultaneous absorption of both photons in the detector (i.e., when electron and positron annihilate in the detector's centre) this event cannot be discriminated from a single photon with twice of the energy. These events produce a sum peak at an energy of 1022 keV. The excited state of ^{22}Ne* turns into its ground-state under emission of a single photon with the energy of 1275 keV and results the photopeak. The net peak areas N_{511}, N_{1022} and N_{1275} were evaluated after $N = 20000$ total detector events and the activity was given by

$$A = \left(\frac{N_{511} + N_{1022}}{1.8\eta_{511}} + \frac{N_{1275}}{\eta_{1275}} \right) t^{-1} , \tag{3.2}$$

where t is the total counting time and η_{511} and η_{1275} are the energy-dependent detector efficiencies for the energy of 511 keV and 1275 keV, respectively. The detector efficiencies were analysed with the aid of suitable calibration sources and the experimental uncertainty resulting from the gamma analysis can be estimated by $\sqrt{N}/N$ to 3 % for the 511 keV peak.

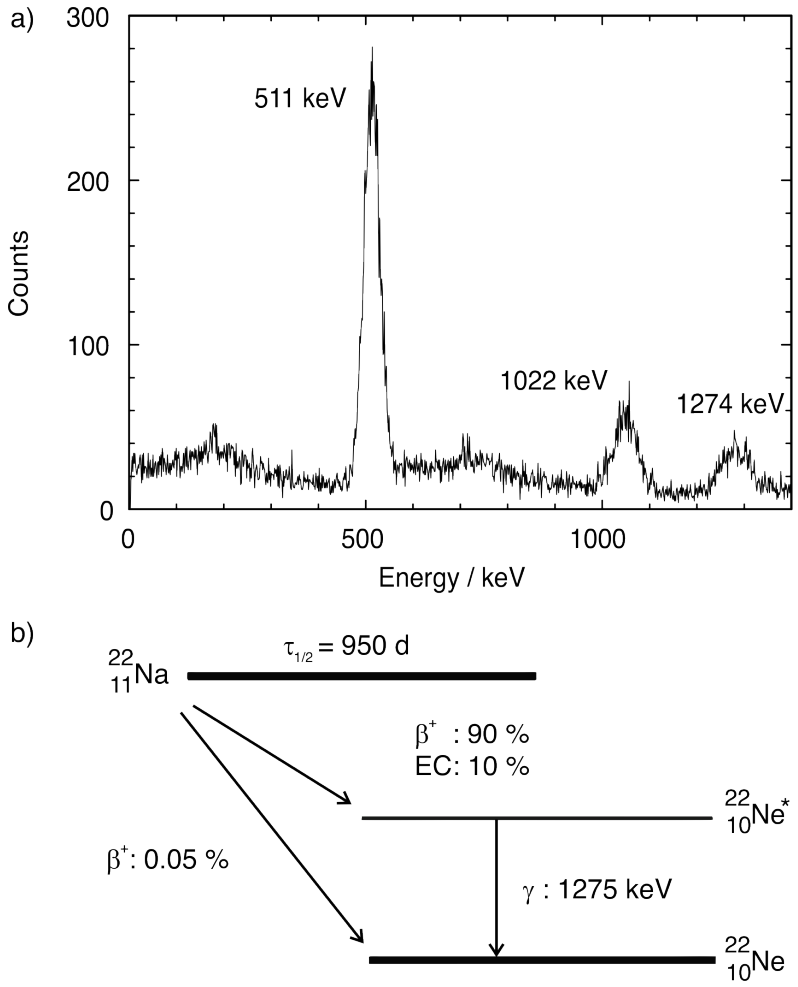

Figure 3.3.: (a) Gamma ray spectrum of ^{22}Na measured in a $3'' \times 3''$ well-type NaI detector after $t = 12\,\mathrm{s}$ counting time. The activity is representative for a surface near section after diffusion annealing. Three major peaks at $511, 1022$ and $1275\,\mathrm{keV}$ are observed, that can be attributed to positron annihilation, the sum peak for simultaneous detection of this process and the photopeak, respectively. (b) A schematic view of the decay from ^{22}Na into ^{22}Ne* and ^{22}Ne with the according decay probabilities and photon energy [48].

3.1.2. Sample Preparation

Macroscopically large samples are required for the radiotracer diffusion method in order to deposit the tracer solution in the centre of the front surface and to avoid diffusion across the edges. The minimum sample dimension in diffusion direction should favourably be several times larger than the intended volume penetration depth $\sqrt{Dt}$, which is typically smaller than 100 µm in the present study. Furthermore, should the sample surface be polished and cleaned before the radiotracer is deposited because the surface roughness has an impact on diffusion profiles for small penetration length (cf. Eschen et al. [49]).
The sample material was prepared from large single crystals of natural feldspars at the University of Vienna. The lattice orientation was determined with a four-circle goniometer and the samples where cut from the large crystal to plates of approximately 8 mm in diameter and 2 mm in height, with a surface corresponding either to the (001) or (010) plane or to a plane that is normal to the [100] direction. Subsequently, the samples were pre-polished by hand on a diamond polishing disc and finally polished on a silk cloth with a 1 µm diamond powder suspension. Because only a small volume of the sample was destructed during each depth profiling and the sample dimension along the diffusion direction was sufficiently large, several radiotracer diffusion experiments were performed with each sample. After each depth profiling the sample surface was repeatedly cut until no measurable activity was contained in the sample and then polished with 3 µm SiC lapping film.

3.2. ^{22}Na diffusion results

Three natural feldspars from different localities and with different compositions were chosen for the radiotracer diffusion experiments. Ordered according to increasing K-concentration these are (i) a sanidine from the Eifel region Rockeskyll, Germany (RK) with the chemical composition $Or_{71}Ab_{26}Cs_2$ and with a minor FeO concentration of about 0.1 to 0.2 weight%. (ii) A sanidine from the Eifel region Volkesfeld (VF) with the composition $Or_{83}Ab_{15}Cs_1$ and with a similar FeO concentration as the RK sanidine. (iii) An orthoclase from Madagascar (MO) with a low Ba concentration and a composition given by $Or_{95}Ab_5$ that contains about 1 weight% FeO. The detailed chemical analysis and structural properties of these feldspars are described in Section 2.1. The study of Na-diffusion in MO feldspar

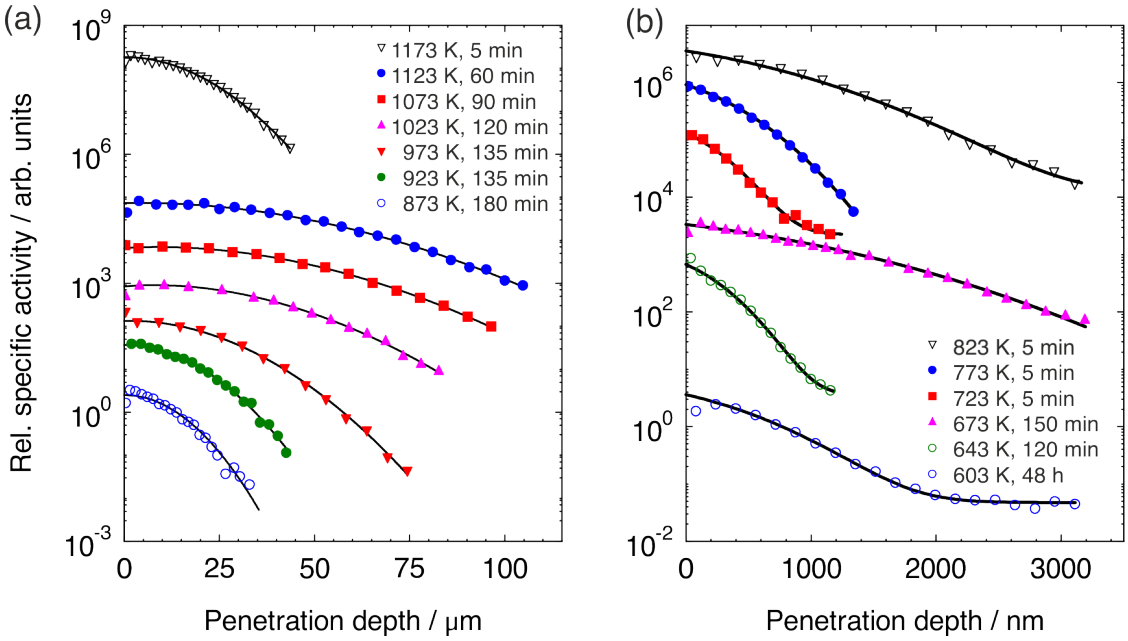

Figure 3.4.: Diffusion profiles of ^{22}Na in alkali feldspar $Or_{83}Ab_{15}Cs_1$ from Volkesfeld (VF) normal to (001) for different annealing temperatures T. To enhance visibility of all slopes the relative concentrations are individually shifted along the ordinate. (a) The profiles are representative for depth profiling by micro grinding and solid lines are fitted to the measured profiles by a Gaussian function. (b) Ion beam sputtered depth profiles are fitted with a complementary error function (solid lines).

$\perp$ (001) and $\perp$ (010) was conducted in the framework of the master thesis of B. Tas Kavakbasi [50] whereas the Na-diffusion in MO feldspar along the direction [100] and in RK feldspar $\perp$ (001) and $\perp$ (010) was investigated in the master thesis of A. Knieschewski [51].

The results for 75 radiotracer diffusion experiments in a temperature interval from 603 K to 1173 K are listed in Tab. A.1 (cf. Appendix A). For a reliable determination of the Na self-diffusion coefficients[1] $\widehat{D}_{\mathrm{Na}}$, tracer penetration profiles were analysed over an activity range of at least a factor of 20 and in most cases over roughly two orders of magnitude. Examples of measured profiles that are representative for serial sectioning by grinding are shown in Fig. 3.4a. To prevent overlapping and intersecting data, the measured profiles were individually shifted along the ordinate. Since thin-film source conditions are expected for high annealing temperatures, a Gaussian solution of the diffusion equation is applied to the diffusion profiles

[1] To reduce the number of indices, the common asterisk for labelling tracer diffusivity (D^*) has been replaced by the 'hat' symbol ($\widehat{D}$) throughout this work.

(cf. Eq. 2.9). In some cases, evaporation of the tracer from the surface, which is expressed by a characteristic concentration decline towards the sample surface can be observed and an adapted function given by Eq. 2.17 is applied.
Depth profiling by ion beam sputtering was employed for penetration lengths on the order of $\sqrt{Dt} = 1\,\mu\text{m}$ and an example of representative diffusion profiles is shown in Fig. 3.4b. Because of smaller $\sqrt{Dt}$ values the boundary conditions of diffusion are better described by a constant source and hence fitting to the measured profiles is achieved by a complementary error function (cf. Eq. 2.14). In some cases, a low constant background concentration is observed, that can be caused by residual ^{22}Na from previous radiotracer diffusion experiments. For these cases the diffusion profiles are well described by a complementary error function that is extended with a constant concentration term. The derived diffusion coefficients for Na-diffusion in RK, VF and MO are listed in Tab. A.1 together with the corresponding annealing temperatures T and time durations t.
The temperature dependence of self-diffusion can be described by the Arrhenius relation

$$\widehat{D}_{\text{Na}}(T) = D_0 \exp\left(-\frac{\Delta H}{k_{\text{B}} T}\right), \tag{3.3}$$

where D_0 is a pre-exponential factor, k_{B} is the Boltzmann constant and ΔH denotes an activation energy. In Fig. 3.5 the Na self-diffusion coefficients for diffusion in RK, VF and MO normal to (001) and in MO in the direction [100] are shown on a logarithmic scale as a function of the inverse temperature together with the Arrhenius relations that are fitted to the data points. Accordingly, in Fig. 3.6 the Na diffusion in RK, VF and MO normal to (010) is presented with the fitted Arrhenius relations. All slopes represent the diffusion data fairly well or well. However, for VF normal to (001) the data at $T = 673$ and 723 K were neglected in the fitting procedure because of deviations that are considerably higher than statistical uncertainties. The resulting activation energies and pre-exponential factors for all Arrhenius relations are presented in Tab. 3.1.

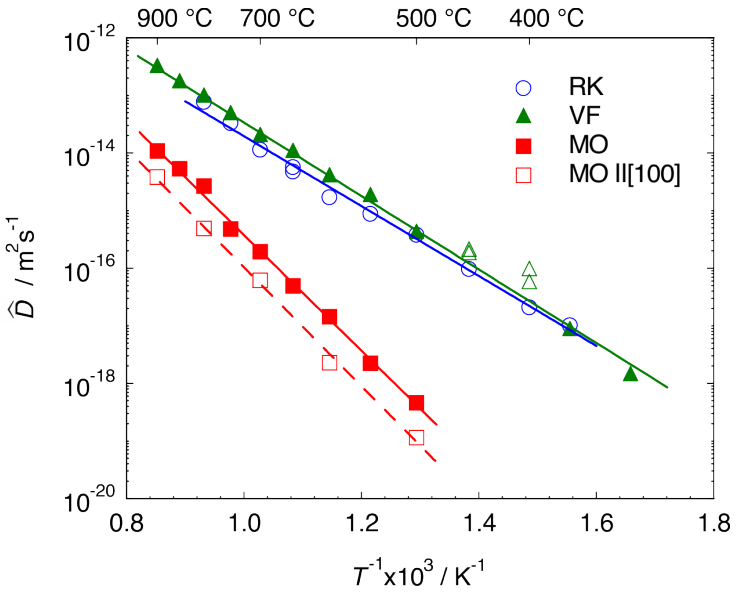

Figure 3.5.: Arrhenius plot of the diffusion coefficients of ^{22}Na in the alkali feldspars RK (open circles [51]), VF (full triangles, open triangles were neglected in the fitting procedure) and MO (solid squares [50]) normal to (001) and in MO parallel to [100] (open squares [51]). Solid and dashed lines correspond to fitting to the experimental data with the Arrhenius relation in Eq. 3.3. The experimental uncertainties of 30 % are smaller than the symbol size.

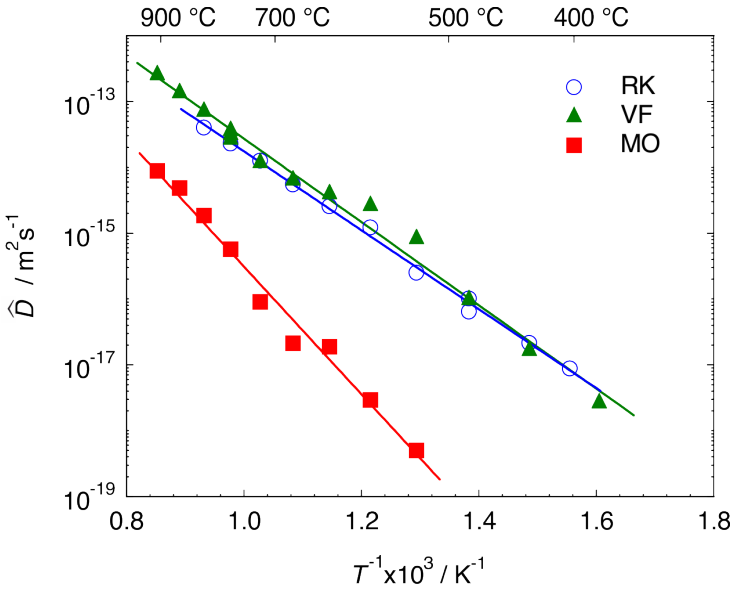

Figure 3.6.: Arrhenius plot of the diffusion coefficients of ^{22}Na in the alkali feldspars RK (open circles [51]), VF (full triangles) and MO (solid squares [50]) normal to (010). Solid lines correspond to fitting to the experimental data with the Arrhenius relation in Eq. 3.3. The experimental uncertainties of 30 % are smaller than the symbol size.

Table 3.1.: Activation energies and pre-exponential factors related to Na self-diffusion in single-crystal alkali feldspar.

Feldspar	Direction	$D_0/\mathrm{m^2 s^{-1}}$	$\Delta H/\mathrm{eV}$
RK	$\perp$ (001)	$\left(2.3^{+1.4}_{-0.9}\right) \times 10^{-8}$	1.20 ± 0.04
RK	$\perp$ (010)	$\left(1.7^{+0.8}_{-0.6}\right) \times 10^{-8}$	1.19 ± 0.03
VF	$\perp$ (001)	$\left(8.0^{+2.4}_{-1.9}\right) \times 10^{-8}$	1.27 ± 0.03
VF	$\perp$ (010)	$\left(5.8^{+4.4}_{-2.5}\right) \times 10^{-8}$	1.26 ± 0.04
MO	$\perp$ (001)	$\left(4.1^{+2.6}_{-1.6}\right) \times 10^{-6}$	2.00 ± 0.04
MO	$\perp$ (010)	$\left(1.5^{+3.2}_{-1.1}\right) \times 10^{-6}$	1.92 ± 0.10
MO	[100]	$\left(2.1^{+2.6}_{-1.2}\right) \times 10^{-6}$	2.05 ± 0.07

3.3. Conclusions

3.3.1. Diffusion anisotropy

The direction dependence of Na self-diffusion shows consistent results along the three investigated feldspars RK, VF and MO. In all cases the Arrhenius relation for the direction normal to (001) is equal to the corresponding relation for the direction normal to (010) within the range of experimental uncertainties. For the K-rich MO feldspar it was additionally possible to prepare samples with a surface that corresponds to the plane normal to the [100] direction. The diffusion coefficients that were obtained for this direction are three to four times smaller along the investigated temperature range when compared with the direction normal to (001). In contrast to the self-diffusion results, the Na-K interdiffusion that has been investigated recently by the Vienna group shows a considerable anisotropy between the directions normal to (001) and normal to (010) i.e. $\tilde{D}_{\perp(001)} \approx 10\tilde{D}_{\perp(010)}$ [11, 12, 13]. It can therefore be concluded that this clear anisotropy is rather caused by diffusion induced lattice strain [16] or by a hypothetically strong anisotropy of the K self-diffusion than from direction effects of the Na self-diffusion.

3.3.2. Composition dependence of Na self-diffusion

Interestingly, the Na self-diffusion exhibits a considerable dependence on composition. Despite the different composition of VF sanidine ($Or_{83}Ab_{15}Cs_1$) compared to RK sanidine ($Or_{71}Ab_{26}Cs_2$) the corresponding diffusion coefficients virtually overlap. For the most K-rich MO feldspar under investigation the diffusion coefficients are 20 to 900 times smaller than those observed for the Eifel sanidines VF and RK. The activation energy of MO feldspar is increased by $\sim 0.7\,\mathrm{eV}$ when compared to the Eifel sanidines, which goes along with a significantly increased value of D_0 (cf. Tab. 3.1). For many thermally activated processes the relation of an increased pre-exponential factor with increasing activation energy has been observed and is denoted as compensation or Meyer-Neldel rule. This rule states that D_0 and ΔH obey the equation $\ln D_0 = a + b\Delta H$ for large activation energies of $\Delta H \geq 1\,\mathrm{eV}$ [52]. From a microscopic point of view this can be interpreted as an exponential relation between the number of different paths to the final state and ΔH. The composition dependence of the activation energy could result from several contributions that are discussed in detail.

Effects resulting from different unit cell volumes

From simple elastic considerations, it can be expected that differences in the unit cell volume cause changes in the migration barrier for atomic migration. In alkali feldspar the unit cell parameter a increases from the Na-rich albite (8.16 Å) to the K-rich sanidine (8.60 Å) by approximately 5 %, whereas the same but weaker effect is observed for the cell parameters b and c that is on the order of 1 % [53]. The larger cell volume reduces the energy barrier of atomic migration in feldspar considerably, which has been demonstrated by Jones et al. for a vacancy mediated diffusion mechanism [54]. In this study, the bottleneck widths for three different ion pathways within the (010) plane were calculated with the according migration barriers for K^+ ions by molecular dynamics methods. Significant differences for the migration barriers that range from 0.99 eV to 2.92 eV were found, whereat it should be noted that long range diffusion can only occur if ions subsequently migrate via all three pathways. Unfortunately, the study specifies the analogue Na migration barriers only for the energetically most favourable pathway and conclusions on the total activation energy of Na diffusion via a vacancy diffusion mechanism would therefore be vague. However, the decreased migration barrier for the energetically most favourable pathway from 1.31 eV for albite compared to

Table 3.2.: Calculated energy barriers and bottleneck widths for vacancy diffusion of Na and K in albite and K-feldspar after Jones et al. [54].

Interstitial ion at saddlepoint	Energy / eV	Bottleneck width / Å	
		Unrelaxed	Relaxed*
K^+ ion in albite	1.86	4.57	5.22
Na^+ ion in albite	1.31	4.57	4.70
K^+ ion in K-feldspar	0.99	5.57	5.65
Na^+ ion in K-feldspar	0.70	5.57	5.30

* Ion at saddlepoint

0.70 eV for K-feldspar that is caused by the volume gain can be assumed to have a clear effect on the composition dependence of Na self-diffusion (cf. Tab. 3.2). In the relatively narrow composition range from MO to VF the same positive correlation would be expected between the migration energy and the Na concentration, but with a weaker expression than in Jones calculations. The present experimental observations, however, are in clear contradiction to this effect. Consequently, an opposed effect which superposes the influence of the composition-dependent unit cell volume on the activation energy must exist.

Effects from Frenkel pair production

Behrens et al. recognized that Frenkel pairs (FP) are energetically more favourable in feldspar than Schottky pairs and are therefore the major point defects [17]. Since the self-diffusion coefficient behaves proportional to the defect concentration, this quantity should be estimated for MO and VF feldspar to obtain further assumptions on the differences in Na diffusivities. The reaction rates for FP production are

$$\mathrm{E_I} + \mathrm{K_S} \rightleftharpoons \mathrm{K_I} + \mathrm{V} \tag{3.4}$$

$$\mathrm{E_I} + \mathrm{Na_S} \rightleftharpoons \mathrm{Na_I} + \mathrm{V}\,, \tag{3.5}$$

where $\mathrm{E_I}$ denotes an empty interstitial site, V is a randomized alkali vacancy, $\mathrm{K_S}$ and $\mathrm{Na_S}$ are sublattice ions, and $\mathrm{K_I}$ and $\mathrm{Na_I}$ are interstitial ions. Applying mass

action law to this equation yields an expression for the sum of concentrations of interstitial K_I and Na_I defects, i.e., (cf. Section 2.3.2)

$$C_{K,I} + C_{Na,I} = \left[C_K \exp\left(-G_K^{FP}/k_B T\right) + C_{Na} \exp\left(-G_{Na}^{FP}/k_B T\right)\right]^{1/2}, \qquad (3.6)$$

where, e.g., $G_{Na}^{FP} = H_{Na}^{FP} - TS_{Na}^{FP}$ can be decomposed into the corresponding enthalpy and entropy contributions and C_K and C_{Na} are the relative concentration of substitutional K and Na atoms on the alkali sublattice, respectively. It may be further assumed that (dissociated) Na_I–V pairs can be more easily formed than the corresponding K_I–V pairs, so that very likely $H_K^{FP} > H_{Na}^{FP}$ holds. For a virtual C_{Na}-independent value of G_{Na}^{FP} it can be estimated

$$C_{Na,I}^{VF}/C_{Na,I}^{MO} \approx \left(C_{Na}^{VF}/C_{Na}^{MO}\right)^{1/2} = (0.15/0.05)^{1/2} \approx 1.7\,,$$

where C_{Na}^{VF} and C_{MO}^{VF} are related to VF and MO feldspar, respectively. It is therefore unlikely that this effect accounts for the clearly different Na diffusion coefficients between MO and the Eifel sanidines.

Correlation effects

From early studies on the correlation effects in a random bcc alloy [20, 21, 22] and in a random fcc alloy [20, 22, 23, 24] it can be deduced that the Na diffusion in the investigated feldspars is affected by considerable correlation effects, if the alkali sublattice is characterised as a random alloy of K and Na atoms that do not interact with the framework silicate. This effect is particularly pronounced if the jump frequencies of Na and K are largely different, i.e., if $w_{Na} \gg w_K$ holds. Under this assumption the Na diffusion can be interpreted by the percolation theory in which the present diffusion problem corresponds to site-percolation. According to this, long-range diffusion of Na under the hypothetical assumption of virtually immobile K ions $w_K = 0$ can only occur if C_{Na} is equal or larger than a threshold concentration. A giant component of connected Na sites always exists under this circumstance and the vertex degree in this theory can be interpreted as the number of nearest-neighbour sites z of a substitutional atom. Unfortunately, an exact and general solution for the percolation on graphs is not known so far and hence this problem has to be treated with numerical methods. However, it may tentatively be concluded from these considerations that the significant increase in activation energy from VF to MO feldspar is caused by a transition from percolated to non-

percolated diffusion that leads to a strong reduction of the correlation factor f that is related to Na self-diffusion. The correlation factor f in binary or multicomponent alloys has an effect on the activation energy according to $\Delta H = H^m + \frac{1}{2}H^f_{\mathrm{FP}} + Q^f$, where H^m is the migration enthalpy of atomic jumps, H^f_{FP} is the Frenkel pair formation enthalpy and $Q^f = -k_{\mathrm{B}} \ln f / \ln 1/T$ holds. The present thesis therefore has a focus on the calculation of correlation effects, which will be systematically addressed using the example of a simple cubic random alloy in Chapters 6, 7 and 8 and more specifically for the alkali feldspar structure in Chapters 6 and 9.

4. Potassium self-diffusion in a K-rich single-crystal alkali feldspar

Most studies on alkali diffusion in alkali feldspar concern the sodium component because of the availability of the radioisotope ^{22}Na with a half-life of $t_{1/2} = 2.6\,\mathrm{a}$ and its suitability for the radiotracer method (see, e.g., the review by Cherniak [55]). Potassium self-diffusion has hitherto been investigated by Lin and Yund [6] by using the long-lived radioisotope ^{40}K $\left(t_{1/2} = 1.3 \times 10^9\,\mathrm{a}\right)$ and by Foland [8] by using the stable isotope ^{41}K (natural abundance of 6.7 %). In both studies, a bulk-exchange method was employed to investigate grains from crushed feldspar. An advantage of this method is that there is no need for large and almost perfect single-crystal alkali feldspar samples, which are rare in nature and cannot be synthesised. However, this method is unable to provide any information about tracer depth distributions and suitable diffusion models must therefore be presumed, making it non-sensitive to inherent features such as diffusion anisotropy or structural inhomogeneities. Moreover, these minerals have not been investigated by impedance spectroscopy and therefore, these diffusion coefficients cannot be compared to ionic conductivity data.

The diversity of investigated alkali feldspars and applied methods has made it difficult to reliably link existing studies with each other and to discuss the underlying mechanisms of alkali diffusion based on sound arguments. So far, it was found that activation energies of K and Na self-diffusion clearly differ so that the ratio of diffusion coefficients $\widehat{D}_{\mathrm{Na}}/\widehat{D}_{\mathrm{K}}$[1] is approximately 1000/1 at 1000 °C [17] for the K-rich orthoclase and approximately 600/1 at 800 °C [9] for the Na-rich albite. Frenkel pairs are likely to be the major point defects in the feldspar structure because the high Si-O bonding energies make Schottky defect formation extremely unfavourable [17]. In general, the vacancy mechanism and the interstitialcy mechanism should

[1] To reduce the number of indices, the common asterisk for labelling tracer diffusivity (D^*) has been replaced by the 'hat' symbol ($\widehat{D}$) throughout this work.

therefore be considered as predominant in alkali diffusion processes. In the latter mechanism, an interstitial Na_I or K_I atom moves by "pushing" a substitutional alkali ion to a neighbouring interstitial site. A further crucial diffusion mechanism is based on direct interstitial jumps of an interstitial ion to a neighbouring interstitial site without exchanging with substitutional atoms of the alkali sublattice.

Self-diffusion of atoms in binary (Na, K sublattice) or multicomponent systems is generally affected by correlation effects among individual atomic movements. The jump direction of a labelled self-atom (tracer) depends on the relative position of the point defect next to it. After a first exchange, the atom is still in direct vicinity to the point defect and therefore has an increased probability for a consecutive jump in reversed direction. This *geometric* correlation effect is influenced by the diffusion mechanism as well as the pertaining crystal structure and can be expressed by correlation factors f in the range $\frac{1}{3} \leq f \leq 1$ [19]. In addition, the distribution of Na and K atoms in the environment of a tracer atom causes a *physical* correlation effect that arises from differences in the temperature dependent jump frequencies ($w_K/w_{Na} \ll 1$) of these components. Influenced by chemical composition and the diffusion mechanism this correlation is potentially strong since both components share the same sublattice. Below a certain site fraction of Na, commonly referred to as percolation threshold p^c, diffusion pathways of the faster moving ions (Na) lose their percolation ability and the Na diffusion coefficient becomes dependent on the jump frequencies of the slower ions (K). A quantitative analysis of correlation effects (e.g. through Monte Carlo simulations which will be presented in Chapters 6, 7, 8 and 9) is an approach to unravel the underlying diffusion mechanisms of alkali diffusion in alkali feldspar, but requires the most precise experimental results available.

The present results on potassium self-diffusion are based on direction-sensitive serial sectioning of gem-quality single-crystal alkali feldspar and the use of ^{43}K $\left(t_{1/2} = 22.3\,h\right)$ as radiotracer. A natural sanidine from Volkesfeld (VF), Germany, that was also investigated in the previous Chapter 3 about Na self-diffusion in the same crystallographic direction, i.e., normal to (001), and in one recent study on ionic conductivity by El Maanaoui et al. [56], as well as for ionic conductivity measurements that will be presented in Chapter 5 was selected as sample material. This allows us to compare alkali transport properties with ionic conductivity in a reliable way. The present study has been published in Physics and Chemistry of Minerals, 2017 [57].

4.1. Experimental procedures

4.1.1. Sample material

In the present chapter, radiotracer measurements of the ^{43}K-diffusion in the framework silicate alkali feldspar (K,Na) [$AlSi_3O_8$] are demonstrated. The investigated material is a natural sanidine from the Eifel, Germany, that was also used for Na self-diffusion measurements (cf. Chapter 3) and is denoted as Volkesfeld (VF) feldspar. For alkali feldspar from the VF provenance the detailed chemical analysis was given by Hofmeister and Rossman [58] and by Demtröder [33] based on electron microprobe analyses (EMPA). The chemical composition of the alkali sublattice is of special interest when K and Na self-diffusion and the diffusion correlation effects pertaining to this are interpreted. Based on the EMPA data the K to cation ratio is approximately $C_\mathrm{K} = c_\mathrm{K}/\left(c_\mathrm{Na} + c_\mathrm{K} + c_\mathrm{Ba} + c_\mathrm{Fe}\right) = 0.83$ (and accordingly $C_\mathrm{Na} = 0.15$) , where C is a site fraction of atoms and c is a concentration in atoms per volume.

The sample pieces where cleaved from a large single crystal along the (001) cleavage plane, cut to a size of approximately 8 mm in diameter and 2 mm in height, pre-polished by hand on a diamond polishing disc and finally polished on a silk cloth with a 1 µm diamond powder suspension. The samples did not intendedly undergo any thermal treatment[2] before the ^{43}K implantations were carried out. After completion of the radiotracer experiments the samples were examined by energy-dispersive X-ray spectroscopy (EDS) for signs of Na-K interdiffusion. Since only a limited volume of the samples was destructed by radiotracer depth-profiling, the near-surface chemistry could be measured and compared to the chemistry at the floor of the etch crater. The resulting EDS maps showed no traceable changes in Na and K concentrations, which indicates that the self-diffusion experiments were not influenced by interdiffusion of these components with the ambience.

For further validation, the sample that was annealed at the lowest temperature, i.e., 1021 K, was subjected to depth-profiling by secondary ion mass spectrometry (ToF-SIMS) at the TU Vienna. This measurement showed no considerable changes in sample chemistry along the investigated depth range. However, ToF-SIMS

[2] [59] reported an unusual fast Al-Si exchange of the VF feldspar compared to other alkali feldspars when heated dry. This effect disappears when the VF feldspar is heated at elevated temperatures $\geq 1050\,^\circ$C for several days. In the present study, any thermal pre-treatment is refrained in order to investigate the VF feldspar under its natural condition, just as in the previous measurements of Na diffusion.

measurements of the 1173 K sample revealed a considerable depletion of Na towards the sample surface whereas K, Al and Si signals remained almost constant over the investigated depth range. By further EDS measurements it could be demonstrated that this observation is probably related to the fact that the investigated spot was in direct contact to a Macor ceramic sample holder during an earlier diffusion experiment using the opposite side of the same sample, and hence this finding does not relate to the sample chemistry within the volume that was examined by the radiotracer experiments.

4.1.2. Implantation and radiotracer experiments

Implantations of ^{43}K with an energy of 50 keV were carried out at the radioactive ion-beam facility ISOLDE at CERN with doses of 4.0×10^{11} atoms cm^{-2}. The collimated ion beam was cut to a size of 5 mm × 5 mm and γ-ray spectra showed no contamination with other γ-emitting isotopes. The corresponding projected range x_0 of ^{43}K in alkali feldspar was determined with an implanted, but otherwise thermally untreated control sample (the same method as for the diffusion measurements was applied and is described below). The measured depth distribution is fairly well described by a Gaussian function

$$C(x) = C_0 \exp\left(-\frac{(x - x_0)^2}{2\sigma^2}\right) \tag{4.1}$$

with a peak concentration C_0 at $x_0 = 54$ nm and a mean width of $\sigma = 26$ nm. In Fig. 4.1 this result is compared to the calculated ion distribution in feldspar obtained by the SRIM software package (version 2013.00) developed by Ziegler et al. [60]. The calculated distribution shows a Gaussian shape and the corresponding values for x_0 and σ (cf. Tab. 4.1) fall closely to those obtained by fitting to the experimental data. The peak concentration C_0, however, slightly differs but it is used as a free fitting parameter in the analysis that is presented in Section 4.2. After implantation, each sample was annealed at temperatures between 1169 K to 1021 K for times between 20 min and 3.2 h in an integral high vacuum[3] diffusion facility that

[3]Vacuum conditions of $p \leq 1$ mPa were maintained during the experiments for ion-beam operation in the employed integral diffusion chamber comprising furnace heating, sputter-sectioning and radioactivity counting. Under these conditions, the sample material was also protected from oxidation during high temperature treatment.

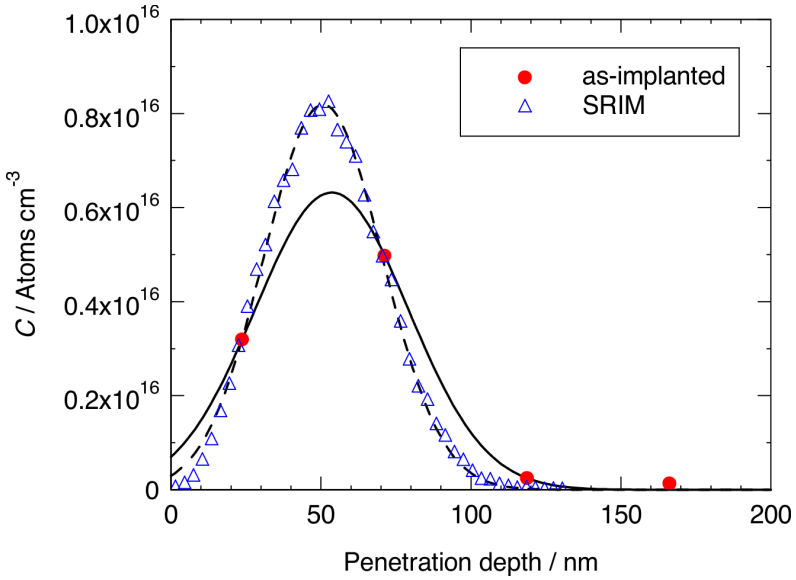

Figure 4.1.: Concentration of implanted ^{43}K as a function of penetration depth obtained by serial sectioning (circles) and by SRIM simulations (triangles) for an implantation energy of 50 keV. A Gaussian function (Eq. 4.1) was fitted to the data points (lines) to determine the mean ion range x_0 and implantation width σ. The area of both distributions was normalized to the ion dose of 4×10^{11} atoms cm^{-2}.

was constructed at the University of Saarbrücken [61]. Sample temperatures were continuously recorded to determine the effective annealing time (21 min to 192 min, cf. Tab. 4.1) during each experiment. After thermal treatment, the samples were sectioned by ion-beam sputtering with a step size of 24 nm to 90 nm, depending on the predefined sputtering time per section. Each section was separately collected on a Kapton film and transported to a NaI-detector to determine its γ-ray count rate. The time between implantation and detection was less than three half-lives in all cases. An appropriate short-lived correction [62] for ^{43}K $\left(t_{1/2} = 22.3\,\mathrm{h}\right)$ was applied to each $\gamma-$ray spectrum to determine the relative tracer concentration. The diffusion profiles, i.e., the relative tracer concentrations as a function of depth x, were then obtained by measuring the total profile depth. This was done by mechanical surface profiling of the samples after sputtering.

Table 4.1.: Diffusion coefficients of ^{43}K in alkali feldspar normal to (001) according to fitting of Eq. 4.2 to the diffusion profiles (cf. Fig. 4.2). The initial tracer distribution after implantation is given by the Gaussian function (Eq. 4.1) with the parameters x_0 and σ.

T / K	t / s	x_0 / nm	σ / nm	k	$\widehat{D}_{\mathrm{K}}$ / (m^2/s)
1169	1244	50.7	19.7	-0.96	$(1.9 \pm 0.6) \times 10^{-16}$
1123	1847	50.7	19.7	-0.94	$(1.0 \pm 0.4) \times 10^{-16}$
1073	3795	50.7	19.7	-0.95	$(4.2 \pm 1.2) \times 10^{-17}$
1021	11,540	50.7	19.7	-0.94	$(5.8 \pm 1.5) \times 10^{-18}$

4.2. ^{43}K diffusion results

The results of four ^{43}K depth distributions in alkali feldspar after diffusion annealing are presented in Fig. 4.2 together with results for the as-implanted sample (cf. Fig. 4.1). To prevent overlapping and intersecting data, the measured profiles were individually shifted along the ordinate. It can be seen from the figure that the diffusion length is at least ten times larger than the mean implantation depth $x_0 = 54\,\mathrm{nm}$, in all cases. Consequently, the uncertainty in x_0 and σ (cf. Fig. 4.1) has negligible effects on the deduced values of $\widehat{D}_{\mathrm{K}}$. Furthermore, a characteristic decline in tracer concentration towards the surface is observed in all experiments. It seems less likely that this effect is based on a supersaturation of vacancies due to implantation damage, since at the high temperatures employed a virtually immediate equilibration is expected. A suitable solution of the diffusion equation should converge to the initial tracer distribution described by Eq. 4.1 for negligibly short annealing times t. The solution used for fitting to all diffusion profiles is given by [63]

$$C(x,t) = \frac{C_0/2}{\left(1+\left(2\widehat{D}t/\sigma^2\right)\right)^{1/2}}\left[\mathrm{erfc}\left(\frac{-\left(x_0/2\sigma^2\right)-\left(x/4\widehat{D}t\right)}{\sqrt{\left(1/2\sigma^2\right)+\left(1/4\widehat{D}t\right)}}\right)\exp\left(\frac{-\left(x-x_0\right)^2}{2\sigma^2+4\widehat{D}t}\right)\right.$$
$$\left. +k\,\mathrm{erfc}\left(\frac{-\left(x_0/2\sigma^2\right)+\left(x/4\widehat{D}t\right)}{\sqrt{\left(1/2\sigma^2\right)+\left(1/4\widehat{D}t\right)}}\right)\exp\left(\frac{-\left(x+x_0\right)^2}{2\sigma^2+4\widehat{D}t}\right)\right], \tag{4.2}$$

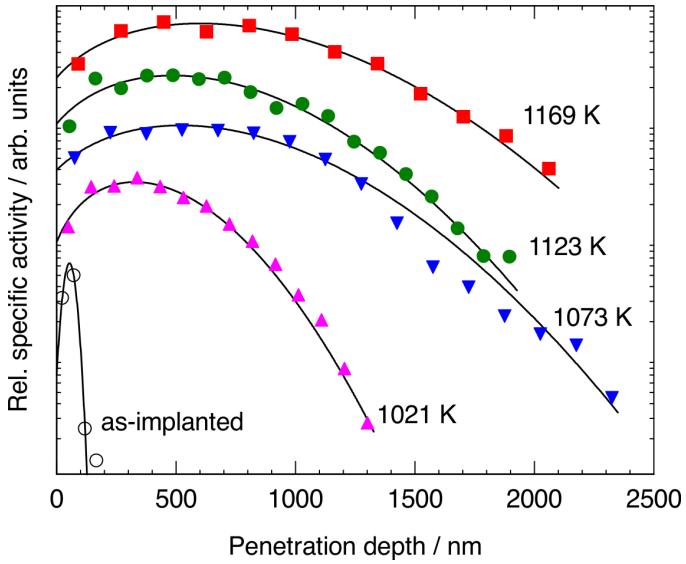

Figure 4.2.: Diffusion profiles of ^{43}K in alkali feldspar normal to (001) for different annealing temperatures T. Solid lines represent fittings to the data points according to Eq. 4.2. To enhance visibility of all slopes the relative concentrations are shifted along the ordinate. The ^{43}K distribution as-implanted is shown for comparison (open circles).

where x is a depth normal to the surface, C_0 is a maximum surface concentration of the implantation profile and $\widehat{D}$ is a self-diffusion coefficient. The parameter k accounts for the fact that the surface can act as a perfect reflector for the atoms ($k = +1$) or as a perfect sink ($k = -1$), or as a boundary with mixed reflector/sink properties ($-1 < k < 1$). The derived diffusion coefficients are listed in Tab. 4.1 together with the corresponding parameters x_0 and σ characterizing the initial tracer distribution. According to the concentration decline at the surface, the deduced k-values are as low as -0.95 and the surface is almost a perfect sink for ^{43}K. The temperature dependence of self-diffusion is commonly described by the Arrhenius relation

$$\widehat{D}_{\mathrm{K}}(T) = D_0 \exp\left(-\frac{\Delta H}{k_{\mathrm{B}} T}\right), \tag{4.3}$$

where D_0 is a pre-exponential factor, k_{B} is the Boltzmann constant and ΔH denotes an activation energy. In Fig. 4.3, the resulting K self-diffusion coefficients $\widehat{D}_{\mathrm{K}}$ normal to (001) are shown on a logarithmic scale as a function of $1/T$. It can be seen that the $\widehat{D}_{\mathrm{K}}$-values are fairly well described by the Arrhenius equation with $\Delta H = (2.4 \pm 0.4)$ eV and $\log_{10}(D_0/\mathrm{m^2 s^{-1}}) = -5.3 \pm 1.7$. The relatively large

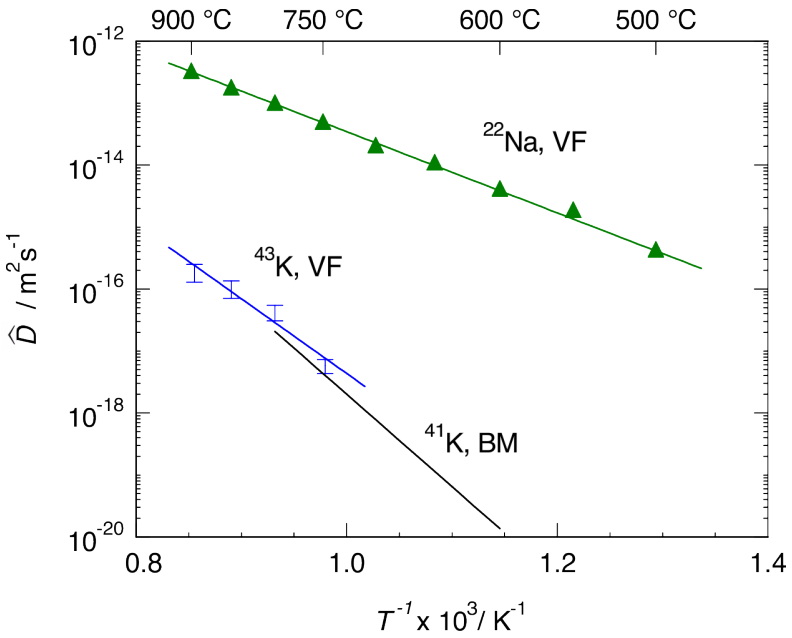

Figure 4.3.: Arrhenius plot of the diffusion coefficients of ^{43}K in alkali feldspar from Volkesfeld (VF), Germany (bars). Corresponding results for the diffusion of ^{22}Na (triangles) are included for comparison [64], as well as the Arrhenius relation for the ^{41}K diffusion from [8] in a more K-rich orthoclase from Benson Mines (BM), USA (solid line, based on a cylindrical grain model).

uncertainties in ΔH and $D_0 = 5 \times 10^{-6}\,\mathrm{m^2/s}$ relate to the fairly narrow temperature range ($1021 - 1169\,\mathrm{K}$), which is constrained both at high and low T by the specific conditions of the experiments (short half-life time, lower limit of annealing time, surface acting as a sink). However, the present results for $\widehat{D}_\mathrm{K}$ are sufficiently reliable and accurate to compare with Na self-diffusion data pertaining to the same alkali feldspar and the same crystallographic direction as will be done in the following sections and to data on ionic conductivity that will be presented in Chapter 5.

4.2.1. Comparison of Na and K self-diffusion

In Fig. 4.3, the Na self-diffusion coefficients $\widehat{D}_\mathrm{Na}$ for Volkesfeld feldspar normal to (001) from Chapter 3 are included for comparison. It can be seen that $\widehat{D}_\mathrm{Na} \gg \widehat{D}_\mathrm{K}$ is fulfilled over the whole investigated temperature range and that, e.g., at 1173 K the ratio $\widehat{D}_\mathrm{Na}/\widehat{D}_\mathrm{K}$ derived from the fitted Arrhenius equation is 1230/1. Since both alkali components share the same sublattice, this finding suggests that the pertaining atomic jump frequencies are greatly different, i.e., $w_\mathrm{Na} \gg w_\mathrm{K}$. Under this assumption, point-defect-based diffusion mechanisms are subject to

significant atomic correlation effects, especially when a K-rich feldspar such as VF is considered. This conclusion can be understood as follows: Below a certain Na site fraction referred to as percolation threshold p^c, long-range diffusion via the vacancy or the interstitialcy mechanism also requires atomic jumps via slow substitutional K atoms. The diffusion coefficient $\widehat{D}_{\mathrm{Na}}$ is then coupled to $\widehat{D}_{\mathrm{K}}$ because both components share the same type of defect acting as a diffusion vehicle. Regardless of the ratio $w_{\mathrm{Na}}/w_{\mathrm{K}}$ this results in an upper limit for the ratio $\widehat{D}_{\mathrm{Na}}/\widehat{D}_{\mathrm{K}}$. For a vacancy-based diffusion model in alkali feldspar, a previous Monte Carlo (MC) study by Wilangowski and Stolwijk [64] determined this ratio to be $\widehat{D}_{\mathrm{Na}}/\widehat{D}_{\mathrm{K}} \leq 3.12$ for a VF-like K site fraction (cf. Chapter 6). This finding is in clear contrast with the experimental data presented in Fig. 4.3 and rules out the possibility that both Na and K diffusion are controlled by vacancies. It can therefore be predicted that the major diffusion mechanism of Na must be less correlated than a vacancy diffusion mechanism and that the percolation threshold pertaining to this mechanism is at a K site fraction which is beyond that of a VF-like feldspar.
An alternative interpretation of the greatly different diffusivities of Na and K is that Na diffusion occurs primarily via a direct interstitial mechanism, which is related to a correlation factor of $f = 1$. It is therefore important to find experimental evidence for the order of the correlation factor f. The comparison of self-diffusion data with data on ionic conductivity gives direct access to the so-called Haven ratio H_{R} and allows for a reliable distinction whether a direct interstitial diffusion mechanism or a diffusion vehicle based mechanism predominantly occurs. The corresponding conductivity measurements and analysis are presented and discussed in Chapter 5.

4.2.2. Concentration dependence of K self-diffusion

^{41}K diffusion experiments were reported by Foland [8] who used a natural orthoclase from Benson Mines (BM), USA, with a K site fraction that is $C_{\mathrm{K}} \approx 0.94$ and therefore, different from VF with $C_{\mathrm{K}} = 0.83$. The activation energy pertaining to K self-diffusion in BM is $\Delta H = 2.95\,\mathrm{eV}$, which is somewhat above the value of 2.4 eV that is obtained for VF in the present work. However, this difference is not significant because of the appreciable uncertainties in ΔH both in this work (± 0.4 eV) and in the work of Foland ($\pm 0.2\,\mathrm{eV}$, based on an estimation from his reported data). A direct comparison between the K diffusion coefficients of both studies at 1073 K (this is the only coincident temperature) gives $\widehat{D}_{\mathrm{K,VF}}/\widehat{D}_{\mathrm{K,BM}} \approx 1.8$ (cf. Fig. 4.3). It should be noted that Foland's evaluation of $\widehat{D}_{\mathrm{K,BM}}$ is based on

two different feldspar grain geometries, a *spherical* and a *cylindrical* one, leading to the relationship $D_{\text{cylindrical}} \approx 2.2\ D_{\text{spherical}}$ (and hence $\widehat{D}_{\text{K,VF}}/\widehat{D}_{\text{K,BM}} \approx 4.0$ for the *spherical* grain model). The following discussion is based on the values from the *cylindrical* diffusion model.

The good agreement between the two $\widehat{D}_{\text{K}}$ values observed for the VF ($C_{\text{K}} = 0.83$) and BM ($C_{\text{K}} \approx 0.94$) feldspars requires further explanations of the concentration dependent effects that control the K self-diffusion. Two major effects are considered: Under the assumption of a non-collinear interstitialcy diffusion mechanism the concentration dependence of correlation factors f_{K} may be estimated from a Monte Carlo study (cf. Chapter 8 and [65]). The slower moving K ions are subject to correlation effects with a weak concentration dependence in the composition range from $C_{\text{K}} = 0.83$ to 0.94, and it can be found $f_{\text{K,VF}}/f_{\text{K,BM}} \approx 2/1$. A second effect on concentration dependence is the concentration of self-interstitials C_{i} acting as diffusion vehicles. In a recent study about ionic conductivity in feldspar by el Maanaoui et al. [56] it was shown that the concentration of Na self-interstitials $C_{\text{Na,i}}$ dominates over K self-interstitials $C_{\text{K,i}}$ by orders of magnitude in the composition regime under discussion. It can therefore be estimated $C_{\text{i}} \approx \left[C_{\text{Na}} \exp\left(G^{\text{FP}}_{\text{Na}}/k_{\text{B}}T\right)\right]^{1/2}$, where $G^{\text{FP}}_{\text{Na}}$ is a virtual C_{Na}-independent free enthalpy of Frenkel pair formation and find $C^{\text{VF}}_{\text{i}}/C^{\text{BM}}_{\text{i}} = \left(C^{\text{VF}}_{\text{Na}}/C^{\text{BM}}_{\text{Na}}\right)^{1/2} = (0.15/0.06)^{1/2} \approx 1.6$. Combination of the two effects gives $\widehat{D}_{\text{K,VF}}/\widehat{D}_{\text{K,BM}} \approx 3$, which is in sufficient agreement with the experimental results when large uncertainties are considered. However, it should be noted that the composition of feldspar may have an effect on atomic potentials and hence on atomic jump frequencies ω, which is not considered here.

4.3. Summary and conclusions

This chapter examined self-diffusion of K in natural alkali feldspar from Volkesfeld, Germany normal to (001) by the radiotracer method after implantation with ^{43}K. It was shown that within the investigated temperature range, i.e., from 1169 K to 1021 K, the diffusivity $\widehat{D}_{\text{K}}$ is described by an Arrhenius equation with activation energy $\Delta H = (2.4 \pm 0.4)$ eV and the pre-exponential factor $\log_{10}(D_0/\text{m}^2\text{s}^{-1}) = -5.3 \pm 1.7$. The ^{43}K diffusion coefficients were compared to those of ^{22}Na in the same alkali feldspar and the same crystallographic direction (cf. Chapter 3). The diffusivity ratio $\widehat{D}_{\text{Na}}/\widehat{D}_{\text{K}}$ is 1230/1 at 1173 K, which is in good agreement

with previous observations from Behrens et al. [17]. From this finding and from previous MC simulations of correlation effects pertaining to a vacancy mechanism in alkali feldspar by Wilangowski and Stolwijk (see Chapter 6 and [64]) it can be concluded that the Na self-diffusion cannot be controlled by a vacancy type of diffusion mechanism, but rather by an interstitialcy (or direct interstitial) diffusion mechanism.

The reported $\widehat{D}_{\mathrm{K,VF}}$ results from this study agree fairly well with $\widehat{D}_{\mathrm{K,BM}}$ data that were reported by Foland [8] for a similar natural orthoclase but with a higher K site fraction of $C_{\mathrm{K}} \approx 0.94$. The virtual independence of $\widehat{D}_{\mathrm{K}}$ from the K site fraction cannot be explained a priori because the following effects account for a concentration dependence on K self-diffusion:

(i) The concentration of self-interstitials C_{i} is primarily determined by the concentration of interstitial Na atoms $C_{\mathrm{Na,i}}$. For a virtual C_{Na}-independent free enthalpy of Frenkel pair formation a *positive* correlation between the K diffusivity $\widehat{D}_{\mathrm{K}}$ and the Na site fraction exists.

(ii) Considering a non-collinear interstitialcy diffusion mechanism, the correlation factor of K self-diffusion f_{K} is *positively* correlated with the Na site fraction.

(iii) The volume gain of the unit cell with *decreasing* Na site-fraction (cf. Section 3.3) results in a *negative* correlation between $\widehat{D}_{\mathrm{K}}$ and the Na site-fraction. In the investigated composition regime, however, this relation is hypothetically small and cannot be quantified by simple elastic models.

The effects (i) and (ii) were estimated and in total only minor differences of $\widehat{D}_{\mathrm{K}}$ result from the differing K site fractions of the two compared alkali feldspars. Beyond that, these small differences fully comply with the measured values of $\widehat{D}_{\mathrm{K,VF}}$ and $\widehat{D}_{\mathrm{K,BM}}$ at a temperature of 1073 K when the uncertainties that result from the choice of grain model in Foland's analysis are considered.

5. Ionic conductivity in single-crystal alkali feldspar

The previous Chapters 3 and 4 focused on the self-diffusion of Na and K ions in alkali feldspar. Another property which is intimately related to self-diffusion is the dc ionic conductivity σ, which comprises the joint contributions of Na^+ and K^+ ions to overall charge transport. A combination of reliable data on mass and charge transport may lead to a consistent physical picture of the diffusion mechanism as has been obtained, e.g., for some alkali halide crystals [18, 19].

The dc ionic conductivity in alkali feldspar for various compositions has so far been systematically observed primarily for synthesized minerals. Published work [66, 67] concerns the conductivity of alkali feldspar at high pressure between 873 K and 1173 K in hot-pressed sintered solid solutions covering the full composition range from albite to K-feldspar. Hu et al. have found a monotonic conductivity increase with increasing Na content of about a factor of 5 from Or_{100} to Ab_{100} [66, 67]. The temperature dependence for each composition is well described by an Arrhenius equation yielding activation energies between 0.84 eV (Ab_{100}) and 0.99 eV (Or_{100}). However, the polycrystallinity of the samples with grain sizes below 74 µm (200 mesh) obscures any anisotropy of σ. Other complications inherent to this study [66, 67] are possible effects because of non-uniform concentrations, the presence of grain boundaries, and high-pressure conditions during the measurement (1.0 GPa).

The ionic dc conductivity of two natural and K-rich alkali feldspars has been investigated in a recent study [56] in the temperature range from 573 K to 1173 K and in the directions normal to (001) and normal to (010). El Maanaoui et al. used the same gem-quality crystals as in the present tracer diffusion studies referred to as VF ($Or_{83}Ab_{15}Cs_1$, cf. Chapters 3 and 4) and RK feldspar ($Or_{71}Ab_{26}Cs_3$, cf. Chapter 3). For most accurate and reliable results two measuring facilities were employed and consistent results have been reported showing a linear Arrhenius behaviour over the full range of temperature with activation energies close to 1.2 eV.

The composition dependence is weak but a remarkably pronounced anisotropy is observed with σ data normal to (001) that exceed σ normal to (010) by up to one order of magnitude. In contrast to this study, radiotracer diffusion measurements of Na self-diffusion show only a weak anisotropy between these directions (see Chapter 3). A complexity inherent to the ionic conductivity measurements is that the transport of other ions than Na^+ and K^+, e.g., H^+ adds to the total conductivity. The amount of residual water should be carefully monitored because even trace amounts increase the electrical conductivity [68, 69, 70, 71]. An alternative approach is the pre-annealing of the minerals at elevated temperature to avoid any water related influence. Due to the absence of the aforementioned methods it has been discussed whether the increased conductivities normal to (001) may result from effects of residual water in this study [56]. Although sound arguments against this assumption have been presented the main motivation of the present study lies in the strict exclusion of any possible effects of water on ionic conductivity.
In this chapter, the ionic dc conductivity of gem-quality alkali feldspar from Volkesfeld, Germany (VF) in the orientation normal to (001) will be presented after the feldspar was pre-annealed at 1323 K for 4 days. Data were obtained from ac impedance spectroscopy at temperatures varying from 673 K to 1053 K. It will be shown that the pre-annealing procedure significantly reduces the conductivity when compared to an untreated sample. A comparison with ^{22}Na and ^{43}K tracer diffusion coefficients (cf. Chapters 3 and 4) based on the Nernst-Einstein equation will provide evidence for the dominant role of Na^+ ions in mass and charge transport at the investigated feldspar composition.

5.1. Experimental procedures

5.1.1. Sample material and preparation

The investigated mineral was a gem-quality sanidine from the Eifel (Germany), which originated from the locality Volkesfeld (VF). The same optically clear single-crystal mineral has been used in the previous chapters for self-diffusion measurements of Na and K (cf. Chapter 3 and 4). The chemistry and microstructure of the VF feldspar was extensively analysed in previous studies by the Vienna group [11, 12] using scanning electron microscopy and electron microprobe analysis. The selected feldspar proves to be chemically homogeneous within the resolution of

the applied methods and is free of twins, exsolutions, second phase precipitates, microcracks or any other structural flaws or heterogeneities. A detailed chemical analysis of the employed feldspar has been reported earlier [12, 33] and is presented in Section 2.1. The compositions of the VF sanidine is $Or_{83}Ab_{15}Cs_1$ with minor iron contents of about 0.1 to 0.2 weight percent Fe_2O_3. On the tetrahedral sites, Al and Si are highly disordered with $2t_1 = 0.61$ (cf. Fig. 2.3) [32]. Here $2t_1 = 2t_2 = 0.5$ means total disorder and $2t_1 = 1$ reflects rigorous order. In the latter case, all Al ions are uniformly accommodated on T1 tetragonal sites, whereas the other half of the T1 tetrahedrons and all T2 sites are occupied by Si. For details on the crystalline structure of alkali feldspars the reader is referred to the review of Kroll and Ribbe [72]. The mass density determined by the Archimedes method was obtained as $2.54\,\mathrm{gcm}^{-3}$ for single-crystal VF, in good agreement with literature data [33].

Pieces of single-crystal feldspar were oriented on an X-ray diffractometer and subsequently cut into plane-parallel plates of $\sim 0.6\,\mathrm{mm}$ thickness and with (001) surfaces. Disc-like samples were machined to an octagonal shape of about 8 mm diameter to approximate an ideal cylindrical geometry. Both faces were polished with diamond paste on a silk cloth down to a finish of 1 µm using a rotary polishing machine. The samples were sealed in a quartz ampule under Ar atmosphere and pre-annealed at 1323 K for 4 days. This is particularly important for two reasons: (i) Freer et al. reported an unusual fat Al-Si exchange for the VF sanidine compared to other K feldspars. After such pre-anneal the Al-Si exchange is as slow as the rate in other feldspars [59]. However, this procedure was omitted in the present Na and K self-diffusion studies. (ii) To preclude any influence of H on the measurements residual water must be effectively removed prior to the impedance analysis because the water content was not monitored in the present work.

A platinum layer of about 100 nm was deposited on both sample faces to warrant optimal electrical contact to the electrodes during the conductivity measurements. This treatment was carried out in a magnetron sputtering system (Bestec GmbH) under ultra-high vacuum conditions. The sample was protected by a cover with circular aperture of 5 mm in diameter during the sputtering procedure to produce well-defined Pt contacts in the centre of the surfaces. This was essential to avoid short-circuiting of the two surfaces through Pt that would otherwise also be sputtered on the sample sides.

5.1.2. Electrochemical impedance spectroscopy (EIS)

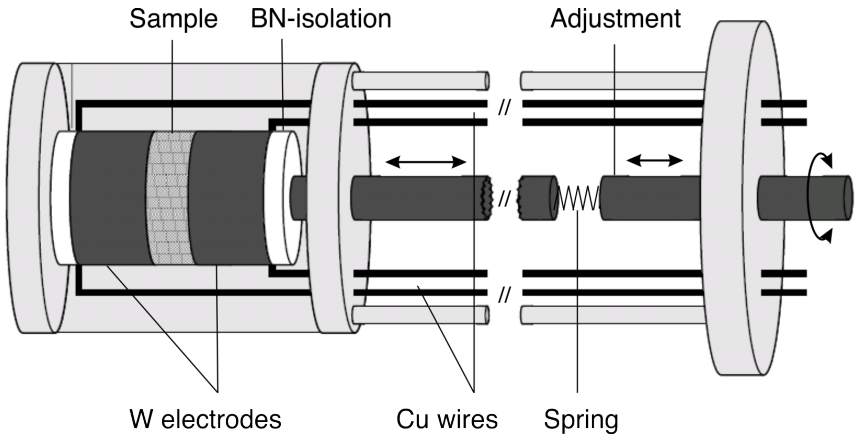

Figure 5.1.: Schematic view of the sample assembly used for the impedance spectroscopy analysis, edited after [73].

The EIS facility shown in Fig. 5.1 consists of an ac signal generator with an integrated impedance analyser (HP Agilent 4192A LF), a movable resistance-heated furnace with temperature controller (Eurotherm), a sample holder with plan-parallel metal electrodes, and a computer with Novocontrol WinDeta software for measurement control and data acquisition. The W disc electrodes with a thickness of 3 mm and a diameter of 9 mm were placed on each end of the sample (Pt coated) and a 0.8 mm Cu wire was connected with each electrode. Temperature was measured by a Ni/NiCr (type K) thermocouple, the end of which was placed in direct contact with one of the electrodes, which are electrically isolated from the rest of the assembly by boron nitride disks. Because the assembly (cf. Fig. 5.1) consists of temperature-resistant metal parts the measurement had to be performed under inert gas atmosphere, which was established by a continuous flow of argon inside a quartz-tube encapsulation [74]. After completing the sample assembly, it was heated to 673 K and held for 1 h before the conductivity measurements. The measuring run started at 673 K with a constant ramp of 0.5 K/min, which was maintained up to the highest temperature of 1053 K. Impedance measurements were done under continuous heating at set-point intervals of 10 K with an applied rms voltage amplitude of 1.0 V. Because a full frequency scan in the range between 5 Hz and 2 MHz only takes about 1 minute, the T-variation within one measurement is well within 1 K. The completed heating cycle was immediately followed by a cooling cycle at the same rate of T-change to the lowest temperature of 673 K. This

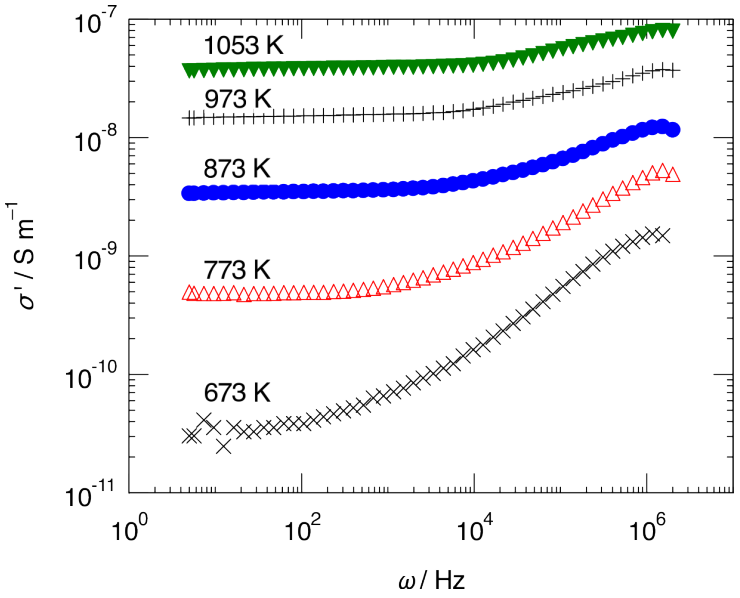

Figure 5.2.: Real part of the conductivity σ' as a function of the ac frequency ω from EIS analysis of VF feldspar normal to (001). The plotted data show monotonic behaviour referring upon heating from 673 K to 1053 K

was followed by a second heating cycle without any manipulation of the sample assembly. Electrochemical impedance spectra were fitted using an equivalent circuit contained in the Zview software.

5.2. Analysis and results

5.2.1. Frequency dependence

The impedance spectra obtained from EIS measurements for the VF feldspar normal to (001) at various temperatures between 673 K and 1053 K are shown as Bode plots in Fig. 5.2. At all temperatures, the double-logarithmic plots reveal a broad plateau-like behaviour of the real part of the complex conductivity $\sigma'(\omega)$ at the low-frequency side, which reflects long-range ionic transport. At higher frequencies, a dispersion region of positive correlation between σ' and the frequency ω is observed for all temperatures. It can be clearly seen from Fig. 5.2 that σ' increases with temperature for fixed frequencies.
Figure 5.3 shows examples of typical Nyquist plots for temperatures between 673 K and 1023 K. The appearance of a single arc at each temperature is consistent

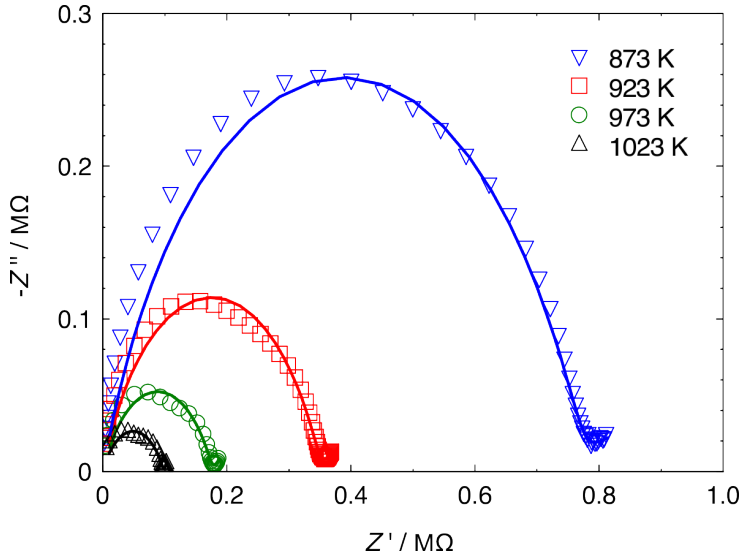

Figure 5.3.: Nyquist plots representing impedance spectra of VF feldspar normal to (001), as measured at various temperatures between 873 and 1023 K. Z' and Z'' are the real and imaginary part of the complex impedance for ac frequencies between 5 Hz and 2 MHz.

with the absence of grain boundaries and with a minor role of electrode effects. All Nyquist plots were analysed by fitting of an equivalent circuit model shown in Fig. 5.4 using the Zview software. The capacitance behaviour of the sample is simulated with a constant phase element (CPE), with the impedance of such element given by

$$Z_{\mathrm{CPE}} = \frac{1}{Q\,(\mathrm{i}\omega)^{\alpha}}\,, \tag{5.1}$$

where Q has the numerical value of the admittance at $\omega = 1\,\mathrm{rad/s}$ and $0 \leq \alpha \leq 1$. In the equivalent circuit model R_1 is the sample resistance, CPE_1 represents the sample capacitance and CPE_2 is the capacitance of the sample-electrode interface. A summary of the findings for the first heating cycle is presented in Tab. 5.1. Although not the full range of the Nyquist plots is accurately represented by fitting of this simple circuit model (solid lines in Fig. 5.3), it is fully suitable and accurate to analyse the sample resistance R_1. This is reflected by a good agreement between the plateau values of the conductivity σ' and the extracted conductivities from the corresponding circuit model analysis.

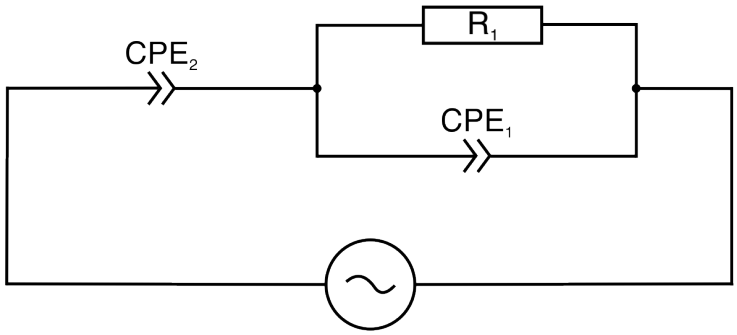

Figure 5.4.: Equivalent circuit model used for fitting to EIS data consisting of the sample resistance R_1, the sample capacitance represented by the constant phase element CPE_1 and the interface capacitance CPE_2.

Table 5.1.: EIS parameters for the first heating cycle of VF feldspar obtained from using the equivalent circuit shown in Fig. 5.4.

T/K	R_1 / MΩ	Q_1 / S s$^{\alpha_1}$	α_1	Q_2 / S s$^{\alpha_2}$	α_2
673	86.9	45.6×10^{-12}	0.80	3.4×10^{4}	1.00
723	20.7	60.2×10^{-12}	0.80	3.5×10^{5}	1.00
773	59.3×10^{-1}	89.1×10^{-12}	0.78	2.3×10^{-7}	1.00
823	19.7×10^{-1}	12.1×10^{-11}	0.77	1.1×10^{-6}	0.73
873	76.8×10^{-2}	14.2×10^{-11}	0.77	5.9×10^{-6}	0.34
923	34.7×10^{-2}	26.8×10^{-11}	0.74	1.2×10^{-5}	0.32
973	17.5×10^{-2}	70.7×10^{-11}	0.68	2.0×10^{-5}	0.35
1023	98.1×10^{-3}	19.2×10^{-10}	0.63	2.0×10^{-5}	0.56
1053	69.3×10^{-3}	26.1×10^{-10}	0.62	2.1×10^{-5}	0.62

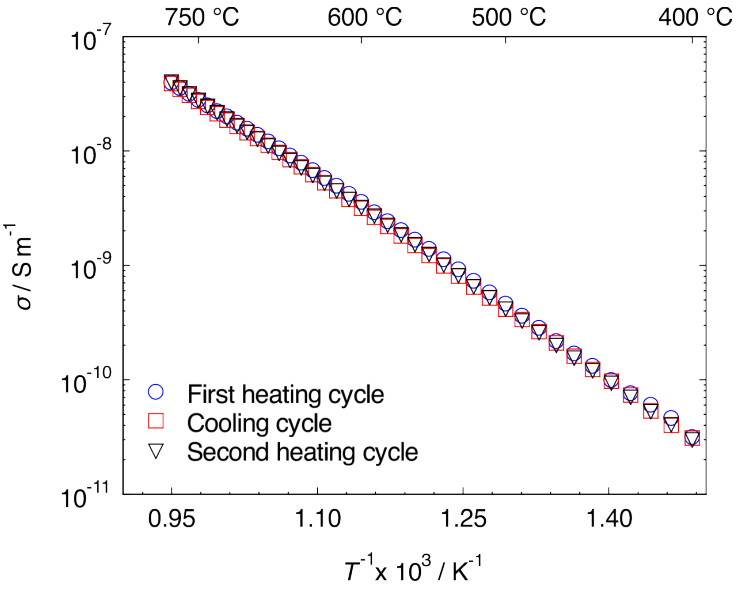

Figure 5.5.: Comparison of the dc conductivity in VF feldspar as a function of inverse temperature for consecutive measurement cycles of the same sample. Data result from EIS analysis upon continuous heating from 673 K to 1053 K, which was immediately followed by a continuous cooling cycle down to 673 K and a second heating cycle up to 1053 K.

5.2.2. Temperature dependence

The temperature dependence of the dc conductivity σ with an interval of 10 K for the consecutive heating, cooling and heating cycles is presented in Fig. 5.5. It can be seen that the variation between the three cycles at nominally the same temperature is within $\sim 10\,\%$. In Fig. 5.6, the results are averaged over all cycles and σT is shown on a logarithmic scale versus $1/T$ with an interval of 20 K. This accounts for the fact that – according to the Nernst-Einstein equation – σT rather than σ is proportional to a diffusivity. In addition, it is commonly assumed that diffusivities represent proper T activated processes which obey the Arrhenius law with a constant (T independent) pre-exponential factor. Indeed, the EIS data (triangles) are well fitted by the Arrhenius expression (solid line)

$$\sigma T = A \exp\left(\frac{-\Delta H}{k_{\mathrm{B}} T}\right), \tag{5.2}$$

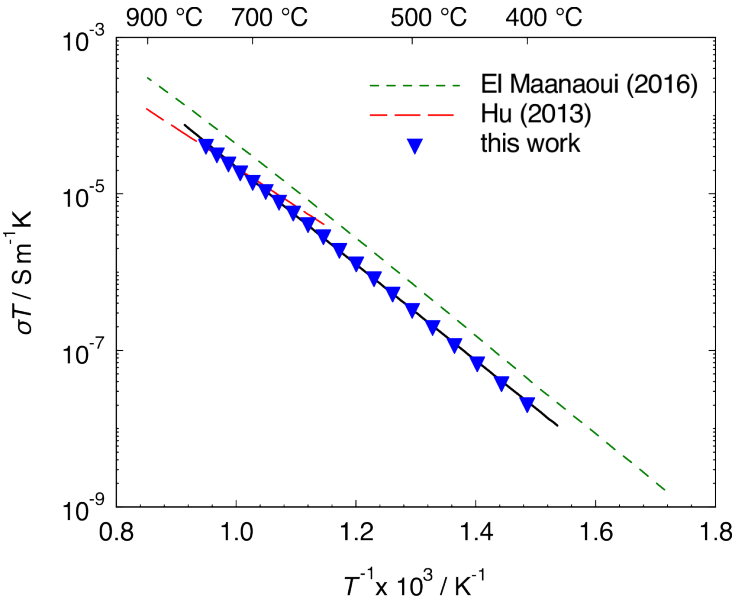

Figure 5.6.: Arrhenius plot of σT normal to (001) in VF feldspar (triangles). Data result from averaging over three EIS analysis cycles of the same sample (heating, cooling and heating, cf. Fig. 5.5). For better clarity, only every second data point is shown. The solid line represents a fit of the Arrhenius equation (Eq. 5.2) to the data points. For comparison, the reported results from El Maanaoui et al. [56] for σT in the same VF feldspar and direction but without thermal pre-treatment and from Hu et al. [67] for a polycrystalline feldspar with a similar K site fraction $C_{\mathrm{K}} = 0.8$ are shown (dashed lines).

where A is a pre-exponential factor, k_{B} is the Boltzmann constant and ΔH denotes an activation energy. Least-square fitting of the logarithmic form of Eq. 5.2 to σT yields

$$\Delta H = (1.226 \pm 0.004)\ \mathrm{eV}\,,$$
$$\ln\left(A/\mathrm{m^2 s^{-1}}\right) = 3.49 \pm 0.07\,.$$

The results are compiled in Fig. 5.6 with σT data from two recent studies by Hu et al. [67] and by El Maanaoui et al. [56] (dashed lines). Hu analysed a synthesized and hence polycrystalline feldspar with the composition $\mathrm{Or_{80}Ab_{20}}$, similar to that of VF feldspar and the study does a priori not reveal a hypothetical anisotropy. The results fall close to those of the present study, although a slightly smaller activation energy of $\Delta H = (0.99 \pm 0.03)$ eV is reported.

El Maanaoui investigated the same VF feldspar in the direction normal to (001) as in the present study, but his feldspar underwent no pre-annealing procedure. It can

be seen from Fig. 5.6 that the activation energies almost perfectly agree, whereas his reported σT data exceeds the present data by a factor of ~ 2 over the investigated range of temperature. This is especially interesting since the same impedance analyser, sample assembly and heating/cooling procedures were employed in both studies. A motivation of the present study is to clarify whether H diffusion has a significant influence on total conductivity in feldspar, which would lead to a more complex situation for the interpretation and comparison between EIS analysis and Na self-diffusion data. In detail, the following aspects have to be considered:
(i) Both samples were coated with a ~ 100 nm Pt layer. However, in El Maanaoui's study the Pt layer covered the whole sample and thus had to be removed from the side surface to avoid direct electrical contact between the two electrodes. In contrast, disks of 5 mm in diameter were sputtered onto the centre of the two plane-parallel sample surfaces in the present study.
(ii) El Maanaoui's samples were used consecutively for several EIS analyses because of the limitation of available sample material. It may therefore have suffered from first approaches because in-diffusion of the electrode material into the bulk sample could have an effect on conductivity. However, the surface layers of these samples were subsequently grinded and polished after these preliminary experiments.
(iii) In El Maanaoui's study, the content of water in the minerals stays undetermined and no high temperature treatment was performed prior to the EIS analysis [56]. However, the high temperatures that occurred during preliminary heating and cooling cycles prior to the final measurement should be sufficient to remove residual water from the sample and it is reported that water is therefore expected to have a negligible effect on conductivity. Beyond that, it might be expected that the H^+ charge transport is connected to a different activation energy than Na and K transport and thus kinks or curvatures in the Arrhenius plot should be expected when a large temperature range is observed.
(iv) The thermal pre-treatment at 1323 K for 4 days has an influence on the Al-Si ordering in the feldspar sample of the present study. Although the VF feldspar is already highly disordered ($2t_1 = 0.61$ [32]) a change in the ordering state might also have an influence on the Na diffusion but this effect has so far not been investigated systematically.
In total, the disparity of the two studies may therefore not be given by a single convincing reason, such as different water contents.

5.2.3. Comparison of mass and charge transport

For alkali feldspar, it is assumed that positively charged monovalent Na^+ and K^+ ions form a binary sublattice within a negatively charged rigid silicate framework. Beyond that, it is assumed that all other impurity ions in VF feldspar (e.g., Ba^{2+}, Sr^{2+}) have low, essentially negligible mobility and do not significantly contribute to the conductivity. These effects can be described through the Nernst-Einstein equation by the charge or conductivity diffusivity D_σ, i.e., [75]

$$D_\sigma = \frac{k_\mathrm{B}T}{e^2 N_\mathrm{ion}}\sigma = C_\mathrm{I} D_\mathrm{I}\,, \tag{5.3}$$

where $N_\mathrm{ion} = N_\mathrm{Na} + N_\mathrm{K}$ is the volume concentration of ions, $C_\mathrm{I} = C_\mathrm{Na,I} + C_\mathrm{K,I}$ is the site fraction of self-interstitials and D_I denotes the diffusion coefficient of the generalized interstitial carrying a charge unit e. It should be emphasized that D_σ generally differs from the (alkali) ion tracer diffusivity because of diffusion correlation effects pertaining to a certain diffusion mechanism [19, 76]. The quantitative differences between mass and charge transport can be expressed by the Haven ratio H_R, which for the interstitialcy mechanism in binary lattices is generally given by

$$H_\mathrm{R} = \frac{\widehat{D}}{D_\sigma} = \frac{C_\mathrm{Na}\widehat{D}_\mathrm{Na} + C_\mathrm{K}\widehat{D}_\mathrm{K}}{C_\mathrm{I} D_\mathrm{I}}\,, \tag{5.4}$$

where $\widehat{D} = C_\mathrm{Na}\widehat{D}_\mathrm{Na} + C_\mathrm{K}\widehat{D}_\mathrm{K}$ has been introduced as a mean tracer diffusivity[1] and C_Na and C_K is the site fraction of Na and K, respectively [75, 76]. It can be seen from Eq. 5.4 that D_σ has the dimension of a transport coefficient and should be compared to $C_\mathrm{Na}\widehat{D}_\mathrm{Na}$ and $C_\mathrm{K}\widehat{D}_\mathrm{K}$ rather than to the associated self-diffusion coefficients. In Fig. 5.7 the transport data is shown together with D_σ based on the ion concentrations $N_\mathrm{K} = 4.67\times10^{21}\,\mathrm{cm}^{-3}$ and $N_\mathrm{Na} = 8.01\times10^{20}\,\mathrm{cm}^{-3}$ for VF feldspar. It can be seen that although $N_\mathrm{Na} < N_\mathrm{K}$ holds true for the ion concentrations, the transport coefficient of Na clearly dominates over K over the whole temperature range, i.e. $C_\mathrm{Na}\widehat{D}_\mathrm{Na} \gg C_\mathrm{K}\widehat{D}_\mathrm{K}$. The influence of the K transport coefficient to the total ion transport may therefore be neglected. Furthermore, the

[1] To reduce the number of indices, the common asterisk for labelling tracer diffusivity (D^*) has been replaced by the 'hat' symbol ($\widehat{D}$) throughout this work.

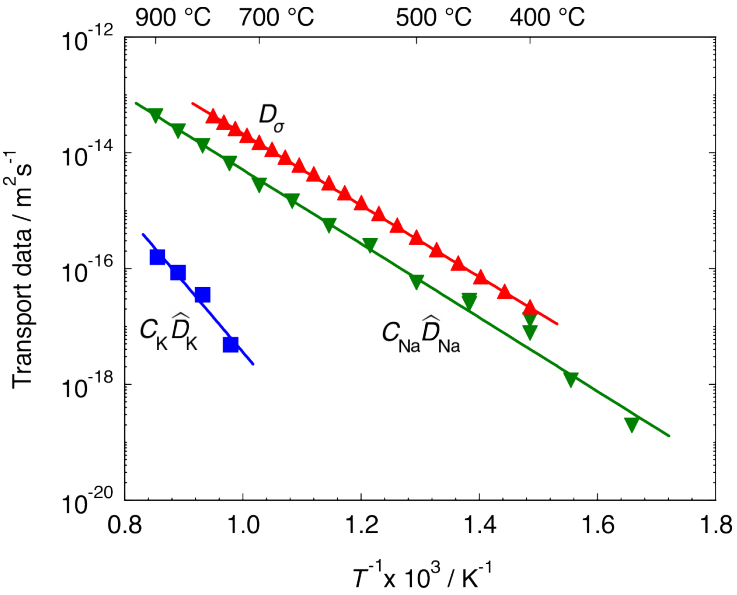

Figure 5.7.: Arrhenius plot of the transport coefficients for VF feldspar normal to (001) related to ionic conductivity D_σ, Na self-diffusion $C_{\mathrm{Na}}\widehat{D}_{\mathrm{Na}}$ and K self-diffusion $C_{\mathrm{K}}\widehat{D}_{\mathrm{K}}$, as indicated. D_σ is derived according to Eq. 5.3. It can be seen that the ionic conductivity is primarily connected to Na ions because the associated transport data exceeds the K transport by more than two orders of magnitude.

partial Haven ratios $H_{\mathrm{R,Na}}$ and $H_{\mathrm{R,K}}$ may be introduced, so that $H_{\mathrm{R}} = H_{\mathrm{R,Na}} + H_{\mathrm{R,K}}$ holds, and it can be found

$$H_{\mathrm{R}} \approx H_{\mathrm{R,Na}} = \frac{C_{\mathrm{Na}}\widehat{D}_{\mathrm{Na}}}{C_{\mathrm{I}} D_{\mathrm{I}}} \,. \tag{5.5}$$

From Fig. 5.7 it can be inferred that $C_{\mathrm{Na}}\widehat{D}_{\mathrm{Na}} < D_\sigma$, which can be expressed as $H_{\mathrm{R}} < 1$. The results derived for H_{R} from Eq. 5.4 are shown in Fig. 5.8 as a function of T. Open symbols represent data points that were obtained by inserting extrapolated conductivity data according to Eq. 5.2 into Eq. 5.4. Uncertainties in H_{R} are based on the experimental uncertainties of the radiotracer diffusion measurements and of the EIS analysis given by 30 %, each. It can be seen that H_{R} is in the range from 0.11 to 0.40 and that H_{R} slightly increases with increasing T. A direct interstitial mechanism operating alone predicts a Haven ratio of $H_{\mathrm{R}} = 1$, which implies that charge and mass transport are equal [77]. It should therefore be concluded that such a mechanism does not dominate the diffusion of Na atoms. Apparently, direct interstitial (I-I) jumps are much less frequent than interstitialcy (I-S/S-I) jumps for Na in VF feldspar.

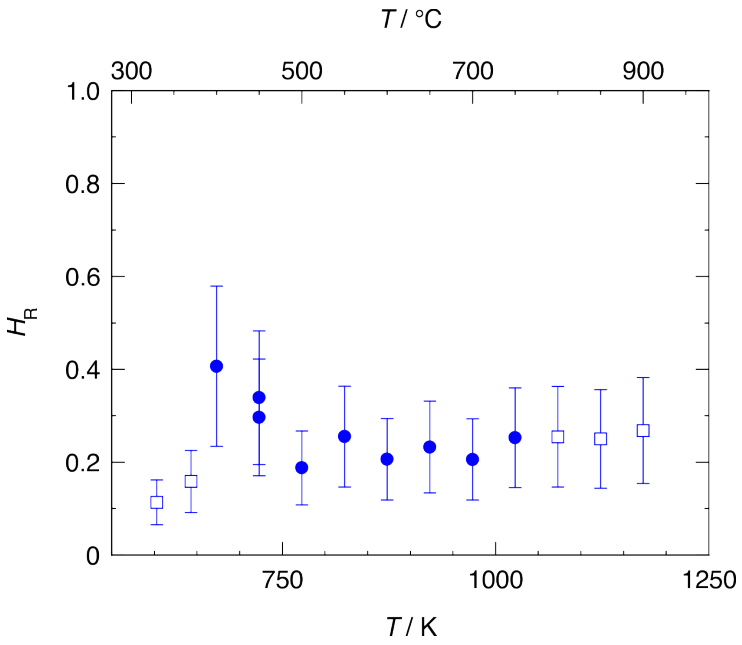

Figure 5.8.: Haven ratio H_R for VF feldspar normal to (001) as a function of temperature T derived from the present EIS analysis and from Na self-diffusion results (cf. Section 3.2) according to Eq. 5.4. Solid circles represent H_R from direct insertion of data into Eq. 5.4, whereas open squares are based on extrapolated σ values according to Eq. 5.2.

The results and considerations demand an explanation for $H_\mathrm{R} \approx 0.2$ within a suitable diffusion model because the Haven ratio is intimately connected with correlation effects. The development of such model and calculations of the correlation effects pertaining to it is presented along the following chapters. This implies practical attempts to reproduce the $\widehat{D}_\mathrm{Na}/\widehat{D}_\mathrm{K}$ ratios and H_R values that are found experimentally.

5.3. Summary and conclusions

The dc ionic conductivity in natural alkali feldspar from Volkesfeld, Germany normal to (001) was examined by EIS analysis after pre-annealing at 1323 K for 4 days. It was shown that within the investigated temperature range varying from 673 K to 1053 K, the product σT is described by an Arrhenius equation with an activation energy $\Delta H = (1.226 \pm 0.004)$ eV and a pre-exponential factor $\ln(A/\mathrm{m^2 s^{-1}}) = 3.49 \pm 0.07$. The findings are in good agreement with the reported conductivity data [67] for a polycrystalline feldspar with the composition $\mathrm{Or_{80}Ab_{20}}$, although the activation energy of $\Delta H = (0.99 \pm 0.03)$ eV slightly differed.

El Maanaoui et al. [56] investigated the ionic dc conductivity of the same VF feldspar as in the present study but they refrained from annealing the minerals at an elevated temperature prior to the EIS analysis. A comparison of the conductivity normal to (001) between the untreated and the pre-annealed mineral showed a significant decline by a factor of $\sim$ 2 due to the pre-annealing procedure. The disparity may be caused by the out-diffusion of H from the mineral at elevated temperatures. However, El Maanaoui et al. suggested that an effect of H^+ charge transport to the total conductivity causes kinks or curvatures in the Arrhenius plot, which was not observed in their experimental data [56]. Another property that could have an influence on the Na charge transport after the thermal pre-treatment is the ordering state of Al-Si. However, the difference in the ordering state might affect the potential barriers for Na jumps and hence, also show an effect on the activation energy rather than shifting σ along the ordinate. The disparity of the two studies may therefore not be given by a single convincing reason.
Based on the Nernst-Einstein equation the charge diffusivity D_σ was determined and compared with tracer diffusion data for ^{22}Na and ^{43}K (see Chapters 3 and 4). The Na transport data exceeded the K data by orders of magnitude, suggesting a dominant role of Na^+ ions in overall mass and charge transport at the investigated feldspar composition. The so-called Haven ratio H_R is intimately connected with correlation effects pertaining to a certain diffusion mechanism. For VF feldspar H_R ranges from 0.11 to 0.40 in the direction normal to (001) (cf. Fig. 5.8). The deviation from $H_\mathrm{R} = 1$ gives strong evidence that the Na self-diffusion is significantly correlated and implies that direct interstitial jumps are much less frequent than those jumps related to an exchange with a diffusion vehicle, e.g., interstitialcy jumps. In the following chapters, the tracer and defect correlation factors are analysed in detail for a vacancy diffusion mechanism (cf. Chapter 6) and for a collinear (cf. Chapter 7) and non-collinear (cf. Chapter 8) interstitialcy diffusion mechanism. This analysis enables to compare the experimental results for the Have-ratio with calculated data from Monte Carlo simulations for either diffusion mechanism, which is an important contribution to the interpretation of the predominant mechanism of the alkali diffusion in alkali feldspar.

6. Vacancy-related diffusion correlation effects in a simple cubic random alloy and on the Na-K sublattice of alkali feldspar

Diffusion correlation effects play an important role in concentrated alloys and other binary or multi-component material systems [19]. Most prominent and frequent cases concern diffusion via the vacancy mechanism. In this mechanism, the tracer correlation factor of a constituent element takes into account that a subsequent atom-vacancy exchange has a higher than statistical probability to reverse the former exchange of the atom with the same vacancy. In elemental crystals, the tracer correlation factor is a dimensionless geometrical quantity, which for the simple cubic lattice results as $f_0 = 0.6531$ [78]. However, in binary systems AB the tracer correlation factors of A and B atoms take different values between 0 and 1, so that commonly $f_A \neq f_B$. Moreover, diffusion correlation effects are in general composition dependent implying that f_A and f_B are functions of the mole fraction $C_B = 1 - C_A$. As these correlation factors may become extremely small at low temperatures, they are relevant for the analysis of tracer self-diffusion experiments in binary and multi-component materials.

In the vacancy mechanism, the tracer correlation factors f_A and f_B have to be distinguished from the vacancy correlation factor f_V. In a pure crystal, vacancy migration is a fully random process. This reference case is characterised by the absence of correlation effects as expressed for cubic lattices by $f_V = 1$. In binary systems, however, f_V is usually less than unity and it may adopt very low values for large differences between the atom-vacancy jump rates w_A and w_B [21]. Consideration of f_V is important for the evaluation of ion conductivity measurements in ionic systems, where electrical current is mediated by mobile

vacancies carrying an effective charge [76, 79]. It can be noted that f_V is a special case of the so-called *physical* correlation factor [23, 76], which reflects the variety of jump rates of the diffusion vehicle and the binding states of the components but no geometrical effects, at least in highly symmetric lattices. Moreover, f_V can be derived from the collective correlation factors introduced by Allnatt [79, 80, 81].

There is a vast literature on diffusion correlation effects in solids, mainly dealing with cubic crystals or other systems of high symmetry. In the present chapter, correlation effects in alkali feldspar are investigated to analyse and interpret mass and charge transport date including ^{22}Na tracer diffusion coefficients (see Chapter 3 and [64]), ^{43}K diffusion coefficients (see Chapter 4 and [57]) and ion conductivity results (see Chapter 5 and [56]). In the case of alkali feldspar a supposedly disordered Na-K sublattice is considered which shares the monoclinic symmetry of the alumino-silicate framework structure. It seems plausible that transport processes on the alkali sublattice are mediated by point defects originating from Frenkel pair formation. However, whether vacancies or interstitials are the dominating diffusion vehicles is subject to the present work. The calculation of correlation factors f_{Na}, f_K and f_V on the Na-K sublattice in monoclinic alkali feldspar is a first step to unravel a complex situation of ion conduction and ionic self-diffusion.

An important step forward in the treatment and understanding of diffusion correlation effects was the introduction of the random alloy model by Manning [14, 45]. In this context, it has to be distinguished between the underlying physical model on one hand and the analytical framework to derive mathematical expressions for the pertinent correlation factors on the other. Manning's physical model foots on the assumption that all interactions among atoms (A,B) and between atoms and vacancies (V) can be neglected, which implies the total absence of short- and long-range ordering effects. Provided that the vacancy concentration C_V (site fraction) is negligibly low, this random alloy is further characterised by its composition $C_B = 1 - C_A$ and the atom-vacancy exchange frequencies w_A and w_B, which do not depend on the actual nearest-neighbour environment of the jumping atom.

In addition, Manning's analytical framework provides the mathematical equations to calculate the correlation factors f_A, f_B, and f_V [14, 45]. The formalism is based on reasonable assumptions, which partly are intuitive and partly hold to a fair approximation only. For example, Manning supposes that the effective escape

frequency of the vacancy (termed H) from the atom it just exchanged with is independent of the type of atom (A or B). However, the relationship $H = H_A = H_B$ has shown to be poorly obeyed in the range of concentrated alloys [21].

Thus, although Manning's analytical expressions include some fundamental features of diffusion in disordered concentrated alloys, they are not exact. This has become clear over the years by comparison with Monte Carlo (MC) simulations of binary cubic lattices with random order. In principle, Monte Carlo simulation enables us to compute correlation factors within Manning's *physical* model to any desired degree of accuracy, provided that enough computer capacity is available. Specifically, it was recognised over the last decades – along with the progress in computer technology – that Manning's analytical expressions do *not* provide good approximations to f_A and f_B in the concentrated alloy regime, except for small differences in jump frequencies ($0.1 < w_A/w_B < 10$) [20, 82, 21, 22]. For f_V, the agreement between MC simulation and Manning's derivations is much better [23, 82, 21]. Nevertheless, the numerical evaluation of f_V values by MC methods has been an issue of concern for many years [23, 82, 21]. Established MC calculation schemes for unbiased f_V results may involve collective correlation factors [81, 79] or simulated electric fields [21]. Still there seems to be a lack of reliable f_V data for (random) alloy structures, at least for large differences between w_A and w_B.

The present study, which has been published in Philosophical Magazine, 2015 [83] and in Defect and Diffusion Forum, 2015 [64] aims to understand and to quantify diffusion correlation effects on the Na-K sublattice of alkali feldspar by MC simulation of the vacancy mechanism. To the best of our knowledge, this is the first MC study of this type dealing with a binary monoclinic structure. The only related MC report so far concerns foreign-atom diffusion in (monoclinic) naphtalene [84]. Based on the symmetry relations of the monoclinic Bravais lattice, alkali diffusion in alkali feldspar can be described by a second rank tensor with four independent matrix elements [11, 12]. Therefore, the correlation factors to be calculated depend in principle on crystallographic direction.

To check the validity and reliability of the MC procedures, test simulations were performed on a simple cubic lattice with random order. During this test period efficient schemes for the calculation of f_V, were developed which also involve the evaluation of the partial correlation factors (PCFs) f_V^A and f_V^B [85, 14, 45]. Comparing the results from the novel schemes with published f_V data on cubic

random alloys reveals some shortcomings of the earlier MC work. Furthermore, the present f_V data enable us to derive accurate values for the site-percolation threshold and the corresponding critical exponent, both in the simple cubic case and for the monoclinic structure.

6.1. Computational procedures

The present calculations are based on an atomistic Monte Carlo approach by computer simulations. Initially, each atom in the simulation box was determined to be of type A or B by a random number generator and the site-occupancy probability $p_A = 1 - p_B = N_A/N$, where N_A is the number of A atoms and N is the total number of lattice sites. For a simple cubic lattice of dimensions $160a \times 160a \times 160a$, where a is the lattice parameter, this box contained $N = 4.096 \times 10^6$ sites with one vacant lattice site at a particular initial position. The vacancy moves through site exchange with one of its nearest-neighbour atoms. In the sc random alloy, the exchange frequency of an atom with the vacancy only depends on the atomic species ($w_A \neq w_B$). The identity of the six adjacent atoms determines the individual exchange probability $p_i \in [0, 1)$ for atom i as $p_i = w_i / \sum_j^6 w_j$. The effective exchange was then assigned to one atom by a pseudo-random number $r \in [0, 1)$ generated by the Mersenne Twister algorithm [86].
Periodic boundary conditions were applied in all simulations. The number of exchanges and displacements relative to the initial site were saved in the computer memory for each atom individually and for the vacancy. For each composition and jump frequency ratio, a Monte Carlo run with up to $n_V = 10^{11}$ (but at least 10^{10}) vacancy jumps was executed. This routine was properly tested for sc and fcc lattices by calculating tracer correlation factors and the results were in excellent agreement with reported data [22].

6.1.1. General calculation schemes for correlation factors

In general, the correlation factor is defined as the ratio $f = \langle X^2 \rangle_{\text{uncorr}} / \langle X^2 \rangle_{\text{corr}}$ of the correlated to the uncorrelated mean square displacement of a particle. A common approach in calculating tracer correlation factors is based on the relation

$$f_A = \lim_{n_A \to \infty} \langle X_A^2 \rangle / \langle n_A \rangle \lambda^2, \tag{6.1}$$

where $\langle n_\mathrm{A}\rangle$ is the mean number of jumps of length λ and $\langle X_\mathrm{A}^2\rangle$ is the mean square displacement of all atoms of type A. Thus, in this so-called *displacement method* the displacements of each A atom are monitored individually to determine f_A. This procedure has proven to be highly efficient in numerous MC simulations for computing tracer correlation factors. In the above formulation, it is implicitly made allowance for the direction dependence of diffusion by considering displacements along a chosen x-axis. In cubic crystals, however, it is more economic to replace $\langle X^2\rangle$ by the corresponding 3D quantity $\langle R^2\rangle$.
In more complicated situations involving, e.g., different jump types the calculation of *partial* correlation factors (PCFs) may provide some additional insight into the diffusion correlation effects [87, 88]. PCFs may be also useful to check the results obtained by the displacement method. To evaluate PCFs, Eq. 6.1 has to be extended in terms of projections x_i of individual atomic jumps on the x-axis [85]

$$f_\mathrm{A} = 1 + 2\sum_{i=1}^{\infty}\langle x_i x_{i+1} + x_i x_{i+2} + ...\rangle / \sum_{i=1}^{\infty}\langle x_i^2\rangle, \tag{6.2}$$

where x_{i+j} is the jth step after jump i of an atom of species A. Using this general expression PCFs were introduced by Howard [89] as

$$f_\alpha = 1 + 2\langle S_\alpha\rangle / \langle n_\alpha\rangle x_\alpha^2\,, \tag{6.3}$$

where $S_\alpha = \sum_i \sum_j (x_{\alpha,i} x_{\alpha,i+j})$ contains $x_{\alpha,i+j}$ being the jth displacement after the ith jump of type α. The *total* tracer correlation factor f_A can be calculated as a weighted sum of the PCFs for different jump types.
In calculations of f_α with Eq. 6.3, S_α has to be determined for each particle individually. Moreover, in a long sequence of jumps of a particle a large number of jumps of type α occur. For each of these jumps all terms $x_\alpha x_{\alpha,j}$ with $j \in [\alpha+1, \infty)$ add to the sum S_α. An example of S_α with the first, third and fifth jump being of type α is given by

$$\begin{aligned} S_\alpha = x_\alpha x_2 + x_\alpha x_3 + x_\alpha x_4 + x_\alpha x_5 + x_\alpha x_6 + x_\alpha x_7 + \cdots \\ + x_\alpha x_4 + x_\alpha x_5 + x_\alpha x_6 + x_\alpha x_7 + \cdots \\ + x_\alpha x_6 + x_\alpha x_7 + \cdots \\ \vdots\,. \end{aligned} \tag{6.4}$$

The summation S_α was executed by a convenient algorithm that caused no significant increase in computation time compared to the displacement method. This novel scheme is based on the fact, that all terms $x_\alpha x_{\alpha,j}$ are contained in the sequence of jumps after the first jump of type α of a certain particle. S_α was therefore calculated by firstly executing the operation $S_\alpha = S_\alpha + n_\alpha x_\alpha \cdot x$ at each atomic exchange during the simulation run, where x is the current jump vector, and secondly, by increasing the counter n_α when a new jump of type α occurred. All counters were properly initialised at the beginning of a Monte Carlo run.
Essentially, the calculation of S_α relies on the summation of scalar products, which in turn involve the cosine of the angle between jumps of the same atom. The introduction of these cosines in MC simulations was first done by Kelly and Sholl [41] and further pursued by Qin and Murch [90, 91].
The displacement and PCF method can also be employed for the MC calculation of vacancy correlation factors f_V. However, since only one vacancy is contained in the simulation box, f_V cannot be obtained by averaging over many particles at the end of a MC run. Instead a long vacancy trajectory of length n_V was divided into N_run sequences of n_L jumps, each. Then the best estimate for f_V is the mean value over N_run runs. Unless otherwise specified, the simulations were performed with $N_\mathrm{run} = 5 \times 10^5$ and $n_\mathrm{L} = 2 \times 10^4$.
An additional feature of vacancy correlation is that a distinction can be made between the PCFs f_V^A and f_V^B, where A and B refer to the first exchange in a long vacancy trajectory, respectively. The overall correlation factor is a weighted sum of these PCFs, i.e.,

$$f_\mathrm{V} = r_\mathrm{A} f_\mathrm{V}^\mathrm{A} + r_\mathrm{B} f_\mathrm{V}^\mathrm{B} \,, \tag{6.5}$$

where for a random alloy, e.g., r_A is given by [14]

$$r_\mathrm{A} = \frac{C_\mathrm{A} w_\mathrm{A}}{C_\mathrm{A} w_\mathrm{A} + C_\mathrm{B} w_\mathrm{B}} \,. \tag{6.6}$$

In turn, f_V^A and f_V^B can be further decomposed in jump-type-specific PCFs (e.g., $f_{\mathrm{V},\alpha}^\mathrm{A}$) depending on the crystal structure. Conversely, jump-type-specific PCFs $f_{\mathrm{V},\alpha}$ calculated without discrimination of the atom type (A, B) making the first exchange are the weighted sum of the corresponding atom-specific PCFs of vacancy diffusion, i.e., – in self-explanatory notation – $f_{\mathrm{V},\alpha} = r_\alpha^\mathrm{A} f_{\mathrm{V},\alpha}^\mathrm{A} + r_\alpha^\mathrm{B} f_{\mathrm{V},\alpha}^\mathrm{B}$.

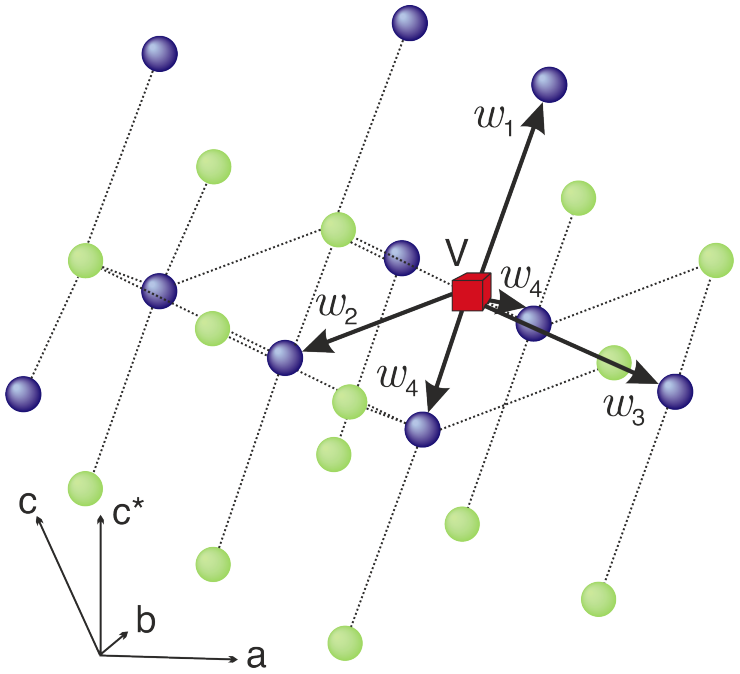

Figure 6.1.: Illustration of the Na-K sublattice of alkali feldspar that comprises a C_2 symmetry. Along the c^*-axis, a vacancy can exchange with four nearest-neighbour atoms in negative direction and with one such atom in positive direction. The signs of these directions alter with each jump. The monoclinic system discriminates between four types of jump ($\alpha = 1$ to 4) with the corresponding frequency w_α.

6.1.2. Calculation scheme for monoclinic feldspar

Compared to cubic structures the monoclinic alkali sublattice of feldspar is more complex and correlation effects are generally not isotropic. Correlation factors then have to be determined in the directions of the principal axes of the diffusion tensor D. Since only diffusion in the b-direction ($\perp$ (010)) and c^*-direction ($\perp$ (001)) have experimentally been investigated hitherto [64], the simulations are restricted to these two directions. The simulated alkali lattice was composed of $80a \times 80b \times 80c$ unit cells, each containing four alkali atoms. The K and Na atoms were randomly distributed and several jump frequency ratios $w_\mathrm{K}/w_\mathrm{Na} < 1$ were investigated. The following considerations apply both to tracer and vacancy correlation factors.
Figure 6.1 shows that a vacancy has five nearest-neighbour alkali atoms, which – by assumption – do not interact with the $AlSi_3O_8$ network structure. Depending on its position relative to the vacancy an atom performs one out of four jump types $\alpha(= 1$ to 4) with the corresponding frequency w_α. The two atoms adjacent to the vacancy that have a non-zero displacement $\lambda_b = b/2$ along the b-axis both perform

the same type of jump ($\alpha = 4$), since b is the axis of two-fold symmetry in the monoclinic structure. Correlation factors in b-direction were determined by

$$f_b = 1 + 2\langle S_b \rangle / \langle n_b \rangle \lambda_b^2 \,, \tag{6.7}$$

with S_b successively updated during a diffusion run according to $S_b = S_b + \lambda_b \left(n_b^+ - n_b^- \right) \cdot x$. In Eq. 6.7, the total number of jumps with non-zero b-component, $n_b = n_b^+ + n_b^-$, is decomposed into jumps in the same (n_b^+) and opposite direction (n_b^-) regarding the first jump.

For diffusion along the $c^\star$-axis all four types of jumps do contribute with their *projected* lengths $\lambda_1 = 4.692$ Å and $\lambda_2 = \lambda_3 = \lambda_4 = 1.764$ Å. In monoclinic feldspar (Fig. 6.1), the jump types $\alpha = 2$ and $\alpha = 3$ refer to two sublattice sites with a major displacement along the a-axis. Although their projected jump lengths on the b-axis ($\lambda_b = 0$) and the $c^\star$-axis ($\lambda_2 = \lambda_3$) are equal, this is not true for projections on the a-axis and thus $w_2 \neq w_3$ in general. Another structural feature is that two types of alkali lattice sites with symmetry C_2 have to be distinguished and that for a moving particle the type of site alters with each nearest-neighbour exchange. Consequently, the vacancy can perform either one of four jumps in negative $c^\star$-direction or one jump of type $\alpha = 1$ in positive $c^\star$-direction. Thus, after each jump of an atom, regardless of which type, the signs of these directions are interchanged. The PCF for each jump type α is given by

$$f_{c^\star,\alpha} = 1 + 2\langle S_\alpha \rangle / \langle n_\alpha \rangle \lambda_\alpha^2, \tag{6.8}$$

where $S_\alpha = S_\alpha + \lambda_\alpha \left(n_\alpha^+ - n_\alpha^- \right) \cdot x$. The PCFs are weighted by

$$r_\alpha = k_\alpha w_\alpha \lambda_\alpha^2 / \sum_i k_i w_i \lambda_i^2 \tag{6.9}$$

in order to obtain the total correlation factor as

$$f_{c^\star} = \sum_{\alpha=1}^{4} r_\alpha f_{c^\star,\alpha} \,. \tag{6.10}$$

In Eq. 6.9, k_α accounts for the fact that the feldspar structure includes twice as many jumps of type $\alpha = 4$ than all other jump types and hence $k_4 = 2$ while $k_1 = k_2 = k_3 = 1$. Eqs. 6.7 to 6.10 were used to calculate vacancy correlation factors by averaging over N_{run} sequences of vacancy jumps.

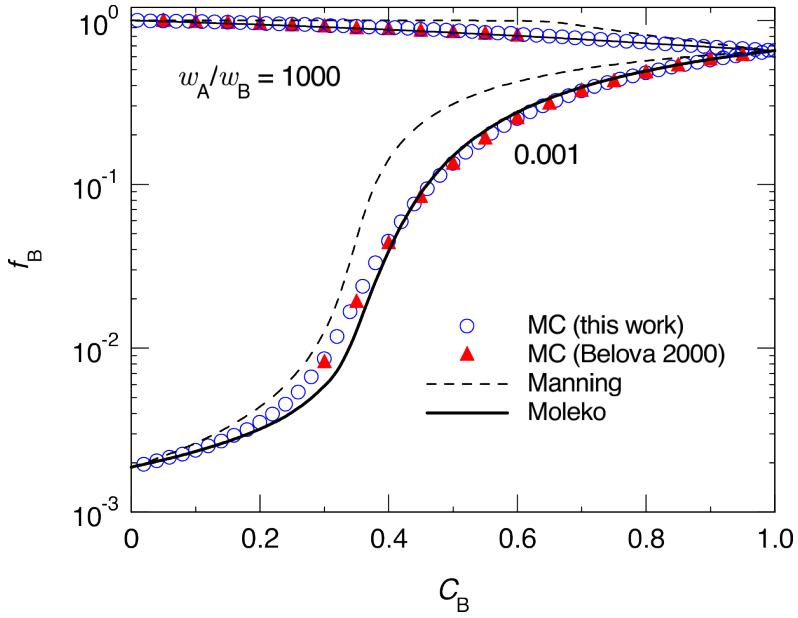

Figure 6.2.: Tracer correlation factor f_B as a function of composition C_B in the simple cubic random alloy for two different values of w_A/w_B. Circles: MC simulations (this work, every second data point); triangles: previous MC simulations [22]; Solid lines: formalism of Moleko et al. [92]; Dashed lines: Manning's formalism [14, 45].

6.2. Results and discussion

6.2.1. Correlation factors in a simple cubic alloy

Tracer correlation factors

To verify the correctness of the computational procedures, the diffusion by the vacancy mechanism in a sc random alloy AB was simulated. Figure 6.2 displays the tracer correlation factor as a function of composition C_B for two greatly different jump frequency ratios, i.e., $w_A/w_B = 1000$ and $w_A/w_B = 0.001$. The data were obtained by the displacement method for C_B steps of 0.01 over the whole composition range. In contrast to common practice, f_B is plotted on a logarithmic scale. This representation has the advantage that several orders in magnitude of the correlation factor can be clearly displayed. In particular, also the low f_B values near $C_B = 0$ can be read from Fig. 6.2 with satisfactory accuracy. Another benefit is that deviations and errors are displayed in relative proportions, as $\Delta \ln f_B \approx \Delta f_B / f_B$. Therefore, logarithmic plotting is preferred throughout this work.

The utmost right-hand side $C_B = 1$ corresponds to B self-diffusion. Here, the true geometrical f_B value, $f_0 = 0.6531$ [78] is reproduced within 3 digits. It is seen that the present data (circles) match the MC simulation results of Belova and Murch [22] (triangles), which could be taken with sufficient accuracy from their corresponding linear plot (Fig. 5 in [22]) only for $f_V > 0.01$. Figure 6.2 further shows that Manning's analytical results (dashed lines) substantially deviate from the MC simulations, especially in the central composition range. However, the formalism of Moleko et al. [92] (solid lines) yields a much better approximation. These findings have been extensively discussed in the literature [82, 21, 22].

Vacancy correlation factors

Vacancy correlations factors in the sc lattice were also determined by MC simulation in this work. An extreme case is shown in Fig. 6.3 representing f_V for $w_A/w_B = 10^{-5}$. The initial division of the composition axis consisted of 101 equidistant points. Additional simulations were done at intermediate compositions where the slope in the f_V-versus-C_B plot is very steep, i.e, near $C_B = 0$ and $C_B = 0.3$. All simulation data in Fig. 6.3 were obtained by the displacement method for the same total number of vacancy jumps $n_V = 10^{11}$. Reliable results were obtained for the division of n_V in $N_{run} = 10^3$ runs of $n_L = 10^8$ jumps, as shown by the open circles. Figure 6.3 also reveals that other splitting of n_V in number of runs and run length produce strong deviations for $C_B \leq 0.35$. This feature will be obscured by a linear f_V plot, as has been published for fcc [82] and bcc [21] random alloys. It is further seen that Manning's formalism leads to an excellent match in wide ranges of either B-rich or B-poor compositions. It can be noted that in the case of f_V the Moleko formalism coincides with Manning's expressions [24]. However, clear discrepancies between MC simulation and the analytical results appear near $C_B \approx 0.3$. This finding apparently relates to the occurrence of a site-percolation threshold close to $C_B = 0.3$ in the sc lattice. By contrast, both the Manning and Moleko theories place the percolation threshold at $1 - f_0$ [23], which equals 0.3469 for the sc lattice. Indeed, the derivation of the solid line in Fig. 6.3 yields a maximum at $C_B = 0.347$. The percolation topic will be further discussed in Sect. 6.2.3.
It can be noted that the optimal choice of N_{run} and n_L within a given total number of vacancy jumps is found to depend on composition. It may be recognised from Fig. 6.3 that for relatively high N_{run} values and corresponding short run lengths the data (squares, triangles) show less scatter than for the reverse reference case

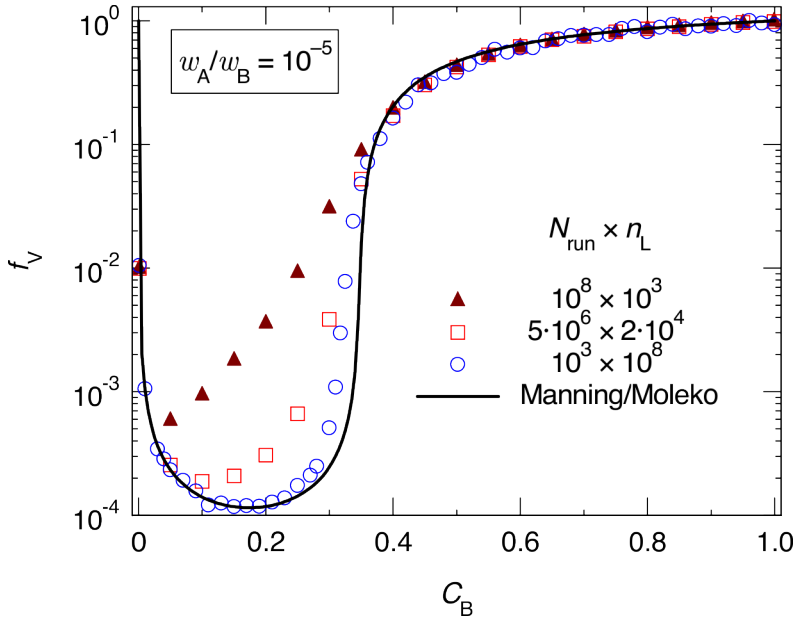

Figure 6.3.: Vacancy correlation factor f_V as a function of composition C_B in the simple cubic random alloy for the jump frequency ratio $w_A/w_B = 10^{-5}$. The symbols represent MC simulations for different numbers of runs (N_{run}) and run lengths (n_L) with the same total number of jumps (10^{11}), as indicated. For clarity, every second circle has been omitted. The solid line reproduces the coinciding analytical results of Manning [14, 45] and Moleko et al. [92].

(circles). Thus, if B is the much more mobile component (e.g. $w_A/w_B = 10^{-5}$), short run lengths obviously yield unbiased results [93] for B-rich compositions while a large N_{run} value leads to the reduction of the statistical error. However, short run lengths start to produce systematically too high f_V values upon approaching the percolation limit near $C_B = 0.3$ from the B-rich side.

This behaviour is demonstrated in Fig. 6.4 for a series of simulations at the composition $C_B = 0.3$ with a fixed number of runs ($N_{run} = 1000$) and with the run length increasing from $n_L = 10^3$ to 10^8. The MC data suggest an exponential decay of f_V with increasing n_L for the shorter runs, and moreover, illustrate the final convergence towards the true value of 5×10^{-5} for the longer runs with $n_L \approx 5 \times 10^6$ jumps or larger. The Manning result of $f_V = 2 \times 10^{-5}$ is also indicated in Fig. 6.4. It can be noted that the data on the left-hand side in Fig. 6.4 show appreciable scatter, which relates to the small values of both N_{run} and n_L. Altogether, the picture provided by Fig. 6.4 confirms the validity of the data for long runs in Fig. 6.3 (circles, $n_L = 10^8$). Mishin and Farkas [21] used $n_L = 10^3$ together with $N_{run} = 10^6$ for f_V simulation in bcc random alloys with $w_A/w_B = 10^{-5}$. Based on

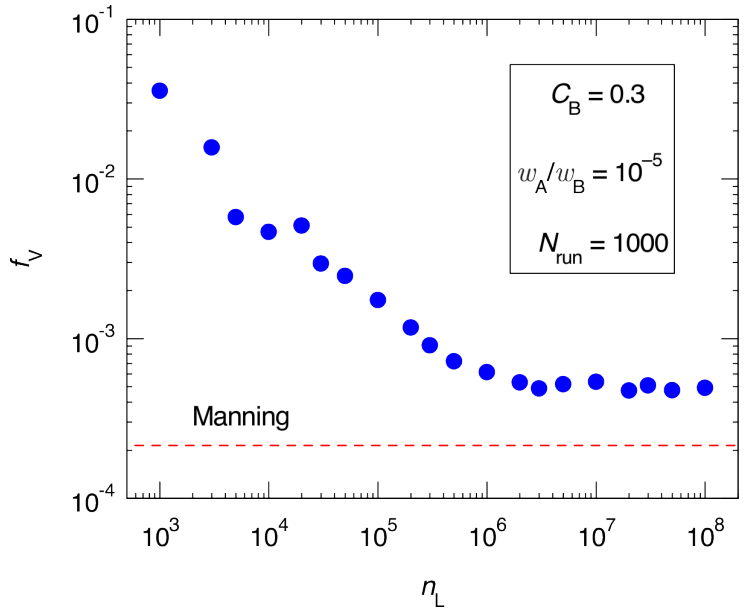

Figure 6.4.: Vacancy correlation factor f_V as a function of run length n_L for the sc random alloy with $C_B = 0.3$ and $w_A/w_B = 10^{-5}$. Each data point results from MC simulation by averaging over 1000 consecutive runs of length n_L. The analytical result of Manning [14, 45] is reproduced by the dashed line.

the present analysis, it can be concluded that their f_V data for C_B near and below the percolation limit suffer from a bias towards the high value range.

It seems reasonable to assume that for a reliable determination of f_V also the less mobile component, in this case A, should make a sufficient number of jumps. In a random alloy, the fraction of A jumps equals r_A given by Eq. 6.6. Thus, for $w_A/w_B = 10^{-5}$ and $C_B = 0.3$ it follows $r_A \approx 2.3 \times 10^{-5}$. Hence, in a single vacancy run of n_L jumps the number of exchanges with A amounts to $r_A n_L$. According to Fig. 6.4, f_V attains its true plateau value for n_L near 5×10^6 implying that about 100 A jumps per run are required. Numbers of this order of magnitude are also necessary for the reliable determination of f_A, as has been reported previously [22]. In view of the above argument, it may surprise that for C_B-rich alloys rather short run lengths of 1000 jumps are enough to evaluate f_V with negligible error (cf. Fig. 6.3). However, this can be rationalised by the different situations below and beyond the percolation threshold near $C_B = 0.3$. Below the percolation threshold, vacancy migration proceeds mainly through B-rich clusters that are poorly connected among each other. With small n_L values, the vacancy is not able to escape from these clusters. Then the simulation is biased to B-rich environments,

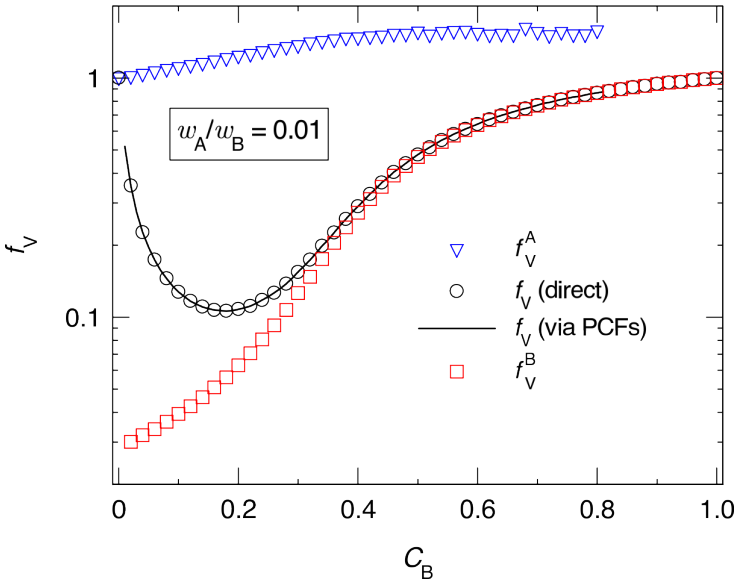

Figure 6.5.: Partial and total vacancy correlation factors as a function of composition C_B in the simple cubic random alloy for the jump frequency ratio $w_A/w_B = 10^{-2}$. The total correlation factor f_V (solid line) calculated from f_V^A (triangles) and f_V^B (squares) via the PCF method coincides with f_V directly simulated by the displacement method. For clarity, every second symbol has been omitted.

where f_V locally adopts higher values (triangles, left-hand side of Fig. 6.3). With sufficiently long trajectories, the vacancy is able to break free from the B-rich clusters giving rise to unbiased statistical sampling and eventually determination of the true correlation factor (circles, left-hand side of Fig. 6.3). By contrast, for B concentrations sufficiently far above the percolation limit there is a well-connected network of B-rich regions. In this situation, the main effect of A atoms is site-blocking, which constraints the choice of trajectories available to the vacancy and thereby causes f_V to be smaller than unity. Then, the influence of some rare A jumps among many B-V exchanges may apparently be neglected.

Partial correlation factors of vacancy diffusion

In the 'PCF method' described in Sect. 6.2.1 f_V is evaluated by suitable monitoring and bookkeeping of the two-jump scalar products appearing in the expression for the partial correlation factors f_V^A and f_V^B (cf. Eqs. 6.3 and 6.4). The results of this PCF method are exemplarily displayed for the sc random alloy with $w_A/w_B = 0.01$ in Fig. 6.5. It is seen that f_V^A (triangles), associated with the less mobile component, assumes values greater than unity, i.e., from 1 to about 1.5. This is no contradiction,

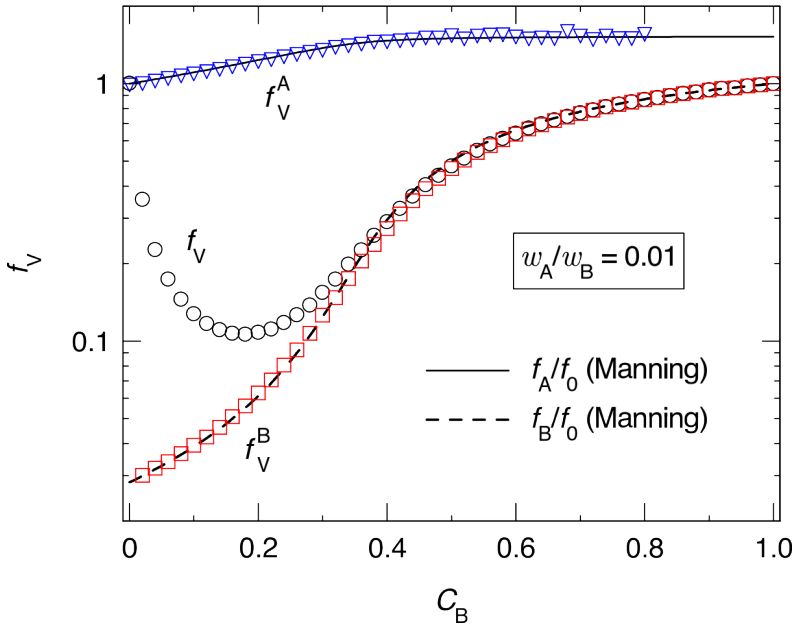

Figure 6.6.: Partial and total vacancy correlation factors as a function of composition C_B in the simple cubic random alloy for the jump frequency ratio $w_A/w_B = 10^{-2}$ (same data points as in Fig. 6.5). Solid and dashed lines: f_0-normalized tracer correlation factor f_A and f_B, respectively, as derived within Manning's formalism [14, 45].

since PCFs are calculatory quantities without obvious physical meaning [94]. The f_V^A results for $C_B > 0.8$ suffer from poor statistics and are therefore omitted in Fig. 6.5. In contrast, the f_V^B data (squares), related to the more mobile component and spanning the range from about 0.03 to 1, are reliable for all compositions.

According to Eq. 6.5 the total vacancy correlation factor is a weighted sum of the two PCFs [14] and represented by the solid line in Fig. 6.5. It should be emphasised that this line perfectly coincides with the f_V data directly obtained by the displacement method (circles). It may therefore be concluded that the PCF method is fully equivalent to the displacement method, both in terms of reliability and computing time. However, the PCF method provides some additional insight into the correlations that mostly contribute to f_V. Figure 6.5 reveals that for $C_B > 0.4$ f_V coincides with f_V^B, which relates to the fact that r_A is very small in this region (cf. Eq. 6.6).

Figure 6.6 exhibits the same data points as Fig. 6.5 but they are now used for a comparison with Manning's analytical expressions. In particular, Fig. 6.6 bears out the notion that f_A/f_0 analytically derived within the Manning formalism (solid line) well approximates the simulated f_V^A data for $w_A/w_B = 0.01$. The same is

true for f_B/f_0 (dashed line) with respect to the f_V^B data. It is worth noting that the agreement shown in Fig. 6.6 for the PCFs is distinctly better than Manning's predictions for the simulated (or true) atomic correlation factors f_A and f_B. A direct comparison of the latter kind for the sc random alloy with $w_A/w_B = 0.01$ has been published by Belova and Murch [22] (see also Fig. 6.2). This leads to the conclusion that the Manning formalism yields – first and foremost – good estimates for the vacancy correlation factors. However, Manning's predictions for the tracer correlation factors are much less accurate. Obviously, the relationships $f_A = f_V^A f_0$ and $f_B = f_V^B f_0$ playing a crucial role in his theory are only very approximate.
Vacancy correlation factors and PCFs can also be calculated from the so-called collective correlation factors (CCFs), as shown in detail in the literature [79, 24]. In fact, f_{BB} and f_{AA} were determined from simulations within the sc random alloy with $w_A/w_B = 0.01$ in the present study. Using published equations [79, 24], f_V^A, f_V^B, and f_V can be derived from the simulated f_{BB} data in excellent agreement with the results from the PCF and displacement method. However, the evaluation of CCFs required 20 times longer CPU times than the other methods. Hence, after this first proof of consistency the CCF route was refrained.

6.2.2. Correlation factors on the alkali sublattice in feldspar

Vacancy and tracer correlation factors on the Na-K sublattice of alkali feldspar were simulated by the computational procedures described in Section 6.1 for the directions b and $c^\star$. Since pertinent experimental or theoretical data on atom-vacancy exchange rates are lacking, differences between w_{Na} and w_K were allowed but it is assumed that both of them are independent of jump type $\alpha = 1$ to 4 ($w_{i,1} = w_{i,2} = w_{i,3} = w_{i,4} = w_i$ for i = K,Na).

Mono-atomic case

First, the fundamental case of a mono-atomic sublattice was examined, which may refer to pure K-feldspar. The results for the *tracer* correlation factor are $f_{0,b} = 0.5909$ and $f_{0,c^\star} = 0.5634$ for diffusion in b- and $c^\star$-direction, respectively. Furthermore, the vacancy correlation factors were obtained as $f_{V,b} = 1.0000$ and $f_{V,c^\star} = 0.9676$. The latter result is remarkable, as in other mono-atomic structures f_V has always been found to be equal to unity, that is, in the limit of low vacancy concentrations. This finding is attributed to a different number of positively and

negatively directed jumps along the $c^\star$-axis (see Fig. 6.1). The f_V results can be readily checked analytically by using Howard's matrix method [85]. Indeed, this rigorous derivation yields $f_{V,c^\star} = 0.96757$, in excellent agreement with the simulated value.

Also, vacancy-related PCFs in $c^\star$-direction for the different jump types α in the pure monoclinic sublattice with uniform vacancy exchange rates were calculated. The PCF related to jump type 1 was found as $f^1_{V,c^\star} = 1.101 \pm 0.001$. For the other PCFs a uniform value resulted, which is given by $f^i_{V,c^\star} = 0.732 \pm 0.001$ with $i = 2$, 3 or 4.

Na-K sublattice with random order

To investigate the orientation dependence of f_V in alkali feldspar MC simulations were performed as a function of composition C_{Na}. Figure 6.7 compares the results for the directions $\perp$ (001) ($c^\star$) and $\perp$ (010) (b) in the case when $w_K/w_{Na} = 0.01$ holds. It is seen that f_V anisotropy is a uniform feature over the whole composition range and characterised by the ratio $f_{V,c^\star}/f_{V,b} = 0.9676$. Figure 6.7 also shows the PCFs in $c^\star$-direction for initial vacancy exchanges of type 1 to 4. Here, no discrimination was made between the types of atom (Na, K) making the first jump. In each case examined, the full consistency between displacement and PCF method was confirmed.

In further analysis, the simulations of f_V in the $c^\star$-direction ($\perp$ (001)) of feldspar were extended to jump frequency ratios spanning the range from $w_K/w_{Na} = 0.1$ to 10^{-5}. For the latter frequency ratio, n_L was chosen as 2×10^7. The results shown in Fig. 6.8 clearly demonstrate that correlation effects may become very strong in the concentrated regime with $C_{Na} < 0.4$. As a consequence, the ionic conductivity based on the vacancy mechanism can be reduced by many orders of magnitude. Obviously, this phenomenon relates to vacancy percolation via the more mobile Na atoms and the site-blocking effect of the less mobile K atoms.

Figure 6.8 also exhibits the prediction from Manning's equations using $f_{0,c^\star} = 0.5634$ and applying a correction factor of 0.9676 which accounts for the fact that in the mono-atomic case f_V deviates from unity (cf. Sect. 6.2.2). Good agreement is obtained for either Na-rich or K-rich compositions but not in the C_{Na}-range between about 0.3 and 0.5.

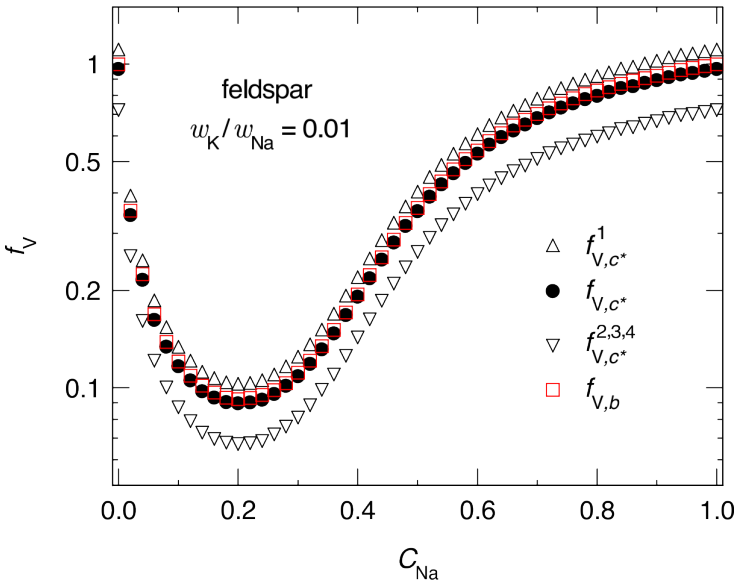

Figure 6.7.: Partial and total vacancy correlation factors from MC simulations as a function of composition C_{Na} on the Na-K sublattice of alkali feldspar for the jump frequency ratio $w_{\mathrm{K}}/w_{\mathrm{Na}} = 10^{-2}$. The total f_{V} values for the b-direction (open squares) are compared with those for the $c^\star$-direction (solid circles). The PCFs in $c^\star$-direction for the four different jump types ($\alpha = 1$ to 4) are also displayed (open triangles).

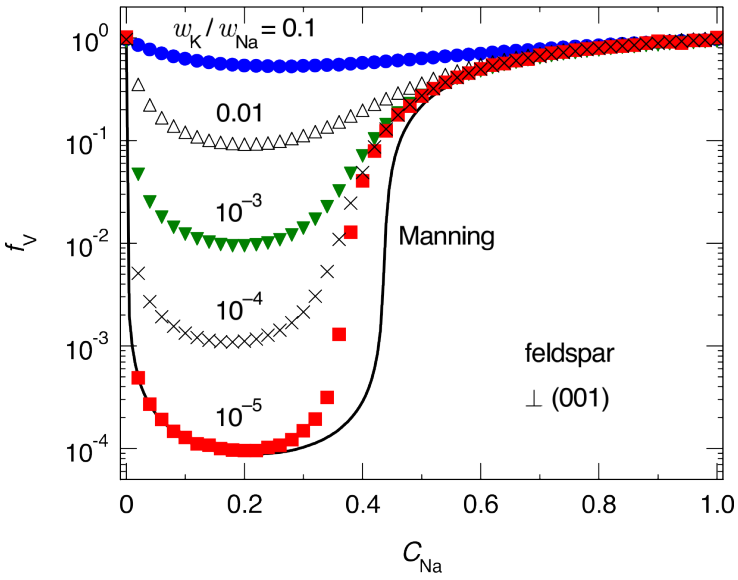

Figure 6.8.: Vacancy correlation factors f_{V} in $c^\star$-direction as a function of composition C_{Na}on the Na-K sublattice of alkali feldspar for different jump frequency ratios $w_{\mathrm{K}}/w_{\mathrm{Na}}$. Solid line: Manning's formalism for $w_{\mathrm{K}}/w_{\mathrm{Na}} = 10^{-5}$ using the MC results for f_0 and f_{V} in the mono-atomic case.

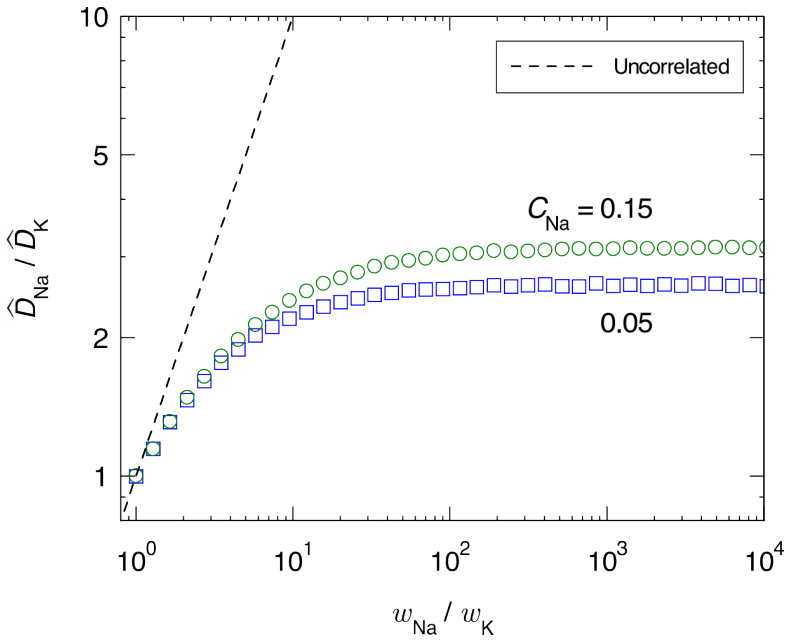

Figure 6.9.: Ratio of Na and K diffusivities $\widehat{D}_{\mathrm{Na}}/\widehat{D}_{\mathrm{K}}$ as a function of $w_{\mathrm{Na}}/w_{\mathrm{K}}$ in alkali feldspar with diffusion by the vacancy mechanism. Note that for $w_{\mathrm{Na}} > w_{\mathrm{K}}$ all curves fall below the dashed line, which represents the hypothetical case with $f_{\mathrm{Na}} = f_{\mathrm{K}} = 1$.

Beyond the effect of f_{V} on ionic conductivity, also the tracer diffusion coefficients[1] of the more mobile Na component $\widehat{D}_{\mathrm{Na}}$ can be reduced by orders of magnitude in the concentrated regime. Taking the example of Volkesfeld feldspar (VF) with an alkali sublattice that supposedly consists of Na and K atoms only ($C_{\mathrm{Na}} + C_{\mathrm{K}} = 1,\ C_{\mathrm{Na}} = 0.15$) the diffusivity ratio as a function of jump frequencies $w_{\mathrm{Na}}/w_{\mathrm{K}}$ can be derived from the tracer correlation factors f_{Na}, f_{K} according to

$$\frac{\widehat{D}_{\mathrm{Na}}}{\widehat{D}_{\mathrm{K}}} = \frac{f_{\mathrm{Na}} w_{\mathrm{Na}}}{f_{\mathrm{K}} w_{\mathrm{K}}}. \tag{6.11}$$

In Fig. 6.9 tracer diffusivity ratios are presented over a wide range of jump frequencies from $w_{\mathrm{Na}}/w_{\mathrm{K}} = 1$ to 10^4. The findings are compared with data obtained for a second composition of $C_{\mathrm{Na}} = 0.05$ which represents diffusion in the more K-rich Madagascar orthoclase (MO). It can be seen that the diffusivity ratios of VF and MO feldspar reach an upper limit for roughly $w_{\mathrm{Na}}/w_{\mathrm{K}} \geq 100$, that is $\widehat{D}_{\mathrm{Na}}/\widehat{D}_{\mathrm{K}} \leq 3.12$ for VF and $\widehat{D}_{\mathrm{Na}}/\widehat{D}_{\mathrm{K}} \leq 2.57$ for MO, respectively. With reference

[1] To reduce the number of indices, the common asterisk for labelling tracer diffusivity (D^*) has been replaced by the 'hat' symbol ($\widehat{D}$) throughout this work.

to Chapter 4 where experimental tracer diffusion results for ^{43}K and ^{22}Na were presented, the diffusivity ratio for VF feldspar $\widehat{D}_{\mathrm{Na}}/\widehat{D}_{\mathrm{K}}$ is 1230/1 at 1173 K – more than two orders of magnitude above the upper limit pertaining to a vacancy diffusion mechanism. Obviously, the upper limits for vacancy diffusion in VF and MO feldspar are associated with the occurrence of a site-percolation threshold at a composition somewhere above $C_{\mathrm{Na}} = 0.15$. The percolation behaviour will be more accurately analysed in the next section.

6.2.3. Vacancy percolation behaviour

As indicated above, f_{V} will be small in binary random systems when the choice of 'fast' vacancy migration paths along chains and clusters of the more mobile component (B) becomes very restricted. In the limiting case, $w_{\mathrm{A}}/w_{\mathrm{B}} = 0$, the slower component (A) is fully immobile. This leads to the occurrence of a threshold composition $C_{\mathrm{B}}^{\mathrm{p}}$ below which long-range diffusion is not possible ($f_{\mathrm{V}} = 0$). The concentration dependence of f_{V} just above the percolation threshold $C_{\mathrm{B}}^{\mathrm{p}}$ may be described by [23, 21]

$$f_{\mathrm{V}} = k(C_{\mathrm{B}} - C_{\mathrm{B}}^{\mathrm{p}})^{\delta},\ C_{\mathrm{B}} \geq C_{\mathrm{B}}^{\mathrm{p}}\,, \tag{6.12}$$

where δ is a critical exponent and k a dimensionless proportionality constant. It can be noted that the parameters entering this expression have been determined for the fcc random alloy with $w_{\mathrm{A}}/w_{\mathrm{B}} = 0$ by a number of different MC calculation schemes [23]. Mishin and Farkas [21] have shown for the bcc lattice that k, $C_{\mathrm{B}}^{\mathrm{p}}$, and δ may be also estimated from MC simulations of f_{V} for extremely small values of $w_{\mathrm{A}}/w_{\mathrm{B}}$. This approach will be used for the sc random alloy and the alkali sublattice of feldspar in the following sections.

Vacancy percolation in the sc random alloy

Vacancy percolation behaviour in the sc random alloy was analysed by using the f_{V} data for $w_{\mathrm{A}}/w_{\mathrm{B}} = 10^{-5}$ depicted in Fig. 6.3. To this aim, the data in a narrow concentration interval above $C_{\mathrm{B}} \approx 0.3$ were fitted with Eq. 6.12, as illustrated in Fig. 6.10. Most consistent results were obtained by fitting of $\ln f_{\mathrm{V}}$ using the logarithmic form of Eq. 6.12 (dashed line in Fig. 6.10). The best estimates of $C_{\mathrm{B}}^{\mathrm{p}}$, δ, and k are compiled in Tab. 6.1.

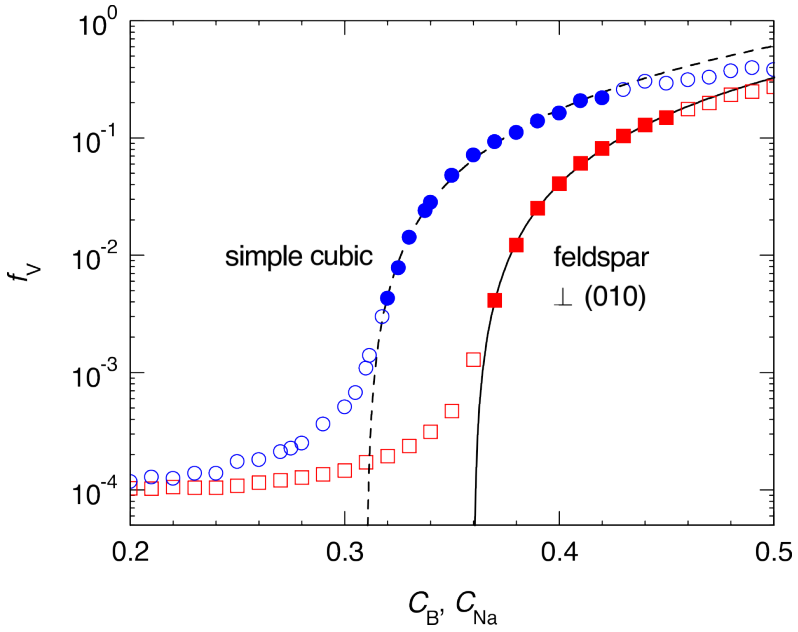

Figure 6.10.: Vacancy correlation factors f_V in the sc random alloy and on the Na-K sublattice of alkali feldspar in b-direction as a function of composition near the respective percolation thresholds. The data are representative of $w_K/w_{Na} = 10^{-5}$ as also displayed in Fig. 6.3 (sc, circles) and Fig. 6.8 (feldspar, squares). The dashed and solid line are fits based on Eq. 6.12 to the solid symbols for sc and feldspar, respectively.

It can be noted that the value obtained for C_B^p, 0.310 ± 0.001, is very close to the literature value of the sc site-percolation threshold $p^c = 0.3116$ [95]. The critical exponent $\delta = 1.67 \pm 0.06$ may be compared with similar values for fcc ($\delta = 1.45$ [23]) and bcc ($\delta = 1.326$ [21]) random alloys. Also the prefactor $k = 9.8 \pm 1.6$ is of similar magnitude as reported for the bcc lattice ($k = 5.65$ [21]). These results, in particular the C_B^p value, support the reliability of the present simulation procedures.

Alkali vacancy percolation in monoclinic feldspar

The composition dependence of f_V in feldspar can also be described by the general expression in Eq. 6.12, i.e., by replacing C_B and C_B^p with C_{Na} and C_{Na}^p, respectively. This is demonstrated for the b-direction by the good agreement between the MC data and the fitted solid line. The resulting parameter values are listed in Tab. 6.1 together with similar data for the $c^\star$-direction.
For both directions, the percolation threshold is obtained as $C_{Na}^p = 0.360$ within a small error tolerance of ± 0.001. Presumably, this is the first report of a percolation limit in the monoclinic structure. The present finding implies that for $C_{Na} < 0.36$

Table 6.1.: Parameter values characterizing the vacancy percolation behaviour in the simple cubic random alloy and on the Na-K sublattice of alkali feldspar in two different directions; cf. Eq. 6.12.

Case	$C_{\mathrm{B}}^{\mathrm{p}}$, $C_{\mathrm{Na}}^{\mathrm{p}}$	δ	k
simple cubic	0.310 ± 0.001	1.67 ± 0.06	9.8 ± 1.6
feldspar: b-direction	0.360 ± 0.001	1.67 ± 0.06	8.7 ± 1.2
feldspar: $c^\star$-direction	0.360 ± 0.001	1.65 ± 0.06	8.1 ± 1.0

the diffusion of the relatively mobile Na atoms will be highly correlated with that of the much slower moving K atoms [64]. Moreover, the ion conductivity due to the vacancy mechanism is predicted to be strongly reduced for K-rich compositions.
The critical exponents $\delta = 1.67$ and 1.65 found for the b- and $c^\star$-direction, respectively, agree well within their error bounds of ± 0.06. Furthermore, these values virtually coincide with the sc result (cf. Tab. 6.1). This may point to a structure-independent generality of the critical behaviour near vacancy diffusion percolation limits. The proportionality constant k has been derived with greater uncertainties. Nonetheless, the values obtained are of closely similar magnitude in all three cases (cf. Tab. 6.1). The small difference between the b- and $c^\star$-direction in feldspar, $k = 8.7 \pm 1.2$ and 8.1 ± 1.0, respectively, may be largely due to the difference in the magnitude of f_{V} given by the ratio 1/0.9645 (cf. Fig. 6.7 and Section 6.2.2), which adds to some scatter in δ. Altogether, the consistency among the individual results lends credibility to the employed calculation schemes.

6.3. Summary and conclusions

This work focused on the calculation of vacancy correlation factors f_{V} for diffusion in binary atomic or ionic systems with random order using Monte Carlo simulation techniques. Efficient computation schemes were tested on simple cubic alloys and then for the first time used for the evaluation of vacancy correlation effects on the Na-K sublattice in the monoclinic structure of alkali feldspar. The results of this study may be summarised as follows:
(i) A numerical Monte Carlo procedure devised for the efficient calculation of f_{V} includes the determination of partial correlation factors (PCFs) – either jump-type

or atom-type specific – without significant additional costs in terms of CPU time.
(ii) The unbiased and accurate evaluation of f_V within a sufficiently large total number of vacancy jumps (e.g., 10^{11}) requires a suitable splitting in run length and number of runs. The best choice is found to depend on composition (C_B) and jump frequency ratio (w_A/w_B).
(iii) The Manning random alloy model accurately describes f_V in the sc lattice both for A-rich and B-rich compositions. However, deviations from the simulated data appear in the concentrated alloy regime roughly between $C_B = 0.2$ and $C_B = 0.6$. These deviations increase with decreasing jump frequency ratio w_A/w_B.
(iv) Analysis of the vacancy percolation behaviour from the simulated f_V data in the sc lattice yields values for the compositional percolation limit ($C_B^p = 0.310$) and the corresponding critical exponent ($\delta = 1.67$) that closely agree with literature data.
(v) The reduced atomic correlation factors f_A/f_0 and f_B/f_0 (with correlation factor $f_0 = 0.6531$ for a pure sc crystal) analytically derived within the Manning formalism well approximate the vacancy-related PCFs f_V^A and f_V^B obtained by MC simulation.
(vi) The calculation of f_V through the simulation of collective correlation factors leads to fully consistent results but is costly in terms of computer time.
(vi) For the Na-K sublattice in monoclinic alkali feldspar, simulations were carried out for different compositions C_{Na} and various jump frequency ratios w_K/w_{Na} but with uniform frequencies of the different jump types for either component.
(vii) The alkali tracer correlation factor in the pure feldspar sublattice results as $f_0 = 0.5634$ for the crystallographic $c^\star$-direction ($\perp$ (001)) and as $f_0 = 0.5909$ for the b-direction ($\perp$ (010)).
(viii) Simulations of f_V in monoclinic alkali feldspar also show differences between different crystallographic orientations. For the $c^\star$-direction f_V is smaller than unity even for the pure sublattice ($C_{Na} = 0$ or 1).
(ix) The total correlation factor f_V along the $c^\star$-direction is the weighted sum of four PCFs associated with the different types of jump on the Na-K lattice in feldspar
(x) Within the pertinent simulation model, alkali vacancy diffusion in alkali feldspar is characterised by a percolation threshold of $C_{Na}^p = 0.360$ independent of crystallographic orientation.
The results and considerations from this chapter include important aspects for an interpretation of the diffusion mechanism that controls Na self-diffusion and ionic conductivity in alkali feldspar. From experimental data of the K-rich VF feldspar it

was demonstrated in Chapter 4 that the Na diffusivity $\widehat{D}_{\mathrm{Na}}$ exceeds $\widehat{D}_{\mathrm{K}}$ by several orders of magnitude with a difference in activation energy of $\Delta H_{\mathrm{K}} - \Delta H_{\mathrm{Na}} = 1.1\,\mathrm{eV}$. This observation indicates that the Na self-diffusion is not subject to site-blocking effects of the less mobile K atoms. A common vacancy mechanism of Na and K, however, is characterised by a percolation threshold $C^{\mathrm{p}}_{\mathrm{Na}} = 0.360$ and hence, the Na diffusivity via vacancies is significantly reduced in VF feldspar. Moreover, the activation energies of Na and K self-diffusion via vacancies can be expected to be almost balanced in VF feldspar due to correlation effects. In conclusion, the Na self-diffusion is controlled by another less correlated diffusion mechanism such as an interstitialcy mechanism. This mechanism has so far been investigated primarily in the mono-atomic case and basic studies concerning self-diffusion and ionic conductivity in binary AB alloys are an important approach for the development of a microscopic diffusion model in alkali feldspar. These studies concern diffusion via the collinear interstitialcy mechanism in the simple cubic (sc) structure (see Chapter 7) and diffusion via the non-collinear interstitialcy mechanism with allowance for direct-interstitial jumps in the sc lattice (see Chapter 8). It will be demonstrated in Chapter 9 that based on the groundwork concerning the sc lattice an interstitialcy diffusion model can be successfully developed for monoclinic alkali feldspar.

7. Monte Carlo simulation of diffusion and ionic conductivity in a simple cubic random alloy via the interstitialcy mechanism

In the past, numerous studies on correlation factors including Monte Carlo (MC) simulation focused on diffusion via lattice vacancies, which is the most prominent mobile point defect in metals. The vacancy-related correlation effects on the monoclinic Na-K sublattice of alkali feldspar were extensively investigated and discussed in the previous Chapter 6. For a general survey on this matter the reader is referred to textbooks and reviews papers [19, 96]. In contrast, correlation effects related to the *interstitialcy* diffusion mechanism have been only sparsely investigated so far. Some pertinent examples concern self-diffusion in non-stoichiometric uranium oxide [97] and other ionic crystals, such as NaCl, AgCl and CaF_2 [98, 99]. Because of the low packing density of crystals based on the diamond lattice, self-interstitials play an important role as diffusion vehicles in some elemental (Si) and compound (e.g., GaAs) semiconductors [100, 38, 101] and in the completely miscible SiGe random alloy semiconductor system [102, 103]. A corresponding early evaluation of the tracer correlation factor $f_0 = 0.727$ for self-diffusion by the interstitialcy mechanism in the diamond structure was reported by Compaan and Haven [104]. An analytical calculation of a similar correlation factor in the simple cubic lattice yields $f_0 = \frac{6}{7}$ [105]. Another study presents a combination of theoretical and MC calculations for interstitialcy diffusion in a two-dimensional triangular lattice [106]. However, to our knowledge there is no other published report dealing with the interstitialcy mechanism in a binary or multicomponent (sub)lattice. It is this gap that the present work – published in Journal of Physics: Condensed Matter, 2015 [75] – intends to bridge.

The present MC study is motivated by the wish to identify the mechanisms of cation diffusion in single-crystal alkali feldspar from experimental data on the ^{22}Na tracer diffusivity (see Chapter 3 and [64]), ^{43}K diffusivity (see Chapter 4 and [57]) and the ionic conductivity (see Chapter 5 and [56]). It is known from Chapter 4 and from early tracer experiments [107, 9] that Na diffusion is several orders of magnitude faster than K diffusion in alkali feldspar. However, this observation cannot be reconciled with a common vacancy mechanism of the two species, as was shown by the MC simulations presented in Chapter 6. Therefore, it seems natural to explore whether the interstitialcy mechanism could be able to explain the experimental findings. It is not easy, however, to start from scratch with such interstitialcy MC simulations because of the low symmetry of the monoclinic structure and the concomitant direction dependence of diffusion. For these reasons, this chapter focuses on the simple cubic (sc) lattice, which may be considered as a first step to reveal some major characteristics of interstitialcy diffusion in a binary random alloy.

In the interstitialcy mechanism, the point defect acting as diffusion vehicle (self-interstitial) is simultaneously a constituent atom of the host lattice. This native interstitial atom migrates by replacing an adjacent substitutional atom. The replaced atom in turn is forced to occupy an adjacent interstitial site and subsequently exchanges with a neighbouring atom. In this chapter, it is only dealt with the *collinear* interstitialcy mechanism. In this case, the interstitial and substitutional sites involved in a single migration event are aligned in one crystallographic direction. For the sc lattice this is a $\langle 111 \rangle$ direction. In the *non-collinear* interstitialcy mechanism, treated in Chapter 8, the replaced substitutional atom may be 'kicked-out' toward different adjacent interstitial sites.

The correlation effect of the interstitialcy mechanism takes into account that the *initially interstitial* atom has a higher than statistical probability to return to its previously occupied interstitial site by successively exchanging with the same atom. Moreover, in a binary alloy AB the probability for such a reverse jump may be increased compared to a single-component structure. This process can be illustrated, e.g., by considering one interstitial and one adjacent substitutional atom of the same species B in the vicinity of only A atoms. If the exchange rate of B atoms is high compared to the exchange rate of A atoms, there is a high probability for a long sequence of exchanges exclusively between the two B atoms.

For an atom starting at a substitutional site of an elemental crystal, the *geometrical* correlation of interstitialcy diffusion is interrupted immediately after the first jump. This is because the second jump, now as self-interstitial, can take place in each nearest-neighbour direction with equal probability. However, what remains in a binary alloy is the *physical* correlation effect [76], which relates to the different jump frequencies of A and B atoms. Commonly, physical correlation is much stronger than geometrical correlation [76].
Considering self-diffusion in a binary random sc alloy, the interstitialcy mechanism seems more complicated than the vacancy mechanism, i.e., for the following reasons. (i) Two types of site exchanges have to be distinguished: interstitial-to-substitutional and substitutional-to-interstitial. (ii) Each interstitialcy exchange involves two atomic jumps. (iii) The jump length of the interstitialcy considered as interstitial defect or charge carrier is twice as large as the jump length of the two participating atoms. (iv) The point defect acting as diffusion vehicle appears in two different forms: as A-type or B-type interstitial.
It will be shown in the present MC study that the special features of the interstitialcy mechanism give rise to distinctive correlation effects which greatly differ from those of the vacancy mechanism. The composition dependence of the correlation factors appears to be strongly affected by a peculiar percolation behaviour for the interstitialcy type of diffusion. In particular, there is a shift of the site-percolation threshold to lower concentration compared to the vacancy mechanism and a virtual second-order percolation threshold which relates to the abundance of different jump types.

7.1. Theoretical background

7.1.1. Random alloy model with interstitialcy diffusion

The random alloy model was introduced by Manning to study diffusion by the vacancy mechanism in binary and multicomponent alloys [14, 45]. His work focused on the calculation of tracer and vacancy correlation factors, which play a crucial role in the description of atomic transport processes in alloy systems. A distinction has to be made between Manning's general physical model and his analytical framework pertaining to diffusion via vacancies in particular. In the present work, only Manning's physical model of a binary random alloy AB is considered which will

be adapted to the special requirements of diffusion via the interstitialcy mechanism. Manning's physical model foots on the assumption that all interactions among atoms (A,B) can be neglected, which implies the total absence of short- and long-range ordering effects. Thus, the distribution of A and B atoms over the lattice sites is purely statistical. Since the concentration of point defects is supposed to be negligibly low, the random alloy AB is characterised by its composition $C_{\mathrm{B}} = 1 - C_{\mathrm{A}}$ expressed in site fractions. The only relevant type of point defect considered in this study is the interstitial defect or interstitialcy rather than the vacancy. However, in an AB alloy it has to be distinguished between interstitials of type A and B, that is, between $\mathrm{A_I}$ and $\mathrm{B_I}$, respectively, which both may act as diffusion vehicle. Another crucial assumption of the random alloy model is that the interaction between atoms and the point defects acting as diffusion vehicle can be ignored. In the present case, this implies that the elementary diffusion step, i.e., the *collinear* exchange between the interstitialcy and a nearest-neighbour substitutional atom, is independent of the type of interstitial. Therefore, the exchange frequency is only determined by the identity (A or B) of the jumping substitutional atom and only two different exchange frequencies, w_{A} and w_{B}, enter the calculations.
Under these conditions, diffusion may be described in terms of quasichemical reactions, which for tracer atoms $\widehat{\mathrm{A}}_{\mathrm{S}}$ and $\widehat{\mathrm{A}}_{\mathrm{I}}$ can be written as

$$\widehat{\mathrm{A}}_{\mathrm{I}} + \mathrm{A}_{\mathrm{S}} \rightleftharpoons \widehat{\mathrm{A}}_{\mathrm{S}} + \mathrm{A}_{\mathrm{I}} \tag{7.1}$$

and

$$\widehat{\mathrm{A}}_{\mathrm{I}} + \mathrm{B}_{\mathrm{S}} \rightleftharpoons \widehat{\mathrm{A}}_{\mathrm{S}} + \mathrm{B}_{\mathrm{I}}\,. \tag{7.2}$$

It is implied that the interstitial (index I) and substitutional (index S) atoms are at nearest-neighbour positions. Similar reactions can be given if the diffusion of B atoms is considered. In the *collinear* variant of the interstitialcy mechanism, the positions of all particles involved in a single reaction step are located along a $\langle 111 \rangle$ direction of the sc lattice. The reaction rates of I-S interchange have to be identified with the jump frequencies w_{A} and w_{B} introduced above, which only depend on the type of the participating S-atom. Accordingly, in Eq. 7.1 both the forward and reverse reaction rate is determined by w_{A}. In Eq. 7.2, however, the reaction rates are different and given by w_{B} and w_{A} for the forward and reverse direction, respectively.

In thermal equilibrium, the concentrations of products and educts in a reaction are interrelated through the reaction rates. Specifically, based on Eq. 7.2 mass action law predicts

$$\frac{r_\mathrm{A}}{r_\mathrm{B}} = \frac{C_\mathrm{A,I}}{C_\mathrm{B,I}} = \frac{C_\mathrm{A} w_\mathrm{A}}{C_\mathrm{B} w_\mathrm{B}}\,, \tag{7.3}$$

where $C_\mathrm{A,I}(C_\mathrm{B,I})$ is the concentration (site fraction) of $\mathrm{A_I}$ ($\mathrm{B_I}$). Moreover, r_A designates the normalised or relative concentration of A-type interstitials, i.e.,

$$r_\mathrm{A} = \frac{C_\mathrm{A,I}}{C_\mathrm{A,I} + C_\mathrm{B,I}} = \frac{C_\mathrm{A,I}}{C_\mathrm{I}} = 1 - r_\mathrm{B}\,. \tag{7.4}$$

Another useful expression is

$$r_\mathrm{A} = \frac{C_\mathrm{A} w_\mathrm{A}}{C_\mathrm{A} w_\mathrm{A} + C_\mathrm{B} w_\mathrm{B}}\,. \tag{7.5}$$

It can be noted that r_A may be interpreted as the probability that a 'generalised interstitial defect' I with concentration $C_\mathrm{I} = C_\mathrm{A,I} + C_\mathrm{B,I}$ is of type $\mathrm{A_I}$. In particular, $C_\mathrm{A,I}$ and $C_\mathrm{B,I}$ can be conveniently expressed in terms of the total concentration of interstitials as

$$C_\mathrm{A,I} = r_\mathrm{A} C_\mathrm{I}\,, \quad C_\mathrm{B,I} = r_\mathrm{B} C_\mathrm{I}\,. \tag{7.6}$$

It can be noted that C_I in a binary random alloy with interstitialcy diffusion is the counterpart of C_V in the same alloy with vacancy (V) diffusion.

7.1.2. Tracer diffusion coefficients

The tracer diffusion coefficient[1] of A atoms is given by

$$\widehat{D}_\mathrm{A} = \lim_{t\to\infty} \frac{\langle X_\mathrm{A}^2 \rangle}{2t} = f_\mathrm{A} \frac{\langle X_\mathrm{A}^2 \rangle_\mathrm{uncorr}}{2t}\,, \tag{7.7}$$

where t is a sufficiently long time and $\langle X_\mathrm{A}^2 \rangle$ denotes the mean square displacement in x-direction within this time. The right-hand side of this equation implicitly defines

[1] To reduce the number of indices, the common asterisk for labelling tracer diffusivity (D^*) has been replaced by the 'hat' symbol ($\widehat{D}$) throughout this work.

the tracer correlation factor f_A by introducing the (hypothetical) *uncorrelated* mean square displacement as

$$\begin{aligned}\langle X_\mathrm{A}^2\rangle_\mathrm{uncorr} &= \langle n_\mathrm{AA}+n_\mathrm{AB}\rangle l_x^2 \\ &= \langle (n_\mathrm{AA}^\mathrm{IS}+n_\mathrm{AA}^\mathrm{SI})+(n_\mathrm{AB}^\mathrm{IS}+n_\mathrm{AB}^\mathrm{SI})\rangle l_x^2\,. \end{aligned} \tag{7.8}$$

Thus, f_A accounts for the fact that in the interstitialcy mechanism subsequent jumps of the same atom are generally correlated. In Eq. 7.8, $n_\mathrm{AA}^\mathrm{IS}$ and $n_\mathrm{AA}^\mathrm{SI}$, for example, are the number of $\widehat{\mathrm{A}}_\mathrm{I}$-$\mathrm{A}_\mathrm{S}$ and $\widehat{\mathrm{A}}_\mathrm{S}$-$\mathrm{A}_\mathrm{I}$ interstitialcy events, respectively, and the $\langle\ \rangle$ brackets stand for expectation value (ensemble average). Furthermore, all atomic jump lengths along the x-axis of the sc lattice are equal to $l_x = a/2$, with lattice constant a.

In a long sequence of jumps of a single tracer atom $\widehat{\mathrm{A}}$, it has to be taken into account that the probabilities $p_\mathrm{A,I}$ and $p_\mathrm{A,S}$ to be at interstitial and substitutional sites, respectively, differ from each other. In fact, $p_\mathrm{A,I}$ is given by

$$p_\mathrm{A,I} = \frac{C_\mathrm{A,I}}{C_\mathrm{A,I}+C_\mathrm{A,S}} \approx \frac{C_\mathrm{A,I}}{C_\mathrm{A}}\,, \tag{7.9}$$

whereas

$$p_\mathrm{A,S} = 1 - p_\mathrm{A,I} \approx 1\,. \tag{7.10}$$

The right-hand sides of these equations rely on the assumption that $C_\mathrm{A,I} \ll C_\mathrm{A,S}$ holds to a very good approximation. This complies with the concept of a random alloy with negligibly low defect concentrations, so that $C_\mathrm{A,S}$ and $C_\mathrm{B,S}$ are virtually equal to C_A and C_B, respectively.

With the quantities introduced above and using Eq. 7.6, both $\langle n_\mathrm{AA}^\mathrm{IS}\rangle/t = p_\mathrm{A,I}C_\mathrm{A}w_\mathrm{A}z$ and $\langle n_\mathrm{AA}^\mathrm{SI}\rangle/t = p_\mathrm{A,S}C_\mathrm{A,I}w_\mathrm{A}z$ are equal to $w_\mathrm{A}r_\mathrm{A}zC_\mathrm{I}$, which leads to

$$\langle n_\mathrm{AA}\rangle/t = 2w_\mathrm{A}r_\mathrm{A}zC_\mathrm{I}\,. \tag{7.11}$$

Similarly, by using Eq. 7.3 the relations $\langle n_\mathrm{AB}^\mathrm{IS}\rangle/t = p_\mathrm{A,I}C_\mathrm{B}w_\mathrm{B}z = w_\mathrm{A}r_\mathrm{B}zC_\mathrm{I}$ and $\langle n_\mathrm{AB}^\mathrm{SI}\rangle/t = p_\mathrm{A,S}C_\mathrm{B,I}w_\mathrm{A}z = w_\mathrm{A}r_\mathrm{B}zC_\mathrm{I}$ are obtained, so that

$$\langle n_\mathrm{AB}\rangle/t = 2w_\mathrm{A}r_\mathrm{B}zC_\mathrm{I} \tag{7.12}$$

holds true. With the aid of Eqs. 7.7, 7.8, 7.11, and 7.12 and using $r_\mathrm{A} + r_\mathrm{B} = 1$ the tracer diffusivity of component A results as

$$\widehat{D}_\mathrm{A} = \frac{1}{2} f_\mathrm{A} (2 w_\mathrm{A}) z C_\mathrm{I} l_x^2 = 2 f_\mathrm{A} w_\mathrm{A} C_\mathrm{I} a^2 \,. \tag{7.13}$$

A similar expression holds for $\widehat{D}_\mathrm{B}$, so that the diffusivity ratio for the two components is given by

$$\frac{\widehat{D}_\mathrm{A}}{\widehat{D}_\mathrm{B}} = \frac{f_\mathrm{A} w_\mathrm{A}}{f_\mathrm{B} w_\mathrm{B}} \,. \tag{7.14}$$

7.1.3. Tracer correlation factors

For each jump type of either component a partial tracer correlation factor ($\mathrm{PCF_T}$) can be introduced as f_{jk}^IS or f_{jk}^SI with $j, k = $ A,B. Thus, $f_\mathrm{AB}^\mathrm{IS}$ refers to jump sequences of A atoms, where the first exchange takes place from an interstitial site ($\mathrm{A_I}$) to a substitutional site initially occupied by a B atom ($\mathrm{B_S}$; cf. Eq. 7.2). So, for both A and B atoms there exist four different $\mathrm{PCF_T}$s at the base level of jump-type discrimination. Averaging over I-S and S-I exchanges yields for $j, k = $ A,B

$$f_{jk} = \frac{\langle n_{jk}^\mathrm{IS} \rangle f_{jk}^\mathrm{IS} + \langle n_{jk}^\mathrm{SI} \rangle f_{jk}^\mathrm{SI}}{\langle n_{jk}^\mathrm{IS} \rangle + \langle n_{jk}^\mathrm{SI} \rangle} = \frac{1}{2} (f_{jk}^\mathrm{IS} + f_{jk}^\mathrm{SI}) \,, \tag{7.15}$$

because $\langle n_{jk}^\mathrm{IS} \rangle = \langle n_{jk}^\mathrm{SI} \rangle$ in thermal equilibrium. With these definitions, it is easy to derive that the total correlation factor of A tracer atoms may be obtained as

$$f_\mathrm{A} = \frac{\langle n_\mathrm{AA} \rangle f_\mathrm{AA} + \langle n_\mathrm{AB} \rangle f_\mathrm{AB}}{\langle n_\mathrm{AA} \rangle + \langle n_\mathrm{AB} \rangle} = r_\mathrm{A} f_\mathrm{AA} + r_\mathrm{B} f_\mathrm{AB} \,. \tag{7.16}$$

In a similar way, f_B takes the form

$$f_\mathrm{B} = r_\mathrm{A} f_\mathrm{BA} + r_\mathrm{B} f_\mathrm{BB} \,. \tag{7.17}$$

In the mono-atomic case (C_B, $r_\mathrm{B} = 0$), the tracer correlation factor reduces to $f_\mathrm{A} = (f_\mathrm{AA}^\mathrm{IS} + f_\mathrm{AA}^\mathrm{SI})/2$.

7.1.4. Interstitialcy diffusivity and related correlation factors

In the interstitialcy mechanism, the interstitialcy diffusivity D_I is the analogon of the vacancy diffusivity D_V in case of the vacancy mechanism. Both diffusion coefficients appear as crucial quantities in the evaluation of ionic conductivity data in binary or multicomponent crystalline systems [76]. Interstitials in binary ionic sublattice AB carry an effective charge, which may be independent of the type of interstitial, $\mathrm{A_I}$ or $\mathrm{B_I}$. Thus, according to the Nernst-Einstein equation the dc conductivity σ may be written in terms of generalised monovalent interstitials I as [108]

$$\sigma = \frac{e^2}{k_\mathrm{B}T} N_\mathrm{I} D_\mathrm{I} = \frac{e^2 N_0}{k_\mathrm{B}T} C_\mathrm{I} D_\mathrm{I}\,, \tag{7.18}$$

where e is the electronic charge, N_I is the volume concentration of interstitials (number density) and N_0 denotes the volume concentration of interstitial sites and k_B is the Boltzmann constant. It can be noted that in the sc lattice the number of interstitial (I) and substitutional (S) sites are equal. Furthermore, the Nernst-Einstein equation applies to non-interacting particles (charge carriers), as is true for the extremely low I concentrations ($C_\mathrm{I} \ll 1$) considered in this study.
Using similar concepts and derivations as in Sect. 7.1.2, D_I can be expressed as

$$D_\mathrm{I} = \frac{1}{2} f_\mathrm{I} w_\mathrm{I} z l_{\mathrm{I},x}^2 = 4 f_\mathrm{I} w_\mathrm{I} a^2\,, \tag{7.19}$$

where f_I is the interstitialcy correlation factor and w_I is the mean interstitial jump frequency given by

$$w_\mathrm{I} = C_\mathrm{A} w_\mathrm{A} + C_\mathrm{B} w_\mathrm{B}\,. \tag{7.20}$$

In Eq. 7.19 it is used that the interstitial jump length along the principal x-axis, $l_{\mathrm{I},x} = a$, is twice as large as the atomic jump distance l_x. Moreover, compared to Eq. 7.7 the factor 2 preceding the jump frequency is missing. This relates to the fact that one interstitialcy exchange involves two atom jumps.
The total interstitialcy correlation factor f_I may be decomposed into 4 partial correlations factors ($\mathrm{PCF_I}$s) denoted as $f_{\mathrm{I},j}^k$ with j,k = A,B. For example, $f_{\mathrm{I,A}}^\mathrm{B}$ refers to a $\mathrm{PCF_I}$ for which the interstitial is of type $\mathrm{A_I}$ and the first jump takes place toward a nearest-neighbour $\mathrm{B_S}$ site. The frequency of each interstitial jump type is given by

$$\langle n_\mathrm{I}^{jk} \rangle / t = r_j C_k w_k\,, \quad \text{with} \quad j,k = \mathrm{A,B}\,. \tag{7.21}$$

Combining $f^{\mathrm{A}}_{\mathrm{I,A}}$ and $f^{\mathrm{A}}_{\mathrm{I,B}}$ to a $\mathrm{PCF_I}$ of higher level yields

$$f^{\mathrm{A}}_{\mathrm{I}} = r_{\mathrm{A}} f^{\mathrm{A}}_{\mathrm{I,A}} + r_{\mathrm{B}} f^{\mathrm{A}}_{\mathrm{I,B}} \,, \tag{7.22}$$

where it is used that $\langle n^{\mathrm{A}}_{\mathrm{I,A}} \rangle + \langle n^{\mathrm{A}}_{\mathrm{I,B}} \rangle = C_{\mathrm{A}} w_{\mathrm{A}} t$. Similarly, it is obtained

$$f^{\mathrm{B}}_{\mathrm{I}} = r_{\mathrm{A}} f^{\mathrm{B}}_{\mathrm{I,A}} + r_{\mathrm{B}} f^{\mathrm{B}}_{\mathrm{I,B}} \,. \tag{7.23}$$

It can be noted that $f^{\mathrm{A}}_{\mathrm{I}}$ ($f^{\mathrm{B}}_{\mathrm{I}}$) relates to correlated jump sequences starting with an $\mathrm{A_S}$ ($\mathrm{B_S}$) atom displaced by a generalised interstitial I. Thus, $f^{\mathrm{A}}_{\mathrm{I}}$ and $f^{\mathrm{B}}_{\mathrm{I}}$ are the counterparts of $f^{\mathrm{A}}_{\mathrm{V}}$ and $f^{\mathrm{B}}_{\mathrm{V}}$ in case of a random alloy with vacancy-mediated diffusion [14, 83] (see Chapter 6). A further PCF recombination results in the *total* correlation factor of the interstitialcy, i.e.,

$$f_{\mathrm{I}} = r_{\mathrm{A}} f^{\mathrm{A}}_{\mathrm{I}} + r_{\mathrm{B}} f^{\mathrm{B}}_{\mathrm{I}} \,, \tag{7.24}$$

because, e.g., $\langle n^{\mathrm{A}}_{\mathrm{I}} \rangle = \langle n^{\mathrm{A}}_{\mathrm{I,A}} \rangle + \langle n^{\mathrm{A}}_{\mathrm{I,B}} \rangle$ is proportional to $C_{\mathrm{A}} w_{\mathrm{A}}$.

7.2. Computational methods

All calculations presented here are based on an atomistic MC method by computer simulation. Correlation effects were investigated for an alloy of two randomly ordered atomic species in a sc structure. The atoms migrate by the collinear interstitialcy mechanism as described in the previous section. The numerical diffusion system was constructed from two interpenetrating sc lattices, both of size $160a \times 160a \times 160a$, where a is the lattice constant. In some cases, the size was extended to $400a \times 400a \times 400a$ lattice sites to perform the most demanding simulations with high accuracy.

The 'substitutional' lattice is completely occupied by the A and B atoms with concentrations $C_{\mathrm{A}} + C_{\mathrm{B}} = 1$. The 'interstitial' lattice, which is shifted by $(a/2, a/2, a/2)$ relative to the substitutional lattice, contains only vacant sites except for one site that is occupied. The atom residing here can be either of species A or B and represents the interstitialcy defect I. In the present model, the I-S *exchange rate* only depends on the substitutional species involved ($w_{\mathrm{A}} \neq w_{\mathrm{B}}$) but neither on the identity of the interstitial nor on that of the atoms adjacent to the exchanging ones. However, the identities of the $z = 8$ S-atoms in the vicinity of

the I-atom determine the individual *exchange probability* $p_i \in [0,1)$ for S-atom i as $p_i = w_i / \sum_j^8 w_j$. The effective jump is then assigned to one S-atom by a randomly generated number. Immediately after this first jump of the I-atom to the MC-selected S-site, the S-atom that previously occupied this site is pushed to an adjacent I-site. In the collinear mechanism under consideration, the I-S and S-I exchanges of the two atoms participating in one migration step proceed in the same direction. Hence, the displaced S-atom is able to attain only one adjacent I-site.

The calculation of the correlation factors for one distinct concentration C_B and one set of exchange rates $w_\mathrm{A}/w_\mathrm{B}$ was based on at least $n = 10^{10}$ (but up to 5×10^{11}) exchanges of the interstitialcy defect. Hence, suitable periodic boundary conditions were applied to the finite volume of the simulation box. Total correlation factors were then calculated by the displacement method, based on the relation

$$f_\mathrm{A} = \lim_{n_\mathrm{A} \to \infty} \langle X_\mathrm{A}^2 \rangle / \langle n_\mathrm{A} \rangle l_x^2, \tag{7.25}$$

where $\langle n_\mathrm{A} \rangle$ is the mean number of jumps of projected length l_x per A atom. To analyse partial correlation factors, the so-called PCF-method was employed [83]. The scalar products of jump vectors given by $S_\alpha = \sum_i \sum_j (x_{\alpha,i} \cdot x_{\alpha,i+j})$, where $x_{\alpha,i+j}$ denotes the jth jump after the ith exchange of type α, were simultaneously computed during each simulation run by a simple and efficient algorithm [83]. The PCFs were then calculated using the relation

$$f_\alpha = 1 + 2\langle S_\alpha \rangle / \langle n_\alpha \rangle \cdot x_\alpha^2, \tag{7.26}$$

where $\langle n_\alpha \rangle$ is the number of jumps of type α averaged over all particles of the same species and x_α is the projected length of this jump type in x-direction.

7.3. Results and Discussion

Simulations were carried out for jump ratios $w_\mathrm{A}/w_\mathrm{B}$ ranging from 10^{-1} to 10^{-5} for all alloy compositions C_B between 0 and 1. Tracer and interstitialcy correlation factors (f_A, f_B, and f_I) were calculated by the displacement method, whereas the associated PCFs were evaluated during the same simulation runs by the PCF-method. The results are presented and discussed in the two following subsections, after which the percolation behaviour revealed by the correlation effects will be

analysed in detail. A further subsection deals with the differences between the diffusion coefficient of the mobile (B) and less mobile (A) component as a function of composition. Finally, the consequences for the Haven ratio are elaborated, which compares mass and charge transport in the simulated random-alloy diffusion system.

7.3.1. Tracer correlation factors

Composition dependence of f_A

The results of f_A and f_B for $w_A/w_B = 10^{-2}$ are presented in Fig. 7.1 together with the corresponding PCF_Ts. The data points are equally spaced in steps of 0.02 over the composition axis. Additional simulations were done for compositions where the slope of f_A is steep, i.e., for $C_B < 0.02$. In Fig. 7.1a, the f_{AA}^{SI} data for $C_B > 0.8$ are omitted because of a too low number of n_{AA}^{SI} jumps. The same is true for f_{AA}^{IS} beyond $C_B = 0.9$. Moreover, 'mixed-atom PCFs' in Fig. 7.1a involving both A and B are not well-defined for $C_B = 0$, which corresponds to a pure A lattice. Here, the data shown at the outermost left-hand side were calculated for the limiting composition $C_B = 10^{-3}$. In the case of A self-diffusion, the true geometrical correlation factor $f_0 = \frac{6}{7}$ in the sc lattice [105] is reproduced by f_A within an accuracy of 0.03 %. According to Eqs. 7.5, 7.15 and 7.16, this value is a plain average of the two PCFs $f_{AA}^{IS} = \frac{5}{7}$ and $f_{AA}^{SI} = 1$. This result can be understood as follows: In self-diffusion, a S-atom that just has jumped to an I-site will not be affected by correlation ($f_{AA}^{SI} = 1$), since its next exchange occurs randomly with one of 8 adjacent S-atoms. In contrast, the I-atom that has just exchanged with the S-atom will be in direct proximity to the new interstitial atom. In this situation, there is a higher than statistical probability that the next jump of this original I-atom occurs in the opposite direction to the first jump. The net probability for the forward jump is $t_f = P_+ - P_- = -\frac{1}{7}$ [105] and therefore $f_{AA}^{IS} = 1 + 2t_f = \frac{5}{7}$ [14, 19].
Starting from the lowest C_B value, f_A steeply decreases towards a global minimum with increasing B concentration. This finding can be explained by the concentration-dependent contribution of the four PCF_Ts. All associated PCF_Ts are weighted according to Eqs. 7.15 and 7.16 by r_A or r_B yielding f_A as solid line in Fig. 7.1a. The fact that this line intersects the f_A data obtained by the displacement method demonstrates the consistency of the calculations. Despite a low concentration of B atoms, r_B can be relatively large because of a high jump frequency ($w_B = 100 w_A$,

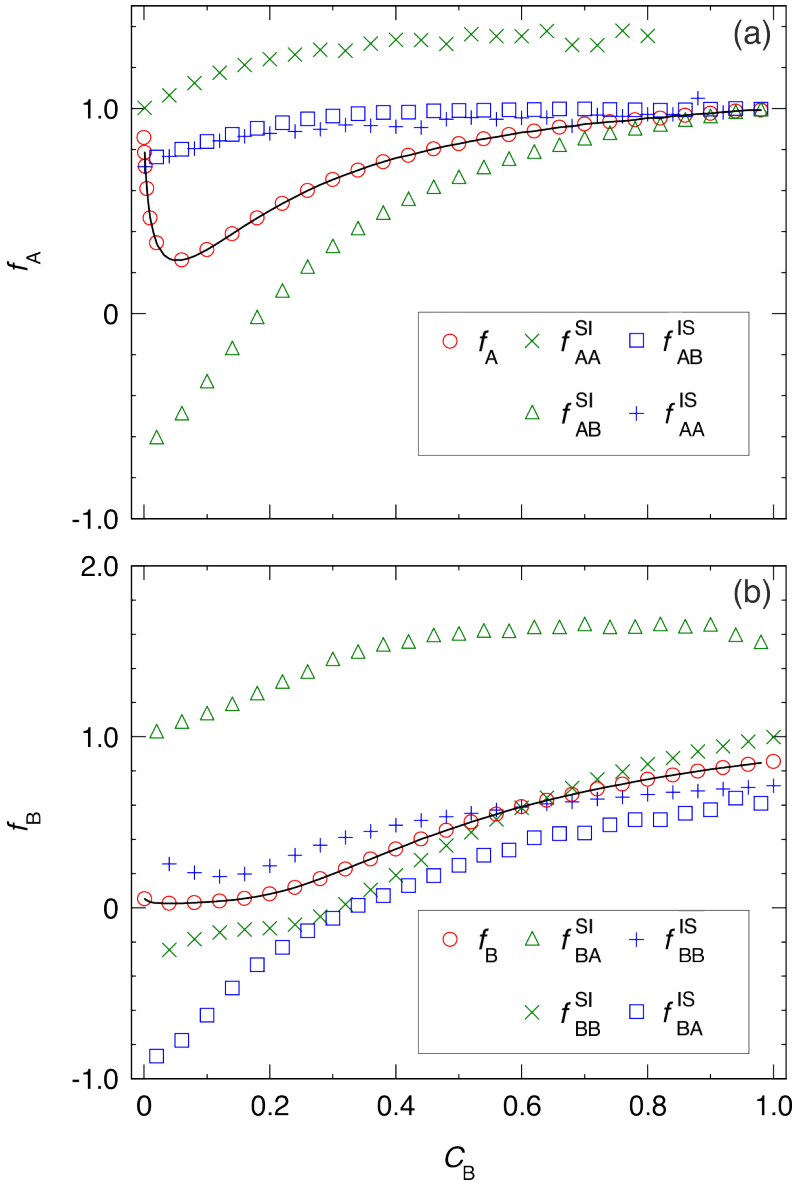

Figure 7.1.: Total tracer correlation factors f_A (a) and f_B (b) and the associated partial correlation factors (PCF_Ts) for $w_A/w_B = 10^{-2}$ as a function of composition C_B. For clarity, every second data point has been omitted, except for parts where the gradient is high. Circles: f_A and f_B directly calculated via the displacement method. Solid lines: f_A and f_B calculated from the weighted PCF_T contributions according to Eq. 7.16 and 7.17.

cf. Eq. 7.5). It turns out that the occurrence of a minimum in f_A relates to a transition from $\langle n_{AA} \rangle > \langle n_{AB} \rangle$ to $\langle n_{AA} \rangle < \langle n_{AB} \rangle$. Since at higher C_B diffusion of A atoms mainly takes place by exchanges of A with B, the total correlation factor f_A is controlled by the two PCF$_T$s f_{AB}^{SI} and f_{AB}^{IS}. These A-B exchanges are strongly correlated over a large range of compositions and f_{AB}^{SI} becomes even negative for $C_B < 0.2$ with a limiting value of -0.656 for $C_B \to 0$. This reflects that in this B-poor composition range an A_S atom that has just interacted with a B_I atom has a high probability to immediately exchange with the same B atom again.
It should be emphasised that the occurrence of a global minimum in the f_A-versus-C_B plot signifies a clear difference with regard to the vacancy mechanism, where the correlation factor of the less mobile component exhibits monotonic behaviour between f_0 and 1 over the whole composition range [22, 83]. The interstitialcy-related minimum observed here seems to be related to a second-order percolation threshold, which will be discussed in more detail in Sect. 7.3.3.
The right-hand side in Fig. 7.1a corresponds to A diffusion in a B-rich host crystal. Here, except for f_{AA}^{SI} all PCF$_T$s and f_A increase towards a value of 1. As indicated above, the f_{AA}^{SI} data are omitted for $C_B > 0.8$ because of substantial scatter due to poor statistics. However, at high B concentrations f_{AA}^{SI} is apparently limited by a value of ~ 1.36. This value greater than unity can be interpreted by the small probability of an A_S atom to exchange with the same A atom after its initial exchange with A_I. In contrast, there is a high probability for the atom to exchange with one of the numerous B atoms. Therefore, the next jump of an original A_S atom will be in the same direction as the first jump with a higher than statistical probability.

Composition dependence of f_B

Tracer correlation factors related to diffusion of B atoms were also calculated within the same MC simulation runs. The f_B results are represented in Fig. 7.1b as a function of composition C_B. In analogy to f_A, the outermost right-hand side (rhs) of the plot corresponds to B self-diffusion which implies the same geometrical value $f_0 = \frac{6}{7}$ as for A self-diffusion (lhs of Fig. 7.1a). Similar identity relations are: $f_{BB}^{SI}(C_B \to 1) = f_{AA}^{SI}(C_B \to 0) = 1$ and $f_{BB}^{IS}(C_B \to 1) = f_{AA}^{IS}(C_B \to 0) = \frac{5}{7}$.
For B-rich compositions, only a minor influence of B-A exchanges to the total correlation factor f_B is observed. Instead B-B interactions comprise most of the B diffusion over a wide range of compositions. However, for low C_B the PCF$_T$s

associated with B-B exchanges are significantly reduced which even leads to f_{BB}^{SI} values falling below zero. This behaviour is caused by a site-percolation effect close to $C_B = 0.2$ related to B-B constellations, and will be further discussed in Sect. 7.3.3. In the extremely B-poor range of $C_B \leq 0.02$, the proportion of B-A exchanges is significantly enhanced ($C_A w_A > C_B w_B$), which results in an increase of r_A and a concomitant weak increase of f_B for $C_B \to 0$.
The PCF$_T$s f_{BA}^{SI} and f_{BA}^{IS} can be interpreted in close analogy to the previous discussion on f_{AA}^{SI} and f_{AB}^{SI}, respectively. The approximate limiting values of these correlation factors are found to be $f_{BA}^{SI} = 1.64$ for $C_B \to 1$ and $f_{BA}^{IS} = -0.88$ for $C_B \to 0$.

Dependence of f_A and f_B on the jump frequency ratio

The previous discussion on tracer correlation effects applies to the jump frequency ratio $w_A/w_B = 10^{-2}$ of the two components. In addition, MC simulations were done for a wide range of exchange-rate differences ranging from $w_A/w_B = 10^{-5}$ to 10^5. The results for f_B are given in Fig. 7.2 on a logarithmic scale as a function of C_B (data points spaced by 0.02, additional data near $C_B = 0.02$, terminal lhs composition $C_B = 10^{-3}$). Special attention should be given to the data for $w_A/w_B = 10^5$ because in this case B is the slower moving species by exception. Here, only minor correlation effects of the B atoms are observed except for compositions in close vicinity to the percolation threshold related to B-A exchanges (cf. Section 7.3.3). It should be noted that this percolation effect occurs at the right-hand side of Fig. 7.2 due to the inverse identity of the faster moving species. The lowest f_B value appears at $C_B \approx 0.98$ and has a deviation from the geometrical value of more than three orders of magnitude. Less extreme cases with B as the slower component ($w_A/w_B = 10^1$ to 10^4) show a similar f_B behaviour, however, with less pronounced minima at the B-rich side. In all cases with B as the faster moving species ($w_A/w_B = 10^{-1}$ to 10^{-5}), minor correlation effects are found in the range from intermediate to high C_B. For $C_B \leq 0.25$ the correlation factor f_B shows a clear dependence on the jump frequency ratio. This effect is linked to the percolation threshold for B diffusion via B-B exchanges. For $w_A/w_B = 10^{-3}$ and less, the additional influence of a second-order percolation effect related to B-A exchanges can be observed. Going from $C_B \approx 0.2$ to zero concentration, this is manifested by a local plateau followed by a second steep decrease of f_B, which subsequently passes through a minimum.

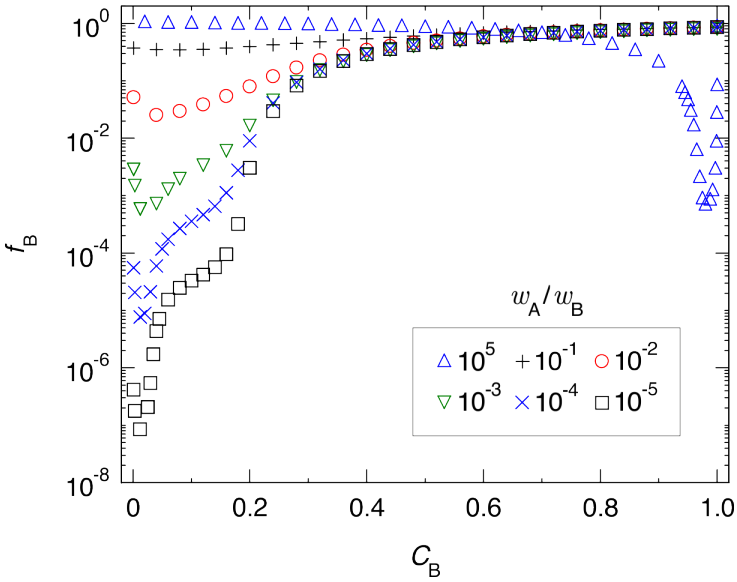

Figure 7.2.: Tracer correlation factor f_B as a function of composition C_B for jump frequency ratios w_A/w_B ranging from 10^5 to 10^{-5}, as indicated. For clarity, every second data point has been omitted, except for parts where the gradient is high. Steep gradients are indicative of percolation effects related to consecutive B-B or B-A exchanges.

7.3.2. Interstitialcy correlation factors

To calculate correlation factors related to the diffusion of the interstitialcy defect, the two atomic exchanges I-S and S-I that simultaneously occur with a displacement length a are considered as one jump of length $2a$ (cf. Sect. 7.1.4). Since only one interstitial atom exists at a time in the present MC simulations, the total trajectory was split into N_{run} sequences of n_{L} jumps. The correlation factor was then calculated by averaging over N_{run} sequences at the end of one long simulation run consisting of up to 5×10^{11} jumps. Figure 7.3 presents simulated f_{I} values obtained by the displacement method for $w_{\mathrm{A}}/w_{\mathrm{B}} = 10^{-2}$ and sequences of $n_{\mathrm{L}} = 2\times10^4$ jumps (but up to 10^7 in some cases). The four basic PCF$_{\mathrm{I}}$s were simultaneously calculated by applying the PCF-method. At the outermost left-hand side of Fig. 7.3, the three PCF$_{\mathrm{I}}$s involving B jumps were evaluated for concentrations as low as $C_{\mathrm{B}} = 4\times10^{-3}$. In the case of self-diffusion ($C_{\mathrm{B}} = 0, 1$) no correlation is observed because $f_{\mathrm{I}} = 1$, which implies that the walk of the interstitial atom is completely random. For small C_{B}, a steep decrease towards a global f_{I} minimum appears in Fig. 7.3. This effect is can be rationalised by the contributions of the four PCF$_{\mathrm{I}}$s to the total correlation factor, which greatly differ near the f_{I} minimum. According to Eqs. 7.22, 7.22 and

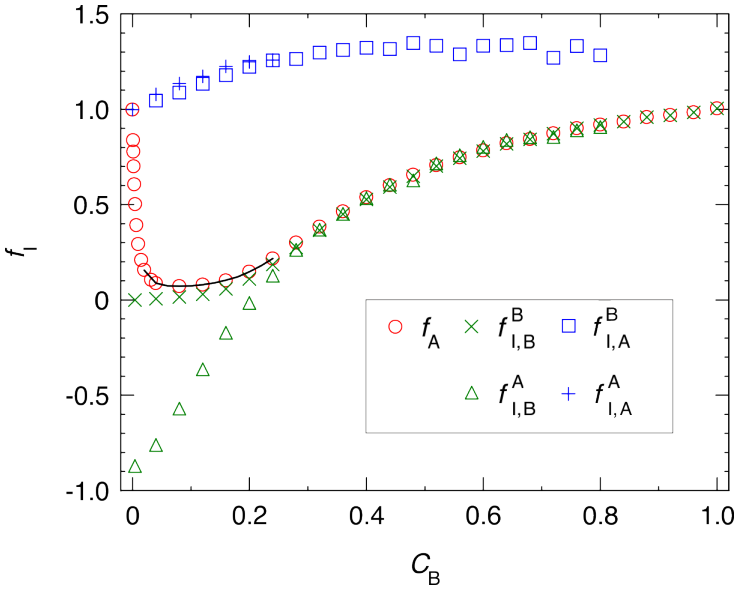

Figure 7.3.: Total interstitialcy correlation factor f_I and its associated partial correlation factors ($\mathrm{PCF_{IS}}$) as a function of composition C_B for $w_\mathrm{A}/w_\mathrm{B} = 10^{-2}$, as indicated. For clarity, every second data point has been omitted, except for parts where the gradient is high. Circles: f_I directly calculated via the displacement method. Solid line: f_I calculated from the weighted $\mathrm{PCF_I}$ contributions according to Eqs. 7.22 and 7.24.

7.24 these contributions are weighted through r_A and r_B by $C_\mathrm{A}w_\mathrm{A}$ and $C_\mathrm{B}w_\mathrm{B}$, respectively. As discussed in Sect. 7.3.1 for f_A, diffusion of A atoms by $\mathrm{A_I}$-$\mathrm{A_S}$ exchanges is predominant for $C_\mathrm{B} < 0.02$. Here, A-A exchanges virtually occur without correlation, whereas exchanges of two (highly mobile) B atoms are mostly reversed during the next jump leading to $f^\mathrm{B}_\mathrm{I,B} \to 0$. For $C_\mathrm{B} \to 0$, the limiting value for $f^\mathrm{A}_\mathrm{I,B}$ is ~ -0.88. It should be noted that this value converges to -1 for increasingly larger differences of the exchange rates. This obviously relates to the fact that an $\mathrm{B_I}$ atom, that just has exchanged with $\mathrm{A_S}$, has an extremely high probability to subsequently exchange with the same atom because there are no other B atoms in the vicinity. It should be noted that Eq. 7.26 permits negative values for partial correlation factors. In fact, the lower limit -1 applies to $\langle n_\alpha \rangle \to 1$ and a truncation of correlated exchange after the reverse jump. In this case, $\langle S_\alpha \rangle$ simplifies to a single scalar product. For intermediate to high C_B values, B-B-interactions occur with the highest probability of all types of exchange. Consequently, the simulated $f^\mathrm{A}_\mathrm{I,A}$ data suffer from scatter and are therefore omitted in Fig. 7.3 for $C_\mathrm{B} > 0.24$. The same applies to $f^\mathrm{B}_\mathrm{I,A}$ and $f^\mathrm{A}_\mathrm{I,B}$ for $C_\mathrm{B} > 0.80$. It can be observed that $f^\mathrm{A}_\mathrm{I,A}$ and $f^\mathrm{B}_\mathrm{I,A}$ reach values greater than unity. However, their contribution to f_I is only very minor.

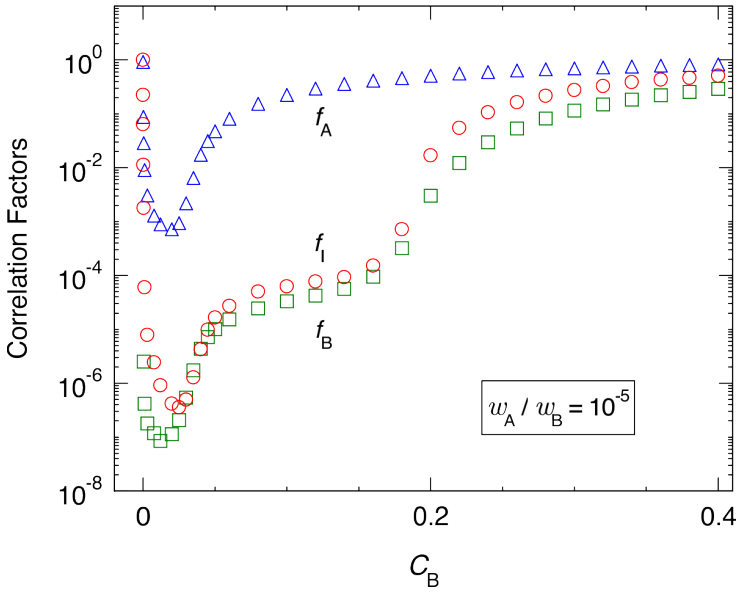

Figure 7.4.: Comparison of the tracer correlation factors f_A (triangles) and f_B (squares) with the correlation factor related to the interstitialcy defect f_I (circles) for the jump frequency ratio $w_A/w_B = 10^{-5}$.

7.3.3. Percolation behaviour

As shown above, tracer correlation factors for diffusion via interstitialcies can become very small in binary random alloys, if the jump rates of the two components differ considerably. This is also true for the 'physical correlation factor' f_I which enters the ion conductivity of a disordered ionic AB system [76] (cf. Sect. 7.3.5). Figure 7.4 presents a comparison of f_A, f_B, and f_I for $w_A/w_B = 10^{-5}$ as a function of composition ($0 \leq C_B \leq 0.4$). As indicated before, distinct steps appearing in these plots may relate to the percolation of atoms or defects along chains and clusters of the more mobile atoms. In this section, this percolation behaviour is analysed in more detail, especially with the aid of the simulated f_I data. To reduce statistical scatter, f_I values close to threshold compositions are based on longer sequences of $n_L = 10^7$ interstitialcy jumps within a larger simulation box of up to $400a \times 400a \times 400a$ atoms. Moreover, to accurately describe the correlation behaviour in cases approaching diffusion in pure A, the f_I values comprise very low concentrations down to $C_B = 10^{-5}$.

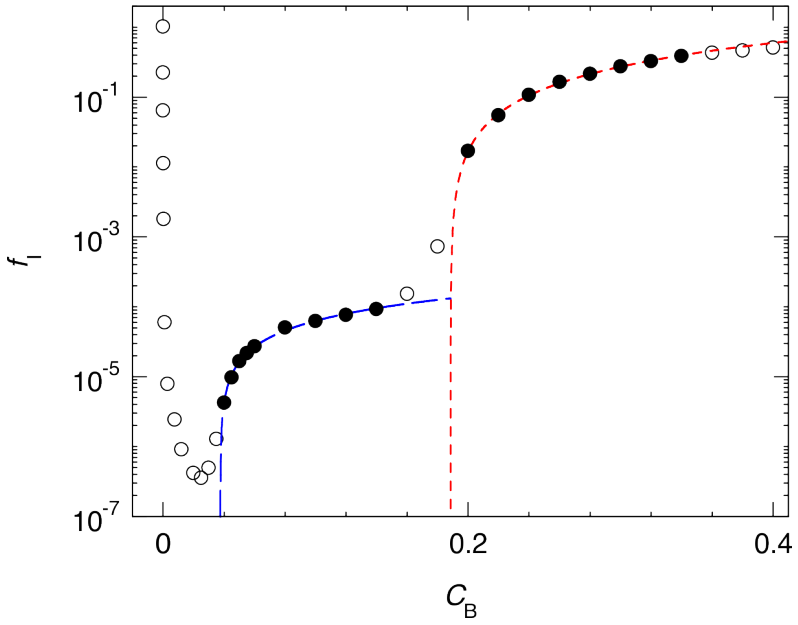

Figure 7.5.: Interstitialcy correlation factors f_I in the sc random alloy as a function of composition for $C_B \leq 0.4$ revealing two distinct percolation thresholds. The data are representative of $w_A/w_B = 10^{-5}$ as also displayed in Fig. 7.4 (circles). The short- and long-dashed lines are separate fits to the solid symbols based on Eq. 7.27.

Constellations of type B-B

It is seen in Fig. 7.4 that f_I and f_B exhibit a similar variation with composition. Both plots show steep gradients near $C_B = 0.02$ and near $C_B = 0.2$. Also, f_A shows steep gradients near $C_B = 0.02$ but near $C_B = 0.2$ it reveals only a weak composition dependence. This indicates that in the latter concentration range f_I and interstitialcy diffusion are not affected by site-percolation of the 'slower' A atoms but rather by the percolation along chains and clusters of the 'faster' B atoms. In the limiting case, $w_A/w_B = 0$, the A atoms are completely immobile and hence neither B-A nor A-B exchanges occur. This leads to the appearance of a first-order threshold composition C_B^p, below which long-range diffusion is not possible ($f_I = 0$, $f_B = 0$).

The concentration dependence of f_I just above the percolation threshold C_B^p may be described – in analogy to diffusion via vacancies – by [23, 21]

$$f_I = k(C_B - C_B^p)^\delta, \; C_B \geq C_B^p \,, \tag{7.27}$$

where δ is a critical exponent and k is a dimensionless proportionality constant. As an approximation to the case of fully immobile A atoms, Eq. 7.27 was fitted in the narrow range $C_\mathrm{B} \in [0.2, 0.35]$ to the f_I data for $w_\mathrm{A}/w_\mathrm{B} = 10^{-5}$, which is illustrated at the right-hand side of Fig. 7.5. Most consistent results were obtained by fitting of $\ln(f_\mathrm{I})$ using the logarithmic form of Eq. 7.27. The best estimates of C_B^p, δ and k are compiled in Tab. 7.1, and compared with corresponding data related to vacancy diffusion in an sc structure.The findings from this analysis can be summarised as follows: The present threshold, $C_\mathrm{B}^\mathrm{p}(\mathrm{I}) = 0.1885$, is distinctly lower than the vacancy-related value $C_\mathrm{B}^\mathrm{p}(\mathrm{V}) = 0.3116$ [95, 83]. This may relate to the higher coordination number for the interstitialcy mechanism, $z(\mathrm{I}) = 8$, compared to the vacancy mechanism, $z(\mathrm{V}) = 6$. The critical exponent $\delta(\mathrm{I})$ is slightly smaller than $\delta(\mathrm{V})$ [83], which leads to a stronger curvature of the f_I plot at compositions close to the percolation threshold. The fitted proportionality constant $k(\mathrm{I})$ is only about half of the $k(\mathrm{V})$ value [83], causing a weaker composition dependence for $C_\mathrm{B} \gg C_\mathrm{B}^\mathrm{p}$. Altogether, I-related correlation is less pronounced than V-related correlation far above the pertaining site-percolation threshold but more significant in the proximity of C_B^p.

In an attempt to rationalise the simulated $C_\mathrm{B}^\mathrm{p}(\mathrm{I})$ value of 0.1885 by geometrical arguments, a two-dimensional (2D) sc lattice is considered consisting of two randomly ordered species AB. As illustrated in Fig. 7.6, an interstitialcy defect I surrounded by $z = 4$ nearest-neighbour (NN) S-atoms is able to reach z I-sites (squares) via I-S exchange. In a subsequent jump, the defect can either exchange with the same atom, or attain another I-site by exchanging with one of the $z^2 - z$ next-nearest-neighbour (NNN) atoms of the initial defect site. To estimate C_B^p, the minimum number of B atoms must be found that is necessary to enable diffusion along chains consisting of two adjacent B atoms. It can be assumed that for each dimension, at least two chains (one in positive and one in negative direction) are needed for site-percolation. In the 2D case, these are $z' = 4$ chains consisting of two B atoms each in a lattice area of $z^2 = 16$ atoms. With the dimension number d this reasoning leads to the expressions

$$C_\mathrm{B}^\mathrm{p} = \frac{2z'}{z^2} = \frac{4d}{4^d}\,, \tag{7.28}$$

yielding the 2D result as $C_\mathrm{B}^\mathrm{p} = 0.5$. This value is in excellent agreement with

Table 7.1.: Parameters characterising the percolation behaviour for interstitialcy diffusion in the simple-cubic (3D) and square (2D) lattice. Results originate from least-squares fitting with Eq. 7.27 to simulated f_I data (MC) and from direct calculations (calc.) using Eqs. 7.28 and 7.29. Similar data from previous studies characterising vacancy diffusion in the sc lattice are given for comparison.

Defect	Dim.	Chain	Reference	C_B^c (MC)	δ	k	C_B^c (calc.)	Eq.
I								
	2D	B-B	this work	0.500 ± 0.002	1.11 ± 0.03	3.6 ± 0.3	0.5	7.28
	2D	A-B*	this work	0.164 ± 0.002			0.1667	7.29
I								
	3D	B-B	this work	0.1885 ± 0.0011	1.23 ± 0.05	4.0 ± 0.4	0.1875	7.28
	3D	A-B	this work	0.0376 ± 0.0004	0.84 ± 0.04	$(6.4 \pm 0.7) \times 10^{-4}$	0.0375	7.29
V								
	3D	B-B	[83]	0.310 ± 0.001	1.67 ± 0.06	9.8 ± 1.6		
	3D	B-B	[95]	0.311608				

* Value obtained by fitting to f_A data and thus, δ and k cannot be compared.

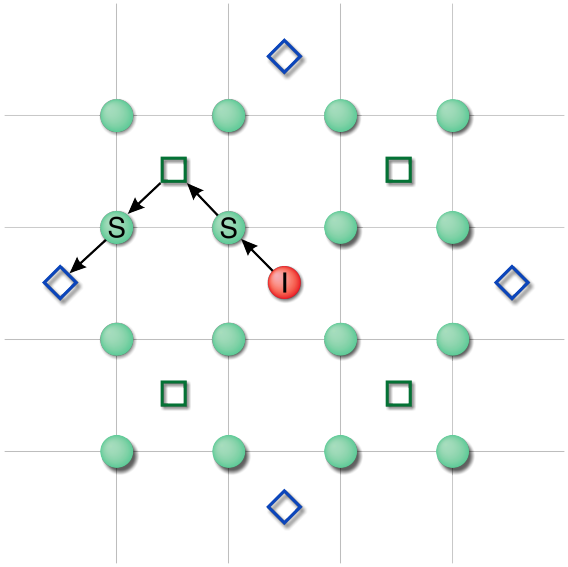

Figure 7.6.: 2D-analogon of a simple-cubic lattice (square lattice) including $z^2 = 16$ substitutional atoms (S) and one interstitialcy defect (I). The defect is able to attain four interstitial sites (squares) via a first I-S exchange. Each of these sites must be in the proximity of a second mobile B atom to establish fast pathways that lead to further interstitial sites (diamonds). The threshold composition according to Eq. 7.28 is $C_{\mathrm{B}}^{\mathrm{p}} = 0.5$.

0.500 ± 0.002 that was obtained in this work by MC simulation in a square lattice (cf. Tab. 7.1).

In the 3D case, the percolation threshold is determined by $z = 8$ NN atoms and $z' = 6$ chains and thus, $C_{\mathrm{B}}^{\mathrm{p}} = 0.1875$. This result agrees within error tolerance with the MC value (0.1885) obtained from the composition dependence of f_{I} (cf. Tab. 7.1). Also, the 1D threshold, $C_{\mathrm{B}}^{\mathrm{p}} = 1$, is correctly predicted by the above expression. Nonetheless, it should be noted that Eq. 7.28 stays without rigorous proof here.

Constellations of type A-B

At compositions close to $C_{\mathrm{B}} = 0.02$ all three total correlation factors show a steep gradient towards a global minimum (cf. Fig 7.4). This effect can be observed for $w_{\mathrm{A}} \neq 0$ only, because otherwise f_{B} and f_{I} are equal to zero below the percolation threshold for B-B constellations ($C_{\mathrm{B}} < 0.1885$). The coherent correlation behaviour of A, B and I suggests, that this effect is based on a second-order percolation threshold ($C_{\mathrm{B}}^{\mathrm{p},2}$) involving chains of type A-B-A-B ...

At compositions just above the threshold value, diffusion occurs to a significant proportion along chains of alternating A and B atoms, since no 'fast' pathways of connected B atoms are available. A restricted choice of these A-B migration paths leads to the occurrence of a threshold composition $C_{\mathrm{B}}^{\mathrm{p},2}$, below which long-range diffusion occurs via the 'slow' A-A exchanges only. The concentration dependence of f_{I} just above the percolation threshold $C_{\mathrm{B}}^{\mathrm{p},2}$ may be described in a similar way as in the preceding case pertaining to B-B chains. Hence, Eq. 7.27 was fitted for $C_{\mathrm{B}} \in [0.04, 0.15]$ to the f_{I} data obtained for $w_{\mathrm{A}}/w_{\mathrm{B}} = 10^{-5}$ (cf. Fig. 7.5). The best estimates of $C_{\mathrm{B}}^{\mathrm{p},2}$, δ and k characterizing this quasi-percolation behaviour are compiled in Tab. 7.1. Specifically, the threshold value results as $C_{\mathrm{B}}^{\mathrm{p},2} = 0.0376$, which is just above the f_{I} minimum in Fig. 7.4.

In analogy to the discussion on B-B percolation, it can be assumed that the actual value for the threshold composition can be deduced from simple arguments. It can be noted that the following reasoning holds both for 2D and 3D. It is based on the hypothesis that quasi-percolation requires at least z' chains consisting of alternating A and B atoms embedded in an A-rich lattice domain. Again, it has to be found the number of atoms that possibly interact with the interstitialcy defect I along its walk. Thus, to imply two B atoms per chain, four I-S exchanges have to be taken into account. I is assumed to be of type B and the first exchange necessarily occurs with one of the z NN atoms. In a second I-S exchange, $z^2 - z$ *new* atoms can be attained, leading to z^2 possible 'target atoms' after two I-S exchanges.

After these two exchanges, the interstitialcy I will be of type B again (because of alternating A-B) and occupies one of z' possible I-sites. In the subsequent two I-S exchanges again z^2 atoms can be reached per I-site, which makes up $z' \times z^2$ atoms in total. However, z^2 of these atoms have already been considered for the first two I-S exchanges, and are therefore counted twice. Altogether, regarding a random walk of four I-S exchanges I has the possibility to exchange with $(z' - 1)\, z^2$ atoms yielding

$$C_{\mathrm{B}}^{\mathrm{p},2} = \frac{2z'}{(z' - 1)\, z^2} = \frac{4d}{[1 + 2^{(d-1)}]4^d}\,. \tag{7.29}$$

Here, the factor 2 preceding z' accounts for two B atoms per chain. Similar to B-B site-percolation (cf. Eq. 7.28) the required number of A-B percolation chains z' is taken as 4 in 2D and 6 in 3D. In the denominator on the right-hand side of Eq. 7.29, the factor $z' - 1 = 2d - 1$ was changed to $[1 + 2^{(d-1)}] = 1 + z/2$, which does not affect the 2D and 3D case. In the latter form, however, Eq. 7.29 reproduces also the correct 1D value, i.e., $C_{\mathrm{B}}^{\mathrm{p},2} = 0.5$.

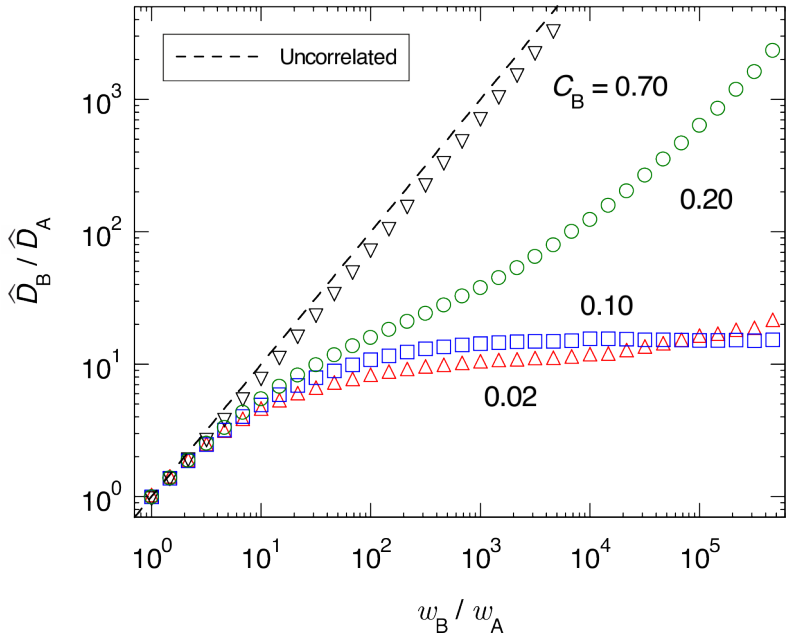

Figure 7.7.: Tracer diffusivity ratio $\widehat{D}_B/\widehat{D}_A$ as a function of jump frequency ratio w_B/w_A in a random binary AB alloy with diffusion by the interstitialcy mechanism. Note that for $w_B > w_A$ all curves fall below the dashed line, which represents the hypothetical case with $f_A = f_B = 1$.

The results obtained by Eq. 7.29 are compiled in Tab. 7.1. For 3D, the estimate of $C_B^{p,2}(\text{calc.}) = 0.0375$ is almost equal to the simulated value of 0.0376. To check the accuracy of the estimated expression in 2D, $C_B^{p,2} = 0.1667$, additional MC simulations of interstitialcy diffusion on a square lattice were carried out. Then correlation factor analysis like that shown in Fig. 7.5 yields $C_B^{p,2}(\text{calc.}) = 0.1664$. Again, the values agree within the numerical uncertainty. Nonetheless, this cannot be seen as a proof for the rigorous correctness of Eq. 7.29.

7.3.4. Comparison of tracer diffusion coefficients

The ratio of the higher to the lower tracer diffusivity is according to Eq. 7.14 given by $\widehat{D}_B/\widehat{D}_A = w_B f_B/(w_A f_A)$. The MC data for f_A and f_B were used as key parameters to calculate this ratio as a function of w_B/w_A ranging from 1 to 10^5. Figure 7.7 displays the results for four different compositions C_B that each represent a distinct regime of diffusion correlation. First, $C_B = 0.7$ specifies a B host crystal with a substantial amount of less mobile A atoms. Minor correlation effects are observed for the diffusion of both A and B atoms. Hence, in Fig. 7.7 the diffusivity

ratio (down-triangles) is slightly below the dashed line with slope 1 representing uncorrelated diffusion ($f_A = f_B = 1$). Second, the composition $C_B = 0.2$ is close to the threshold for site-percolation regarding B-B occurrences. A significant effect on the diffusivity ratio can be observed in Fig. 7.7 (circles) but no limitation on the $\widehat{D}_B/\widehat{D}_A$ value is apparent. In contrast, for a third composition given by $C_B = 0.1$ (squares), which is below the site-percolation threshold C_B^p, a limiting value of $\widehat{D}_B/\widehat{D}_A \approx 15$ is found. Finally, the same behaviour is displayed by the data representing $C_B = 0.02$ (up-triangles), that is, a composition even below the second-order threshold $C_B^{p,2}$. In this case, the diffusivity ratio slightly increases for $w_B/w_A > 10^4$, which, however, may be an artefact due to simulation runs of insufficient length.

7.3.5. Comparison of mass and charge transport

To compare tracer diffusion coefficients with the ionic conductivity these quantities have to be transformed to the same dimensionality. Using the Nernst-Einstein equation, the measured tracer diffusivity of A atoms (ions), $\widehat{D}_A$, may be converted into a conductivity $\widehat{\sigma}_A$,, i.e.,

$$\widehat{\sigma}_A = \frac{e^2}{k_B T} N_A \widehat{D}_A = \frac{e^2 N_0}{k_B T} C_A \widehat{D}_A \,, \tag{7.30}$$

where $N_A = N_0 C_A$ is the number density of A atoms, k_B is the Boltzmann constant and e is the charge unit. A similar expression holds for the partial conductivity $\widehat{\sigma}_B$ deduced from the B tracer diffusivity, so that the total 'tracer-derived' conductivity $\widehat{\sigma}$ is given by

$$\widehat{\sigma} = \widehat{\sigma}_A + \widehat{\sigma}_B \tag{7.31}$$

Alternatively, based on the Nernst-Einstein relation the ionic conductivity may be converted to the so-called charge diffusivity D_σ, i.e.,

$$D_\sigma = \frac{k_B T}{e^2 N_{ion}} \sigma = C_I D_I \,, \tag{7.32}$$

where $N_{ion} = N_A + N_B$ is the total ion density. Hence, D_σ reflects the mean effect of A and B ions. The right-hand side equality of Eq. 7.32 follows from Eq. 7.18 and $N_{ion} = N_0$. In addition, a mean tracer diffusivity can be introduced, i.e.,

$$\widehat{D} = C_A \widehat{D}_A + C_B \widehat{D}_B \,. \tag{7.33}$$

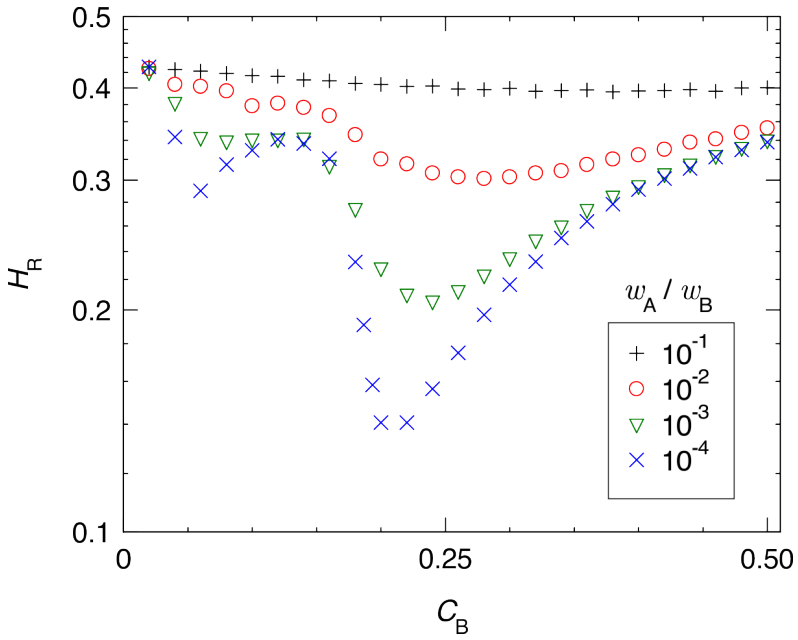

Figure 7.8.: Haven ratio H_R calculated with Eqs. 7.35 and 7.36 as a function of composition C_B for interstitialcy diffusion in the sc lattice. Data points represent the results for various jump frequency ratios $w_\mathrm{A}/w_\mathrm{B}$, as indicated.

With the quantities defined above, mass and charge transport can be compared in terms of the Haven ratio [76], i.e.,

$$H_\mathrm{R} = \frac{\widehat{\sigma}}{\sigma} = \frac{\widehat{D}}{D_\sigma} = \frac{C_\mathrm{A}\widehat{D}_\mathrm{A} + C_\mathrm{B}\widehat{D}_\mathrm{B}}{C_\mathrm{I}D_\mathrm{I}} \,. \tag{7.34}$$

Using Eqs. 7.13, 7.19 and 7.20, this expression simplifies to

$$H_\mathrm{R} = 2\frac{\widehat{f}}{f_\mathrm{I}}\frac{l_x^2}{l_{\mathrm{I},x}^2} = 0.5\frac{\widehat{f}}{f_\mathrm{I}} \,, \tag{7.35}$$

with

$$\widehat{f} = r_\mathrm{A}f_\mathrm{A} + r_\mathrm{B}f_\mathrm{B} \,. \tag{7.36}$$

The fact that Eq. 7.35 reproduces the well-known expression for the mono-ionic case [76] may be taken as a proof of consistency.

The results following from the present simulations are displayed in Fig. 7.8 over the composition range from 0.02 to 0.5 for different jump frequency ratios. The data show only rather small (negative) deviations from the mono-ionic case ($H_\mathrm{R} = f_0/2 = 0.4286$) for most compositions and $w_\mathrm{A}/w_\mathrm{B}$ values. However, in the

proximity of the site-percolation threshold $C_{\mathrm{B}}^{\mathrm{p}} = 0.1885$, a global minimum appears and H_{R} is strongly diminished for greatly different exchange rates. Specifically, for $w_{\mathrm{A}}/w_{\mathrm{B}} = 10^{-4}$ the Haven ratio results as $H_{\mathrm{R}} \approx 0.14$, which means a reduction by a factor of ~ 3. Another minimum, local in nature, develops for decreasing $w_{\mathrm{A}}/w_{\mathrm{B}}$ near the second-order percolation threshold $C_{\mathrm{B}}^{\mathrm{p};2} = 0.0376$. Altogether, H_{R} exhibits capricious behaviour over the range of compositions poor in the highly mobile component B, which will be most relevant for the interpretation of experimental data.It may be interesting to determine the relative contributions of either ionic species to $\widehat{\sigma}$ and σ (or to $\widehat{D}$ and D_σ). This can be done by means of the ratios

$$\frac{\widehat{\sigma}_{\mathrm{A}}}{\widehat{\sigma}_{\mathrm{A}} + \widehat{\sigma}_{\mathrm{B}}} = \frac{C_{\mathrm{A}}\widehat{D}_{\mathrm{A}}}{C_{\mathrm{A}}\widehat{D}_{\mathrm{A}} + C_{\mathrm{B}}\widehat{D}_{\mathrm{B}}} = \frac{r_{\mathrm{A}} f_{\mathrm{A}}}{\widehat{f}} \tag{7.37}$$

and

$$\frac{\sigma_{\mathrm{A}}}{\sigma_{\mathrm{A}} + \sigma_{\mathrm{B}}} = \frac{C_{\mathrm{A}} w_{\mathrm{A}} f_{\mathrm{I}}^{\mathrm{A}}}{C_{\mathrm{A}} w_{\mathrm{A}} f_{\mathrm{I}}^{\mathrm{A}} + C_{\mathrm{B}} w_{\mathrm{B}} f_{\mathrm{I}}^{\mathrm{B}}} = \frac{r_{\mathrm{A}} f_{\mathrm{I}}^{\mathrm{A}}}{f_{\mathrm{I}}}\,, \tag{7.38}$$

where with reference to Eq. 7.18 the relation $\sigma = \sigma_{\mathrm{A}} + \sigma_{\mathrm{B}}$ obviously holds. Equation 7.38 is further based on Eqs. 7.19, 7.20 and 7.24. Experimental studies of ionic transport properties in solids often rely on measurements of the conductivity and self-diffusion coefficients as a function of temperature. If only tracer diffusion data of one component, say A, is available it makes sense to determine the ratio

$$\frac{\widehat{\sigma}_{\mathrm{A}}}{\sigma} = \frac{C_{\mathrm{A}}\widehat{D}_{\mathrm{A}}}{C_{\mathrm{I}} D_{\mathrm{I}}} = 0.5 \frac{C_{\mathrm{A}} f_{\mathrm{A}} w_{\mathrm{A}}}{f_{\mathrm{I}} w_{\mathrm{I}}} = 0.5 \frac{r_{\mathrm{A}} f_{\mathrm{A}}}{f_{\mathrm{I}}}\,. \tag{7.39}$$

Like in Eq. 7.35, the factor 0.5 results from differences in jump length and jump frequency between atom A and defect I. Simulated data were employed to calculate $\widehat{\sigma}_{\mathrm{A}}/\sigma$ according to Eq. 7.39 as a function of composition. Figure 7.9 shows the results for different jump frequency ratios. It is found that for A-rich compositions with $C_{\mathrm{B}} < C_{\mathrm{B}}^{\mathrm{p}}$ the conductivity relies on substantial contributions from the less mobile A-type ions. By contrast, for compositions above the site-percolation threshold $\widehat{\sigma}_{\mathrm{A}}/\sigma$ becomes increasingly smaller for decreasing values of $w_{\mathrm{A}}/w_{\mathrm{B}}$. Conversely, this means that for $C_{\mathrm{B}} > C_{\mathrm{B}}^{\mathrm{p}}$ charge transport is almost completely carried by the highly mobile ionic component, in this case the B component. This conclusion is meaningful for the combined analysis of self-diffusion and conductivity data in ionic crystals.

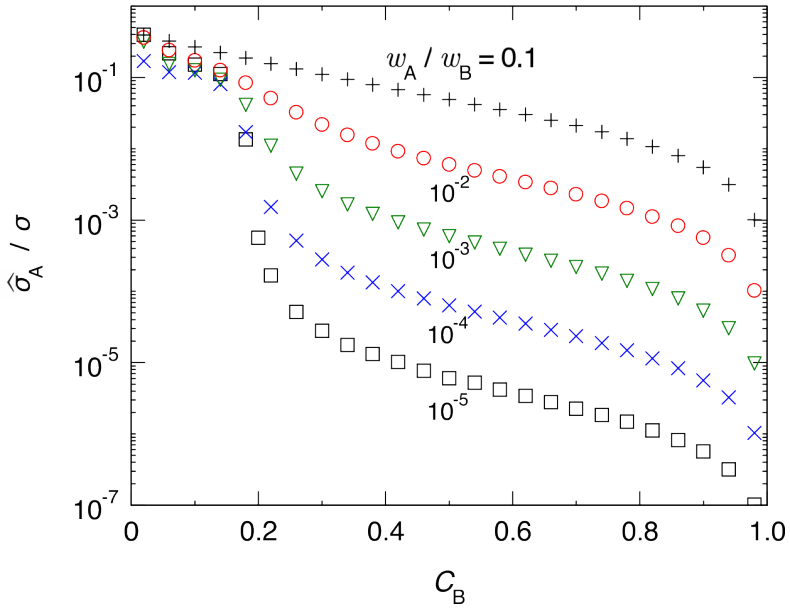

Figure 7.9.: Ratio $\hat{\sigma}_A/\sigma$ according to Eq. 7.39 for various jump frequency ratios w_A/w_B, as indicated. Above the threshold for site-percolation, $C_B^p = 0.1885$, the conductivity σ appears to be controlled by the diffusion of the more mobile B atoms(ions).

7.4. Summary and conclusions

The main features and results of this work may be summarised as follows:

(i) Diffusion and ionic conduction by the collinear interstitialcy mechanism in a random AB alloy was analysed in the limit of low interstitialcy concentration by means of Monte Carlo simulation.

(ii) Tracer and interstitialcy correlation factors (f_A, f_B and f_I) were calculated as a function of composition (C_B) and jump frequency ratio (w_A/w_B).

(iii) An analytical framework was established to describe partial correlation factors on various levels of discrimination.

(iv) Analysis of the interstitialcy percolation behaviour from the simulated f_I data yields an estimate for the first-order site-percolation limit ($C_B^p = 0.1885$) related to unbroken chains of the mobile component in the sc lattice.

(v) The same type of analysis reveals a second-order percolation threshold ($C_B^{p,2} = 0.0376$), which relates to the abundance of nearest-neighbour A-B occurrences.

(vi) For both percolation thresholds simple analytical estimations are given that

reproduce the corresponding numerical values within the uncertainty of the Monte Carlo results.
(vii) In sc random alloys, correlation effects and tracer diffusivity ratios ($\widehat{D}_{\mathrm{B}}/\widehat{D}_{\mathrm{A}}$) related to the interstitialcy mechanism may significantly differ from those related to the vacancy mechanism.
(viii) Simple expressions are given that allow for comparing the tracer diffusion coefficients with the ionic conductivity and to quantify the partial contribution of either component to overall charge transport.
(ix) Above the site-percolation threshold $C_{\mathrm{B}}^{\mathrm{p}}$, the ionic conductivity is controlled by the transport properties of the more mobile component.
This basic study concerning correlation effects by the *collinear* interstitialcy diffusion mechanism in a sc random alloy displays important features for the reconstruction of the diffusion mechanism acting in alkali feldspar. Assuming that the B component is representing the more mobile Na in alkali feldspar (and A is representing K) it was demonstrated that the site-percolation threshold associated with the interstitialcy mechanism is considerably shifted towards lower Na concentrations compared to the vacancy mechanism ($C_{\mathrm{B}}^{\mathrm{p}} = 0.310$ in a hypothetical sc structure of alkali feldspar). The experimental data for tracer diffusion (see Chapter 4) suggested that the Na diffusivity is not diminished due to site-blocking effects from slower moving K atoms in VF feldspar with the Na site-fraction $C_{\mathrm{Na}} = 0.15$. In conclusion, the diffusion mechanism acting in VF feldspar should be associated with a site-percolation threshold $C_{\mathrm{Na}}^{\mathrm{p}} \leq C_{\mathrm{Na}}\,(\mathrm{VF}) = 0.15$. The presented *collinear* interstitialcy mechanism in a sc lattice still bears a slightly larger threshold value of $C_{\mathrm{B}}^{\mathrm{p}} = 0.1885$. It is well known [109, 110, 111, 112] that the threshold value intimately depends on the coordination number z pertaining to a specific crystal lattice, that is $z = 8$ for interstitialcy diffusion in the sc structure. In addition, also the number of sites z_2 from which a second exchange of the interstitialcy I can occur following an arbitrarily chosen first jump determines the number of available pathways and hence, has an influence on $C_{\mathrm{B}}^{\mathrm{p}}$. This number accounts for $z_2^{\mathrm{c}} = 7$ in the *collinear* case and $z_2^{\mathrm{nc}} = 15$ in a pure *non-collinear* case. It will therefore be investigated in the following Chapter 8 how non-collinear jumps affect the percolation behaviour in a randomly ordered sc lattice. This study will be an important step in the interpretation of the diffusion mechanism controlling self-diffusion and ionic conductivity in alkali feldspar.

8. A Monte Carlo study of ionic transport in a simple cubic random alloy via the interstitialcy mechanism: Effects of non-collinear and direct interstitial jumps

The previous MC simulations of diffusion by the interstitialcy mechanism were confined to the simplest possible 3D crystallographic structure and a single elementary type of atomic jumps (see Chapter 7 and [75]). Specifically, a simple cubic lattice AB with exclusively *collinear* interstitialcy site-exchange showed a number of remarkable features with regard to correlation effects and their consequences for tracer diffusivity and ionic conductivity. The most important results can be summarised as follows: (i) Correlation factors f_{B} of the more mobile component B adopt very low values for extreme differences in jump frequency ($w_{\mathrm{A}}/w_{\mathrm{B}} < 10^{-2}$), when the alloy composition falls below the B-site percolation limit $C_{\mathrm{B}}^{\mathrm{p}} = 0.1885$ (site-fraction units). (ii) All correlation factors (f_{A}, f_{B}, and f_{I} pertaining to the 'generalised interstitialcy defect' I) reveal a pronounced minimum near a second-order percolation limit $C_{\mathrm{B}}^{\mathrm{p},2} = 0.0376$, which relates to the occurrence of non-interrupted A-B chains. (iii) Comparing the tracer diffusivity of A and B, differences in jump frequency are generally levelled off by correlation effects. In particular, for $C_{\mathrm{B}} < C_{\mathrm{B}}^{\mathrm{p}}$ the tracer diffusivity[1] ratio $\widehat{D}_{\mathrm{B}}/\widehat{D}_{\mathrm{A}}$ approaches an upper limit close to 15 for $w_{\mathrm{B}}/w_{\mathrm{A}}$ going to values of 10^4 and higher. (iv) Above the site-

[1] To reduce the number of indices, the common asterisk for labeling tracer diffusivity (D^*) has been replaced by the 'hat' symbol ($\widehat{D}$) throughout this work.

percolation threshold $C_{\mathrm{B}}^{\mathrm{p}}$, the ionic conductivity almost fully relies on the transport properties of the more mobile B component.

The question arises how this clear-cut picture will change when some of the model restrictions are relieved. A natural extension of the model can be obtained by taking into account additional jump types. Apart from the *collinear* exchange, where the two atomic displacements involved in an interstitialcy event are aligned along the same $\langle 111 \rangle$ direction, the sc lattice allows for a number of different *non-collinear* jumps. This work is restricted to the most likely variant, for which the deviation in jump direction between the two atoms displaced in conjunction is the smallest. This *non-collinear* variant has a multiplicity of three in the sc structure.

Another extension of an interstitialcy-type diffusion scheme takes into consideration the occurrence of *direct* interstitial jumps. Having interstitial atoms mediating diffusion through I-S and S-I exchange, it seems natural to additionally conceive of I-I jumps. These jumps will provide alternative pathways and thus, become particularly important in cases when diffusion via the true interstitialcy mechanism is severely hampered because of percolation problems. Therefore, it may be expected that I-I jumps will have a strong impact for the (more mobile, smaller) B atoms in B-poor compositions even when the probability of these jumps is comparatively low. Consequently, the diffusion properties may greatly change as a function of C_{B} due to the competition between *direct* and *indirect* interstitial exchange.

This study – published in Philosophical Magazine, 2016 [65] – successively explores the influence of non-collinear and direct interstitial jumps on mass and charge transport via the collinear interstitialcy mechanism. More specifically, it will be shown that both extensions of the jump-type variety lead to reduced diffusion correlation effects and thus, to (partly considerable) increases of the pertinent correlation factors f_{A}, f_{B}, and f_{I}. These findings have serious consequences for the composition dependence of the individual tracer self-diffusion coefficients, the charge diffusivity, and the appearance of percolation thresholds. Moreover, shifts in the proportions of mass to charge transport lead to remarkably high values of the Haven ratio. In general, the present results for the sc lattice have an exemplary character and will be significant for the interpretation of experimental data on alkali feldspar.

8.1. Theoretical background

8.1.1. Random alloy model with diffusion via self-interstitials

Starting point of the calculations is Manning's physical model of a binary random alloy AB [14, 45], in which atomic interactions are completely negligible. As a consequence, the distribution of A and B atoms over the lattice sites is purely statistical and thus, not subject to any ordering tendency. The atomic concentrations (in site-fractions) obey the relationship $C_\mathrm{A} + C_\mathrm{B} = 1$, which implies a negligibly low concentration of point defects. In this work, self-interstitials are considered as the only relevant point defects and the characteristics of their operation in mass and charge transport is explored. In particular, it has to be distinguished between self-interstitials of type A and B, that is, $\mathrm{A_I}$ and $\mathrm{B_I}$, respectively, which both may act as diffusion vehicle. Another crucial assumption of the random alloy model is that the interaction between atoms and point defects can be ignored. Moreover, the extremely low concentrations of $\mathrm{A_I}$ and $\mathrm{B_I}$ prevent any interference among these interstitials, e.g., by crossing-over of diffusion pathways. Diffusion via the interstitialcy mechanism in a random alloy AB may be described in terms of quasichemical reactions, which for tracer atoms $\widehat{\mathrm{B}}_\mathrm{S}$ and $\widehat{\mathrm{B}}_\mathrm{I}$ can be written as

$$\widehat{\mathrm{B}}_\mathrm{I} + \mathrm{B_S} \rightleftharpoons \widehat{\mathrm{B}}_\mathrm{S} + \mathrm{B_I} \tag{8.1}$$

and

$$\widehat{\mathrm{B}}_\mathrm{I} + \mathrm{A_S} \rightleftharpoons \widehat{\mathrm{B}}_\mathrm{S} + \mathrm{A_I}\,. \tag{8.2}$$

Here, it is implied that the interstitial (index I) and substitutional (index S) atoms are at nearest-neighbour positions. Similar reactions can be given if the diffusion of A atoms is considered.

In the previous Chapter 7 the *collinear* variant of the interstitialcy mechanism was considered in which the positions of all particles involved in a single reaction step are located along a $\langle 111 \rangle$ direction of the sc lattice; see Fig. 8.1b. For simplicity and in consistency with the random-alloy concept, it was assumed that there are only two different jump frequencies, i.e., w_A and w_B, depending on the substitutional atom involved in I-S exchange. Thus, the jump probability is in all cases independent of the type of the participating interstitial, $\mathrm{A_I}$ or $\mathrm{B_I}$.

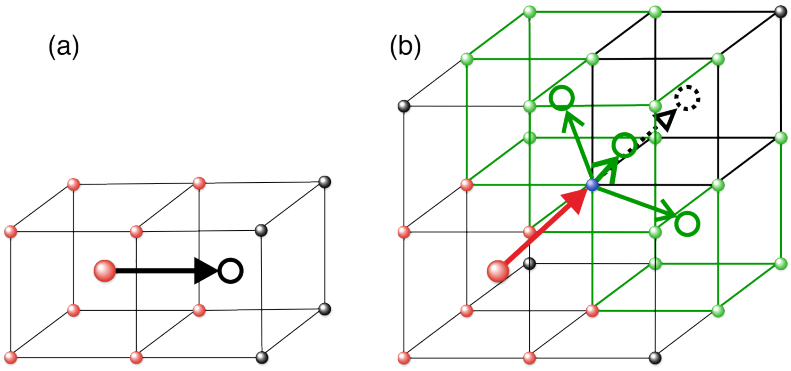

Figure 8.1.: Direct interstitial (a) and interstitialcy (b) jumps in a simple cubic structure. Two types of interstitialcy exchange are indicated: *collinear* exchange (I-S full/solid arrow with subsequent S-I open/dashed arrow) and *non-collinear* exchange entailing an oblique angle (109.47°) between the partial steps (I-S full/solid arrow together with one of three equivalent S-I simple arrows).

Accordingly, in Eq. 8.1 w_{B} determines both the forward and reverse *collinear* reaction rate. However, in Eq. 8.2 the opposite *collinear* reaction rates are different and given by w_{A} and w_{B} for the forward and reverse direction, respectively.

8.1.2. Interstitialcy diffusion mechanism including non-collinear exchange

Jump types and basic quantities

In the present study, allowance is made for *non-collinear* exchanges in such a way that the total jump frequencies w_{A} and w_{B} related to the S-atoms do not change. Starting from an interstitial at the position (0,0,0) the sc lattice with lattice constant a offers - apart from, e.g., the a(1,1,1) target position of the I-atom related to the *collinear* exchange - three other target positions a(1,1,0), a(1,0,1) and a(0,1,1) defining three mutually equivalent *non-collinear* interstitialcy jumps. This situation is schematically displayed in Fig. 8.1b. The (oblique) angle between the partial I-S and S-I steps within these *non-collinear* exchanges amounts invariantly to 109.47°. Other possible non-collinear jumps entailing smaller angles are considered as less likely and therefore neglected in this work. Thus, w_{B} splits up in collinear (index c) and non-collinear (index nc) contributions according to

$$w_{\mathrm{B}}^{\mathrm{c,nc}} = w_{\mathrm{B}}^{\mathrm{c}} + 3w_{\mathrm{B}}^{\mathrm{nc}} \equiv w_{\mathrm{B}}(p^{\mathrm{c}} + 3p^{\mathrm{nc}})\,, \tag{8.3}$$

where the sum of the probabilities (p^{c}, p^{nc}) equals unity, so that $w_{\mathrm{B}}^{\mathrm{c,nc}} = w_{\mathrm{B}}$ holds true. Similar quantities and relationships are adopted for component A. It is noted that the distribution among c- and nc-jumps is the same for both components, as expressed by the common probabilities p^{c} and p^{nc} which are independent of A or B.

In thermal equilibrium, the concentrations of products and educts in a reaction are interrelated through the reaction rates. Specifically, based on Eq. 8.2 mass action law predicts

$$\frac{r_{\mathrm{B}}}{r_{\mathrm{A}}} = \frac{C_{\mathrm{B,I}}}{C_{\mathrm{A,I}}} = \frac{C_{\mathrm{B}} w_{\mathrm{B}}}{C_{\mathrm{A}} w_{\mathrm{A}}}\,, \tag{8.4}$$

where $C_{\mathrm{B,I}}$ ($C_{\mathrm{A,I}}$) is the concentration (site fraction) of $\mathrm{B_I}$ ($\mathrm{A_I}$). Moreover, r_{B} designates the normalised or relative concentration of B-type interstitials, i.e.,

$$r_{\mathrm{B}} = \frac{C_{\mathrm{B,I}}}{C_{\mathrm{A,I}} + C_{\mathrm{B,I}}} = \frac{C_{\mathrm{B,I}}}{C_{\mathrm{I}}} = 1 - r_{\mathrm{A}}\,. \tag{8.5}$$

Another useful expression for r_{B} is

$$r_{\mathrm{B}} = \frac{C_{\mathrm{B}} w_{\mathrm{B}}}{C_{\mathrm{A}} w_{\mathrm{A}} + C_{\mathrm{B}} w_{\mathrm{B}}} = \frac{C_{\mathrm{B}} w_{\mathrm{B}}}{\bar{w}}\,, \tag{8.6}$$

which contains the mean atomic jump frequency

$$\bar{w} = C_{\mathrm{A}} w_{\mathrm{A}} + C_{\mathrm{B}} w_{\mathrm{B}}\,. \tag{8.7}$$

It is noted that r_{B} may be interpreted as the probability that a generalised interstitial defect I with concentration $C_{\mathrm{I}} = C_{\mathrm{A,I}} + C_{\mathrm{B,I}}$ is of type $\mathrm{B_I}$. In particular, $C_{\mathrm{A,I}}$ and $C_{\mathrm{B,I}}$ can be conveniently expressed in terms of the total concentration of interstitials as

$$C_{\mathrm{A,I}} = r_{\mathrm{A}} C_{\mathrm{I}} \quad \text{and} \quad C_{\mathrm{B,I}} = r_{\mathrm{B}} C_{\mathrm{I}}\,. \tag{8.8}$$

Tracer diffusion coefficients

The tracer diffusion coefficient of B atoms is defined as

$$\widehat{D}_{\mathrm{B}} = \lim_{t\to\infty} \frac{\langle X_{\mathrm{B}}^2 \rangle}{2t} = \lim_{t\to\infty} f_{\mathrm{B}} \frac{\langle X_{\mathrm{B}}^2 \rangle_{\mathrm{uncorr}}}{2t}\,, \tag{8.9}$$

where t is a sufficiently long time and $\langle X_{\mathrm{B}}^2 \rangle$ denotes the mean square displacement in x-direction within this time. The right-hand side of this equation contains the tracer

correlation factor f_B and the *uncorrelated* mean square displacement $\langle X_\mathrm{B}^2 \rangle_\mathrm{uncorr}$, which includes contributions of both *collinear* and *non-collinear* jumps. In the previous chapter, the *collinear* contribution was decomposed in (mean) numbers of different jump types multiplied by the square of their common jump length in x-direction, i.e., $l_x = a/2$. For B atoms, this leads to a sequence of terms comprising B-A and B-B exchanges both of I-S and S-I type. Extending this procedure to include *non-collinear* jumps, it can be made use of the fact that each atomic displacement in such interstitialcy event is also of length l_x. Then, it can be readily shown that the tracer diffusion coefficient of component B is given by[2]

$$\widehat{D}_\mathrm{B}^\mathrm{c,nc} = \frac{1}{2} f_\mathrm{B}^\mathrm{c,nc} 2(w_\mathrm{B}^\mathrm{c} + 3w_\mathrm{B}^\mathrm{nc}) z_\mathrm{IS} C_\mathrm{I} l_x^2 = 2 f_\mathrm{B}^\mathrm{c,nc} w_\mathrm{B} C_\mathrm{I} a^2 \,, \tag{8.10}$$

with coordination number $z_\mathrm{IS} = 8$. The correlation factor $f_\mathrm{B}^\mathrm{c,nc}$, now involving collinear and non-collinear jumps, has to be calculated by Monte Carlo methods. A similar expression holds for $\widehat{D}_\mathrm{A}^\mathrm{c,nc}$, so that the diffusivity ratio of the two components reads

$$\frac{\widehat{D}_\mathrm{B}^\mathrm{c,nc}}{\widehat{D}_\mathrm{A}^\mathrm{c,nc}} = \frac{f_\mathrm{B}^\mathrm{c,nc} w_\mathrm{B}}{f_\mathrm{A}^\mathrm{c,nc} w_\mathrm{A}} \,. \tag{8.11}$$

Charge or conductivity diffusion coefficient

The occurrence of *non-collinear* jumps may also affect the ionic conductivity, when it is assumed that A and B are positively charged, monovalent ions and the considered sc random alloy forms a sublattice in a crystal structure with a negatively charged rigid framework. These effects can be described through the Nernst-Einstein equation by the charge or conductivity diffusivity D_σ, i.e., [75]

$$D_\sigma = \frac{k_\mathrm{B} T}{e^2 N_\mathrm{ion}} \sigma = C_\mathrm{I} D_\mathrm{I} \,, \tag{8.12}$$

where $N_\mathrm{ion} = N_\mathrm{A} + N_\mathrm{B}$ is the total number density of ions, D_I denotes the diffusion coefficient of the generalised interstitial carrying a charge unit and k_B is the Boltzmann constant. In analogy to the simplest case only allowing for *collinear*

[2] To reduce the number of indices, the common asterisk for labelling tracer diffusivity (D^*) has been replaced by the 'hat' symbol ($\widehat{D}$) throughout this work.

jumps [75], it is easy to derive that the interstitial diffusivity for mixed c-nc exchanges can be written as

$$D_{\mathrm{I}}^{\mathrm{c,nc}} = \frac{1}{2} f_{\mathrm{I}}^{\mathrm{c,nc}} (w_{\mathrm{I}}^{\mathrm{c}} + 2w_{\mathrm{I}}^{\mathrm{nc}}) z_{\mathrm{IS}} l_{\mathrm{I},x}^2 = 4 f_{\mathrm{I}}^{\mathrm{c,nc}} w_{\mathrm{I}}^{\mathrm{c,nc}} a^2 \,. \tag{8.13}$$

Here, $f_{\mathrm{I}}^{\mathrm{c,nc}}$ denotes the interstitialcy correlation factor and $w_{\mathrm{I}}^{\mathrm{nc}}$ is the mean partial I jump frequency for one out of three possible nc target positions given by

$$w_{\mathrm{I}}^{\mathrm{nc}} = C_{\mathrm{A}} w_{\mathrm{A}}^{\mathrm{nc}} + C_{\mathrm{B}} w_{\mathrm{B}}^{\mathrm{nc}} \,. \tag{8.14}$$

A similar definition holds for $w_{\mathrm{I}}^{\mathrm{c}}$. In Eq. 8.13 it is used that the jump length of I along a principal axis, e.g., $l_{\mathrm{I},x}$, equals the lattice constant a. However, only 2 out of 3 different nc-jumps have a displacement component in x-direction. This explains the term $2w_{\mathrm{I}}^{\mathrm{nc}}$ compared to similar terms $3w_{\mathrm{B}}^{\mathrm{nc}}$ in Eqs. 8.3 and 8.10; thus, the mean total I jump frequency $w_{\mathrm{I}}^{\mathrm{c,nc}}$ is obtained as

$$w_{\mathrm{I}}^{\mathrm{c,nc}} = w_{\mathrm{I}}^{\mathrm{c}} + 2w_{\mathrm{I}}^{\mathrm{nc}} \,. \tag{8.15}$$

Quantitative differences between mass and charge transport can be expressed by the Haven ratio H_{R}, which for the interstitialcy mechanism in binary lattices is generally given by[3]

$$H_{\mathrm{R}} = \frac{\widehat{D}}{D_\sigma} = \frac{C_{\mathrm{A}} \widehat{D}_{\mathrm{A}} + C_{\mathrm{B}} \widehat{D}_{\mathrm{B}}}{C_{\mathrm{I}} D_{\mathrm{I}}} \,, \tag{8.16}$$

where $\widehat{D} = C_{\mathrm{A}} \widehat{D}_{\mathrm{A}} + C_{\mathrm{B}} \widehat{D}_{\mathrm{B}}$ has been introduced as a mean tracer diffusivity [76, 75]. With the extension to *non-collinear* jumps and using Eqs. 8.10, 8.13 and 8.14 the Haven ratio can be written as

$$H_{\mathrm{R}}^{\mathrm{c,nc}} = \frac{f^{\mathrm{c,nc}}}{2 f_{\mathrm{I}}^{\mathrm{c,nc}}} \cdot \frac{w_{\mathrm{I}}^{\mathrm{c}} + 3w_{\mathrm{I}}^{\mathrm{nc}}}{w_{\mathrm{I}}^{\mathrm{c}} + 2w_{\mathrm{I}}^{\mathrm{nc}}} \,, \tag{8.17}$$

with $f^{\mathrm{c,nc}} = r_{\mathrm{A}} f_{\mathrm{A}}^{\mathrm{c,nc}} + r_{\mathrm{B}} f_{\mathrm{B}}^{\mathrm{c,nc}}$. Thus, the Haven ratio is essentially determined by correlation effects, whereas the last factor in Eq. 8.17 takes values between 1 ($w_{\mathrm{I}}^{\mathrm{nc}} = p^{\mathrm{nc}} = 0$) and $\frac{3}{2}$ ($w_{\mathrm{I}}^{\mathrm{c}} = p^{\mathrm{c}} = 0$).

[3] Minor changes to Eq. 8.16 are necessary if the number of lattice sites and interstices are different.

In addition to the overall Haven ratio of Eqs. 8.16 and 8.17, the partial Haven ratios $H_{\mathrm{R,A}}$ and $H_{\mathrm{R,B}}$ may be introduced as

$$H_{\mathrm{R,A}} = \frac{C_{\mathrm{A}}\widehat{D}_{\mathrm{A}}}{C_{\mathrm{I}}D_{\mathrm{I}}} \qquad H_{\mathrm{R,B}} = \frac{C_{\mathrm{B}}\widehat{D}_{\mathrm{B}}}{C_{\mathrm{I}}D_{\mathrm{I}}}\,, \tag{8.18}$$

so that $H_{\mathrm{R}} = H_{\mathrm{R,A}} + H_{\mathrm{R,B}}$ holds true.

8.1.3. Interstitialcy diffusion with allowance for direct interstitial jumps

Tracer correlation factors

Having the interstitialcy mechanism with self-interstitials as diffusion vehicles, it seems natural to consider I-I jumps in addition to I-S/S-I exchanges, as depicted in Fig. 8.1a. In this case, the uncorrelated squared displacement of a B atom in x-direction has to be extended, i.e.,

$$\langle X_{\mathrm{B}}^2\rangle_{\mathrm{uncorr}} = \langle n_{\mathrm{BA}} + n_{\mathrm{BB}}\rangle l_x^2 + \langle n_{\mathrm{B},x}^{\mathrm{i}}\rangle (l_x^{\mathrm{i}})^2\,. \tag{8.19}$$

Here, the first term refers to *collinear* interstitialcy exchanges (both I-S and S-I) with their number of occurrences $\langle n_{\mathrm{BA}}\rangle = 2w_{\mathrm{B}}r_{\mathrm{A}}z_{\mathrm{IS}}C_{\mathrm{I}}t$ and $\langle n_{\mathrm{BB}}\rangle = 2w_{\mathrm{B}}r_{\mathrm{B}}z_{\mathrm{IS}}C_{\mathrm{I}}t$ within diffusion time t [75], all of which have a component l_x in x-direction. The second term in Eq. 8.19 accounts for I-I jumps in x-direction (index i) having a greater length $l_x^{\mathrm{i}} = a$, where

$$\langle n_{\mathrm{B},x}^{\mathrm{i}}\rangle = 2p_{\mathrm{B,I}}C_{\mathrm{E}}u_{\mathrm{B}}t = 2\frac{w_{\mathrm{B}}}{\bar{w}}C_{\mathrm{I}}u_{\mathrm{B}}t\,. \tag{8.20}$$

In the derivation of this equation it was used that the I-I jump frequency u_{B} is independent of direction in the sc lattice and that from each I-site 2 opposite jumps along the x-axis are possible. Virtually all I-sites are empty, so that the lattice-site normalised concentration C_{E} acting as probability equals 1. Furthermore, the probability that a B atom resides on a I-site, $p_{\mathrm{B,I}} \equiv C_{\mathrm{B,I}}/C_{\mathrm{B}}$, results as $(w_{\mathrm{B}}/\bar{w})C_{\mathrm{I}}$ by using Eqs. 8.6 and 8.8.
With the aid of Eqs. 8.9, 8.19 and 8.20 the B tracer diffusivity $\widehat{D}_{\mathrm{B}}^{\mathrm{c,i}}$ is obtained as

$$\widehat{D}_{\mathrm{B}}^{\mathrm{c,i}} = 2f_{\mathrm{B}}^{\mathrm{c,i}}w_{\mathrm{B}}\left(1 + \frac{u_{\mathrm{B}}}{2\bar{w}}\right)C_{\mathrm{I}}a^2\,, \tag{8.21}$$

where the upper index c,i refers to taking into account both *collinear* (c) interstitialcy exchanges and direct interstitial (i) jumps. Compared to the reference case with $u_\mathrm{B} = 0$ [75] the tracer diffusivity is affected by a higher jump frequency due to the factor in parentheses and by a different correlation factor ($f_\mathrm{B}^{\mathrm{c,i}}$). Assuming that for the larger A atom (ion) I-I jumps may be neglected ($u_\mathrm{A} = 0$) the diffusivity ratio can be written as

$$\frac{\widehat{D}_\mathrm{B}^{\mathrm{c,i}}}{\widehat{D}_\mathrm{A}^{\mathrm{c,i}}} = \frac{f_\mathrm{B}^{\mathrm{c,i}} w_\mathrm{B}}{f_\mathrm{A}^{\mathrm{c,i}} w_\mathrm{A}} \left(1 + \frac{u_\mathrm{B}}{2\bar{w}}\right) . \tag{8.22}$$

This expression reflects that through correlation effects also the tracer diffusivity of A ($f_\mathrm{A}^{\mathrm{c,i}}$) may be affected by I-I jumps of B.

Charge or conductivity diffusion coefficient

With the extension to direct interstitial B jumps the uncorrelated squared displacement in x-direction obtains an additional contribution, which is equal to $r_\mathrm{B} u_\mathrm{B} a^2$. Thus, the charge diffusivity takes the form

$$D_\sigma^{\mathrm{c,i}} = 4 f_\mathrm{I}^{\mathrm{c,i}} w_\mathrm{I} \left(1 + \frac{r_\mathrm{B} u_\mathrm{B}}{4 w_\mathrm{I}}\right) C_\mathrm{I} a^2 , \tag{8.23}$$

where $w_\mathrm{I} = \bar{w}$, as for the exclusively *collinear* interstitialcy case [75]. For the Haven ratio, it can be readily derived

$$H_\mathrm{R}^{\mathrm{c,i}} = \frac{f^{\mathrm{c,i}}}{2 f_\mathrm{I}^{\mathrm{c,i}}} \cdot \frac{1 + 2(f_\mathrm{B}^{\mathrm{c,i}}/f^{\mathrm{c,i}})\alpha_\mathrm{B}}{1 + \alpha_\mathrm{B}} , \tag{8.24}$$

with $f^{\mathrm{c,i}} = r_\mathrm{A} f_\mathrm{A}^{\mathrm{c,i}} + r_\mathrm{B} f_\mathrm{B}^{\mathrm{c,i}}$ and $\alpha_\mathrm{B} = r_\mathrm{B} u_\mathrm{B}/4\bar{w}$.

8.2. Numerical procedures

The numerical model is based on the conception that an interstitialcy defect I performs I-S jumps with frequencies (w_A, w_B) that do not depend on the type of defect, but rather on the type of its neighbouring atoms (cf. Sect. 2.1). Initially, the I atom is set in the centre of a simple cubic 'interstitial' lattice that is otherwise completely empty. A second, 'substitutional' lattice is shifted by $(a/2, a/2, a/2)$ relative to the 'interstitial' lattice and both lattices are of size $160a \times 160a \times 160a$. All atoms of type A and B are tagged and randomly distributed

within the 'substitutional' lattice according to their concentrations C_A and C_B, respectively. The total jump frequency of I is then evaluated by examining the type of neighbouring S-atoms and given by $\sum_i^8 w_i$ with $w_i = w_\mathrm{A}, w_\mathrm{B}$, respectively. In cases when allowance for direct interstitial jumps of the B atoms is made, the total jump frequency of a $\mathrm{B_I}$ defect is increased by $6u_\mathrm{B}$ because of six possible I-I jump directions. One jump direction is chosen by a random number generator (RNG) according to the individual jump probabilities. After an I-S exchange, the directions of the consecutive S-I jump are weighted by a given ratio $p^\mathrm{c}/3p^\mathrm{nc}$ (the three non-collinear jumps have equal probabilities) and subjected to RNG selection, as well. Sufficiently long runs of I jumps need to be executed to compute correlation factors with acceptably small uncertainties. It has been proven effective to introduce periodic boundary conditions to sustain runs of necessary length, i.e., consisting of $n = 5 \times 10^{10}$ jumps.

In all simulations, partial correlation factors (PCFs) were computed first by evaluating the scalar product of jump vectors for each atom, given by $S_\alpha = \sum_i \sum_j (x_{\alpha,i} \cdot x_{\alpha,i+j})$, where $x_{\alpha,i+j}$ denotes the jth jump after the ith exchange of type α [83]. By averaging over S_α for all atoms of the same type the corresponding PCF is given by

$$\tilde{f}_\alpha = 1 + 2\langle S_\alpha \rangle / \langle n_\alpha \rangle \cdot x_\alpha^2, \tag{8.25}$$

where $\langle n_\alpha \rangle$ is the number of jumps of type α and x_α is the projected length. Total correlation factors are then obtained by weighted averages of the pertaining PCFs. For instance, in the case of B atoms subject to both *collinear* interstitialcy and *direct interstitial* exchange the relation

$$f_\mathrm{B}^\mathrm{c,i} = \frac{\tilde{f}_\mathrm{B}^\mathrm{c} \langle n_\mathrm{BB} + n_\mathrm{BA} \rangle l_x^2 + \tilde{f}_\mathrm{B}^\mathrm{i} \langle n_{\mathrm{B},x}^\mathrm{i} \rangle (l_x^\mathrm{i})^2}{\langle n_\mathrm{BB} + n_\mathrm{BA} \rangle l_x^2 + \langle n_{\mathrm{B},x}^\mathrm{i} \rangle (l_x^\mathrm{i})^2} = \frac{2\bar{w}\tilde{f}_\mathrm{B}^\mathrm{c} + u_\mathrm{B}\tilde{f}_\mathrm{B}^\mathrm{i}}{2\bar{w} + u_\mathrm{B}} \tag{8.26}$$

holds true. Here, the calculation of $\tilde{f}_\mathrm{B}^\mathrm{c}$ relies on sequences starting with an I-S or S-I exchange. By contrast, $\tilde{f}_\mathrm{B}^\mathrm{i}$ refers to jump sequences, in which the first jump is of type I-I. This PCF-based scheme has been proven to be as effective as the usually employed *displacement* method [75, 83]. An advantage of PCF calculations is, however, that they provide more detailed information being useful in complex situations.

Interstitialcy correlation factors f_I were calculated by the same PCF-scheme, except for the averaging over many particles (at any time, there is only one I defect in the simulation box). Instead, the total run made up of n jumps was split into N_run

sequences of n_L jumps and f_I was obtained by averaging over all sequences. f_I values were first calculated as a function of n_L during trials. The data converged for $n_L \geq 2 \times 10^6$ and hence, all present data points are based on this choice of n_L.

8.3. Results and discussion

8.3.1. Effects of non-collinear exchange

Tracer correlation factors

Figure 8.2a shows the effects of non-collinearity on the tracer correlation factor f_A as a function of C_B for $w_A/w_B = 10^{-5}$. It is generally observed that the allowance for *non-collinear* jumps leads to higher f_A values in the B-poor alloy regime (note the truncation of the concentration axis at $C_B = 0.41$). Particularly, replacing only 1 percent of the *collinear* exchanges by the *non-collinear* variant ($p^c/3p^{nc} = 0.99/0.01$) results in an increase of the minimum f_A value by about a factor of 6 (left-hand side of Fig. 8.2a. At the same time this minimum shifts to a smaller C_B value, i.e., from about 0.02 to 0.003. A further drastic increase of the *non-collinear* contribution to 75 % ($p^c/3p^{nc} = 0.25/0.75$) is accompanied by another increase of the f_A minimum by somewhat more than a factor of 3, whereas its position only minimally shifts to a lower B concentration. A final change to the *fully non-collinear* case with $p^c = 0$ does not significantly alter the f_A behaviour anymore. For B-rich compositions the changes due to nc-jumps are minor and f_A converges to unity for $C_B \to 1$.

Similar observations are made for f_B in Fig. 8.2b. Also for the B atoms a 1 % admixture of nc-jumps causes an increase of the tracer correlation factor, which is particularly strong for $C_B < 0.2$. Further increasing the nc contribution goes along with higher f_B values but the relative increment becomes gradually smaller. However, the fully non-collinear f_B values (c/nc = 0/100) are found to fall below those representing c/nc = 25/75. This relates to the fact that in the nc-only case the number of target positions in the interstitialcy exchange is less than in the mixed c/nc modes, which reduces the number of diffusion pathways. Interestingly, the two-step behaviour of the c-only plot exhibited by the logarithmic representation of Fig. 8.2b is found to disappear with increasing substitution of nc-jumps. Referring to the previous Chapter 7 these observations can be elucidated by inspecting the percolation behaviour for the different simulated cases.

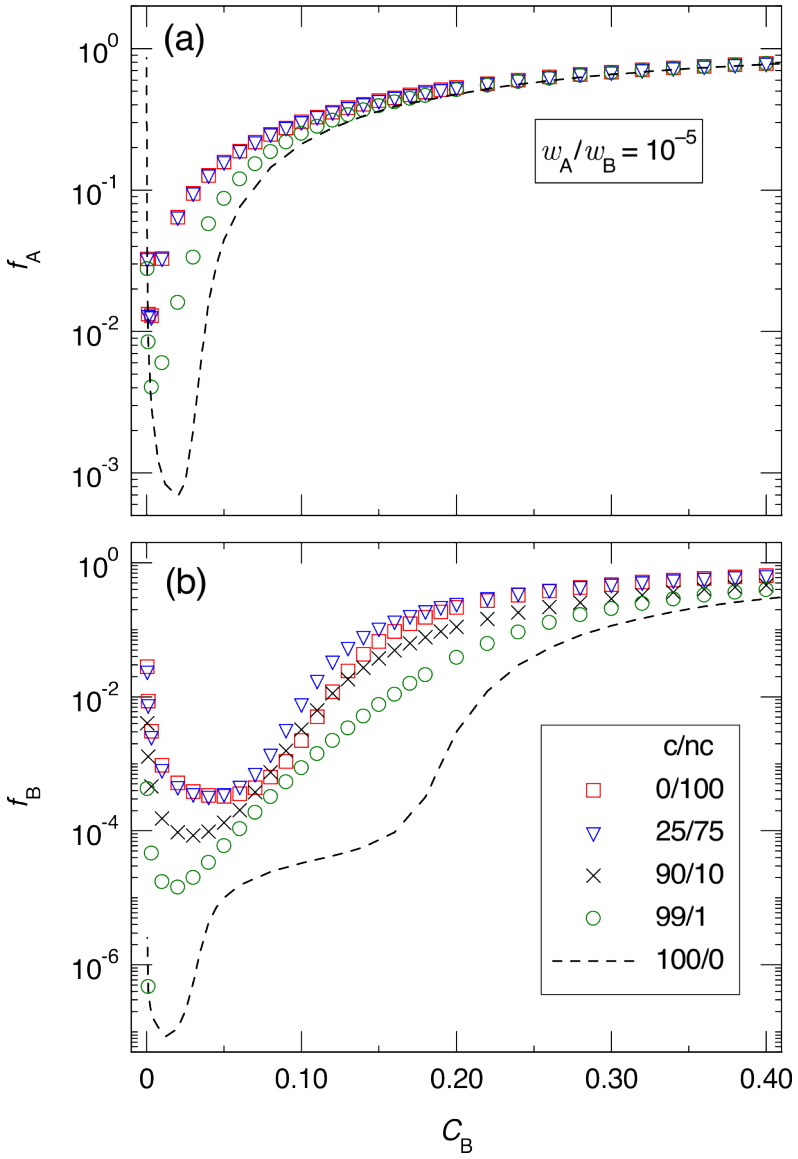

Figure 8.2.: Tracer correlation factors f_A (a) and f_B (b) for diffusion by the interstitialcy mechanism in a sc random alloy AB with $w_A/w_B = 10^{-5}$ as a function of composition $C_B \leq 0.4$. The data pertain to different proportions of collinear (c) to non-collinear jumps (nc) as indicated by c/nc ratios in percent.

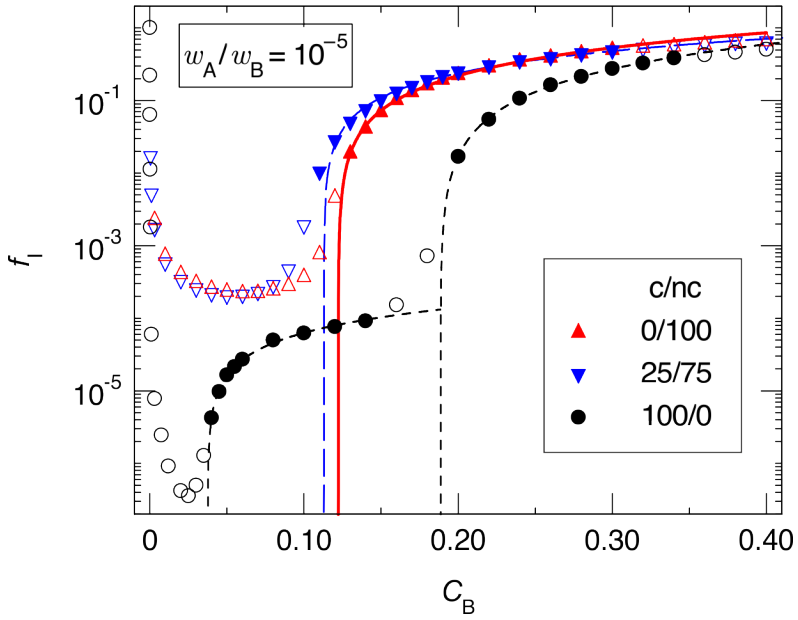

Figure 8.3.: Interstitialcy correlation factors f_I in the sc random alloy AB with $w_A/w_B = 10^{-5}$ as a function of composition $C_B \leq 0.4$ for different proportions c/nc of collinear to non-collinear jumps, as indicated by solid and open symbols. Dashed and solid lines represent individual fits to the solid symbols based on Eq. 8.27 and their intersections with the C_B-axis mark percolation thresholds.

Percolation behaviour

Figure 8.3 displays a selection of interstitialcy correlation factors f_I for $w_A/w_B = 10^{-5}$, which are associated with some of the f_A and f_B plots in Fig. 8.2. It should be noted that for all c/nc ratios f_I converges to unity for C_B approaching 0 and 1. As discussed in Chapter 7, distinct steps in such plots for extreme jump frequency ratios may relate to the percolation along chains and clusters of the (much more) mobile atoms, which is characterised by a specific percolation threshold C_B^p [21, 75]. In the *purely collinear* case (100/0) f_I reveals two steps (circles in Fig. 8.3), which were each fitted by the equation [23, 21, 75]

$$f_I = k(C_B - C_B^p)^\delta, \; C_B \geq C_B^p \,, \tag{8.27}$$

where δ is a critical exponent and k is a dimensionless proportionality constant. The same equation was used for fitting the observed single f_I step in the 25/75 and 0/100 cases. The resulting parameter values are listed in Tab. 8.1.
Passing from B-rich to B-poor alloy compositions the first percolation threshold $C_B^{p,1}$

Table 8.1.: Parameter values resulting from MC simulations characterizing the interstitialcy percolation behaviour in the simple cubic random alloy for different proportions c/nc of *collinear* (c) to *non-collinear* (nc) jumps; cf. Eq. 8.27.

c/nc	$C_{\mathrm{B}}^{\mathrm{p},1}$	δ	k	Reference
100/0	0.1885 ± 0.0011	1.23 ± 0.05	4.0 ± 0.4	[75]
25/75	0.109 ± 0.002	1.03 ± 0.04	2.8 ± 0.3	This work
0/100	0.122 ± 0.002	1.07 ± 0.04	3.4 ± 0.3	This work

is connected with the disappearance of uninterrupted B-B chains. At this critical composition, f_{I} and concomitantly the ionic conductivity (or D_σ) totally vanish for $w_{\mathrm{A}}/w_{\mathrm{B}}$ converging to zero. Going from *collinear-only* (100/0) to *non-collinear-only* (0/100) exchange $C_{\mathrm{B}}^{\mathrm{p},1}$ shifts from 0.1885 to 0.122, whereas δ (from 1.23 to 1.07) and k (from 4.0 to 3.4) remain closely similar, respectively. The lower $C_{\mathrm{B}}^{\mathrm{p},1}$ value for the nc-only case is due to a higher number of (different) sites from which a second exchange of the interstitialcy I can occur following an arbitrarily chosen first jump ($z_2^{\mathrm{nc}}/z_2^{\mathrm{c}} = 15/7$). However, the mixed case 25/75 shows an even smaller $C_{\mathrm{B}}^{\mathrm{p},1}$ value (0.109). Obviously, this relates to the slightly higher second-jump coordination number in a mixed c/nc situation, i.e., $z_2^{\mathrm{c,nc}} = 16$. Apparently, substituting a substantial fraction of c-jumps for nc-jumps in an nc-only starting situation (from 0/100 to 25/75) has rather minor effects on the correlation and percolation behaviour. Conversely, substituting nc- for c-jumps has a strong impact, as shown by Fig. 8.2b.

In Fig. 8.3, the second f_{I} step appearing for the c-only mode (100/0) yielded a second(-order) percolation threshold $C_{\mathrm{B}}^{\mathrm{p},2} = 0.0376$, which reflects the disruption of connected A-B chains upon progressing C_{B} decrease [75]. $C_{\mathrm{B}}^{\mathrm{p},2}$ appears for small values of $w_{\mathrm{A}}/w_{\mathrm{B}}\,(\neq 0)$ and marks a strong decrease in ionic conductivity, which below this threshold concentration is governed by the low mobility of A ions. $C_{\mathrm{B}}^{\mathrm{p},2}$ seems to be absent in the nc-only (0/100) and the mixed (25/75) modes (see open symbols in Fig. 8.3).

More insight into the $C_{\mathrm{B}}^{\mathrm{p},2}$ behaviour may be gained from inspecting the composition-dependence of f_{A} for the various c/nc cases. In the purely *collinear* mode it was observed that the $C_{\mathrm{B}}^{\mathrm{p},2}$-related decrease of f_{I} with decreasing B concentration is mimicked by a similar decrease of f_{A} (cf. Fig. 7.4 in Chapter 7). This can be understood from the notion that for compositions just above this A-B chain

related percolation threshold most atomic jumping takes place in domains which are comparatively rich in B. This is due to the fact that the defect I kinetically bounds to the B atoms with their much higher mobility. Thus, a jump sequence of an arbitrarily selected A atom (tracer) involves a large number of reverse jumps ($f_\mathrm{A} \ll 1$) within B-rich domains of limited size but still forming a connected network through A-B bridges and chains. Further lowering of C_B towards $C_\mathrm{B}^{\mathrm{p},2}$ leads to smaller domains and consequently to lower f_A values. Finally, the domain connectivity gets lost at the A-B percolation limit and f_A passes through a minimum at a composition close to $C_\mathrm{B}^{\mathrm{p},2}$. To demonstrate the close connection between f_A and f_I for the 100/0 mode the C_B-dependence of f_A was fitted in the relevant composition range by Eq. 8.27. Indeed, the resulting f_A-related threshold concentration of 0.034 ± 0.002 is only slightly smaller than the f_I-related, 'true' A-B percolation limit $C_\mathrm{B}^{\mathrm{p},2} = 0.0376 \pm 0.0004$ [75]). Moreover, the critical exponents δ reflecting the curvatures of the plots near $C_\mathrm{B}^{\mathrm{p},2}$ (cf. Fig. 8.2a for f_A) are similar in both cases and take values close to 1.0.
Analysing the f_A data for the 0/100 mode (cf. Fig. 8.2a) in a similar way as for the 100/0 mode given above produces best $C_\mathrm{B}^{\mathrm{p},2}$ values that deviate from zero by at most ~ 0.001. Also for 25/75, fits of f_A versus C_B with Eq. 8.27 yield a threshold value $C_\mathrm{B}^{\mathrm{p},2}$ that cannot be distinguished from zero within statistical uncertainty. Indeed, for all examined cases containing nc jumps it was verified that f_A can be similarly well described by Eq. 8.27 when $C_\mathrm{B}^{\mathrm{p},2} = 0$ enters the fitting procedure as a fixed value. Apparently, the occurrence of $C_\mathrm{B}^{\mathrm{p},2}$ within the sc random alloy regime is a special feature of the *collinear-only* interstitialcy mode.

Tracer diffusivities and transport coefficients

Figure 8.4 displays the tracer diffusivity ratio $\widehat{D}_\mathrm{B}^\mathrm{nc}/\widehat{D}_\mathrm{A}^\mathrm{nc}$ for the purely *non-collinear* mode as a function of $w_\mathrm{B}/w_\mathrm{A}$ ranging from 1 to 5×10^5. According to Eq. 8.11 this diffusivity ratio depends on 'effective jump frequencies' (fw) containing the corresponding correlation factor (f) as multiplication variable. For all compositions, correlation leads to an attenuation of the differences in diffusivity with respect to the differences in jump frequency. For a B-rich alloy with $C_\mathrm{B} = 0.70$, this attenuation is weak, amounting to $f_\mathrm{B}^\mathrm{nc}/f_\mathrm{A}^\mathrm{nc} = 0.95$ for $w_\mathrm{B}/w_\mathrm{A} = 10^5$. For a composition just beyond the percolation threshold $C_\mathrm{B}^{\mathrm{p},1}$, i.e., $C_\mathrm{B} = 0.15$, the attenuation factor reduces to about 0.16 at the same jump frequency ratio. Nonetheless, $\widehat{D}_\mathrm{B}^\mathrm{nc}/\widehat{D}_\mathrm{A}^\mathrm{nc}$ appears to increase monotonically with $w_\mathrm{B}/w_\mathrm{A}$ for

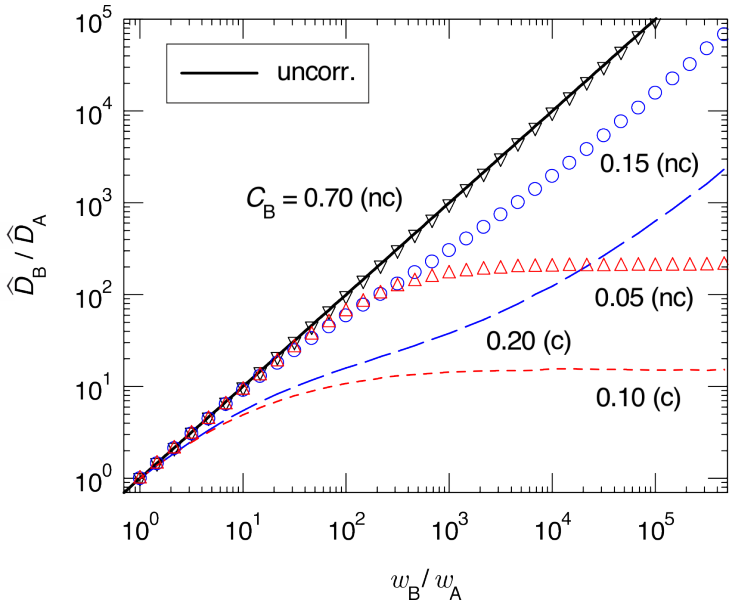

Figure 8.4.: Tracer diffusivity ratio $\widehat{D}_B/\widehat{D}_A$ as a function of jump frequency ratio w_B/w_A in a sc random binary alloy AB subject to diffusion by the interstitialcy mechanism. Symbols represent data of the non-collinear (nc) mode for the compositions $C_B = 0.70$, 0.15, and 0.05. Dashed lines reproduce data of the collinear (c) mode for the compositions $C_B = 0.20$ and 0.10 [75]. Solid line represents a hypothetical 'uncorrelated case' with $f_A = f_B = 1$, which is independent of concentration.

$C_B > C_B^{p,1}$, which agrees with similar observations for the *collinear* case [75]. Below the percolation threshold, however, $\widehat{D}_B^{nc}/\widehat{D}_A^{nc}$ converges to a maximum value when w_B/w_A becomes increasingly larger. Figure 8.4 shows that for $C_B = 0.05$ this maximum is close to 210. A similar behaviour was also found for the collinear case [75], but there the limiting value for the subthreshold concentration $C_B = 0.10$ was obtained to be as low as $\sim$ 15 (cf. solid line in Fig. 8.4). In general, it is observed that $\widehat{D}_B^{nc}/\widehat{D}_A^{nc}$ exceeds $\widehat{D}_B^{c}/\widehat{D}_A^{c}$ at the same values of w_B/w_A for comparable compositions. Thus, diffusion correlation appears to have a less strong attenuating effect on jump frequency differences when *non-collinear* jumps are compared with *collinear* ones. This can be understood from the three-fold multiplicity of the nc-exchange leading to a greater variety of diffusion pathways.

Additional insight may be obtained by examining the physical quantities directly connected with *transport* of mass and charge in a narrower sense. To this aim, Fig. 8.5 shows the transport coefficients $C_A\widehat{D}_A^{nc}$ and $C_B\widehat{D}_B^{nc}$ in comparison to $C_I D_I^{nc} = D_\sigma^{nc}$ for $w_A/w_B = 10^{-5}$. The data are plotted in dimensionless units with $w_B = C_I = a = 1$. It is seen that for all compositions transport of B atoms/ions

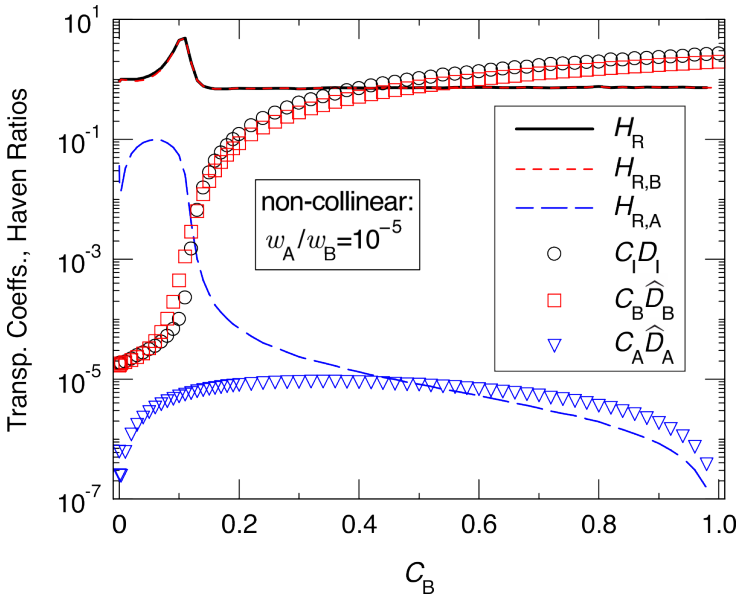

Figure 8.5.: Transport coefficients and Haven ratios in the sc random alloy AB with $w_A/w_B = 10^{-5}$ as a function of composition C_B. Symbols represent (dimensionless) transport data for the *non-collinear* case with $w_B = C_I = a = 1$, as indicated. The pertaining Haven ratios were calculated based on Eqs. 8.16 to 8.18.

is more effective than that of A atoms/ions by one to many orders of magnitude. Moreover, $C_B\widehat{D}_B^{nc}$ and $C_I D_I^{nc}$ do not greatly differ in this logarithmic plot and exhibit a similar composition dependence. These observations strongly indicate that for low values of w_A/w_B charge transport is governed by B ions, even for B-poor compositions. This finding for the nc-mode contrasts with that for the c-mode, because there it is observed (but not shown) that $C_A\widehat{D}_A^{c}$ starts to exceed $C_B\widehat{D}_B^{c}$ for compositions falling below the second-order percolation threshold $C_B^{p,2}$ [75].

Relations between mass to charge transport are usually discussed in terms of Haven ratios. Figure 8.5 shows that $H_{R,A}^{nc} \ll H_{R,B}^{nc}$ holds for all compositions, so that the overall Haven ratio H_R^{nc} virtually coincides with its B-related component $H_{R,B}^{nc}$. This is just another representation of the nc-transport picture outlined above. More interesting is the composition dependence of H_R^{nc}, which exhibits a pronounced maximum of 4.9 at $C_B = 0.11$. Specifically, H_R^{nc} adopts values greater than unity over the range $0.001 < C_B < 0.13$ which is close to and below the percolation threshold $C_B^{p,1} = 0.122$. In contrast, $H_R^{nc} < 1$ prevails for all other concentrations. For instance, near the end-member compositions H_R^{nc} results as 0.96 ($C_B \to 0$) and 0.73 ($C_B \to 1$).

It is sometimes believed that the Haven ratio should be less than unity. This is

probably true for the vacancy mechanism and only one diffusing component, but it is not necessarily the case for all diffusion mechanisms in crystalline materials [99]. LeClaire [25] has indeed shown that with cation interstitialcy exchange in AgCl and CsCl structures, H_R can reach values as large as 1.4464 and 1.8240, respectively, when specific *non-collinear* jump types are considered[4]. Now, even higher H_R values for the nc interstitialcy mechanism in a random binary sc structure are found. It can be noted that similar findings were made for the mixed c/nc modes examined (99/1, 90/10, and 25/75; not shown) but not for the c-only mode (cf. Fig. 8.11).

8.3.2. Effects of direct interstitial exchange

Tracer and partial correlation factors

Additional I-I jumps with jump frequency u_B affect diffusion correlation in an otherwise *collinear* interstitialcy mode. In Fig. 8.6a, this is illustrated for f_A in the case when w_A/w_B equals 10^{-5} and for $u_B/w_B = 3 \times 10^{-6}$ and 3×10^{-2}. In the composition domain well above the percolation threshold of the reference mode ($u_B/w_B = 0$, dashed line in Fig. 8.6a), the influence tends to be very minor. Indeed, all three data plots converge to $f_A = 1$ for $C_B \to 1$ (note the truncation of the concentration axis at $C_B = 0.41$). However, appreciable increases of f_A are observed in the B-poor region below about $C_B^{p,1} = 0.122$. Apparently, the f_A minimum, originally located at $C_B \approx 0.02$ shifts to lower B concentrations (0.001-0.003). For $C_B \to 0$, f_A consistently attains the value $\frac{6}{7}$ for self-diffusion in a pure sc lattice [105].

Figure 8.6b shows the even more drastic effects of u_B on f_B for $w_A/w_B = 10^{-5}$. Also in this case, substantial changes of the correlation factor are confined to compositions being poor in B. It is seen that f_B monotonically increases with u_B/w_B increasing from 3×10^{-6} to 3×10^{-2}. Furthermore, the two-step character of the collinear reference data ($u_B/w_B = 0$, dashed line in Fig. 8.6b) fully disappears yet for the smallest u_B value in the simulations. Instead, a single broad minimum evolves, which at the B-poor side is bounded by a steep rise up to $f_B = 0.98$ for the lowest C_B value (0.0003) and the two highest u_B values.

Some deeper insight into correlation effects may be gained by inspecting individual PCFs (cf. Sect. 8.2). In fact, $\tilde{f}_B^c$ and $\tilde{f}_B^i$ were extracted from the simulations with

[4] In the terminology of LeClaire [25], the present collinear and non-collinear jumps are denoted as *direct* and *indirect* interstitialcy jumps

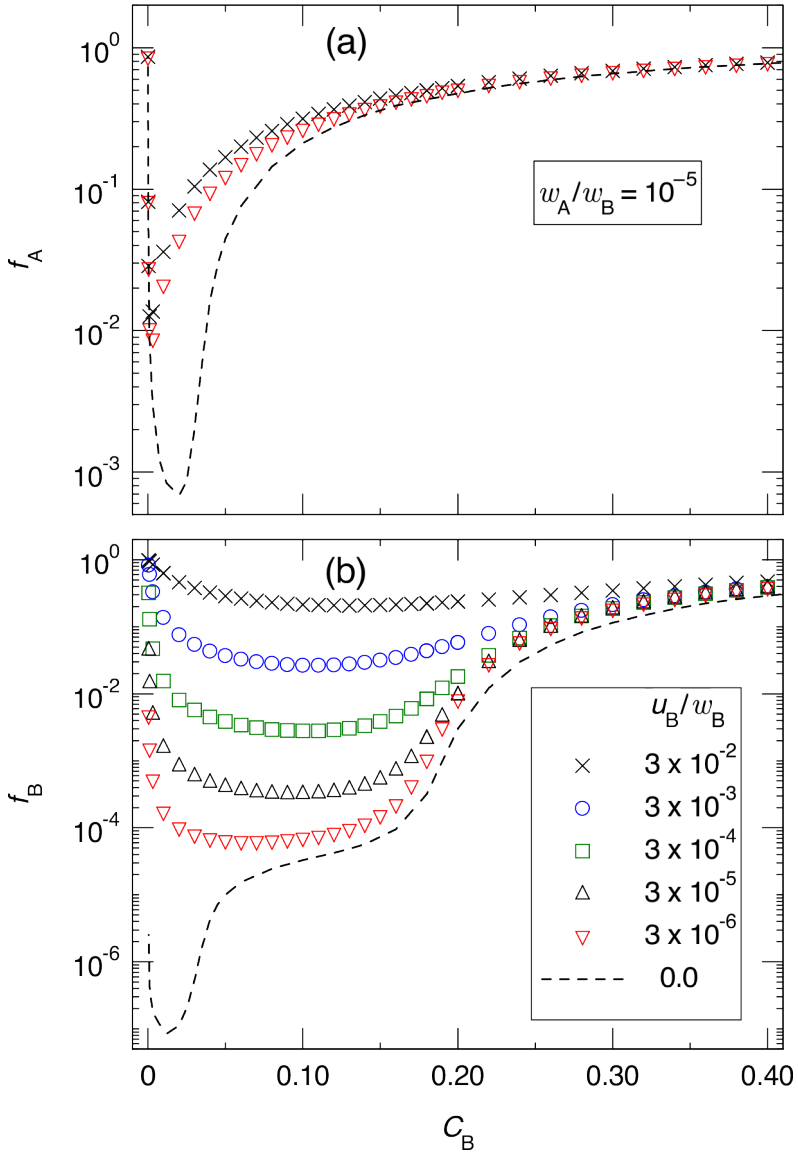

Figure 8.6.: Tracer correlation factors f_A (a) and f_B (b) for diffusion by the interstitialcy mechanism in a sc random alloy AB with $w_A/w_B = 10^{-5}$ as a function of composition $C_B \leq 0.4$. Data pertain to the *collinear* interstitialcy mode in conjunction with *direct interstitial* jumps of B atoms of varying frequency u_B, as indicated. The reference case $u_B = 0$ (dashed lines) was taken from Chapter 7.

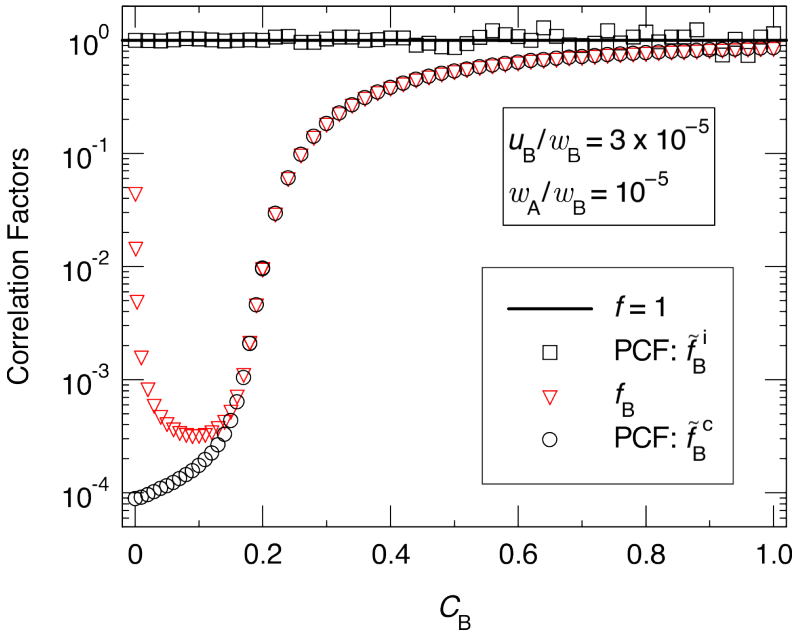

Figure 8.7.: Correlation factors for diffusion in a sc random alloy AB as a function of composition C_B demonstrating the contribution of PCFs ($\tilde{f}_B^c$, $\tilde{f}_B^i$) to the total correlation factor (f_B) based on Eq. 8.26. Data pertain to the *collinear* interstitialcy mechanism (c) with $w_A/w_B = 10^{-5}$ in conjunction with *direct interstitial* jumps of B atoms (i) with $u_B/w_B = 3 \times 10^{-5}$, as indicated.

$w_A/w_B = 10^{-5}$ and $u_B/w_B = 3 \times 10^{-5}$. Figure 8.7 shows that $\tilde{f}_B^i = 1$ holds within statistical error for all compositions. This complies with the notion that I-I jumps take place with equal probability in the six directions along the principal axes of the sc lattice. On the other hand, the partial correlation factor $\tilde{f}_B^c$ (circles) exhibits a distinct composition dependence, which for $C_B > 0.1885$ virtually coincides with f_B (crosses). This overall correlation factor was calculated by a weighted sum of the PCFs according to Eq. 8.26. What may be learned from Fig. 8.7 is the circumstance that additional I-I jumps with $w_A < u_B \ll w_B$ have significant influence on B diffusion only for compositions below or near the *collinear* percolation threshold. This influence may even become predominant for very low B concentrations, as indicated by the steep increase of f_B for $C_B < 0.02$ towards $\tilde{f}_B^i$.

Percolation behaviour

Whereas diffusion via the (collinear) interstitialcy mechanism in a binary random alloy is greatly affected by percolation, direct interstitial diffusion is not. This relates to the fact that the interstices are virtually empty, so that mobile B_I

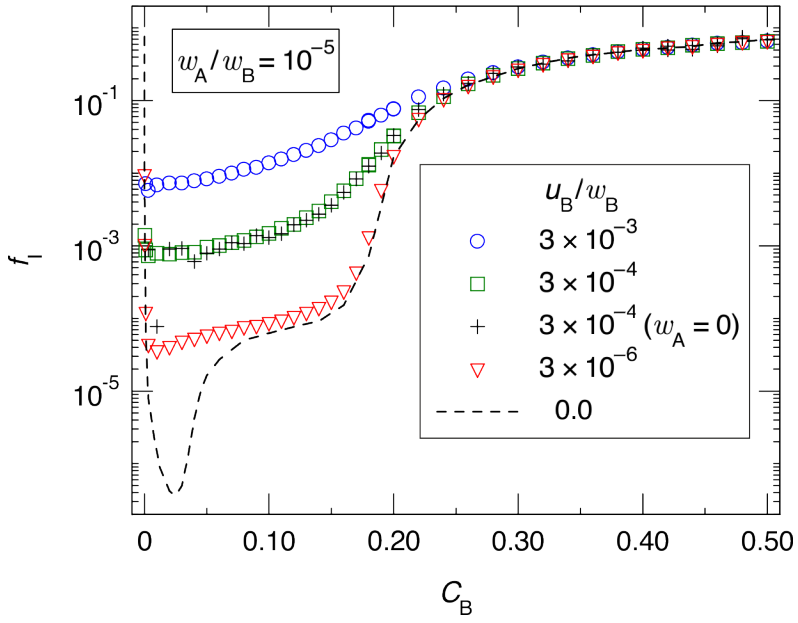

Figure 8.8.: Interstitialcy correlation factors f_I for diffusion by the interstitialcy mechanism in a sc random alloy AB as a function of composition $C_B \leq 0.5$. Data pertain to the *collinear* interstitialcy mode with $w_A/w_B = 10^{-5}$ or $w_A/w_B = 0$ in conjunction with *direct interstitial* jumps of B atoms of varying frequency u_B, as indicated. The reference case $u_B = 0$ (dashed lines) was taken from Chapter 7.

atoms cannot be blocked by immobile A atoms. Therefore, when combining the two mechanisms it may be expected that the strict percolation threshold pertaining to the collinear IS/SI diffusion component ($C_B^{p,1} = 0.1885$) will be bypassed through I-I jumps of the B atoms. This is exactly the picture emerging from the f_I plots in Fig. 8.8.

As argued before [21, 75], diffusion percolation behaviour in the present case is reflected by the composition dependence of f_I for extreme differences in the mobility of A and B atoms. Such plots are displayed in Fig. 8.8 for $w_A/w_B = 10^{-5}$ and different values of u_B/w_B ranging from 0 to 3×10^{-3}. In all cases with $u_B \neq 0$, the second-order threshold (related to A_S-B_S chains) close to the f_I global minimum for the pure IS/SI case ($u_B = 0$) has disappeared. However, the impact of the first threshold $C_B^{p,1} = 0.1885$ (related to $B_S - B_S$ chains) is still strong for low u_B values but becomes weaker for higher ones. In particular, the following observations seem to be important: (i) For B-poor alloys, f_I monotonically increases with increasing u_B suggesting the significant role of I-I jumps in this concentration region. (ii) (Pseudo-)percolation thresholds evaluated from the (steep) decrease of f_I in appropriate

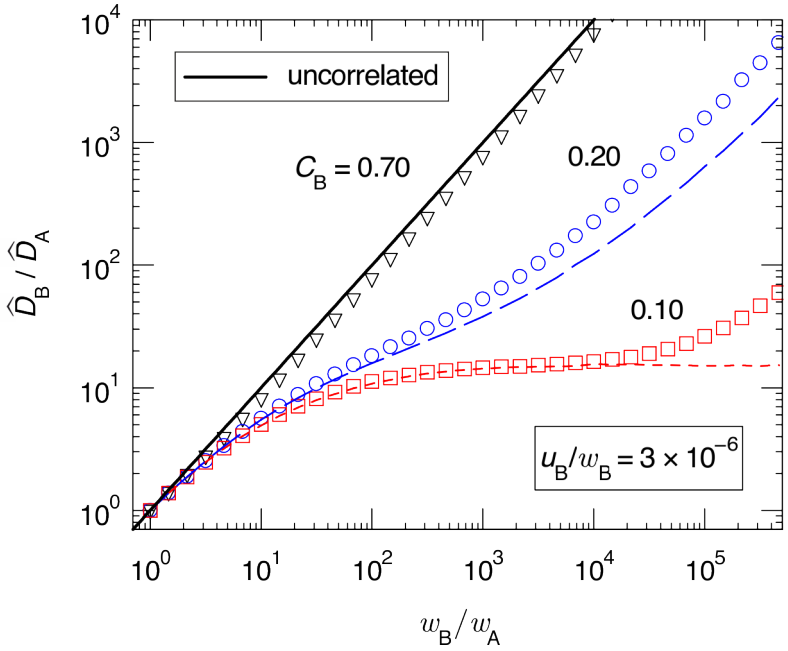

Figure 8.9.: Tracer diffusivity ratio $\hat{D}_B/\hat{D}_A$ as a function of jump frequency ratio w_B/w_A in a sc random binary alloy AB simultaneously subject to diffusion by the *collinear* interstitialcy mechanism and to B diffusion by *direct interstitial* jumps with $u_B/w_B = 3 \times 10^{-6}$. Symbols represent data for the compositions $C_B = 0.70$, 0.20, and 0.10, as indicated. Dashed lines reproduce data of the collinear interstitialcy mode ($u_B = 0$) for the compositions $C_B = 0.20$ and 0.10 (see Chapter 7). Solid line represents a hypothetical 'uncorrelated case' with $f_A = f_B = 1$, which is independent of concentration.

composition ranges (cf. Eq. 8.27 and Fig. 8.4) are compatible with $C_B^{p,1} = 0.1885$ for $u_B = 0$ within the pertaining error bounds. (iii) A direct f_I comparison for $u_B/w_B = 3 \times 10^{-4}$ between $w_A/w_B = 10^{-5}$ (triangles) and $w_A/w_B = 0$ (crosses) in Fig. 8.8 shows virtually no difference. Thus, percolation is given despite the immobility of A atoms. Altogether, it may be concluded that the percolation behaviour can be well understood based on the individual characteristics of the combined diffusion mechanisms.

Tracer diffusivities and transport coefficients

Figure 8.9 reveals the changes to $\widehat{D}_B/\widehat{D}_A$ of a collinear interstitialcy mechanism caused by taking into account I-I jumps of low frequency. Specifically, $\widehat{D}_B/\widehat{D}_A$ is plotted as a function of w_B/w_A for a fixed value of $u_B/w_B = 3 \times 10^{-6}$ and for three different compositions. For B-rich compositions, e.g. $C_B = 0.70$, the effect is negligibly small. For compositions well below the I-S/S-I percolation threshold,

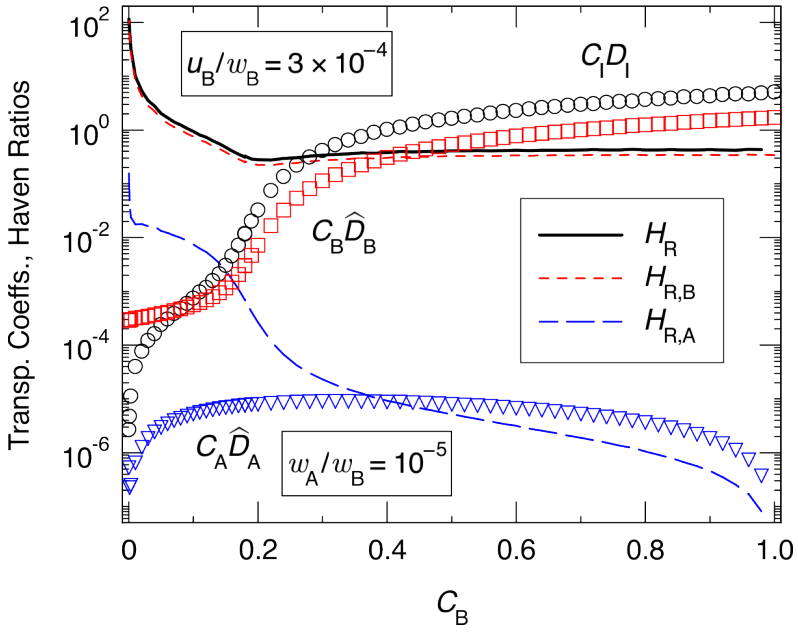

Figure 8.10.: Transport coefficients and Haven ratios in the sc random alloy AB as a function of composition C_B. Symbols represent (dimensionless) transport data (setting $w_B = C_I = a = 1$) for the *collinear* case with $w_A/w_B = 10^{-5}$ in conjunction with *direct interstitial* jumps of B atoms with $u_B/w_B = 3 \times 10^{-4}$, as indicated. The pertaining Haven ratios were calculated based on Eqs. 8.16 to 8.18.

e.g., $C_B = 0.10$, a distinct increase of $\widehat{D}_B/\widehat{D}_A$ is visible for $w_B/w_A > 10^4$. For a composition just above the I-S/S-I percolation threshold, e.g., $C_B = 0.20$, the impact of I-I jumps becomes already manifest for $w_B/w_A \approx 10^2$, reaching $\widehat{D}_B/\widehat{D}_A$ enhancement factors of ~ 3 for much higher jump frequency ratios. According to Eq. 8.22 the changes observed for $\widehat{D}_B/\widehat{D}_A$ in Fig. 8.9 must be essentially due to correlations effects, because $u_B/\bar{w} \ll 1$ is small for all cases displayed. Indeed, further examination for $C_B = 0.20$ reveals (not shown here) that $f_B^{c,i}/f_B$ is distinctly larger than $f_A^{c,i}/f_A$, which is only slightly greater than unity for all w_B/w_A. Here f_A and f_B refer to the mere *collinear* case ($u_B = 0$).

Transport coefficients and Haven ratios for $w_A/w_B = 10^{-5}$ and $u_B/w_B = 3 \times 10^{-4}$ are displayed in Fig. 8.10 by setting $w_B = C_I = a = 1$. It is found that $C_B \widehat{D}_B^{c,i} \gg C_A \widehat{D}_A^{c,i}$ for all compositions. To be specific, B transport exceeds A transport by at least two orders of magnitude, even for alloys poor in B. Moreover, charge transport represented by $C_I D_I^{c,i}$ is larger than $C_B \widehat{D}_B^{c,i}$ by a factor of 3 for B-rich systems. However, upon going to low B contents $C_I D_I^{c,i}$ starts to fall below $C_B \widehat{D}_B^{c,i}$ at $C_B \approx 0.08$, thereby approaching $C_A \widehat{D}_A^{c,i}$ for $C_B \to 0$. This behaviour is

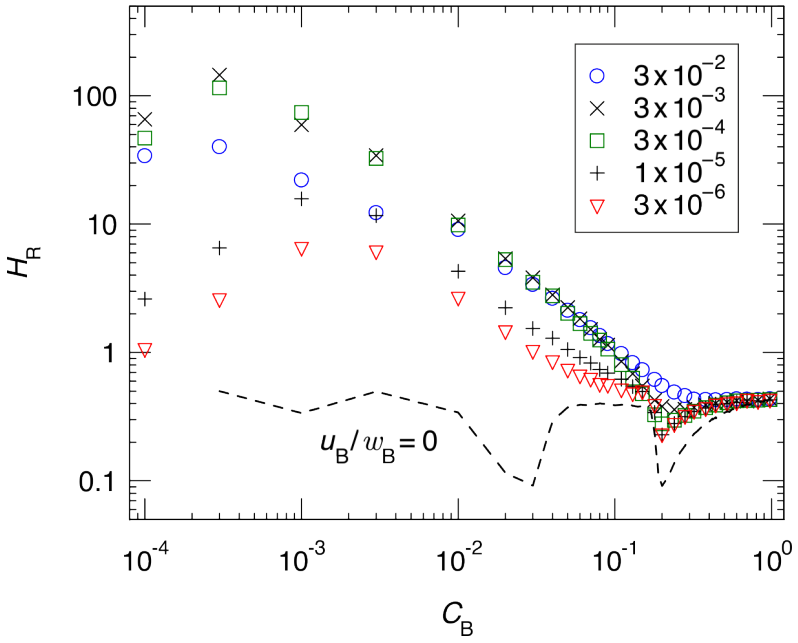

Figure 8.11.: Haven ratios H_R for diffusion in a sc random alloy AB as a function of composition C_B. Data pertain to the *collinear* interstitialcy mode with $w_A/w_B = 10^{-5}$ in conjunction with *direct interstitial* jumps of B atoms of varying frequency u_B, as indicated. For clarity, the number of data points at the right-hand side has been reduced.

also reflected by the partial and overall Haven ratios depicted in Fig. 8.10. In the B-rich region, $H_R^{c,i}$ converges to the theoretical value 0.4286 holding for the collinear case ($u_B = 0$) [75]. For C_B getting lower than 0.1, $H_R^{c,i}$ exceeds its common limit of 1.0 and increases up to 115 for the lowest composition investigated, i.e., at $C_B = 0.0003$.

Figure 8.11 presents in a double-logarithmic form an expansion of the $H_R^{c,i}$ results for the B-poor domain. Apart from the case depicted in Fig. 8.10, the composition dependence for $u_B/w_B = 0$, 3×10^{-6}, and 3×10^{-2} is depicted. The plots indicate that $H_R^{c,i}$ passes through a *maximum* clearly larger than unity in all simulations with $u_B > 0$. Here, the location and height of the maximum appear to shift systematically with the u_B value. However, the observed behaviour is not monotonic but exhibits a reversal. However, the Haven ratio *minimum* close to $C_B = 0.20$ gradually disappears with increasing u_B. Thus, the introduction of I-I jumps has a substantial impact on transport coefficients and Haven ratios in B-poor alloys.

It can be noted that the range of extremely low B concentrations has not been sufficiently explored in this study. Letting $C_B \to 0$ entails the transition across the kick-out diffusion regime, in which B_S exceeds B_I and A_I in terms

of solubility ($C_{\mathrm{B,S}} \gg C_{\mathrm{B,I}}, C_{\mathrm{A,I}}$) and $\mathrm{B_I}$ dominates over $\mathrm{A_I}$ in terms of transport capacity ($C_{\mathrm{B,I}} D_{\mathrm{B,I}} \gg C_{\mathrm{A,I}} D_{\mathrm{A,I}}$) [113, 100]. Within the present formalism, the latter requirement (with $C_{\mathrm{A,I}} D_{\mathrm{A,I}} \approx C_{\mathrm{I}} D_{\mathrm{I}}$ for C_{B} sufficiently small) can be expressed as $C^{\mathrm{eq}}_{\mathrm{B,S}} w_{\mathrm{B}} u_{\mathrm{B}} / (2w_{\mathrm{A}})^2 \gg 1$, where $C^{\mathrm{eq}}_{\mathrm{B,S}}$ is the $\mathrm{B_S}$ impurity concentration settled at the surface under the prevailing diffusion conditions. Upon B tracer diffusion into a virtually perfect (sink-free) crystal of pure A, these conditions may give rise to an depth-dependent $\mathrm{A_I}$ supersaturation, which can be recognised by penetration profiles of particular shape [114, 19].

8.4. Summary and conclusions

In this chapter, the effects of additional atomic jump types on diffusion by *collinear* interstitialcy exchange in a simple cubic random binary alloy AB were studied by Monte Carlo simulation. The considered jump types were either *non-collinear* interstitialcy jumps which partly or totally replaced the collinear ones or supplementary *direct interstitial* jumps of the *more mobile* B atoms. It was shown that in both cases pronounced changes to the collinear reference model occurred for B-poor alloys, i.e., with B concentrations near and below the (collinear) site-percolation threshold ($C_{\mathrm{B}}^{\mathrm{p},1} = 0.1885$) related to B-B chains.

A basic observation was the reduction of diffusion correlation effects, as revealed by the strong increase of the tracer correlation factor for B atoms, which exceeded a corresponding but smaller increase for A atoms. Consequently, the tracer diffusivity ratio $\widehat{D}_{\mathrm{B}}/\widehat{D}_{\mathrm{A}}$ increased for either added jump type under consideration. Nonetheless, at compositions poor in B this ratio converged to a maximum value ($\ll w_{\mathrm{B}}/w_{\mathrm{A}}$) for increasing jump frequency ratios $w_{\mathrm{B}}/w_{\mathrm{A}} \gg 1$.

Addition of either jump type caused the disappearance of second-order percolation threshold that relates to the occurrence of uninterrupted A-B chains ($C_{\mathrm{B}}^{\mathrm{p},2} = 0.0375$). Moreover, replacement of *collinear* by *non-collinear* jumps shifts $C_{\mathrm{B}}^{\mathrm{p},1}$ to lower values, where the partly replacement has an even stronger effect than the total one. By contrast, the superposition of *direct interstitial* jumps circumvents the strict B-B percolation threshold of the *collinear* model when A atoms are totally immobile.

Mass and charge transport coefficients were calculated and compared with each other by deducing Haven ratios. It was found that highly mobile B atoms dominate over lowly mobile A atoms in terms of mass transport over the whole composition

range. Remarkably, both extensions of the *collinear* model, either by *non-collinear* or *direct interstitial* jumps, lead to overall Haven ratios distinctly larger than unity in certain ranges of low B concentration.

Although this study pertains to a random binary alloy of simple cubic structure the major results obtained may be exemplary for multi-component crystalline materials in which diffusion by the interstitialcy mechanism plays a prominent role. More specifically, the experimental tracer diffusion results for Na and K in VF feldspar (cf. Chapters 3 and 4) may be interpreted by a similar mechanism because the largely different diffusivities comply, e.g., with a percolation threshold $C_{\mathrm{B}}^{\mathrm{p},1} = 0.122$ of the sc non-collinear-only case. The associated Haven ratio was found to be $H_{\mathrm{R}} \sim 0.7$ in the near to VF composition regime which is smaller than unity but significantly larger than the experimentally observed values ranging from $H_{\mathrm{R}} = 0.11$ to 0.40 normal to (001). It will therefore be an essential demand for a microscopic diffusion model for alkali feldspar to feature small values of H_{R} as well as a percolation threshold at a close to K end-member composition. In the following Chapter 9, it will be demonstrated that these effects may not be expressed in the framework of a randomly ordered sublattice model but rather by considering an effective short-range interaction energy between the cations. This expansion of the present interstitialcy diffusion model will be successfully transferred to the more complex monoclinic feldspar structure.

9. Monte Carlo simulation of diffusion and ionic conductivity on the Na-K sublattice of alkali feldspar via the interstitialcy mechanism

The discussion about the main diffusion mechanism of alkali atoms in alkali feldspar has been focused over the last decades on the analysis of experimental data on a macroscopic scale from self-diffusion and ionic conductivity [7, 8, 9, 17, 66, 67]. So far, only Jones et al. [54] studied jump barriers for the vacancy diffusion mechanism within the (010) plane of albite and K-feldspar via molecular dynamics methods and found good agreement with data from dielectric spectroscopy. Inherent features of long-range diffusion stay, however, unconsidered in their study. On the one hand, long-range diffusion in feldspar via the vacancy mechanism relies on the contribution from different jump types (see Chapter 6 and [83]). On the other hand, correlation effects in binary or multicomponent alloys may strongly affect diffusion coefficients if the migration of one component is hampered by site-blocking effects (see Chapter 7 and [75]). The analysis of correlation effects is therefore a promising approach to elucidate a microscopic model of diffusion, which was presented in Chapter 6 for a vacancy type of mechanism.

The correlation effects in binary alloys via the interstitialcy diffusion mechanism were presented in Chapter 7 and 8 for the simple cubic (sc) structure. This pathbreaking work demonstrates that the existence of a percolation threshold for the interstitialcy mechanism in the sc reference structure complies with experimental data on tracer diffusion in feldspar (see Chapter 3). An interstitialcy type of mechanism therefore seems to be the most promising candidate to act as

predominating mechanism for Na and/or K diffusion. In the present chapter, the concepts and methods to compute the correlation factors by Monte Carlo (MC) simulations will be transferred to a more complex monoclinic structure of feldspar. Having measured ionic conductivity and self-diffusion the experimental values for the Haven ratio normal to (001) were determined, i.e., H_{R} ranges from 0.11 to 0.40 (see Chapter 5). The lower limit obtained for H_{R} disagrees with the computed numerical values for collinear and non-collinear diffusion in the sc reference structure (cf. Chapters 7 and 8). An essential demand for the present interstitialcy diffusion model therefore is to reflect these numerical values within experimental uncertainties. One approach will be the extension of the regular I-S interstitialcy scheme by I-S-S double interstitialcy jump types. Almost collinear chains of one interstitial and two substitutional atoms enhance the ionic conductivity, which implies a reduction of the numerical value for H_{R}. A second approach comprises the analysis of short-range ordering effects on the sublattice of feldspar. An abundance of studies concerning correlation factors in binary or ternary alloys with long- and short-range order exists [115, 116, 117, 97, 118, 93, 119] and similar concepts will be used to analyse the correlation effects on the sublattice of feldspar as a function of the interaction energy. It will be shown that both extensions are essential features of the present interstitialcy diffusion model in order to successfully link the computed diffusivities with the experimental data on self-diffusion and ionic conductivity from previous studies.

9.1. Theoretical background

9.1.1. Random alloy model for diffusion via self-interstitials

Starting point of the present approach is once again Manning's random alloy model [14, 45] that proved to be useful for the analysis of correlation effects in the simple cubic structure (cf. Chapters 6, 7 and 8). In a hypothetical binary alloy AB short- and long-range interactions between the atoms are neglected, which implies the absence of ordering effects and thus, a purely statistical distribution of A and B atoms over the lattice sites. Only one type of point defect is considered, i.e., the interstitial defect I. Interstitials of type A and B, however, have to be distinguished that are denoted as $\mathrm{A_I}$ and $\mathrm{B_I}$, respectively. Both may act as diffusion vehicles for the surrounding nearest-neighbour substitutional atoms. In general,

jump frequencies for A_I and B_I jumps can be different and, e.g., for an exchange with a substitutional A_S atom are denoted as w_{AA} and w_{BA}, respectively. The difference between w_{AA} and w_{BA} has, however, not been quantified by, e.g., molecular dynamics calculations so far. The most basic assumption of equal jump frequencies for A_I and B_I is therefore considered and the elementary jump frequencies are only determined by the type of substitutional atom A_S or B_S. Accordingly, two different I-S exchange rates w_A and w_B exist. The concentration of point defects is supposed to be low ($C_I \ll 1$), which implies that interactions between the defects can be neglected and the alloy is characterized by its composition $C_A = 1 - C_B$.
The interstitialcy diffusion mechanism may be described in terms of quasichemical reactions

$$\widehat{A}_I + A_S \rightleftharpoons \widehat{A}_S + A_I \tag{9.1}$$

and

$$\widehat{A}_I + B_S \rightleftharpoons \widehat{A}_S + B_I\,, \tag{9.2}$$

where $\widehat{A}_S$ and $\widehat{A}_I$ relate to tracer atoms[1]. A precondition for these reactions is that the substitutional atom is in direct proximity to the interstitial atom. In analogy to Eqs. 9.1 and 9.2 similar relations for the B component hold. In Eq. 9.1, the exchange rate for both forward and reverse reaction is w_A. In contrast, the type of S atom is altered in Eq. 9.2 and the forward and reverse exchange rates have to be distinguished, i.e., w_B and w_A, respectively.
The so called stoichiometric coefficient η_A of component A (and η_B of component B) can be introduced to classify quasichemical reactions. This coefficient is positive if, globally, the species is produced and negative if the species is consumed. Non-zero values for η_A and η_B occur for the reaction given in Eq. 9.2, which implies that the concentrations of interstitial A atoms, $C_{A,I}$ (site fraction), and interstitial B atoms, $C_{B,I}$, are controlled by the related forward and reverse exchange rates. In thermal equilibrium and based on Eq. 9.2 mass action law predicts

$$\frac{r_A}{r_B} = \frac{C_{A,I}}{C_{B,I}} = \frac{C_A w_A}{C_B w_B}\,, \tag{9.3}$$

[1]To reduce the number of indices, the common asterisk for labelling tracer diffusivity (D^*) has been replaced by the 'hat' symbol ($\widehat{D}$) throughout this work.

where r_A designates the normalised or relative concentration of A-type interstitials, i.e.,

$$r_\mathrm{A} = \frac{C_\mathrm{A,I}}{C_\mathrm{A,I} + C_\mathrm{B,I}} = \frac{C_\mathrm{A,I}}{C_\mathrm{I}} = 1 - r_\mathrm{B} \,. \tag{9.4}$$

Another useful expression for r_A – also denoted as the probability that a 'generalised interstitial defect' I with concentration $C_\mathrm{I} = C_\mathrm{A,I} + C_\mathrm{B,I}$ is of type $\mathrm{A_I}$ – is

$$r_\mathrm{A} = \frac{C_\mathrm{A} w_\mathrm{A}}{C_\mathrm{A} w_\mathrm{A} + C_\mathrm{B} w_\mathrm{B}} \,. \tag{9.5}$$

It is straightforward to show that $C_\mathrm{A,I}$ and $C_\mathrm{B,I}$ can be expressed in terms of the total concentration of interstitials as

$$C_\mathrm{A,I} = r_\mathrm{A} C_\mathrm{I} \,, \quad C_\mathrm{B,I} = r_\mathrm{B} C_\mathrm{I} \,. \tag{9.6}$$

9.1.2. Interstitialcy diffusion in alkali feldspar along the *b*-axis

Correlation effects for diffusion on the monoclinic sublattice of alkali feldspar are analysed in the present study. For non-cubic systems correlation effects are generally non-isotropic and projections of diffusivities and correlation factors to a direction of particular interest are therefore discussed. The *b*-axis, i.e., in the direction normal to (010) shows a two-fold symmetry and is one of the principal axes of diffusion in monoclinic feldspar. A schematic view of the *b*-*c*-plane is given in Fig. 9.1 where displacements of the substitutional atoms along the *a*-axis are not considered. As illustrated in the figure, the interstitial sites are located at $\left(0, 0, \frac{1}{2}\right)$ and equivalent positions [7]. An interstitial defect may jump to four substitutional sites via I-S exchange as far as only jumps with a non-zero displacement along the *b*-axis are considered. In an exemplary elementary jump step (see Fig. 9.1) the interstitial atom $\mathrm{A_I}$ jumps to a neighbouring site 'a' along a trajectory l_7. The substitutional atom $\mathrm{A_S}$ that is initially located at 'a' simultaneously jumps to an empty interstitial site 'b' along l_8 and adopts the role of $\mathrm{A_I}$. In total, $z_b = 4$ paths for the same geometrical type of non-collinear I-S jump are found with the projected length of the jump vectors l_7 and l_8 to the *b*-axis given by l_b.

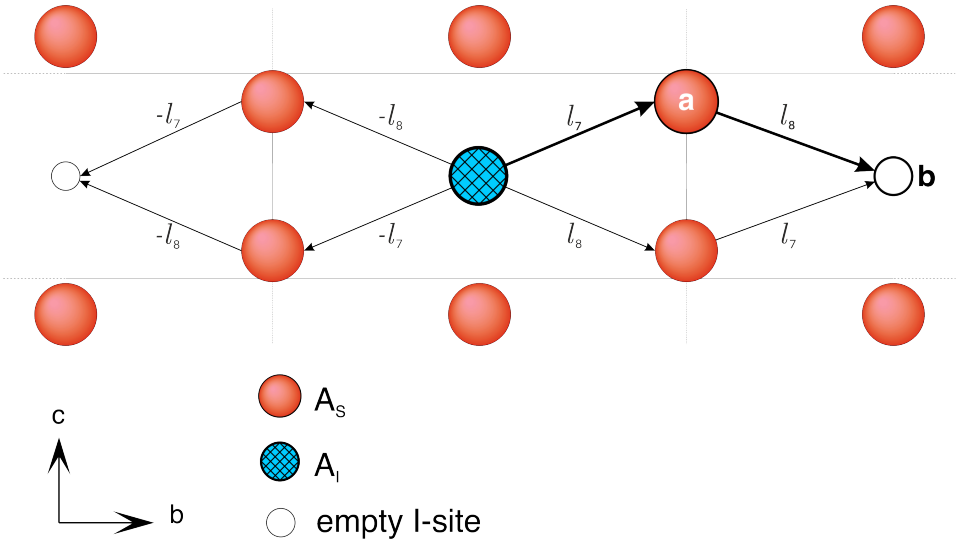

Figure 9.1.: Schematic view of the *b*-*c*-plane in alkali feldspar according to Phillips and Ribbe [120]. For clarity, only atoms of the alkali sublattice are illustrated (solid circles) together with empty interstitial sites (open circles). One central interstitial atom (crosshatched circle) jumps via the interstitialcy mechanism to a substitutional site 'a' along a trajectory l, as indicated. In turn, the atom initially located at 'a' jumps to an empty interstitial site 'b'.

Tracer and interstitialcy diffusion coefficients

The formalism for a hypothetical alloy AB is now transferred to the specific problem of a Na-K sublattice in alkali feldspar with K ≡ A and Na ≡ B. The tracer diffusion coefficient of Na atoms is then given by

$$\widehat{D}_{\mathrm{Na},b} = \lim_{t\to\infty} \frac{\langle X^2_{\mathrm{Na}} \rangle}{2t} = f_{\mathrm{Na},b} \frac{\langle X^2_{\mathrm{Na}} \rangle_{\mathrm{uncorr}}}{2t} \,, \tag{9.7}$$

where t is a sufficiently long time and $\langle X^2_{\mathrm{Na}} \rangle$ denotes the mean square displacement in b-direction within this time. By introducing the (hypothetical) *uncorrelated* mean square displacement on the right-hand side of this equation the tracer correlation factor $f_{\mathrm{Na},b}$ is implicitly defined, which accounts for a correlated motion of subsequent jumps of the same atom. The mean square displacement of Na atoms may be decomposed into the numbers of events involving interstitialcy jumps of two Na atoms, $n_{\mathrm{Na,Na}}$, and into those jumps comprising a Na and a K atom, $n_{\mathrm{Na,K}}$.

Taking advantage of the fact that all projected jump vectors to the b-axis are of equal length l_b the resulting expression is

$$\begin{aligned}\langle X^2_{\mathrm{Na}}\rangle_{\mathrm{uncorr}} &= \langle n_{\mathrm{Na,Na}} + n_{\mathrm{Na,K}}\rangle l_b^2 \\ &= \langle (n^{\mathrm{IS}}_{\mathrm{Na,Na}} + n^{\mathrm{SI}}_{\mathrm{Na,Na}}) + (n^{\mathrm{IS}}_{\mathrm{Na,K}} + n^{\mathrm{SI}}_{\mathrm{Na,K}})\rangle l_b^2 \,. \end{aligned} \tag{9.8}$$

In this equation, $n_{\mathrm{Na,Na}}$ for example is further decomposed into the numbers of $\widehat{\mathrm{Na}}_{\mathrm{I}} + \mathrm{Na}_{\mathrm{S}}$ and $\widehat{\mathrm{Na}}_{\mathrm{S}} + \mathrm{Na}_{\mathrm{I}}$ interstitialcy events, i.e., $n^{\mathrm{IS}}_{\mathrm{Na,Na}}$ and $n^{\mathrm{SI}}_{\mathrm{Na,Na}}$, respectively, and $\langle\ \rangle$ brackets indicate the ensemble average.
Taking a single tracer atom $\widehat{\mathrm{Na}}$ into account it is obvious that during a long sequence of jumps both I and S sites will be occupied. The probabilities $p_{\mathrm{Na,I}}$ and $p_{\mathrm{Na,S}}$ to be at interstitial and substitutional sites, respectively, differ from each other and are given by

$$p_{\mathrm{Na,I}} = \frac{C_{\mathrm{Na,I}}}{C_{\mathrm{Na,I}} + C_{\mathrm{Na,S}}} \approx \frac{C_{\mathrm{Na,I}}}{C_{\mathrm{Na}}}\,, \tag{9.9}$$

whereas

$$p_{\mathrm{Na,S}} = 1 - p_{\mathrm{Na,I}} \approx 1\,. \tag{9.10}$$

These equations take advantage of the concept of very low defect concentrations ($C_{\mathrm{I}} \ll 1$), which implies that the quantities $C_{\mathrm{Na,S}}$ and $C_{\mathrm{K,S}}$ are virtually equal to C_{Na} and C_{K}, respectively and $C_{\mathrm{Na,I}} \ll C_{\mathrm{Na,S}}$ holds to a very good approximation. Combining the relations $C_{\mathrm{K,I}} = r_{\mathrm{K}} C_{\mathrm{I}}$ and $C_{\mathrm{Na,I}} = r_{\mathrm{Na}} C_{\mathrm{I}}$ (cf. Eq. 9.6) together with Eq. 9.3 and the quantities introduced above gives the formal solution

$$\begin{aligned}\langle n^{\mathrm{IS}}_{\mathrm{Na,Na}}\rangle/t &= p_{\mathrm{Na,I}} C_{\mathrm{Na}} w_{\mathrm{Na}} z_b = r_{\mathrm{Na}} w_{\mathrm{Na}} z_b C_{\mathrm{I}} \\ \langle n^{\mathrm{SI}}_{\mathrm{Na,Na}}\rangle/t &= p_{\mathrm{Na,S}} C_{\mathrm{Na,I}} w_{\mathrm{Na}} z_b = r_{\mathrm{Na}} w_{\mathrm{Na}} z_b C_{\mathrm{I}} \\ \langle n^{\mathrm{IS}}_{\mathrm{Na,K}}\rangle/t &= p_{\mathrm{Na,I}} C_{\mathrm{K}} w_{\mathrm{K}} z_b = r_{\mathrm{K}} w_{\mathrm{Na}} z_b C_{\mathrm{I}} \\ \langle n^{\mathrm{SI}}_{\mathrm{Na,K}}\rangle/t &= p_{\mathrm{Na,S}} C_{\mathrm{K,I}} w_{\mathrm{Na}} z_b = r_{\mathrm{K}} w_{\mathrm{Na}} z_b C_{\mathrm{I}}\,. \end{aligned} \tag{9.11}$$

With $r_{\mathrm{K}} + r_{\mathrm{Na}} = 1$ and with the aid of Eqs. 9.7, 9.8 and 9.11 the diffusivity $\widehat{D}_{\mathrm{Na},b}$ is given by

$$\begin{aligned}\widehat{D}_{\mathrm{Na},b} &= \tfrac{1}{2} f_{\mathrm{Na},b}\, 2 w_{\mathrm{Na}} z_b C_{\mathrm{I}} l_b^2 \\ &= 4 f_{\mathrm{Na},b}\, w_{\mathrm{Na}} C_{\mathrm{I}} l_b^2\,. \end{aligned} \tag{9.12}$$

In analogy to the above equation it is now straightforward to derive an expression for the diffusion coefficient of the K component, i.e.,

$$\begin{aligned} \widehat{D}_{\mathrm{K},b} &= \tfrac{1}{2} f_{\mathrm{K},b}\, 2 w_{\mathrm{K}} z_b C_{\mathrm{I}} l_b^2 \\ &= 4 f_{\mathrm{K},b}\, w_{\mathrm{K}} C_{\mathrm{I}} l_b^2 \,. \end{aligned} \tag{9.13}$$

A crucial quantity for a quantitative comparison of the tracer diffusion coefficient with the ionic conductivity is the interstitialcy diffusivity D_{I} [76]. Interstitial atoms as well as substitutional atoms of the alkali sublattice carry an effective charge that is independent of the type of cation Na^+ or K^+. In terms of 'generalised monovalent interstitials' I the conductivity can be expressed according to the Nernst-Einstein relation as [108, 75]

$$\sigma = \frac{e^2}{k_{\mathrm{B}} T} N_{\mathrm{I}} D_{\mathrm{I}} = \frac{e^2 N_0}{k_{\mathrm{B}} T} C_{\mathrm{I}} D_{\mathrm{I}} \,, \tag{9.14}$$

where e is the electronic charge, N_{I} is the volume concentration of interstitials (number density), k_{B} is the Boltzmann constant, and N_0 denotes the volume concentration of interstitial sites. It should be noted that the Nernst-Einstein equation holds for non-interacting charge carriers, which is fulfilled by the very low I concentrations ($C_{\mathrm{I}} \ll 1$) considered in the present model.
Using the formalism and similar concepts as for the tracer diffusion coefficients derived above D_{I} can be expressed as

$$D_{\mathrm{I},b} = \tfrac{1}{2} f_{\mathrm{I},b}\, 4 w_{\mathrm{I}} z_b l_b^2 = 8 f_{\mathrm{I},b} w_{\mathrm{I}} l_b^2 \,, \tag{9.15}$$

where $f_{\mathrm{I},b}$ is the interstitialcy correlation factor and w_{I} is the mean interstitial jump frequency given by

$$w_{\mathrm{I}} = C_{\mathrm{Na}} w_{\mathrm{Na}} + C_{\mathrm{K}} w_{\mathrm{K}} \,. \tag{9.16}$$

Division of the sum of Na and K transport products by $C_{\mathrm{I}} D_{\mathrm{I},b}$ gives the Haven ratio for the direction along the b-axis according to

$$H_{\mathrm{R},b} = \frac{C_{\mathrm{Na}} \widehat{D}_{\mathrm{Na},b} + C_{\mathrm{K}} \widehat{D}_{\mathrm{K},b}}{C_{\mathrm{I}} D_{\mathrm{I},b}} \tag{9.17}$$

$$= 0.5 \frac{r_{\mathrm{Na}} f_{\mathrm{Na},b} + r_{\mathrm{K}} f_{\mathrm{K},b}}{f_{\mathrm{I},b}} \,. \tag{9.18}$$

It can be noted that the factor 0.5 in the above equation is well-known from early diffusion studies [108, 121]. It results from the fact that the generalised interstitial I

performs one jump of length $2l_b$ whereas two tracer atoms each jump along the distance l_b at the same time. Furthermore, the squared displacements enter the diffusion equation (Eq. 9.7), which gives a constant geometrical contribution of 0.5 to $H_{\mathrm{R},b}$.

9.1.3. Interstitialcy diffusion along the c^*-axis including double interstitialcy jumps

The direction along the c^*-axis, i.e., normal to (001) is of particular interest because several experimental studies refer to diffusion or ionic conductivity along this direction [11, 12, 13, 56, 64]. In addition to jumps within the b-c-plane of alkali feldspar (see Section 9.1.2) also jumps within the a-c-plane have to be considered. These jumps exhibit a higher degree of complexity because in addition to interstitialcy I-S jumps also double interstitialcy I-S-S jumps involving chains of two neighbouring substitutional atoms may appear.
The interstitialcy diffusion mechanism can be described in terms of quasichemical reactions, which are compiled in Tab. 9.1 together with the corresponding stoichiometric coefficients η_{K} and η_{Na} and reaction rates. In analogy to Eqs. 9.1 and 9.2 the reactions $n = 1$ to 4 refer to interstitialcy I-S diffusion and the jump frequencies depend only on the type of the substitutional atom. In consistency with the considerations for diffusion along the b-axis (cf. Eq. 9.3) mass-action law predicts for thermal equilibrium the relative concentrations of interstitials, i.e.,

$$\frac{r_{\mathrm{K}}}{r_{\mathrm{Na}}} = \frac{C_{\mathrm{K,I}}}{C_{\mathrm{Na,I}}} = \frac{C_{\mathrm{K}} w_{\mathrm{K}}}{C_{\mathrm{Na}} w_{\mathrm{Na}}} \,. \tag{9.19}$$

The state of equilibrium in the above equation is an inherent property of the I-S interstitialcy diffusion model. Under the reasonable assumption that Eq. 9.19 globally holds for all quasichemical reactions double interstitialcy I-S-S jumps may be introduced. In analogy to the above conception for I-S jumps only the configuration of the two substitutional atoms that are involved in an I-S-S jump determine the jump frequency. Moreover, it is presumed that the jump frequency for I-S-S jumps involving only substitutional Na atoms ($n = 6$ and 12 in Tab. 9.1) is equal to the jump frequency for the corresponding I-S reaction ($n = 2$), i.e., w_{Na}. Based on this assumption and with the help of Eq. 9.19 the jump frequencies for the reactions $n = 7, 8, 10$ and 11 are given by w_{K}. In contrast, the reactions

Table 9.1.: Quasichemical reaction equations and the according reaction rates (jump multiplicities are neglected) and stoichiometric coefficients η for alkali diffusion in alkali feldspar. The reactions $n = 1$ to 4 refer to interstitialcy I-S diffusion whereas the reactions $n = 5$ to 12 relate to the double interstitialcy I-S-S mechanism.

n	Reaction	Rate	$\eta_{\mathrm{K},n}$	$\eta_{\mathrm{Na},n}$
1	$\mathrm{K_I} + \mathrm{K_S} \xrightarrow{w_\mathrm{K}} \mathrm{K_S} + \mathrm{K_I}$	$r_1 = w_\mathrm{K} C_\mathrm{K,I} C_\mathrm{K,S}$	0	0
2	$\mathrm{Na_I} + \mathrm{Na_S} \xrightarrow{w_\mathrm{Na}} \mathrm{Na_S} + \mathrm{Na_I}$	$r_2 = w_\mathrm{Na} C_\mathrm{Na,I} C_\mathrm{Na,S}$	0	0
3	$\mathrm{K_I} + \mathrm{Na_S} \xrightarrow{w_\mathrm{Na}} \mathrm{K_S} + \mathrm{Na_I}$	$r_3 = w_\mathrm{Na} C_\mathrm{K,I} C_\mathrm{Na,S}$	-1	$+1$
4	$\mathrm{Na_I} + \mathrm{K_S} \xrightarrow{w_\mathrm{K}} \mathrm{Na_S} + \mathrm{K_I}$	$r_4 = w_\mathrm{K} C_\mathrm{Na,I} C_\mathrm{K,S}$	$+1$	-1
5	$\mathrm{K_I} + \mathrm{K_S} + \mathrm{K_S} \xrightarrow{\frac{w_\mathrm{K}}{w_\mathrm{Na}} w_\mathrm{K}} \mathrm{K_S} + \mathrm{K_S} + \mathrm{K_I}$	$r_5 = \frac{w_\mathrm{K}}{w_\mathrm{Na}} w_\mathrm{K} C_\mathrm{K,I} C_\mathrm{K,S}^2$	0	0
6	$\mathrm{Na_I} + \mathrm{Na_S} + \mathrm{Na_S} \xrightarrow{w_\mathrm{Na}} \mathrm{Na_S} + \mathrm{Na_S} + \mathrm{Na_I}$	$r_6 = w_\mathrm{Na} C_\mathrm{Na,I} C_\mathrm{Na,S}^2$	0	0
7	$\mathrm{K_I} + \mathrm{Na_S} + \mathrm{K_S} \xrightarrow{w_\mathrm{K}} \mathrm{K_S} + \mathrm{Na_S} + \mathrm{K_I}$	$r_7 = w_\mathrm{K} C_\mathrm{K,I} C_\mathrm{K,S} C_\mathrm{Na,S}$	0	0
8	$\mathrm{Na_I} + \mathrm{K_S} + \mathrm{Na_S} \xrightarrow{w_\mathrm{K}} \mathrm{Na_S} + \mathrm{K_S} + \mathrm{Na_I}$	$r_8 = w_\mathrm{K} C_\mathrm{Na,I} C_\mathrm{K,S} C_\mathrm{Na,S}$	0	0
9	$\mathrm{Na_I} + \mathrm{K_S} + \mathrm{K_S} \xrightarrow{\frac{w_\mathrm{K}}{w_\mathrm{Na}} w_\mathrm{K}} \mathrm{Na_S} + \mathrm{K_S} + \mathrm{K_I}$	$r_9 = \frac{w_\mathrm{K}}{w_\mathrm{Na}} w_\mathrm{K} C_\mathrm{Na,I} C_\mathrm{K,S}^2$	$+1$	-1
10	$\mathrm{K_I} + \mathrm{K_S} + \mathrm{Na_S} \xrightarrow{w_\mathrm{K}} \mathrm{K_S} + \mathrm{K_S} + \mathrm{Na_I}$	$r_{10} = w_\mathrm{K} C_\mathrm{K,I} C_\mathrm{K,S} C_\mathrm{Na,S}$	-1	$+1$
11	$\mathrm{Na_I} + \mathrm{Na_S} + \mathrm{K_S} \xrightarrow{w_\mathrm{K}} \mathrm{Na_S} + \mathrm{Na_S} + \mathrm{K_I}$	$r_{11} = w_\mathrm{K} C_\mathrm{Na,I} C_\mathrm{Na,S} C_\mathrm{K,S}$	$+1$	-1
12	$\mathrm{K_I} + \mathrm{Na_S} + \mathrm{Na_S} \xrightarrow{w_\mathrm{Na}} \mathrm{K_S} + \mathrm{Na_S} + \mathrm{Na_I}$	$r_{12} = w_\mathrm{Na} C_\mathrm{K,I} C_\mathrm{Na,S}^2$	-1	$+1$

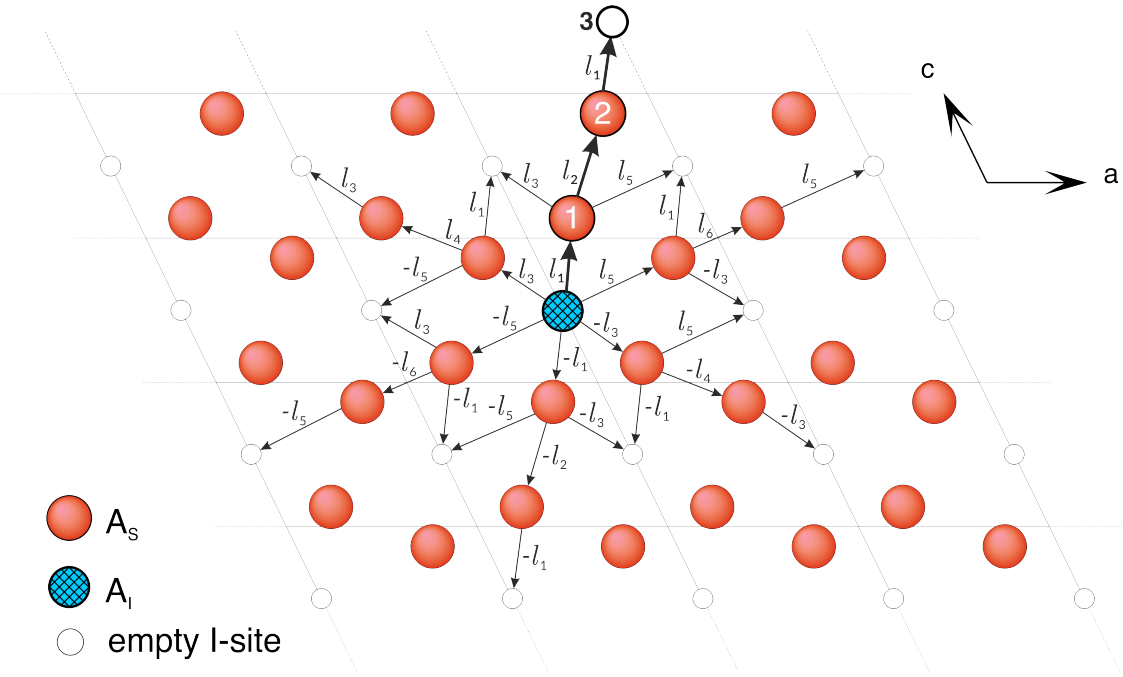

Figure 9.2.: Schematic view of the *a*-*c*-plane in alkali feldspar according to Phillips and Ribbe [120]. Only atoms of the alkali sublattice are illustrated (solid circles) for clarity together with empty interstitial sites (open circles). One central interstitial atom (crosshatched circle) jumps via the double interstitialcy mechanism to a substitutional site '1' along a trajectory l, as indicated. In turn, the atom initially located at '1' jumps to a neighbouring substitutional site '2' and a second substitutional atom jumps from '2' to an empty interstitial site '3' in the same elementary step.

$n = 5$ and 9 both comprise jumps of two substitutional K_S atoms and a third jump frequency, ${w_K}^2/w_{Na}$, is introduced according to Eq. 9.19.

A schematic view of the substitutional and interstitial sites in the *a*-*c*-plane of feldspar is displayed in Fig. 9.2. It is observed that one interstitial atom (crosshatched circle) can jump to 6 neighbouring substitutional sites via the interstitialcy mechanism as far as only jumps with a zero displacement along the *b*-axis are considered. In non-collinear I-S interstitialcy jumps an atom that is initially located at a substitutional site subsequently occupies one of two empty interstitial sites. Apart from that, the substitutional atom can participate in double interstitialcy I-S-S jumps and subsequently move to another substitutional site. An example of this mechanism is illustrated in Fig. 9.2 where the interstitial atom A_I jumps to a neighbouring site '1' along a trajectory l_1. The substitutional atom A_S that is initially located at '1' jumps to another substitutional site '2' along l_2 and, in turn, a second substitutional atom moves from '2' to an empty interstitial site

'3' via l_1 and adopts the role of A_I. In total, four types of I-S interstitialcy jumps exist for diffusion along the c^*-axis (one type of jump has a non-zero displacement along the b-axis, see Fig. 9.1) with a multiplicity given by $z^{IS}_{c^*} = 4$. Beyond that, three types of I-S-S jumps within the a-c-plane are observed with a multiplicity of $z^{ISS}_{c^*} = 2$ each.
In general, also I-S jumps involving one displacement within the a-c-plane in combination with one displacement that is perpendicular to this plane can be found (e.g., l_1+l_7). These jumps show, however, a strong non-collinearity and should occur much less frequently. In MC simulation, it was found that the allowance for these non-collinear jumps leads to enhanced values for the Haven ratio and to a diffusion anisotropy ratio that is $\widehat{D}_{\mathrm{Na},b}/\widehat{D}_{\mathrm{Na},c^*} \sim 3$. This observation is in clear contrast to the measured anisotropy ratio that is discussed in Section 9.3.3 and it is therefore assumed that $l_1 + l_7$ and equivalent jumps occur with a negligibly small frequency.

I-S related tracer and interstitialcy diffusion coefficients

In analogy to the concepts used to derive diffusion coefficients for the direction along the b-axis (see Section 9.1.2) similar relations are derived for a projection to the c^*-axis. Accordingly, the tracer diffusion coefficient of Na atoms is given by

$$\widehat{D}_{\mathrm{Na},c^*} = \lim_{t\to\infty} \frac{\langle X^2_{\mathrm{Na}} \rangle}{2t} = f_{\mathrm{Na},c^*} \frac{\langle X^2_{\mathrm{Na}} \rangle_{\mathrm{uncorr}}}{2t}\,, \tag{9.20}$$

where $\langle X^2_{\mathrm{Na}} \rangle$ denotes the mean square displacement in c^*-direction within a sufficiently long time t. It is helpful to discriminate I-S and I-S-S interstitialcy jumps by introducing the corresponding diffusivities $\widehat{D}^{IS}_{\mathrm{Na},c^*}$ and $\widehat{D}^{ISS}_{\mathrm{Na},c^*}$, respectively. Considering $\widehat{D}^{IS}_{\mathrm{Na},c^*}$, the mean square displacement may be decomposed into $n_{\mathrm{Na,Na}}$ and $n_{\mathrm{Na,K}}$ jump events with the corresponding projected jump lengths l_{i,c^*} where i represents the ith type of jump vector. With the aid of the reaction rates[2] given in

[2]It should be noted that the reaction rates are connected to the transport product (e.g., $C_{\mathrm{Na}}\widehat{D}_{\mathrm{Na}}$) whereas mean square displacements per time are considered to derive diffusivities. Therefore, both expressions vary in a factor C_{Na} or C_{K} for Na and K diffusion, respectively.

Tab. 9.1 and by using the multiplicity $z_{c^*}^{\mathrm{IS}} = 4$ it is easy to derive the Na diffusivity given by

$$\begin{aligned}\widehat{D}_{\mathrm{Na},c^*}^{\mathrm{IS}} &= \tfrac{1}{2} f_{\mathrm{Na},c^*}^{\mathrm{IS}}\, w_{\mathrm{Na}} z_{c^*}^{\mathrm{IS}} C_{\mathrm{I}} \Big[\left(l_{1,c^*}^2 + l_{3,c^*}^2\right) + \left(l_{1,c^*}^2 + l_{5,c^*}^2\right) + \\ &\qquad + \left(l_{3,c^*}^2 + l_{5,c^*}^2\right) + \left(l_{7,c^*}^2 + l_{8,c^*}^2\right) \Big] \\ &= 4 f_{\mathrm{Na},c^*}^{\mathrm{IS}}\, w_{\mathrm{Na}} C_{\mathrm{I}} \left(l_{1,c^*}^2 + 3 l_{3,c^*}^2\right) ,\end{aligned} \tag{9.21}$$

where use was made of the fact that the projected lengths of jump type 3, 5, 7 and 8 have the same numerical value. A similar expression holds for diffusion of the K component, i.e.,

$$\widehat{D}_{\mathrm{K},c^*}^{\mathrm{IS}} = 4 f_{\mathrm{K},c^*}^{\mathrm{IS}}\, w_{\mathrm{K}} C_{\mathrm{I}} \left(l_{1,c^*}^2 + 3 l_{3,c^*}^2\right) . \tag{9.22}$$

The interstitialcy diffusion coefficient can be derived with the same concepts and reaction rates given in Tab. 9.1. However, a striking property is that I-S jumps involving the jump vectors l_5 combined with $-l_3$ and equivalent jumps (see Fig. 9.2) effectively show a zero displacement of the charge carrier for the diffusion along the c^*-axis. The same is true for I-S jumps via l_7 in combination with l_8 and equivalent trajectories (see Fig. 9.1), which gives the expression

$$\begin{aligned}\widehat{D}_{\mathrm{I},c^*}^{\mathrm{IS}} &= \tfrac{1}{2} f_{\mathrm{I},c^*}^{\mathrm{IS}}\, w_{\mathrm{I}} z_{c^*}^{\mathrm{IS}} \left[\left(l_{1,c^*} + l_{3,c^*}\right)^2 + \left(l_{1,c^*} + l_{5,c^*}\right)^2 \right] \\ &= 4 f_{\mathrm{I},c^*}^{\mathrm{IS}}\, w_{\mathrm{I}} \left(l_{1,c^*} + l_{3,c^*}\right)^2 .\end{aligned} \tag{9.23}$$

Based on Eqs. 9.21, 9.22 and 9.23 the Haven ratio for I-S jumps is then given by

$$\begin{aligned}H_{\mathrm{R},c^*}^{\mathrm{IS}} &= \frac{C_{\mathrm{Na}} \widehat{D}_{\mathrm{Na},c^*}^{\mathrm{IS}} + C_{\mathrm{K}} \widehat{D}_{\mathrm{K},c^*}^{\mathrm{IS}}}{C_{\mathrm{I}} D_{\mathrm{I},c^*}^{\mathrm{IS}}} \\ &= \frac{f^{\mathrm{IS}}}{f_{\mathrm{I},c^*}^{\mathrm{IS}}} \frac{\left(l_{1,c^*}^2 + 3 l_{3,c^*}^2\right)}{\left(l_{1,c^*} + l_{3,c^*}\right)^2} = 0.8014 \frac{f^{\mathrm{IS}}}{f_{\mathrm{I},c^*}^{\mathrm{IS}}} ,\end{aligned} \tag{9.24}$$

where $f^{\mathrm{IS}} = r_{\mathrm{Na}} f_{\mathrm{Na},c^*}^{\mathrm{IS}} + r_{\mathrm{K}} f_{\mathrm{K},c^*}^{\mathrm{IS}}$ is a mean correlation factor of Na and K tracer atoms. On the right-hand side of Eq. 9.24 the numerical value for a purely geometrical contribution to H_{R} is indicated. Because of the two types of jumps that do not contribute to diffusion of the charge carriers, i.e., $l_3 - l_5$, $l_7 + l_8$ and equal jumps, this value is enhanced compared to the diffusion along the b-axis, i.e., $0.8014 > 0.5$.

I-S-S related tracer and interstitialcy diffusion coefficients

Similar relations can be derived for diffusion via the I-S-S double interstitialcy mechanism. Starting with $\widehat{D}^{\mathrm{ISS}}_{\mathrm{Na},c^*}$, the mean square displacement is decomposed into contributions that result from the reactions $n = 5$ to 12 comprised in Tab. 9.1. Considering, e.g., the reaction $n = 6$ that involves only Na atoms the numbers of events can be further decomposed into contributions from S-S, I-S and S-I jumps given by

$$\begin{aligned}
\langle n^{\mathrm{SS}}_{\mathrm{Na,Na,Na}}\rangle/t &= p_{\mathrm{Na,S}} C_{\mathrm{Na}} C_{\mathrm{Na,I}} w_{\mathrm{Na}} z^{\mathrm{ISS}}_{c^*} = r_{\mathrm{Na}} C_{\mathrm{Na}} w_{\mathrm{Na}} z^{\mathrm{ISS}}_{c^*} C_{\mathrm{I}} \\
\langle n^{\mathrm{IS}}_{\mathrm{Na,Na,Na}}\rangle/t &= p_{\mathrm{Na,I}} C_{\mathrm{Na}} C_{\mathrm{Na}} w_{\mathrm{Na}} z^{\mathrm{ISS}}_{c^*} = r_{\mathrm{Na}} C_{\mathrm{Na}} w_{\mathrm{Na}} z^{\mathrm{ISS}}_{c^*} C_{\mathrm{I}} \\
\langle n^{\mathrm{SI}}_{\mathrm{Na,Na,Na}}\rangle/t &= p_{\mathrm{Na,S}} C_{\mathrm{Na}} C_{\mathrm{Na,I}} w_{\mathrm{Na}} z^{\mathrm{ISS}}_{c^*} = r_{\mathrm{Na}} C_{\mathrm{Na}} w_{\mathrm{Na}} z^{\mathrm{ISS}}_{c^*} C_{\mathrm{I}} \,,
\end{aligned} \tag{9.25}$$

respectively. On the right-hand side of the above equations use of the relations comprised in Eqs. 9.6, 9.9 and 9.10 was made. Similar relations to Eq. 9.25 can be found for the remaining reactions ($n = 5$, 7, 8, 9, 10, 11 and 12). With respect to the different jump vectors l the Na diffusivity can then be expressed according to Eq. 9.20 by

$$\begin{aligned}
\widehat{D}^{\mathrm{ISS}}_{\mathrm{Na},c^*} &= \tfrac{1}{2} f^{\mathrm{ISS}}_{\mathrm{Na},c^*} z^{\mathrm{ISS}}_{c^*} C_{\mathrm{I}} \Big[\left(C_{\mathrm{Na}} w_{\mathrm{Na}} + C_{\mathrm{K}} w_{\mathrm{K}}\right) \left(l^2_{2,c^*} + l^2_{4,c^*} + l^2_{6,c^*}\right) + \\
&\quad + \left(C_{\mathrm{K}} w_{\mathrm{K}} \left(r_{\mathrm{Na}} + 2\right) + C_{\mathrm{Na}} w_{\mathrm{Na}} \left(r_{\mathrm{Na}} + 1\right) \left(l^2_{1,c^*} + l^2_{3,c^*} + l^2_{5,c^*}\right)\right) \Big] \\
&= f^{\mathrm{ISS}}_{\mathrm{Na},c^*} C_{\mathrm{I}} \Big[\left(C_{\mathrm{Na}} w_{\mathrm{Na}} + C_{\mathrm{K}} w_{\mathrm{K}}\right) \left(l^2_{2,c^*} + 2 l^2_{4,c^*}\right) + \\
&\quad + \left(C_{\mathrm{K}} w_{\mathrm{K}} \left(r_{\mathrm{Na}} + 2\right) + C_{\mathrm{Na}} w_{\mathrm{Na}} \left(r_{\mathrm{Na}} + 1\right)\right) \left(l^2_{1,c^*} + 2 l^2_{3,c^*}\right) \Big] \,,
\end{aligned} \tag{9.26}$$

where the relations $z^{\mathrm{ISS}}_{c^*} = 2$, $l^2_{4,c^*} = l^2_{6,c^*}$ and $l^2_{3,c^*} = l^2_{5,c^*}$ were used. Accordingly, the diffusion coefficient for K tracer atoms is given by

$$\begin{aligned}
\widehat{D}^{\mathrm{ISS}}_{\mathrm{K},c^*} &= f^{\mathrm{ISS}}_{\mathrm{K},c^*} C_{\mathrm{I}} \Big[\left(C_{\mathrm{Na}} w_{\mathrm{K}} + C_{\mathrm{K}} w_{\mathrm{K}} \frac{w_{\mathrm{K}}}{w_{\mathrm{Na}}}\right) \left(l^2_{2,c^*} + 2 l^2_{4,c^*}\right) + \\
&\quad + \left(C_{\mathrm{Na}} w_{\mathrm{K}} \left(r_{\mathrm{K}} + 2\right) + C_{\mathrm{K}} w_{\mathrm{K}} \frac{w_{\mathrm{K}}}{w_{\mathrm{Na}}} \left(r_{\mathrm{K}} + 1\right)\right) \left(l^2_{1,c^*} + 2 l^2_{3,c^*}\right) \,,
\end{aligned} \tag{9.27}$$

and the interstitialcy diffusion coefficient by

$$\begin{aligned}
\widehat{D}^{\mathrm{ISS}}_{\mathrm{I},c^*} = f^{\mathrm{ISS}}_{\mathrm{I},c^*} \Big[& 2 C_{\mathrm{Na}} C_{\mathrm{K}} w_{\mathrm{K}} + C^2_{\mathrm{Na}} w_{\mathrm{Na}} + C^2_{\mathrm{K}} w_{\mathrm{K}} \frac{w_{\mathrm{K}}}{w_{\mathrm{Na}}} \Big] \\
& \Big[\left(2 l_{1,c^*} + l_{2,c^*}\right)^2 + 2 \left(2 l_{3,c^*} + l_{4,c^*}\right)^2 \Big] \,.
\end{aligned} \tag{9.28}$$

With the aid of Eqs. 9.26, 9.27 and 9.28, an expression for the Haven ratio can be given by

$$\begin{aligned} H_{\mathrm{R},c^*}^{\mathrm{ISS}} &= \frac{C_{\mathrm{Na}}\widehat{D}_{\mathrm{Na},c^*}^{\mathrm{ISS}} + C_{\mathrm{K}}\widehat{D}_{\mathrm{K},c^*}^{\mathrm{ISS}}}{C_{\mathrm{I}}D_{\mathrm{I},c^*}^{\mathrm{ISS}}} \\ &= \frac{f^{\mathrm{ISS}}}{f_{\mathrm{I},c^*}^{\mathrm{ISS}}} \frac{\left(l_{2,c^*}^2 + 2l_{4,c^*}^2\right) + 2\left(l_{1,c^*}^2 + 2l_{3,c^*}^2\right)}{\left(2l_{1,c^*} + l_{2,c^*}\right)^2 + 2\left(2l_{3,c^*} + l_{4,c^*}\right)^2} = 0.336\frac{f^{\mathrm{ISS}}}{f_{\mathrm{I},c^*}^{\mathrm{ISS}}} \,. \end{aligned} \tag{9.29}$$

A noticeable result in Eq. 9.29 is that the constant geometrical contribution to H_{R,c^*} is significantly lower than the corresponding value for the I-S interstitialcy mechanism. The finding is related to the occurrence of nearly collinear chains within the *a*-*c*-plane (see Fig. 9.2) with a stronger contribution to $\widehat{D}_{\mathrm{I},c^*}^{\mathrm{ISS}}$ than to $\widehat{D}_{\mathrm{Na},c^*}^{\mathrm{ISS}}$. It may therefore be assumed that the allowance for double interstitialcy I-S-S jumps shows a crucial effect on H_{R}.

9.1.4. Effective short-range interaction between cations

In MC simulations based on a randomly ordered sublattice numerical H_{R} values on the order of ~ 0.6 are observed. In contrast, the experimentally obtained values for H_{R}, ranging from 0.11 to 0.40 (see Fig. 5.7), are significantly below the MC findings, which suggests that the atoms could be subject to short-range ordering and deviate from a completely random distribution. The location of alkali sites in feldspar is primarily determined by interactions of K and Na atoms with the neighbouring O atoms of the silicate framework. Beyond that, different types of cations may show a minor effect on the potential landscape of neighbouring cations, which leads to an effective interaction between cations and hence, to a short-range ordering (or disordering) tendency. Phillips et al. [122] measured the Na-K distribution after annealing at 803 K of a $Or_{49}Ab_{51}$ feldspar by NMR spectroscopy and found experimental evidence for a Na clustering tendency. This observation was further corroborated by heat capacity measurements [123] and density functional theory calculations of heat capacities of alkali feldspar [124].

To investigate the influence on correlation effects the previously discussed hypothetical random alloy is therefore extended by interactions between nearest-neighbour atoms with the effective interaction energies $-v_{\mathrm{K,K}}$, $-v_{\mathrm{Na,Na}}$ and $-v_{\mathrm{Na,K}}$ ($v_{\mathrm{Na,K}} > 0$). According to Stolwijk [93] a so-called ordering energy v can be introduced, i.e.,

$$v = v_{\mathrm{Na,K}} - \tfrac{1}{2}\left(v_{\mathrm{Na,Na}} + v_{\mathrm{K,K}}\right) \,, \tag{9.30}$$

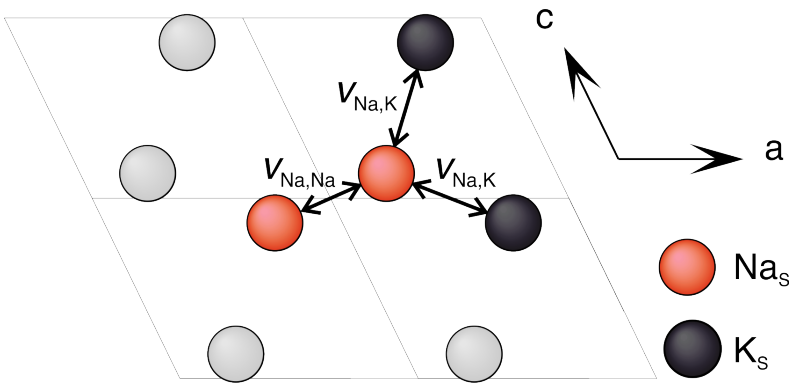

Figure 9.3.: View of the monoclinic *a*-*c*-plane of feldspar showing only substitutional (Na_S, K_S) atoms of the alkali sublattice. Effective interaction energies between one Na atom and three neighbouring atoms are considered with the associated interaction parameters $v_{Na,Na}$ and $v_{Na,K}$, as indicated.

whereby the equilibrium state is fully determined by v/k_BT. Another useful expression is given by

$$U = \frac{v_{Na,Na} - v_{K,K}}{2v}\,, \tag{9.31}$$

where U indicates the variation of interaction energies between Na-Na and K-K pairs. In the present model, Na-Na and K-K bonds are formed at the expense of Na-K bonds if $v < 0$ holds (clustering). The opposite case, i.e., $v > 0$ is referred to as ordering because globally more Na-K bonds are formed than in the random alloy reference case. According to Fig. 9.1, the distance between nearest-neighbours within the same *a*-*c*-plane is significantly smaller than along the *b*-axis. Hence, only those three bonds within the same *a*-*c*-plane are considered as illustrated in Fig. 9.3. The equilibrium state is also expressed through the migration energies of the interstitialcy mechanism. In the random alloy reference case, the jump frequencies only depend on the type of the substitutional atom involved in an I-S interstitialcy jump. For example, the jump frequency of Na atoms is

$$w_{Na}^{IS} = \nu^0 \exp\left(\frac{S_{Na}^m}{k_B}\right) \exp\left(-\frac{H_{Na}^m}{k_BT}\right), \tag{9.32}$$

where S_{Na}^m is the migration entropy of Na atoms, H_{Na}^m is the migration enthalpy of Na atoms and ν^0 is an attempt frequency on the order of the Debye frequency.

In contrast to Eq. 9.32, the introduction of interaction energies shows an influence depending on the nearest-neighbour environment according to

$$w_{\mathrm{Na}}^{\mathrm{IS}} = \nu^0 \exp\left(\frac{S_{\mathrm{Na}}^m}{k_{\mathrm{B}}}\right) \exp\left(-\left(H_{\mathrm{Na}}^m + b_{\mathrm{Na,Na}} v_{\mathrm{Na,Na}} + b_{\mathrm{Na,K}} v_{\mathrm{Na,K}}\right)/k_{\mathrm{B}}T\right), \tag{9.33}$$

where $b_{\mathrm{Na,Na}}$ and $b_{\mathrm{Na,K}}$ are the numbers of Na-Na and Na-K bonds, respectively. For I-S interstitialcy jumps the relation $b_{\mathrm{Na,Na}} + b_{\mathrm{Na,K}} = 3$ is valid. A similar relation is given for I-S interstitialcy jumps of K atoms, i.e.,

$$w_{\mathrm{K}}^{\mathrm{IS}} = \nu^0 \exp\left(\frac{S_{\mathrm{K}}^m}{k_{\mathrm{B}}}\right) \exp\left(-\left(H_{\mathrm{K}}^m + b_{\mathrm{K,K}} v_{\mathrm{K,K}} + b_{\mathrm{K,Na}} v_{\mathrm{Na,K}}\right)/k_{\mathrm{B}}T\right), \tag{9.34}$$

where S_{K}^m and H_{K}^m are the migration entropy and enthalpy of K atoms, respectively and $b_{\mathrm{K,K}}$ is the number of K-K bonds of a substitutional K atom. The jump frequencies of I-S-S interstitialcy jumps are affected in a similar way. As an example, the jump frequency for double interstitialcy jumps through the reaction $n = 10$ (see Tab. 9.1) is given by

$$w_{\mathrm{K,Na}}^{\mathrm{ISS}} = \nu^0 \exp\left(\frac{S_{\mathrm{K}}^m}{k_{\mathrm{B}}}\right) \exp\left(-\left(H_{\mathrm{K}}^m + b_{\mathrm{Na,Na}} v_{\mathrm{Na,Na}} + b_{\mathrm{Na,K}} v_{\mathrm{Na,K}} + b_{\mathrm{K,K}} v_{\mathrm{K,K}}\right)/k_{\mathrm{B}}T\right), \tag{9.35}$$

and the relation $b_{\mathrm{Na,Na}} + b_{\mathrm{Na,K}} + b_{\mathrm{K,K}} = 5$ holds.
The introduction of interaction energies also affects the diffusivities discussed in Sections 9.1.2 and 9.1.3. For example, the probability that a certain type of substitutional atom is neighbouring another substitutional atom in Eq. 9.25 is not reflected by the concentrations C_{K} and C_{Na} as is true for the random alloy reference case. Moreover, the jump frequencies for each combination of neighbouring atoms have to be distinguished. A more convenient method to calculate diffusivities is to extract the mean square displacements directly from MC simulations and, for example, the Na diffusivity along the b-axis is then given by Eqs. 9.7 and 9.8. This method is preferred throughout the present study for all calculations of diffusivities.

9.2. Numerical procedures

To calculate tracer and interstitialcy correlation factors in the monoclinic structure of feldspar, the same numerical approach was employed as in the previous chapters to calculate correlation factors in the simple cubic structure. Adaptions were made

to allow for double interstitialcy I-S-S jumps within the a-c-plane (cf. Section 9.1.3) and for considering an effective interaction energy given by $v < 0$ (clustering) between the cations (cf. Section 9.1.4). The numerical model is based on the conception that an interstitialcy defect I performs either I-S jumps or I-S-S jumps with frequencies that do not depend on the type of defect, but rather on the type of its neighbouring atoms. These frequencies are for the random alloy (RA) reference case w_{Na} and w_{K} for I-S jumps and w_{Na}, w_{K} and ${w_{\mathrm{K}}}^2/w_{\mathrm{Na}}$ for I-S-S jumps, respectively (see Tab. 9.1). Initially, the I atom was set in the centre of a monoclinic 'interstitial' lattice consisting of $\left(0, 0, \frac{1}{2}\right)$ and equivalent sites that was otherwise completely empty. The 'substitutional' lattice, in contrast, was completely filled with tagged atoms of type K and Na that were randomly distributed according to their concentrations C_{K} and C_{Na}, respectively. In all cases the simulation box had a size of $20a \times 20b \times 20c$ unit cells (32,000 substitutional atoms). This was found to be the minimum box size for results that remain unbiased by the periodic boundaries, i.e., the box was surrounded by copies of itself on all sides.
To allow the sublattice to establish thermodynamic equilibrium the well known Metropolis algorithm was applied [125, 126] before the computation of correlation factors. In a first step of this procedure the initial energy of the sublattice given by

$$E = -vN_{\mathrm{Na,K}} \tag{9.36}$$

was determined by counting the number of unlike K-Na bonds $N_{\mathrm{K,Na}}$ throughout the box according to Fig. 9.3. The following steps of the Metropolis algorithm were then applied repeatedly: (i) Two atoms were randomly selected from the substitutional lattice. The procedure was repeated until an unlike K-Na pair was found. (ii) The three atoms neighbouring the K atom were examined and the numbers of K and Na bonds, $b_{\mathrm{K,K}}$ and $b_{\mathrm{K,Na}}$, respectively, were determined. Accordingly, the bonds of the Na atom, $b_{\mathrm{Na,Na}}$ and $b_{\mathrm{Na,K}}$, were identified. (iii) Interchanging the K-Na pair has an effect on the total number of unlike bonds, $N_{\mathrm{K,Na}}$, according to

$$\Delta N_{\mathrm{K,Na}} = 2\left(b_{\mathrm{K,K}} - b_{\mathrm{Na,K}} + \delta\right), \tag{9.37}$$

where δ is unity if the pair atoms are neighbours of themselves and zero if not. The interchange was carried out if $\Delta N_{\mathrm{K,Na}} \leq 0$. If $\Delta N_{\mathrm{K,Na}} > 0$ a random number $r \in [0, 1)$ was compared with the Boltzmann factor

$$f_{\mathrm{Boltzmann}} = \exp\left[\left(\frac{v}{k_{\mathrm{B}}T}\right)\Delta N_{\mathrm{K,Na}}\right], \quad \text{for} \quad v < 0 \tag{9.38}$$

and the interchange was carried out if $r \leq f_{\mathrm{Boltzmann}}$. If $r > f_{\mathrm{Boltzmann}}$ the initial state was retained and the procedure was repeated from step (i) onwards. The Metropolis algorithm was suspended when the system was safely assumed to be in thermal equilibrium.

After the substitutional lattice was created the calculations of correlation factors started by evaluating the total jump frequency of the interstitial atom I. All ten nearest-neighbour S-atoms and those six second-nearest-neighbour atoms that can be involved in I-S-S jumps were examined (see Figures 9.1 and 9.2). Jumps of the same S-atom to different I-sites (or to one S-site in case of an I-S-S exchange) were considered as independent of each other and counted as a single jump. The total jump frequency is then given by $\sum_i^{22} w_i$ with the individual frequencies of the RA reference case $w_i = w_{\mathrm{Na}}, w_{\mathrm{K}}$ and ${w_{\mathrm{K}}}^2/w_{\mathrm{Na}}$, respectively. Variations of the individual jump frequencies from the reference case occurred when effective short-range interactions were considered, i.e., $v \neq 0$, which is discussed in Section 9.1.4. According to the individual jump probabilities one jump direction was chosen by a random number generator (RNG) and the exchange was executed. Sufficiently long runs of I jumps were executed to compute correlation factors with acceptably small uncertainties, i.e., between $n = 5 \times 10^{10}$ and 5×10^{11} jumps.

For the numerical calculation of correlation factors a partial correlation factors method (PCF) – which was introduced in Chapter 6 – was employed. The PCFs were computed by evaluating the scalar product of jump vectors for each atom and each type of jump α, given by $S_\alpha = \sum_i \sum_j (x_{\alpha,i} \cdot x_{\alpha,i+j})$. Here, $x_{\alpha,i+j}$ denotes the jth jump after the ith exchange of type α with x_α being the projected length of the jump vector l_α to the direction under investigation. The PCF corresponding to α jumps is then given by averaging over all atoms of the same type, according to

$$\tilde{f}_\alpha = 1 + 2\langle S_\alpha \rangle / \langle n_\alpha \rangle \cdot x_\alpha^2, \tag{9.39}$$

where $\langle n_\alpha \rangle$ is the average number of jumps of type α. Total correlation factors are then obtained by weighted averages of the associated PCFs.

Interstitialcy correlation factors f_I related to diffusion of the generalised interstitial defect I were obtained by the same PCF method. Because only one single defect was present in the simulation box at any time the correlation factors could not be averaged over many particles. Instead, the total run made up of n jumps was split into N_run sequences of n_L jumps and f_I was obtained by averaging over all sequences. A sequence length consisting of $n_\mathrm{L} = 2\times10^6$ jumps was found to produce unbiased results and was therefore selected for all presented simulations.

9.3. Results and discussion

9.3.1. Percolation behaviour

As discussed in the previous Chapters 7 and 8, the tracer correlation factors for diffusion via interstitialcies can become very small on the binary sublattice of feldspar if the jump rates of Na and K differ considerably. This is also true for the 'physical correlation factor' f_I that is closely related to the tracer correlation factor of the more mobile component (f_B or f_Na, respectively) over a large composition range (see e.g. Fig. 7.4 in Chapter 7). In this section, this percolation behaviour is analysed based on a randomly ordered sublattice with the aid of simulated f_I data for the monoclinic alkali sublattice. Figure 9.4 presents f_I for $w_\mathrm{Na}/w_\mathrm{K} = 10^{-5}$ in the direction normal to (001) as a function of composition ($0 \leq C_\mathrm{Na} \leq 0.45$). The f_I values are based on $n = 5 \times 10^{10}$ interstitialcy jumps per simulation run split up into sequences of $n_\mathrm{L} = 2 \times 10^6$ jumps. It is seen in Fig. 9.4a that f_I shows a steep gradient near $C_\mathrm{Na} \sim 0.12$. In the limiting case, $w_\mathrm{Na}/w_\mathrm{K} = 0$, the Na atoms are completely immobile leading to the appearance of a threshold composition C^p_Na below which long-range diffusion is not possible ($f_\mathrm{I} = 0$, $f_\mathrm{Na} = 0$).
The concentration dependence of f_I just above the percolation threshold C^p_Na may be described – in analogy to diffusion via vacancies and self-interstitials on the simple cubic lattice (see Chapters 6 and 7) – by [23, 21]

$$f_\mathrm{I} = k(C_\mathrm{Na} - C^\mathrm{p}_\mathrm{Na})^\delta,\ C_\mathrm{Na} \geq C^\mathrm{p}_\mathrm{Na}\,, \tag{9.40}$$

where δ is a critical exponent and k is a dimensionless proportionality constant. As an approximation to the case of fully immobile Na atoms, Eq. 9.40 was fitted in the narrow range $C_\mathrm{Na} \in [0.13, 0.28]$ to the f_I data for $w_\mathrm{Na}/w_\mathrm{K} = 10^{-5}$. Most consistent results were obtained by fitting of $\ln(f_\mathrm{I})$ using the logarithmic form of Eq. 9.40

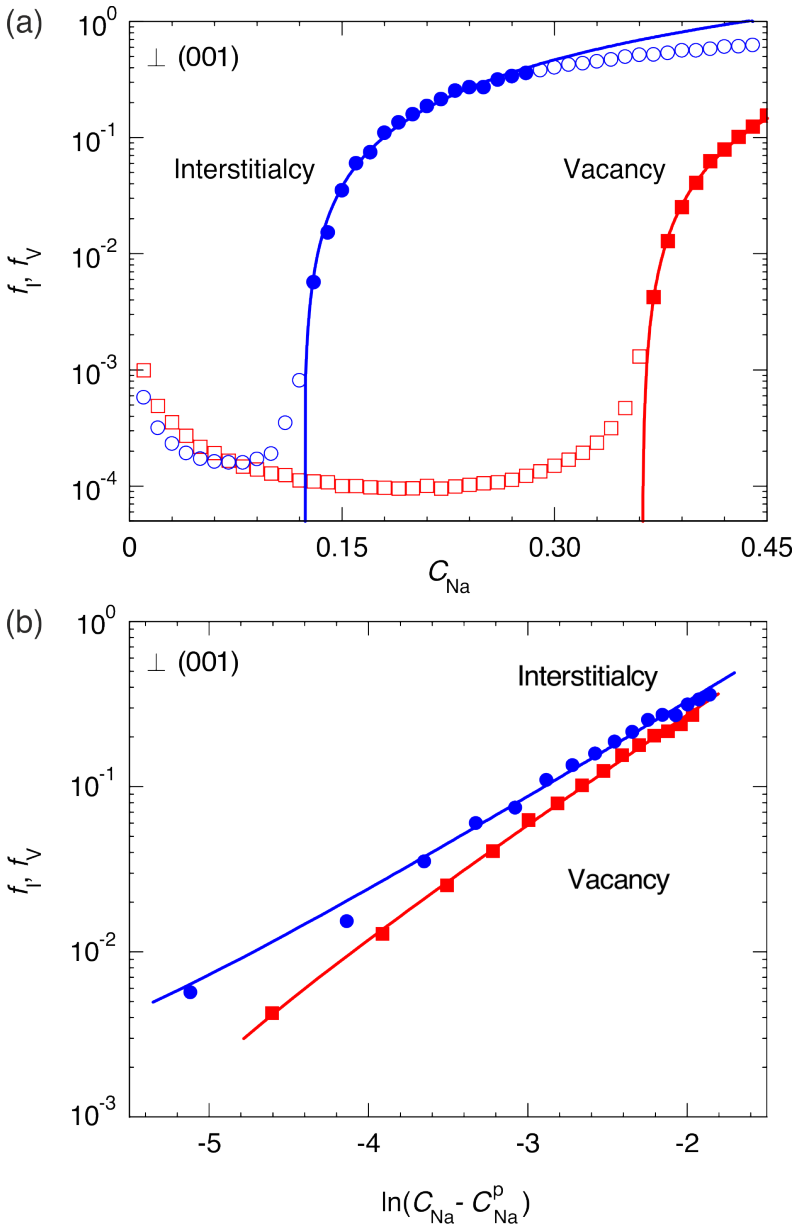

Figure 9.4.: Interstitialcy correlation factors f_I (circles) and vacancy correlation factors f_V (squares) as a function of composition C_Na (a) and as a function of $\ln(C_\mathrm{Na} - C^\mathrm{p}_\mathrm{Na})$ (b) for the monoclinic alkali sublattice of feldspar in the direction normal to (001) for the jump frequencies $w_\mathrm{Na}/w_\mathrm{K} = 10^{-5}$. Solid lines are separate fits to the solid symbols based on Eq. 9.40.

Table 9.2.: Parameter values characterizing the vacancy and interstitialcy percolation behaviour on the Na-K sublattice of alkali feldspar; cf. Eq. 9.40 and Chapter 6.

Diffusion mechanism	$C^{\mathrm{p}}_{\mathrm{Na}}$	δ	k
vacancy	0.360 ± 0.001	1.65 ± 0.06	8.1 ± 1.0
interstitialcy	0.124 ± 0.002	1.35 ± 0.07	4.8 ± 0.7

(see Fig. 9.4b). The best estimates for $C^{\mathrm{p}}_{\mathrm{Na}}$, δ and k are compiled in Tab. 9.2, and compared with corresponding data related to vacancy diffusion in the monoclinic structure (cf. Chapter 6 and square symbols in Fig. 9.4).

In summary, the findings may be interpreted as follows: The present threshold for interstitialcy diffusion, $C^{\mathrm{p}}_{\mathrm{Na}}(\mathrm{I}) = 0.124$, is distinctly lower than the vacancy-related value $C^{\mathrm{p}}_{\mathrm{Na}}(\mathrm{V}) = 0.360$ (cf. Chapter 6). On the one hand, this may relate to the higher coordination number for the interstitialcy mechanism, $z(\mathrm{I}) = 10$, compared to the vacancy mechanism $z(\mathrm{V}) = 5$. On the other hand, the number of sites from which a second exchange of the generalised interstitial may occur is even larger than the coordination number in the interstitialcy case, i.e., $z < z_2 = 14$, whereas these numbers cannot be distinguished in the vacancy case. The critical exponent $\delta(\mathrm{I})$ is slightly smaller than $\delta(\mathrm{V})$ [83], which leads to a stronger curvature of the f_{I} plot at compositions close to the percolation threshold. The fitted proportionality constant $k(\mathrm{I})$ is only about half of the $k(\mathrm{V})$ value [83], causing a weaker composition dependence for $C_{\mathrm{Na}} \gg C^{\mathrm{p}}_{\mathrm{Na}}$. In analogy to those results found for diffusion in the simple cubic structure, I-related correlation is less pronounced than V-related correlation far above the pertaining site-percolation threshold but more significant in the proximity of $C^{\mathrm{p}}_{\mathrm{Na}}$. Most importantly, $C^{\mathrm{p}}_{\mathrm{Na}}(\mathrm{I})$ fully complies with the experimental tracer diffusion data obtained for VF feldspar (see Chapter 4). A common interstitialcy mechanism of Na and K may therefore be a suitable model to describe the alkali diffusivities on the sublattice of VF feldspar in more detail, which will be presented along the following sections.

9.3.2. Dependence on effective short-range interactions between cations

In contrast to the previous section where a randomly ordered sublattice was considered the influence of effective short-range interactions between nearest-neighbour cations on the Na and K diffusivities and on the Haven ratio is analysed. The equilibrium state of the sublattice, fully characterised according to Section 9.1.4 by $v/k_{\mathrm{B}}T$, is established as a function of v for a constant temperature and with the parameter $U = 1.2$, which was a standard case in early correlation studies [117, 118]. It should be noted that according to Eqs. 9.30 and 9.31 the interaction energies $-v_{\mathrm{K,K}}$, $-v_{\mathrm{Na,Na}}$ and $-v_{\mathrm{Na,K}}$ are not unambiguously defined by the selection of v and U. A simple model assumption – without any influence on the ordering state of the system – based on non-interacting K-K pairs, $v_{\mathrm{K,K}} = 0\,\mathrm{meV}$, is therefore discussed.

The main objective of this study is to determine suitable parameters for the interstitialcy diffusion model to reproduce the experimental data found for $\widehat{D}_{\mathrm{K}}$, $\widehat{D}_{\mathrm{Na}}$ and D_{σ}. A full set of these quantities is, so far, only available for the VF feldspar (see Chapters 3, 4 and 5) and the VF composition is therefore selected as a starting point for the MC simulations. As an approximation to the real mineral with the composition $\mathrm{Or_{83}Ab_{15}Cs_1}$ the alkali sublattice is considered as a binary alloy consisting only of K and Na atoms with the concentrations $C_{\mathrm{K}} = 0.85$ and $C_{\mathrm{Na}} = 0.15$, respectively. The simulations were carried out for interaction energies v ranging from $-5\,\mathrm{meV}$ to $-90\,\mathrm{meV}$ at a fixed temperature of $T = 1173\,\mathrm{K}$. The jump frequencies, initially undetermined for this temperature, were set to $w_{\mathrm{Na}}/w_{\mathrm{K}} = 5\times10^{-4}$, which is a reasonable first assumption according to the findings from the following Section 9.3.3. In Fig. 9.5 computed results for $\widehat{D}_{\mathrm{Na}}/\widehat{D}_{\mathrm{K}}$ for the direction normal to (001) are displayed as a function of $-v$ (circles, left-hand side (lhs) ordinate). It can be observed that $\widehat{D}_{\mathrm{Na}}/\widehat{D}_{\mathrm{K}}$ increases linearly from ~ 200 to ~ 500 with decreasing values for the interaction energy v from $-5\,\mathrm{meV}$ down to $-50\,\mathrm{meV}$. For lower values of v ranging from $-50\,\mathrm{meV}$ to $-90\,\mathrm{meV}$ the slope of $\widehat{D}_{\mathrm{Na}}/\widehat{D}_{\mathrm{K}}$ becomes steeper and reaches a maximum value of ~ 2400 for the lowest v value under investigation. The global trend of increasing $\widehat{D}_{\mathrm{Na}}/\widehat{D}_{\mathrm{K}}$ can be understood by considering, e.g., the jump frequencies pertaining to I-S jumps of Na and K in Eqs. 9.33 and 9.34, respectively. For $v_{\mathrm{K,Na}} < 0$ and $v_{\mathrm{Na,Na}} < 0$ the Na jump frequency increases with the absolute values for the interaction energies. In contrast, the K jump frequency is only influenced by the interaction energy for

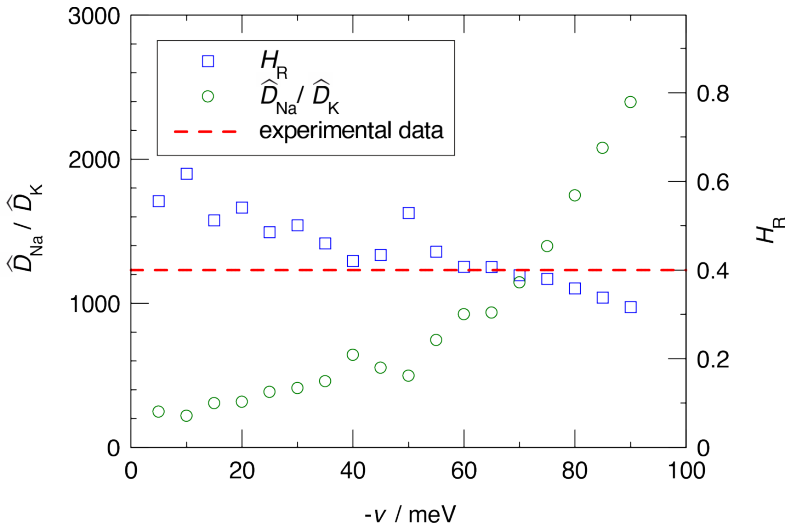

Figure 9.5.: Ratio of the diffusivities $\widehat{D}_{\mathrm{Na}}/\widehat{D}_{\mathrm{K}}$ (circles, lhs ordinate) and Haven ratio H_{R} (squares, rhs ordinate) as a function of the interaction energy v. The results are derived from MC simulations with $w_{\mathrm{Na}}/w_{\mathrm{K}} = 5 \times 10^{-4}$ and $T = 1173\,\mathrm{K}$ for diffusion in alkali feldspar normal to (001). The numerical values obtained for $\widehat{D}_{\mathrm{Na}}/\widehat{D}_{\mathrm{K}}$ and H_{R} from RTD and EIS analyses at 1173 K are represented by the dashed line (cf. Chapters 4 and 5).

K-Na bonds, $v_{\mathrm{K,Na}}$, and K-K bonds show a priori no effect on the frequency due to the selection for $v_{\mathrm{K,K}} = 0$, which leads to the observed $\widehat{D}_{\mathrm{Na}}/\widehat{D}_{\mathrm{K}}$ behaviour.
On the right-hand side (rhs) of Fig. 9.5 the Haven ratio H_{R} obtained for the direction normal to (001) is shown on a second ordinate as a function of $-v$ (square symbols). It can be seen that H_{R} decreases for increasing values of $-v$ from 0.62 to 0.32. If v is negative a number of Na-Na bonds larger than random will be formed at the cost of K-Na bonds. It may therefore be expected that the probability for double interstitialcy I-S-S jumps via Na-Na pairs is increased compared to the RA case. The overall jump rates w_{Na} and w_{I} increase with the numerical value of $-v$ because of the negative interaction energies. This effect is even stronger for w_{I} than for w_{Na} and hence, H_{R} decreases towards the geometrical value for I-S-S jumps, i.e., $H_{\mathrm{R}} = 0.336$ (cf. Eq. 9.29).
The experimental data for H_{R} in VF feldspar were analysed in Chapter 5. For all temperatures under investigation values in the range from 0.11 to 0.40 were observed. For the presently discussed temperature of $T = 1173\,\mathrm{K}$ the Haven ratio was calculated based on extrapolated data for D_{σ}, i.e., $H_{\mathrm{R}} = 0.27 \pm 0.12$. As a reference case for the simulated data a numerical value of $H_{\mathrm{R}} = 0.40$ may therefore be seen as the upper limit for H_{R} in VF feldspar. This experimental value is

Table 9.3.: Best estimates for the energy parameters in VF feldspar under the presumptions of non-interacting K-K pairs and $U = 1.2$.

v / meV	U	$v_{\mathrm{K,Na}}$ / meV	$v_{\mathrm{K,K}}$ / meV	$v_{\mathrm{Na,Na}}$ / meV
-72.0	1.2	-158.4	0	-172.8

represented by the dashed line in Fig. 9.5 and it can be seen that it complies with the simulated data for $v < -65\,\mathrm{meV}$. From corresponding tracer diffusion experiments with ^{22}Na and ^{43}K (see Chapters 3 and 4, respectively) the diffusivity ratio for VF feldspar at $T = 1173\,\mathrm{K}$ was measured, i.e., $\widehat{D}_{\mathrm{Na}}/\widehat{D}_{\mathrm{K}} = 1/1230$. The scale of the lhs ordinate in Fig. 9.5 was adapted that this upper limit is reflected by the horizontal dashed line, which also indicates the upper limit for H_{R}. It can be seen from the figure that it complies with the simulated data for an interaction parameter somewhere between $-70\,\mathrm{meV}$ and $-75\,\mathrm{meV}$. The best estimate for the interaction parameter, i.e., $v = -72.0\,\mathrm{meV}$, is therefore selected for the following analysis and the complete set of interaction parameters is compiled in Tab. 9.3.
According to the previous Section 9.3.1, the percolation behaviour can now be analysed with regard to effective short-range interactions (clustering) based on calculations of f_{I} normal to (001) for extremely low K jump frequencies $w_{\mathrm{Na}}/w_{\mathrm{K}} = 10^{-5}$ and for a constant hypothetical temperature of 1173 K. Fitting of the logarithmic form of Eq. 9.40 in the narrow range $C_{\mathrm{Na}} \in [0.12, 0.26]$ to the results gives $C^{\mathrm{p}}_{\mathrm{Na}}(\mathrm{I}) = 0.103 \pm 0.005$. A slightly shifted percolation threshold towards a smaller absolute value is observed when compared to the random alloy reference case ($C^{\mathrm{p}}_{\mathrm{Na}}(\mathrm{I}) = 0.124 \pm 0.002$) whereas the parameter k is 8.4 ± 4.2 and the critical exponent is $\delta(\mathrm{I}) = 2.8 \pm 0.3$. However, if the percolation threshold is derived from f_{I} normal to (010) the findings agree with the random alloy reference case within the numerical uncertainties. In general, it can be hypothesised that the percolation behaviour should be independent of the direction and hence, it seems likely that this minor disagreement of the percolation threshold results from underestimated uncertainties of $C^{\mathrm{p}}_{\mathrm{Na}}(\mathrm{I})$ when effective short-range interactions are considered.

9.3.3. Dependence of jump frequencies from temperature

The temperature dependence of the jump frequencies $w_{\mathrm{Na}}/w_{\mathrm{K}}$ can be determined based on measured tracer diffusivity ratios $\widehat{D}_{\mathrm{Na}}/\widehat{D}_{\mathrm{K}}$ for VF feldspar normal to (001) with interaction energies according to Tab. 9.3. Two data points, i.e., $T = 1173\,\mathrm{K}$ and $1023\,\mathrm{K}$, are analysed and the corresponding diffusivity ratios from tracer diffusion experiments are $\widehat{D}_{\mathrm{Na}}/\widehat{D}_{\mathrm{K}} = 1/1230$ and $1/5990$, respectively (cf. Chapter 4). An iterative method with simulation runs of at least 500 jumps per K atom was employed until the experimental $\widehat{D}_{\mathrm{Na}}/\widehat{D}_{\mathrm{K}}$ data was reproduced within 10 % tolerance to determine $w_{\mathrm{Na}}/w_{\mathrm{K}}$. The best estimates are $w_{\mathrm{Na}}/w_{\mathrm{K}} = 5.32 \times 10^{-4}$ and 1.33×10^{-4} for $T = 1173\,\mathrm{K}$ and $1023\,\mathrm{K}$, respectively. Based on an interpolation of the two data points and under the assumption of an Arrhenius behaviour the temperature dependence of the jump frequencies is given by

$$w_{\mathrm{Na}}/w_{\mathrm{K}} = \exp\left(\frac{\Delta S^m}{k_{\mathrm{B}}}\right) \exp\left(-\frac{\Delta H^m}{k_{\mathrm{B}} T}\right), \tag{9.41}$$

$$\text{with } \Delta S^m = 1.92^{+1.03}_{-1.26}\, k_{\mathrm{B}} \text{ and } \Delta H^m = 0.96^{+0.10}_{-0.26}\,\mathrm{eV}.$$

The tracer correlation factors for K and Na diffusion, f_{K} and f_{Na}, respectively, are presented on an Arrhenius plot in Fig. 9.6 for the temperature range from 1023 K to 1248 K in steps of 25 K. The corresponding jump frequencies $w_{\mathrm{Na}}/w_{\mathrm{K}}$ according to Eq. 9.41 are given on a second abscissa. The data points – based on averaging over three simulations runs – are displayed for the direction normal to (001) (triangle symbols) and (010) (square and circle symbols). It can be seen from the figure that the correlation factors are ranging from 1.6×10^{-3} to 0.5 and that $f_{\mathrm{K}} \gg f_{\mathrm{Na}}$. In general, correlation factors of the slower moving species are expected to be higher than those of the faster moving species because they are not influenced by site-blocking effects (compare, e.g., with Fig. 7.4 concerning interstitialcy diffusion in a simple cubic random alloy). For both species, K and Na, correlation factors normal to (010) significantly exceed the corresponding correlation factors normal to (001). This behaviour can be understood as follows: The negative interaction energies have an increasing effect on the jump rates w_{K} and w_{Na}, which was discussed earlier. This influence is primarily observed for diffusion normal to (001), because only nearest-neighbour interactions within the *a*-*c*-plane are considered (cf. Section 9.1.4). The enhanced jump rates for diffusion normal to (001) compared to diffusion normal to (010) are, however, counterbalanced by the pertaining correlation factors. In

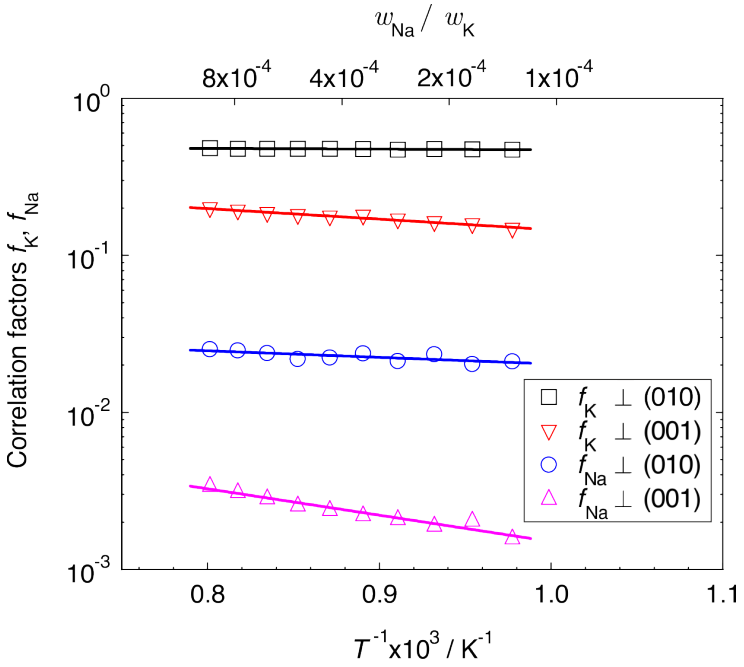

Figure 9.6.: Arrhenius plot of tracer correlation factors for K and Na diffusion via the interstitialcy mechanism in VF feldspar for the directions normal to (010) and normal to (001). Jump frequencies $w_{\mathrm{Na}}/w_{\mathrm{K}}$ are indicated on the top abscissa. Solid lines refer to linear fitting to the computed data with a temperature dependence Q^f according to Eq. 9.43. The findings for Q^f are summarised in Tab. 9.4.

summary, although the correlation factors may be greatly different this must not be true for the diffusivities, which will be demonstrated in the following section.
It can be seen from Fig. 9.6 that the correlation factors increase with increasing temperature. This behaviour is well described by Arrhenius relations that are represented by the solid lines. The total activation energy of a diffusion process can be expressed as

$$\Delta H = \tfrac{1}{2} H^f_{\mathrm{FP}} + H^m + H^b + Q^f \,, \tag{9.42}$$

where H^f_{FP} is the Frenkel pair formation enthalpy, H^m is the migration enthalpy, H^b is the binding energy and

$$Q^f = -k_{\mathrm{B}} \frac{\partial \ln f}{\partial \left(1/T\right)} \tag{9.43}$$

is the temperature dependence of a correlation factor [19]. The results obtained from fitting Eq. 9.43 to the correlations factors are compiled in Tab. 9.4. It can be seen that correlation factors normal to (010) show a weaker temperature

Table 9.4.: Temperature dependence of the tracer correlation factors for Na and K diffusion in VF feldspar normal to (010) and normal to (001). The results are derived according to Eq. 9.43.

Species	Direction	Q^f / eV
K	$\perp$ (010)	0.009 ± 0.002
K	$\perp$ (001)	0.13 ± 0.01
Na	$\perp$ (010)	0.08 ± 0.03
Na	$\perp$ (001)	0.33 ± 0.03

dependence than normal to (001) which may relate to the occurrence of short-range interactions. Beyond that, the faster moving Na atoms are subjected to the strongest temperature dependence of correlation factors which complies with observations from earlier studies (see, e.g., Chapter 7).
The temperature dependence of correlation effects has been calculated earlier, e.g., by Divinski et al. for the Ni self-diffusion in NiAl [127]. The authors reported that the general Ni self-diffusion behaviour agrees with the triple defect diffusion mechanism for Al-rich, stoichiometric and slightly Ni-rich ($\leq 52\,\text{at.}\,\%$) compositions. The temperature dependence of the triple defect mechanism in NiAl is given by $Q^f = 0.18\,\text{eV}$, which is about half of the value obtained for Na diffusion in feldspar normal to (001).

Comparison with tracer diffusion measurements

So far, tracer correlation factors f_K and f_Na for negligibly low defect concentrations ($C_\text{I} \ll 1$) were determined by MC simulations for the sublattice of alkali feldspar in the range from 1023 K to 1248 K. The absolute numerical values of diffusion coefficients $\widehat{D}_\text{K}$ and $\widehat{D}_\text{Na}$ from tracer diffusion measurements with VF feldspar are now replicated by MC simulations. According to, e.g., Eq. 9.7 the tracer diffusion coefficients $\widehat{D}$ are given by a correlation factor f and by a mean square displacement of particles per time $\langle X^2 \rangle / 2t$. The latter quantity is directly accessible because of a detailed accounting during the MC runs and hence, $\widehat{D}$ can be extracted from the simulations. In order to fit computed diffusivities (index 'MC') to experimental data (index 'exp') the migration enthalpy and entropy for one species as well as the Frenkel pair formation enthalpy H^f_FP and entropy S^f_FP are determined by the

following procedure:

(i) The diffusivities are computed by MC simulations based on the parameters

$$\tfrac{1}{2}H^f_{\mathrm{FP}} + H^m_{\mathrm{Na}} = 0 \quad \text{and} \quad \nu^0 \exp\left[\left(\tfrac{1}{2}S^f_{\mathrm{FP}} + S^m_{\mathrm{Na}}\right)/k_{\mathrm{B}}\right] = 1.$$

(ii) The expression

$$\left|\frac{1}{2}\left(\frac{\widehat{D}_{\mathrm{K,MC}}}{\widehat{D}_{\mathrm{K,exp}}} + \frac{\widehat{D}_{\mathrm{Na,MC}}}{\widehat{D}_{\mathrm{Na,exp}}}\right) - 1\right| \geq 0 \tag{9.44}$$

is evaluated for $T = 1023\,\mathrm{K}$ and $1173\,\mathrm{K}$. Initially, the absolute values deviate for obvious reasons from zero.

(iii) The parameters introduced in (i) are adjusted in order to minimize Eq. 9.44 for the data points $1023\,\mathrm{K}$ and $1173\,\mathrm{K}$.

According to the above procedure, the parameters are given by

$$\nu^0 \exp\left(\frac{\frac{1}{2}S^f_{\mathrm{FP}} + S^m_{\mathrm{Na}}}{k_{\mathrm{B}}}\right) = 13.7^{+73.8}_{-11.6}\,\mathrm{THz}$$
$$\text{and } \tfrac{1}{2}H^f_{\mathrm{FP}} + H^m_{\mathrm{Na}} = (1.93 \pm 0.18)\ \mathrm{eV}\,.$$

The computed diffusivities from MC simulations are well described by linear Arrhenius relations. In Fig. 9.7 the results for K and Na (lines) in the direction normal to (001) and normal to (010) are displayed on an Arrhenius plot and compared to the experimentally obtained diffusion coefficients (symbols). The figure demonstrates a generally good agreement between simulated and measured data, which may be seen as an indication for the suitability of the present interstitialcy diffusion model. In accordance to the measurements only a weak anisotropy of the Na diffusion is observed, which decreases with increasing temperature and achieves parity for $T = 1248\,\mathrm{K}$. In contrast, a significant anisotropy for the K diffusion is shown, i.e, $\widehat{D}_{\mathrm{K}}$ is larger normal to (001) than normal to (010) by a factor ranging from 2.5 to 13.0. However, no experimental data is so far available for K diffusion normal to (010) and the presented anisotropy effects are influenced by the selection of interaction energies.

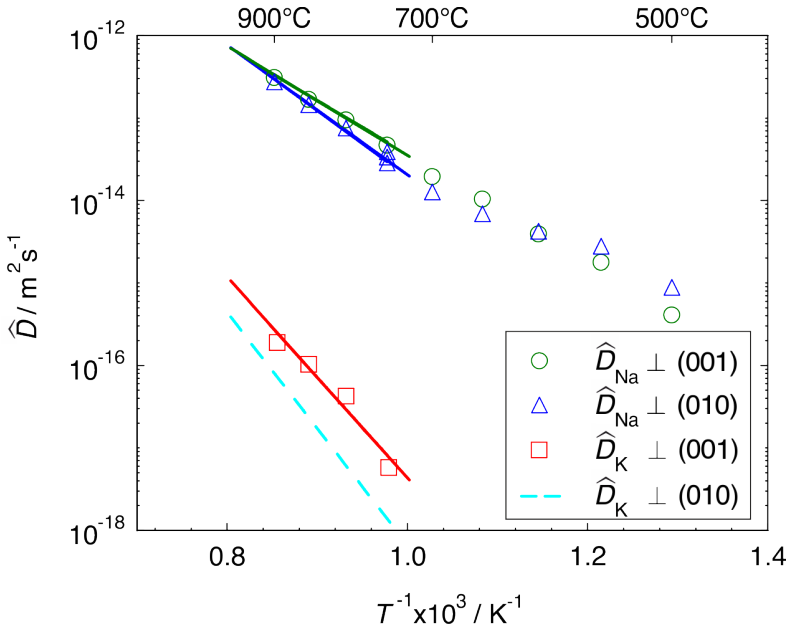

Figure 9.7.: Arrhenius plot of tracer diffusion coefficients $\widehat{D}_{\mathrm{K}}$ and $\widehat{D}_{\mathrm{Na}}$ in VF feldspar based on a fitting of simulation results (lines) to data obtained from tracer diffusion experiments (symbols, cf. Chapters 3 and 4).

Comparison of the Haven ratio from MC simulations and from measurements

In addition to tracer correlation factors f_{K} and f_{Na} also interstitialcy correlation factors f_{I} were computed by MC simulations. Based on the findings for VF feldspar normal to (001) and together with the corresponding f_{K} and f_{Na} data the Haven ratio H_{R} is determined by

$$H_{\mathrm{R}} = \frac{C_{\mathrm{Na}}\widehat{D}_{\mathrm{Na}} + C_{\mathrm{K}}\widehat{D}_{\mathrm{K}}}{C_{\mathrm{I}}D_{\mathrm{I}}} \,. \tag{9.45}$$

The results are presented in Fig. 9.8 as a function of temperature ranging from 1023 K to 1248 K and compared with experimentally obtained data for H_{R}. It can be seen from the figure that the computed H_{R} results increase linearly with increasing temperature (solid line) with the numerical values ranging from 0.29 to 0.45. The observed temperature dependence is not related to a temperature dependence of the jump frequencies but rather to a temperature dependence of correlation factors. The correlation behaviour is characterised by a deviation of $f_{\mathrm{Na}}/f_{\mathrm{I}}$ from 0.84 to 1.23 for $T = 1023\,\mathrm{K}$ and $T = 1248\,\mathrm{K}$, respectively, and the

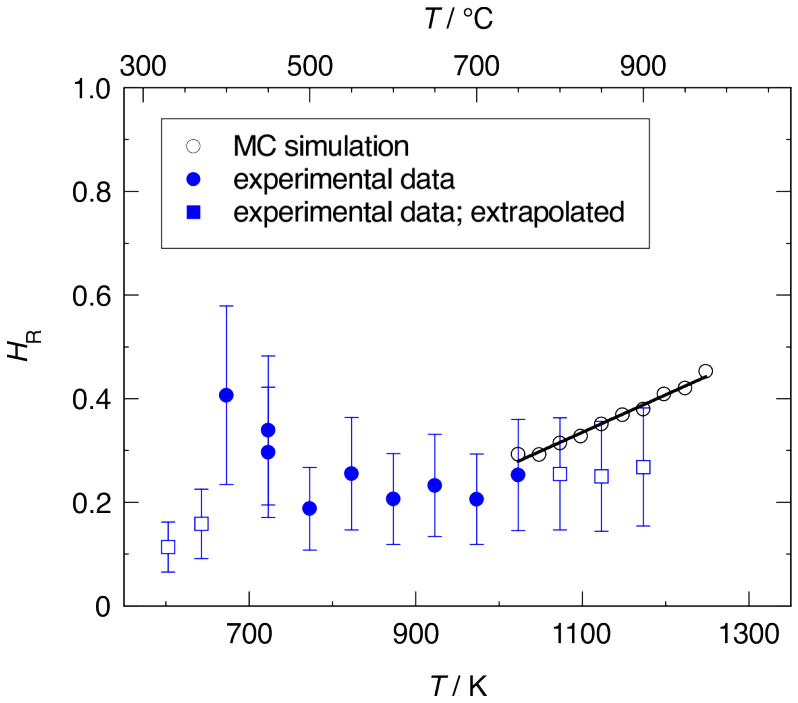

Figure 9.8.: Haven ratio H_R as a function of temperature T from MC simulations for VF feldspar normal to (001) (open circles). The solid line represents linear fitting to the data points. H_R data obtained from measurements of $\widehat{D}_{Na}$ and D_σ (see Chapters 3 and 5) is shown for comparison (solid symbols). Data points for $T \leq 643\,K$ and $T \geq 1073\,K$ are based on extrapolated D_σ results (open squares).

empirical relation $H_R \approx 0.35 f_{Na}/f_I$ holds true over the investigated temperature range. It can be concluded that the geometrical contribution to H_R is mainly influenced by double interstitialcy I-S-S jumps with a theoretical geometrical value of 0.336. A comparison with experimental H_R data in Fig. 9.8 demonstrates the consistency with the computed results within experimental uncertainties.

The Haven ratio may also be determined for the direction normal to (010) over a wide range of temperature based on the ionic conductivity measurements by El Maanaoui et al. [56]. With the aid of ^{22}Na tracer diffusion measurements (see Chapter 3) and Eq. 9.45 the absolute value of the Haven ratio is, e.g., given by $H_R = 0.51 \pm 0.28$ for $T = 1023\,K$. For comparison, the computed Haven ratio from MC simulations is 0.23 ± 0.01 for the same temperature, which is consistent within the experimental uncertainty. However, it should be noted that the experimental data suffers from considerable scatter and thus need to be interpreted with the utmost caution. More experimental evidence is therefore needed to demonstrate whether the present interstitialcy diffusion model sufficiently describes the Haven

ratio also in the direction normal to (010). As a consequence, adaptions of this simple model could be required if H_{R} significantly differs from the current observation.

9.3.4. Correlation effects below the percolation threshold

The occurrence of a percolation threshold is, in general, related to the complete immobility (site-blocking) of one species of an alloy (e.g. $w_{\mathrm{K}} = 0$). Under this circumstance, the migration of other species is restricted to clusters of finite size and long-range diffusion is therefore impossible. However, in the real feldspar mineral the slower moving K-atoms are not fully immobile but rather significantly slower than the Na atoms so that the jump frequencies range from $w_{\mathrm{Na}}/w_{\mathrm{K}} = 1.3 \times 10^{-4}$ to 9.4×10^{-4} for 1023 K and 1248 K, respectively (see Fig. 9.6). The faster moving Na atoms may therefore escape from finite clusters via slow exchanges with K atoms and the long-range diffusion of Na is then bounded to the K diffusivity. This situation of diffusion below the virtual percolation threshold ($C_{\mathrm{Na}} < C_{\mathrm{Na}}^{\mathrm{p}}$) is inspected in the present section by MC simulations of tracer correlation factors. A natural orthoclase mineral originating from Madagascar (MO) with the composition $\mathrm{Or_{95}Ab_5}$ is a suitable reference case under this requirement and experimental data for ^{22}Na tracer diffusion in MO were presented and discussed in Chapter 3. However, experimental data for K diffusion in MO feldspar is lacking which, in turn, may in good approximation be provided from corresponding measurements from VF feldspar. A comparison of this data with the data from Foland's study [8] of alkali diffusion in a feldspar from Benson Mines gives evidence that $\widehat{D}_{\mathrm{K}}$ is subject to only minor composition effects for $0.95 \geq C_{\mathrm{K}} \geq 0.85$, which was discussed in Chapter 4. The assumption of a composition independent behaviour of $\widehat{D}_{\mathrm{K}}$ therefore seems to be justified in good approximation.
Because of virtual site-blocking effects from K atoms for a composition below the percolation threshold the activation energies for Na and K diffusion appear to be similar in tracer diffusion measurements, i.e., $\Delta H = (2.00 \pm 0.04)$ eV and $\Delta H = (2.4 \pm 0.4)$ eV, respectively. The quality for a determination of jump frequencies $w_{\mathrm{Na}}/w_{\mathrm{K}}$ in MO feldspar based on this weak temperature dependence of $\widehat{D}_{\mathrm{Na}}/\widehat{D}_{\mathrm{K}}$ is, a priori, restricted because correlation factors compensate for differences in jump frequencies. Hence, the same temperature relation as for VF feldspar according to Eq. 9.41 with $\Delta S^m = 1.92\, k_{\mathrm{B}}$ and $\Delta H^m = 0.96$ eV must be presumed which holds, beyond doubt, only for a rough estimate.

Table 9.5.: Temperature dependence of the tracer correlation factors for Na and K diffusion in MO feldspar normal to (010) and normal to (001). The results are derived according to Eq. 9.43.

Species	Direction	Q^f / eV
K	$\perp$ (010)	0.020 ± 0.004
K	$\perp$ (001)	0.26 ± 0.01
Na	$\perp$ (010)	1.32 ± 0.01
Na	$\perp$ (001)	1.78 ± 0.01

Tracer correlation factors were computed for a simulation box with the composition $C_{\mathrm{Na}} = 0.05$ and $C_{\mathrm{K}} = 0.95$ and with the energy parameters for short-range interactions according to Tab. 9.3. For $T = 1173\,\mathrm{K}$ simulation boxes ranging from $20a \times 20b \times 20c$ (32,000 substitutional atoms) to $40a \times 40b \times 40c$ (256,000 substitutional atoms) were analysed and no dependence between box size and MC results could be observed. The following findings are therefore based on simulation boxes of $20a \times 20b \times 20c$ in all cases. In Fig. 9.9, the results – based on averaging over three simulations runs – for f_{K} and f_{Na} in the direction normal to (010) and normal to (001) are displayed on an Arrhenius plot for temperatures varying from 1023 K to 1223 K. The associated jump frequencies $w_{\mathrm{Na}}/w_{\mathrm{K}}$ are indicated on a second abscissa. It can be seen from the figure that the correlation factors are increasing with increasing temperature and cover a range from 2.4×10^{-6} to 0.2. When compared with the correlation factors for diffusion in VF feldspar in Fig. 9.6 the same behaviour of larger numerical f values for diffusion normal to (010) than normal to (001) are observed. However, the correlation factors in MO feldspar are considerably reduced compared to VF feldspar, which clearly relates to percolation problems.

The temperature dependence of the correlation factors is well described by a linear relation on the Arrhenius plot with a slope Q^f given by Eq. 9.43. In Table 9.5 the results for fitting of the 'activation energy' Q^f to the computed data is summarised. A distinct increase of Q^f for diffusion in MO feldspar is observed compared to VF feldspar, which particularly concerns the Na diffusion. The observed 'activation energies' on the order of 1 eV seem to be a characteristic property for the Na diffusion for a feldspar composition of $C_{\mathrm{Na}} < C^{\mathrm{p}}_{\mathrm{Na}}$. Beyond that, the findings give reason for the numerical value found for $\widehat{D}_{\mathrm{Na}}/\widehat{D}_{\mathrm{K}}$ from

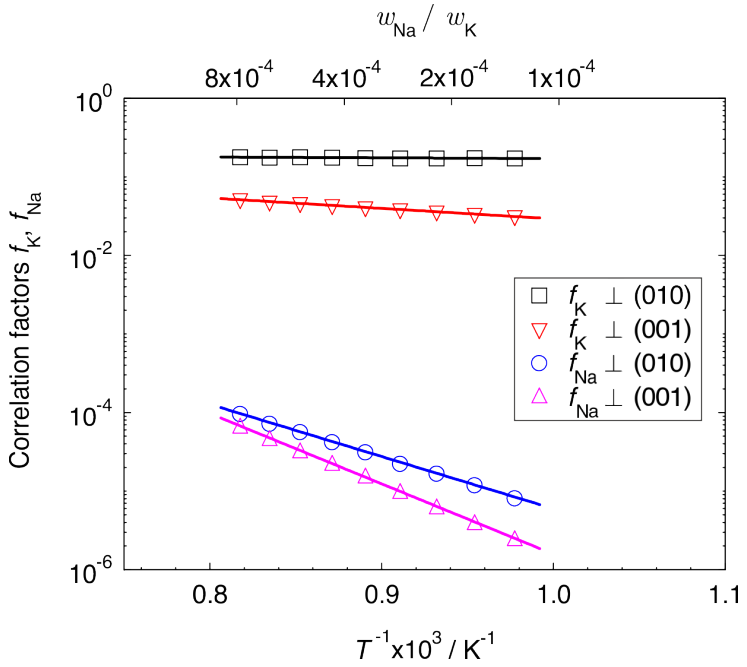

Figure 9.9.: Arrhenius plot of tracer correlation factors for K and Na diffusion via the interstitialcy mechanism in MO feldspar for the directions normal to (010) and normal to (001). Jump frequencies $w_{\mathrm{Na}}/w_{\mathrm{K}}$ are indicated on the top abscissa and derived from the analysis of correlation effects in VF feldspar (see Section 9.3.3). Solid lines refer to linear fitting to the computed data with a temperature dependence Q^f according to Eq. 9.43. The findings for Q^f are compiled in Tab. 9.5.

tracer diffusion measurements, i.e., between 46 and 81 for $T = 1173\,\mathrm{K}$ and $1023\,\mathrm{K}$, respectively. According to the analysis for VF feldspar also absolute numerical values of diffusivities for MO feldspar can be replicated. Fitting of jump frequencies to experimental data for Na diffusion in MO feldspar and K diffusion in VF feldspar in a direction normal to (001) according to Eq. 9.44 gives

$$\nu^0 \exp\left(\frac{\frac{1}{2}S^f_{\mathrm{FP}} + S^m_{\mathrm{Na}}}{k_{\mathrm{B}}}\right) = 1.4^{+19.9}_{-1.3}\,\mathrm{THz}$$
$$\text{and } \tfrac{1}{2}H^f_{\mathrm{FP}} + H^m_{\mathrm{Na}} = (1.45 \pm 0.26)\ \mathrm{eV}.$$

The computed diffusivities for MO feldspar are well described by linear Arrhenius relations. In Fig. 9.10 the results for K and Na (lines) in the direction normal to (001) and normal to (010) are shown on an Arrhenius plot and compared to the experimentally obtained diffusion coefficients (symbols). The Na diffusivity normal to (001) exceeds the diffusivity normal to (001) by a factor of ~ 2, which is revealed

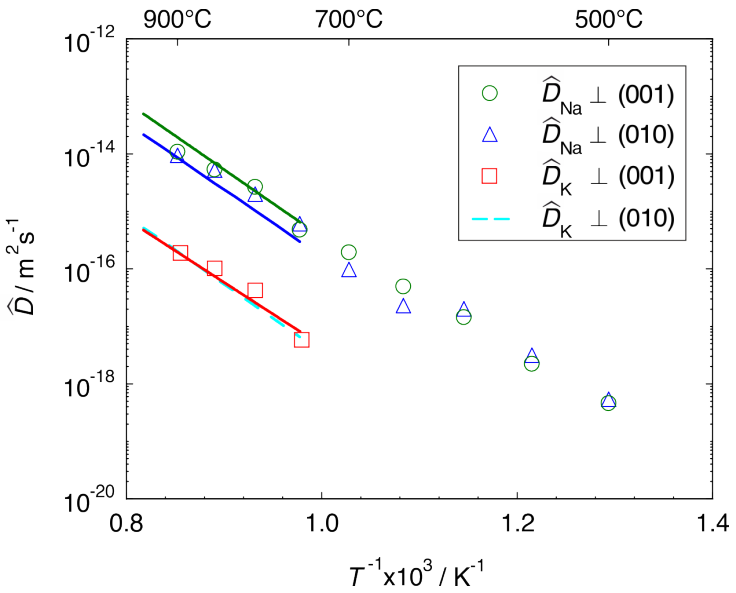

Figure 9.10.: Arrhenius plot of tracer diffusion coefficients $\widehat{D}_{\mathrm{K}}$ and $\widehat{D}_{\mathrm{Na}}$ in MO feldspar. The results are based on a fitting of computed data (lines) to data obtained from ^{22}Na tracer diffusion experiments in MO feldspar and ^{43}K experiments in VF feldspar (symbols, cf. Chapters 3 and 4) under the assumption of a negligibly small composition dependence of K self-diffusion.

in the figure. In contrast, no significant anisotropy is observed for the K component. From the experimental $\widehat{D}_{\mathrm{Na}}$ data a corresponding anisotropic behaviour may not be safely concluded because statistical scatter of the data points could obscure hypothetical variations between the two directions. The computed data agree well with the experimental data and deviations that particularly result from statistical scatter of the experimental data amount to less than 50 %.

9.4. Summary and conclusions

In the present chapter, diffusion on the alkali sublattice of monoclinic feldspar via the interstitialcy mechanism with additional double interstitialcy jumps was studied by Monte Carlo (MC) simulations. Correlation factors were computed with a convenient and effective partial correlation factors (PCF) method that was also employed in Chapters 6, 7 and 8. From computed f_{I} data a numerical value for the site-percolation threshold of $C_{\mathrm{Na}}^{\mathrm{p}} = 0.124 \pm 0.002$ was observed if short-range interactions between the cations are neglected. The findings from the present analysis demonstrate the consistency of an interstitialcy diffusion model in

alkali feldspar with experimental data over a composition range from $C_{\mathrm{Na}} = 0.15$ to 0.05. This regime is of special interest because a transition from percolated to non-percolated Na diffusion is observed that is in accordance with the demonstrated correlation effects.

Based on the concepts of the Ising model short-range interactions between nearest-neighbour atoms were considered for a negative ordering energy, i.e., $v = -72.0\,\mathrm{meV}$. With the help of this approach diffusivities derived from tracer diffusion experiments in VF feldspar ($\mathrm{Or_{83}Ab_{15}Cs_1}$) were successfully replicated by MC simulations. The temperature dependence of jump frequencies is well described by $w_{\mathrm{Na}}/w_{\mathrm{K}} = \exp\left(\Delta S^m/k_{\mathrm{B}}\right)\exp\left(\Delta H^m/k_{\mathrm{B}}T\right)$ with $\Delta S^m = 1.92^{+1.03}_{-1.26}\,k_{\mathrm{B}}$ and $\Delta H^m = 0.96^{+0.10}_{-0.26}\,\mathrm{eV}$. In addition, the jump rate for Na atoms is given by $\nu^0 \exp\left(\left(\frac{1}{2}S^f_{\mathrm{FP}} + S^m_{\mathrm{Na}}\right)/k_{\mathrm{B}}\right) = 13.7^{+73.8}_{-11.6}\,\mathrm{THz}$ and the corresponding enthalpies by $\frac{1}{2}H^f_{\mathrm{FP}} + H^m_{\mathrm{Na}} = (1.93 \pm 0.18)\,\mathrm{eV}$. Similar concepts were used to link MC data with measured Na diffusivities obtained for MO feldspar ($\mathrm{Or_{95}Ab_5}$). The determination of $w_{\mathrm{Na}}/w_{\mathrm{K}}$ was restricted due to a weak temperature dependence of $\widehat{D}_{\mathrm{Na}}/\widehat{D}_{\mathrm{K}}$ and hence, the same results as for VF feldspar were presumed. Based on this approximation, the jump rate for Na atoms is given by $\nu^0 \exp\left(\left(\frac{1}{2}S^f_{\mathrm{FP}} + S^m_{\mathrm{Na}}\right)/k_{\mathrm{B}}\right) = 1.4^{+19.9}_{-1.3}\,\mathrm{THz}$ and the corresponding enthalpies by and $\frac{1}{2}H^f_{\mathrm{FP}} + H^m_{\mathrm{Na}} = (1.45 \pm 0.26)\,\mathrm{eV}$.

A comparison of the derived enthalpies for Na diffusion in MO feldspar and VF feldspar shows that $\frac{1}{2}H^f_{\mathrm{FP}} + H^m_{\mathrm{Na}}$ decreases towards the K-rich end-member composition. This result is remarkable because tracer diffusion experiments suggest the contrary behaviour of a higher activation energy for Na diffusion in MO feldspar than in VF feldspar. In conclusion, the activation energies derived from tracer diffusion experiments can be obscured from extremely large correlation effects, which is the case for Na diffusion in MO feldspar. Furthermore, these findings corroborate predictions from Jones et al. [54] who reported a similar behaviour for the migration energy via vacancies from molecular dynamics computations (see Tab. 3.2).

From measured ionic conductivity (see Chapter 5) and tracer diffusion (see Chapter 3) the experimentally obtained Haven ratio for the direction normal to (001) was reported to range from 0.11 to 0.40. This observation is in good agreement with computed values for the Haven ratio obtained from MC simulations, i.e., between 0.29 and 0.45. It seems therefore rather unlikely that *direct*-interstitial I-I jumps of Na atoms occur at a significant rate since these jumps show an enhancing

effect on H_{R} as demonstrated in Chapter 8. It can be concluded that the present interstitialcy diffusion model with the extension of I-S-S double interstitialcy jumps and short-range interactions is consistent with the percolation behaviour and with H_{R} for alkali diffusion in alkali feldspar.

10. Summary & Outlook

The present thesis focuses on a comprehensive analysis of the Na and K transport on the sublattice of alkali feldspar. Self-diffusion measurements, dc ionic conductivity measurements and Monte Carlo simulations were employed to elucidate the microscopic diffusion mechanism and to interpret the characteristic composition dependent effects of the Na self-diffusion.

The tracer diffusion of ^{22}Na was analysed for three single crystalline alkali feldspar minerals in the composition range from 71 % to 95 % K on the alkali sublattice (cf. Chapter 3). In all cases the Arrhenius relation for the direction normal to (001) is equal to the corresponding relation for the direction normal to (010) within the range of experimental uncertainties, whereas the Na-K interdiffusion is markedly direction dependent [11, 12, 13]. A striking feature of the Na diffusion is the considerable composition dependence from the VF feldspar ($Or_{83}Ab_{15}Cs_1$) to the most K-rich MO feldspar ($Or_{95}Ab_5$). Depending on the temperature the Na diffusivities are 20 and 900 times smaller than those observed for the VF Eifel sanidine at 1173 K and 773 K, respectively. The observed behaviour might be interpreted as being a result of severe percolation problems at the close-to-potassium end-member composition. Furthermore, the activation energy found for the MO feldspar is increased by ~ 0.7 eV compared to the RK and VF Eifel sanidines, which could be a result of a different temperature activation of the pertaining correlation factors.

For the VF feldspar measurements of the ^{43}K tracer diffusion normal to (001) were performed after isotope implantation at the ISOLDE facility at CERN (cf. Chapter 4). The activation energy of the K self-diffusion is (2.4 ± 0.4) eV, which is considerably higher than the activation energy of the Na self-diffusion in the same mineral, i.e., (1.27 ± 0.03) eV. Accordingly, the diffusivity ratio $\widehat{D}_{\mathrm{Na}}/\widehat{D}_{\mathrm{K}}$ ranges from 1230/1 to 5990/1 at 1173 K and 1023 K, respectively. The Arrhenius relation agrees well with the findings from Foland [8] for the K self-diffusion in the more K-rich BM feldspar ($C_{\mathrm{K}} \approx 0.94$), suggesting that the K self-diffusion is

affected by rather minor composition dependent effects. This finding corroborates the interpretation that the slow Na self-diffusion in MO feldspar is caused by severe percolation problems instead of increased migration barriers. So far, there is a deficiency of direction dependent measurements of the K self-diffusion in alkali feldspar, which is important for the interpretation of the markedly direction dependent Na-K interdiffusion data. The investigations into this area are in progress at the University of Vienna with direction dependent measurements of the ^{41}K diffusion in alkali feldspar.

The ionic conductivity was measured in VF feldspar normal to (001) between 673 K and 1053 K (cf. Chapter 5). Effects of water were precluded by high temperature pre-annealing at 1323 K for 4 days. The temperature behaviour is well described by an Arrhenius equation with an activation energy of $\Delta H = (1.226 \pm 0.004)$ eV, similar to the activation energy of the Na self-diffusion in the same mineral. This implies a dominant role of the Na^+ ions in overall mass and charge transport. The Haven ratio H_R for VF feldspar was found to range from 0.11 to 0.40 in the direction normal to (001). The significant deviation from $H_R = 1$ gives strong evidence that the Na self-diffusion is correlated, which implies that direct interstitial jumps are much less frequent than those jumps related to an exchange with a diffusion vehicle, e.g., interstitialcy jumps. In conclusion, the experimental data on self-diffusion of Na and K as well as the ionic conductivity data give good evidence that the migration of Na and K is characterised by a correlated diffusion mechanism with a virtual percolation threshold within the composition range $0.05 < C^p_{Na} < 0.15$.

By using Monte Carlo simulations tracer correlation factors for the vacancy diffusion mechanism in the Na-K sublattice were computed for different compositions C_{Na} and various jump frequency ratios w_K/w_{Na} but with uniform frequencies of the different jump types for either component (cf. Chapters 6). Vacancy jumps to $z = 5$ nearest-neighbour atoms were considered in the pertinent simulation model and the alkali vacancy diffusion is characterised by a percolation threshold of $C^p_{Na} = 0.360$ independent of crystallographic orientation. This percolation threshold clearly disagrees with the above findings from Na tracer diffusion measurements and hence, the diffusion via vacancies has probably a rather minor contribution to the overall alkali transport in the K-rich composition domain.

Manning's random alloy model – originally developed for diffusion via vacancies – was adapted to the special requirements of diffusion via the interstitialcy mechanism (cf. Chapter 7 and 8). In a first approach, the correlation factors for the

interstitialcy diffusion in a randomly ordered simple cubic alloy AB were calculated based on this adapted model via Monte Carlo simulations. It was demonstrated that correlation effects and tracer diffusivity ratios ($\widehat{D}_\mathrm{B}/\widehat{D}_\mathrm{A}$) related to the interstitialcy mechanism may significantly differ from those related to the vacancy mechanism, which is expressed, e.g., by a different percolation threshold. Interestingly, a second-order percolation threshold was observed which is related to the abundance of nearest-neighbour A-B occurrences.

The methods and concepts were adapted to the more complex monoclinic Na-K sublattice of alkali feldspar with $\left(0, 0, \frac{1}{2}\right)$ and equivalent interstitial sites (cf. Chapter 9). Among the I-S interstitialcy jumps to ten nearest-neighbour atoms additional double interstitialcy (I-S-S) jumps within the *a*-*c*-plane were considered in the investigated diffusion model. The basic assumption of uniform frequencies of the different I-S jump types for either component (Na and K) was considered and the pertinent percolation threshold of $C^\mathrm{p}_\mathrm{Na} = 0.124 \pm 0.002$ was observed, which is in excellent agreement with the experimental data (cf. Section 3.2). Behrens et al. [17] recognised that beside the $\left(0, 0, \frac{1}{2}\right)$ interstitial sites further interstitial sites at $\left(\frac{1}{2}, 0, \frac{1}{2}\right)$ and equivalent positions can be identified in the feldspar structure. Elementary jumps from these sites, however, do not lead to an increased number of pathways for interstitialcy exchange and therefore, the correlation factors are unaffected by this property. An analysis whether these sites can be occupied by $\mathrm{Na_I}$ and $\mathrm{K_I}$ self-interstitials might be feasible via state of the art transmission electron microscopy (e.g., FEI Titan Themis G3 300).

Phillips et al. [122] measured the Na-K distribution in alkali feldspar via nuclear magnetic resonance spectroscopy and found experimental evidence for the clustering tendency of Na atoms. Effective short-range interactions between the cations were therefore considered in the diffusion model comprising three nearest-neighbour bonds within the *a*-*c*-plane. Tracer and interstitialcy correlation factors were computed via Monte Carlo simulations as a function of the ordering energy v. When compared with the experimental findings most consistent results for H_R and $\widehat{D}_\mathrm{Na}/\widehat{D}_\mathrm{K}$ were obtained for $v = -0.072\,\mathrm{meV}$ (clustering) with H_R ranging between 0.29 and 0.45 in the direction normal to (010). Based on this model, the diffusivities $\widehat{D}_\mathrm{Na}$ and $\widehat{D}_\mathrm{K}$ obtained from the Monte Carlo simulations were fitted

to the experimental data for VF feldspar. The findings comprise the temperature dependence of jump frequencies, which is well described by

$$w_{\mathrm{Na}}/w_{\mathrm{K}} = \exp\left(\Delta S^m/k_{\mathrm{B}}\right)\exp\left(\Delta H^m/k_{\mathrm{B}}T\right),$$

with $\Delta S^m = 1.92^{+1.03}_{-1.26}\,k_{\mathrm{B}}$ and $\Delta H^m = 0.96^{+0.10}_{-0.26}\,\mathrm{eV}$. The jump rate for Na atoms is given by

$$\nu^0 \exp\left(\left(\tfrac{1}{2}S^f_{\mathrm{FP}} + S^m_{\mathrm{Na}}\right)/k_{\mathrm{B}}\right) = 13.7^{+73.8}_{-11.6}\,\mathrm{THz}$$

and the corresponding enthalpies by

$$\tfrac{1}{2}H^f_{\mathrm{FP}} + H^m_{\mathrm{Na}} = (1.93 \pm 0.18)\ \mathrm{eV}\,.$$

In a similar way, the diffusion coefficients were fitted to the experimental data for the more K-rich MO feldspar, providing a good agreement between the simulated and the measured diffusivities. The temperature dependence of the correlation factor is considerably higher for MO feldspar, i.e., $Q^f = (1.78 \pm 0.01)$ eV in the direction normal to (001), compared to the findings for VF feldspar that is given by $Q^f = (0.33 \pm 0.03)$ eV. Based on this study it is conceivable that the Na and K atoms migrate via a common interstitialcy mechanism on the Na-K sublattice of alkali feldspar. For compositions below a virtual percolation threshold $C_{\mathrm{Na}} < C^{\mathrm{p}}_{\mathrm{Na}} = 0.124 \pm 0.002$ the transport of Na is affected by severe percolation problems, which implies a considerably higher temperature activation of the pertinent correlation factors.

The presented conception is based on the most basic assumption of uniform jump frequencies of the different jump types because of deficient information concerning the migration barriers of the Na and K diffusion. Future work could refine this picture, e.g., through molecular dynamic simulations of the migration barriers, defect formation energies and ordering energies. The limitation of the present study comprising equal jump frequencies for $\mathrm{Na_I}$ and $\mathrm{K_I}$ jumps (the elementary jump frequencies are only determined by the type of substitutional atom) could probably be solved with the aid of such calculations. Furthermore, interactions with the silicate framework structure might be considered to analyse possible effects from the Al-Si ordering degree on the Na and K diffusion in alkali feldspar.

A. ^{22}Na tracer diffusion coefficients

Table A.1.: Diffusion coefficients $\widehat{D}_{\mathrm{Na}}$ of ^{22}Na in alkali feldspars of three different compositions RK ($Or_{71}Ab_{26}Cs_2$), VF ($Or_{83}Ab_{15}Cs_1$) and MO $Or_{95}Ab_5$ normal to (001), normal to (010) and in the direction [100] (only MO). The $\widehat{D}_{\mathrm{Na}}$ values were determined by fitting either a Gaussian or a complementary error function (erfc) to the diffusion profiles. Uncertainties are based on an estimated statistical variation of 30 % for all radiotracer diffusion experiments.

Feldspar	Direction	T/K	t_{diff}/min	Function	$\widehat{D}_{\mathrm{Na}}/\mathrm{m^2s^{-1}}$	Reference
RK	$\perp$ (001)	1073	32	Gauss	$(4.0 \pm 1.2) \times 10^{-14}$	[51]
RK	$\perp$ (001)	1023	70	Gauss	$(2.3 \pm 0.7) \times 10^{-14}$	[51]
RK	$\perp$ (001)	973	130	Gauss	$(1.3 \pm 0.4) \times 10^{-14}$	[51]
RK	$\perp$ (001)	923	300	Gauss	$(5.5 \pm 1.7) \times 10^{-15}$	[51]
RK	$\perp$ (001)	923	300	Gauss	$(2.6 \pm 0.8) \times 10^{-15}$	[51]
RK	$\perp$ (001)	873	5	erfc	$(1.2 \pm 0.4) \times 10^{-15}$	[51]
RK	$\perp$ (001)	823	7	erfc	$(2.5 \pm 0.8) \times 10^{-16}$	[51]
RK	$\perp$ (001)	773	12	erfc	$(6.4 \pm 1.9) \times 10^{-17}$	[51]
RK	$\perp$ (001)	723	20	erfc	$(1.0 \pm 0.3) \times 10^{-16}$	[51]
RK	$\perp$ (001)	673	100	erfc	$(2.2 \pm 0.7) \times 10^{-17}$	[51]
RK	$\perp$ (001)	643	360	erfc	$(8.8 \pm 2.6) \times 10^{-18}$	[51]
RK	$\perp$ (010)	1073	60	Gauss	$(7.6 \pm 2.3) \times 10^{-14}$	[51]
RK	$\perp$ (010)	1023	120	Gauss	$(3.3 \pm 1.0) \times 10^{-14}$	[51]
RK	$\perp$ (010)	973	160	Gauss	$(1.1 \pm 0.4) \times 10^{-14}$	[51]
RK	$\perp$ (010)	923	300	Gauss	$(5.6 \pm 1.7) \times 10^{-15}$	[51]
RK	$\perp$ (010)	873	5	erf	$(4.8 \pm 1.4) \times 10^{-15}$	[51]
RK	$\perp$ (010)	823	4	erfc	$(1.7 \pm 0.6) \times 10^{-15}$	[51]
RK	$\perp$ (010)	773	4	erfc	$(8.4 \pm 2.6) \times 10^{-16}$	[51]
RK	$\perp$ (010)	723	18	erfc	$(3.8 \pm 1.1) \times 10^{-16}$	[51]
RK	$\perp$ (010)	723	80	erfc	$(9.7 \pm 2.9) \times 10^{-17}$	[51]

Feldspar	Direction	T/K	t_{diff}/min	Function	$\widehat{D}_{\mathrm{Na}}/\mathrm{m^2s^{-1}}$	Reference
RK	$\perp$ (010)	673	90	erfc	$(2.1 \pm 0.7) \times 10^{-17}$	[51]
RK	$\perp$ (010)	643	360	erfc	$(1.0 \pm 0.4) \times 10^{-17}$	[51]
VF	$\perp$ (001)	1173	5	Gauss	$(3.1 \pm 1.0) \times 10^{-13}$	[64]
VF	$\perp$ (001)	1123	60	Gauss	$(1.7 \pm 0.5) \times 10^{-13}$	[64]
VF	$\perp$ (001)	1073	90	Gauss	$(9.5 \pm 2.8) \times 10^{-14}$	[64]
VF	$\perp$ (001)	1023	120	Gauss	$(4.7 \pm 1.4) \times 10^{-14}$	[64]
VF	$\perp$ (001)	973	135	Gauss	$(2.0 \pm 0.6) \times 10^{-14}$	[64]
VF	$\perp$ (001)	923	135	Gauss	$(1.0 \pm 0.4) \times 10^{-14}$	[64]
VF	$\perp$ (001)	873	180	Gauss	$(3.9 \pm 1.2) \times 10^{-15}$	[64]
VF	$\perp$ (001)	823	5	erf	$(1.8 \pm 0.6) \times 10^{-15}$	[64]
VF	$\perp$ (001)	773	5	erfc	$(4.1 \pm 1.2) \times 10^{-16}$	[128]
VF	$\perp$ (001)	723	5	erfc	$(1.8 \pm 0.6) \times 10^{-16}$	[128]
VF	$\perp$ (001)	723	10	erfc	$(2.0 \pm 0.6) \times 10^{-16}$	this work
VF	$\perp$ (001)	673	15	erfc	$(5.5 \pm 1.7) \times 10^{-17}$	this work
VF	$\perp$ (001)	673	150	erfc	$(9.2 \pm 2.8) \times 10^{-17}$	[128]
VF	$\perp$ (001)	643	120	erfc	$(8.4 \pm 2.5) \times 10^{-18}$	[128]
VF	$\perp$ (001)	603	2880	erfc	$(1.4 \pm 0.5) \times 10^{-18}$	this work
VF	$\perp$ (010)	1173	5	Gauss	$(2.6 \pm 0.8) \times 10^{-13}$	[128]
VF	$\perp$ (010)	1123	60	Gauss	$(1.4 \pm 0.5) \times 10^{-13}$	[128]
VF	$\perp$ (010)	1073	90	Gauss	$(7.2 \pm 2.2) \times 10^{-14}$	[128]
VF	$\perp$ (010)	1023	60	Gauss	$(3.2 \pm 1.0) \times 10^{-14}$	[128]
VF	$\perp$ (010)	1023	120	Gauss	$(2.7 \pm 0.9) \times 10^{-14}$	[128]
VF	$\perp$ (010)	1023	540	Gauss	$(3.7 \pm 1.1) \times 10^{-14}$	this work
VF	$\perp$ (010)	973	135	Gauss	$(1.2 \pm 0.4) \times 10^{-14}$	[128]
VF	$\perp$ (010)	923	135	Gauss	$(6.5 \pm 2.0) \times 10^{-15}$	[128]
VF	$\perp$ (010)	873	180	Gauss	$(3.9 \pm 1.2) \times 10^{-15}$	[128]
VF	$\perp$ (010)	823	5	Gauss	$(1.8 \pm 0.6) \times 10^{-15}$	[128]
VF	$\perp$ (010)	773	5	erfc	$(4.1 \pm 1.2) \times 10^{-16}$	[128]
VF	$\perp$ (010)	723	5	erfc	$(1.8 \pm 0.6) \times 10^{-16}$	[128]
VF	$\perp$ (010)	673	10	erfc	$(9.2 \pm 2.8) \times 10^{-17}$	[128]
VF	$\perp$ (010)	623	12	erfc	$(8.4 \pm 2.5) \times 10^{-18}$	[128]
MO	$\perp$ (001)	1173	30	Gauss	$(1.1 \pm 0.4) \times 10^{-14}$	[50]
MO	$\perp$ (001)	1123	20	Gauss	$(5.3 \pm 1.6) \times 10^{-15}$	[50]

Feldspar	Direction	T/K	t_{diff}/min	Function	$\widehat{D}_{\mathrm{Na}}/\mathrm{m^2s^{-1}}$	Reference
MO	$\perp$ (001)	1073	480	Gauss	$(2.7 \pm 0.8) \times 10^{-15}$	[50]
MO	$\perp$ (001)	1023	1440	Gauss	$(4.8 \pm 1.4) \times 10^{-16}$	[50]
MO	$\perp$ (001)	973	4320	Gauss	$(1.9 \pm 0.6) \times 10^{-16}$	[50]
MO	$\perp$ (001)	923	180	erfc	$(4.9 \pm 1.5) \times 10^{-17}$	[50]
MO	$\perp$ (001)	873	180	erfc	$(1.4 \pm 0.5) \times 10^{-17}$	[50]
MO	$\perp$ (001)	823	4320	erfc	$(2.2 \pm 0.7) \times 10^{-18}$	[50]
MO	$\perp$ (001)	773	5760	erfc	$(4.6 \pm 1.4) \times 10^{-19}$	[50]
MO	$\perp$ (010)	1173	90	Gauss	$(8.8 \pm 2.6) \times 10^{-15}$	[50]
MO	$\perp$ (010)	1123	180	Gauss	$(4.9 \pm 1.5) \times 10^{-15}$	[50]
MO	$\perp$ (010)	1073	10	Gauss	$(1.9 \pm 0.6) \times 10^{-15}$	[50]
MO	$\perp$ (010)	1023	2880	Gauss	$(5.7 \pm 1.7) \times 10^{-16}$	[50]
MO	$\perp$ (010)	973	180	Gauss	$(9.1 \pm 2.7) \times 10^{-17}$	[50]
MO	$\perp$ (010)	923	240	Gauss	$(2.1 \pm 0.7) \times 10^{-17}$	[50]
MO	$\perp$ (010)	873	240	erfc	$(1.9 \pm 0.6) \times 10^{-17}$	[50]
MO	$\perp$ (010)	823	1440	erfc	$(3.0 \pm 0.9) \times 10^{-18}$	[50]
MO	$\perp$ (010)	773	5760	erfc	$(5.0 \pm 1.5) \times 10^{-19}$	[50]
MO	[100]	1173	90	erfc	$(3.8 \pm 1.1) \times 10^{-15}$	[51]
MO	[100]	1073	23	Gauss	$(4.9 \pm 1.5) \times 10^{-16}$	[51]
MO	[100]	973	60	Gauss	$(6.1 \pm 1.8) \times 10^{-17}$	[51]
MO	[100]	873	240	erfc	$(2.3 \pm 0.7) \times 10^{-18}$	[51]
MO	[100]	773	8640	Gauss	$(1.1 \pm 0.4) \times 10^{-19}$	[51]

Bibliography

[1] F.S. Spear, *Metamorphic phase equilibria and pressure-temperature-time paths*, Mineralogical Society of America Washington, 1995.

[2] R. Abart, E. Petrishcheva, R. Wirth, and D. Rhede, *Exsolution by spinodal decomposition II: perthite formation during slow cooling of anatexites from Ngoronghoro, Tanzania*, Am. J. Sci. 309 (2009), pp. 450–475.

[3] E. Petrishcheva and R. Abart, *Exsolution by spinodal decomposition I: evolution equation for binary mineral solutions with anisotropic interfacial energy*, Am. J. Sci. 309 (2009), pp. 431–449.

[4] E. Petrishcheva and R. Abart, *Exsolution by spinodal decomposition in multicomponent mineral solutions*, Acta Mater. 60 (2012), pp. 5481–5493.

[5] A. Bailey, *Comparison of low-temperature with high-temperature diffusion of sodium in albite*, Geochim. Cosmochim. Acta 35 (1971), pp. 1073–1081.

[6] T. Lin and R. Yund, *Potassium and sodium self-diffusion in alkali feldspar*, Contrib. Mineral. Petr. 34 (1972), pp. 177–184.

[7] R. Petrović, *Alkali Ion Diffusion in Alkali Feldspars*, PhD thesis, Yale University, 1972.

[8] K.A. Foland, *Alkali diffusion in orthoclase*, Geochemical Transport and Kinetics 634 (1974), pp. 77–98.

[9] R. Kasper, *Cation and oxygen diffusion in albite*, PhD thesis, Brown University, 1975.

[10] D. Cherniak, *Cation diffusion in feldspars*, Rev. Mineral. Geochem. 72 (2010), pp. 691–733.

[11] E. Petrishcheva, R. Abart, A. Schaeffer, G. Habler, and D. Rhede, *Sodium-potassium interdiffusion in potassium-rich alkali feldspar I: full diffusivity tensor at 850 °C*, Am. J. Sci. 314 (2014), pp. 1284–1299.

[12] A.K. Schaeffer, E. Petrishcheva, G. Habler, R. Abart, D. Rhede, and G. Giester, *Sodium-potassium interdiffusion in potassium-rich alkali feldspar II: composition- and temperature-dependence obtained from cation exchange experiments*, Am. J. Sci. 314 (2014), pp. 1300–1318.

[13] A.K. Schäffer, *Alkali interdiffusion in alkali feldspars*, Dissertation, Universität Wien, Vienna, Austria, 2014.

[14] J.R. Manning, *Diffusion Kinetics for Atoms in Crystals*, Van Nostrand, Princeton, NJ, 1968.

[15] A.V. Nazarov and K. Gurov, *Calculation of non-equilibrium vacancies in the phenomenological theory of mutual diffusion*, Phys. Met. Metall. 45 (1979), pp. 185–188.

[16] A. Schaeffer, T. Jaepel, S. Zaefferer, R. Abart, and D. Rhede, *Lattice strain across na-k interdiffusion fronts in alkali feldspar: an electron backscatter diffraction study*, Phys. Chem. Min. 41 (2014), pp. 795–804.

[17] H. Behrens, W. Johannes, and H. Schmalzried, *On the mechanisms of cation diffusion processes in ternary feldspars*, Phys. Chem. Minerals 17 (1990), pp. 62–78.

[18] W.J. Fredericks, *Diffusion in solids – recent developments*, chap. Diffusion in alkali halides, Academic Press, New York (1975).

[19] H. Mehrer, *Diffusion in Solids*, Springer, Berlin, 2007.

[20] H.J. de Bruin, G.E. Murch, H. Bakker, and L.P. van der Mey, *Diffusion correlation in random alloys*, Thin Solid Films 25 (1975), pp. 47–62.

[21] Y. Mishin and D. Farkas, *Monte Carlo simulation of correlation effects in a random bcc alloy*, Phil. Mag. 75 (1997), pp. 201–219.

[22] I.V. Belova and G.E. Murch, *Tracer correlation factors in the random alloy*, Phil. Mag. 80 (2000), pp. 1469–1479.

[23] G.E. Murch and S.J. Rothman, *Diffusion, correlation, and percolation in a random alloy*, Phil. Mag. 43 (1981), pp. 229–238.

[24] I.V. Belova and G.E. Murch, *Collective diffusion in the binary random alloy*, Phil. Mag. 80 (2000), pp. 599–607.

[25] A.D. LeClaire, *Physical Chemistry: an Advanced Treatise, Vol. 10*, chap. Correlation effects in diffusion in solids, Academic Press, New York (1970), pp. 261–330.

[26] G.E. Murch, *Diffusion in crystalline solids*, Academic Press, 2012.

[27] L.T. Elkins and T.L. Grove, *Ternary feldspar experiments and thermodynamic models*, Am. Mineral. 75 (1990), pp. 544–559.

[28] H. Kroll, C. Evangelakakis, and G. Voll, *Two-feldspar geothermometry: a review and revision for slowly cooled rocks*, Contrib. Mineral. Petr. 114 (1993), pp. 510–518.

[29] M. Okrusch and S. Matthes, *Mineralogie*, Springer Spektrum, 2014.

[30] B.K. Vainshtein, V.M. Friedkin, and V. Indenbom, *Structure of Crystals*, Springer, Berlin, 1995.

[31] P. Ribbe, *Chemistry, Structure and Nomenclature of Feldspars*, in *Feldspar Mineralogy*, P. Ribbe, ed., Mineralogical Society of America (1983), pp. 1–19.

[32] G. Neusser, R. Abart, F. Fischer, D. Harlov, and N. Norberg, *Experimental Na/K exchange between alkali feldspar and an NaCl-KCl salt melt: chemically induced fracturing and element partitioning*, Contrib. Mineral. Petr. 164 (2012), pp. 341–358.

[33] K. Demtröder, *Untersuchung zur Al/Si-Ordnung an Sanidin Megakristallen aus der Eifel*, Master's thesis, Ruhr-Universität Bochum, 2011.

[34] J. Crank, *The Mathematics of Diffusion*, Oxford University Press, 1975.

[35] J.L. Routbort and S.J. Rothman, *Solution of the Diffusion Equation with Evaporation of the Sample and Exchange of the Diffusant with the Ambient*, in *Defect Diffus. Forum*, Vol. 40. Trans Tech Publ, 1985, pp. 1–12.

[36] J.F. Nye, *Physical Properties of Crystals: Their Representation by Tensors and Matrices*, Oxford University Press, 1957.

[37] J. Bardeen and C. Herring, *Imperfections in nearly perfect crystals*, Weiley, New York (1952), p. 261.

[38] H. Bracht, N.A. Stolwijk, and H. Mehrer, *Properties of intrinsic point defects in silicon determined by zinc diffusion under nonequilibrium conditions*, Phys. Rev. B 52 (1995), pp. 16542–16560.

[39] H. Bracht, *Self-and foreign-atom diffusion in semiconductor isotope heterostructures. I. Continuum theoretical calculations*, Phys. Rev. B 75 (2007), p. 035210.

[40] G. Montet, *Integral methods in the calculation of correlation factors in diffusion*, Phys. Rev. B 7 (1973), pp. 650–662.

[41] S.W. Kelly and C.A. Sholl, *Theory and monte carlo calculation of the tracer correlation factor*, J. Phys. C 20 (1987), pp. 5293–5304.

[42] G.H. Vineyard, *Frequency factors and isotope effects in solid state rate processes*, J. Phys. Chem. Solids 3 (1957), pp. 121–127.

[43] E. Wimmer, W. Wolf, J. Sticht, P. Saxe, C.B. Geller, R. Najafabadi, and G.A. Young, *Temperature-dependent diffusion coefficients from ab initio computations: Hydrogen, deuterium, and tritium in nickel*, Phys. Rev. B 77 (2008), p. 134305.

[44] P. Sowa, A. Biborski, M. Kozłowski, R. Kozubski, I. Belova, and G. Murch, *Atomistic origin of the thermodynamic activation energy for self-diffusion and order-order relaxation in intermetallic compounds i: analytical approach*, Phil. Mag. 97 (2017), pp. 1361–1374.

[45] J.R. Manning, *Correlation factors for diffusion in nondilute alloys*, Phys. Rev. B 4 (1971), pp. 1111–1121.

[46] J. Bastek, *Fremd- und Selbstdiffusion in Dünnschichtsolarzellen auf der Basis mehrkomponentiger Halbleiterverbindungen*, Dissertation, University of Münster, Germany, 2013.

[47] F. Wenwer, A. Gude, G. Rummel, M. Eggersmann, T. Zumkley, N.A. Stolwijk, and H. Mehrer, *A universal ion-beam-sputtering device for diffusion studies*, Meas. Sci. Technol. 7 (1996), pp. 632–640.

[48] C. Patrignani, *et al.*, *Review of Particle Physics, 2016–2017*, Chin. Phys. C 40 (2016), p. 100001.

[49] T. Eschen, K. Hiepko, J. Bastek, and N. Stolwijk, *Impact of surface roughness on tracer depth profiling and its implications for Cd109 and Zn65 diffusion experiments in solar-grade Cu(In,Ga)Se2 layers*, Appl. Surf. Sci. 307 (2014), pp. 428–437.

[50] B. Tas Kavakbasi, *Temperature and Orientation dependence of ^{22}Na tracer diffusion in Madagascar K-feldspar*, Master's thesis, University of Münster, Germany, 2015.

[51] A. Knieschewski, *Sodium radiotracer diffusion in single crystal alkali feldspar*, Master's thesis, University of Münster, Germany, 2015.

[52] A. Yelon and B. Movaghar, *Microscopic explanation of the compensation (Meyer-Neldel) rule*, Phys. Rev. Lett. 65 (1990), pp. 618–620.

[53] H. Kroll, I. Schmiemann, and G. von Cölln, *Feldspar solid solutions*, Am. Mineral. 71 (1986), pp. 1–16.

[54] A. Jones, M. Islam, M. Mortimer, and D. Palmer, *Alkali ion migration in albite and K-feldspar*, Phys. Chem. Minerals 31 (2004), pp. 313–320.

[55] D. Cherniak, *Cation diffusion in feldspars*, Rev. Mineral. Geochem 72 (2010), pp. 691–733.

[56] H. El Maanaoui, F. Wilangowski, A. Maheshwari, H.D. Wiemhöfer, R. Abart, and N.A. Stolwijk, *Ionic conductivity in gem-quality single-crystal alkali feldspar from the Eifel: temperature, orientation and composition dependence*, Phys. Chem. Minerals 43 (2016), pp. 327–340.

[57] F. Hergemöller, M. Wegner, M. Deicher, H. Wolf, F. Brenner, H. Hutter, R. Abart, and N.A. Stolwijk, *Potassium self-diffusion in a K-rich single-crystal alkali feldspar*, Phys. Chem. Minerals 44 (2017), pp. 345–351.

[58] A.M. Hofmeister and G.R. Rossman, *Determination of Fe3+ and Fe2+ concentrations in feldspar by optical absorption and EPR spectroscopy*, Phys. Chem. Minerals 11 (1984), pp. 213–224.

[59] R. Freer, K. Wright, H. Kroll, and J. Göttlicher, *Oxygen diffusion in sanidine feldspar and a critical appraisal of oxygen isotope-mass-effect measurements in non-cubic materials*, Phil. Mag. A 75 (1997), pp. 485–503.

[60] J.F. Ziegler, M. Ziegler, and J. Biersack, *SRIM – the stopping and range of ions in matter*, Nucl. Instrum. Meth. B 268 (2010), pp. 1818–1823.

[61] J. Kronenberg, *Untersuchung der Uphill-Diffusion von Fremdatomen in Te-reichen II–VI Halbleitern*, Dissertation, Saarland University, 2012.

[62] E. Junod, *Corrections of counting losses in gamma-spectrometry of short-lived radionuclides*, J. Radioanal. Nucl. Chem. 20 (1974), pp. 113–134.

[63] A. Strohm, *Selbstdiffusion in Silizium-Germanium-Legierungen*, Dissertation, University of Stuttgart, 2002.

[64] F. Wilangowski, S. Divinski, R. Abart, and N.A. Stolwijk, *Radiotracer experiments and Monte Carlo simulation of sodium diffusion in alkali feldspar: Evidence against the vacancy mechanism*, Defect Diffus. Forum 363 (2015), pp. 79–84.

[65] F. Wilangowski and N.A. Stolwijk, *A Monte Carlo study of ionic transport in a simple cubic random alloy via the interstitialcy mechanism: Effects of non-collinear and direct interstitial jumps*, Phil. Mag. 97 (2017), pp. 108–127.

[66] H. Hu, H. Li, D. Lidong, S. Shuangming, and Z. Chengming, *Electrical conductivity of albite at high temperatures and high pressures*, Am. Mineral. 96 (2011), pp. 1821–1827.

[67] H. Hu, H. Li, D. Lidong, S. Shuangming, and Z. Chengming, *Electrical conductivity of alkali feldspar solid solutions at high temperatures and high pressures*, Phys. Chem. Minerals 40 (2013), pp. 51–62.

[68] S.I. Karato, *The role of hydrogen in the electrical conductivity of the upper mantle*, Nature 347 (1990), pp. 272–273.

[69] B. Zhang, *Diffusion of hydrogen in (Mg, Fe) 2 Sio 4 and high pressure polymorphs refined by the cbΩ model*, J. Asian Earth Sci. 54 (2012), pp. 9–17.

[70] X. Yang, H. Keppler, C. McCammon, and H. Ni, *Electrical conductivity of orthopyroxene and plagioclase in the lower crust*, Contrib. Mineral. Petr. 163 (2012), pp. 33–48.

[71] B. Zhang, S. Shan, and X. Wu, *Modeling H, Na, and K diffusion in plagioclase feldspar by relating point defect parameters to bulk properties*, Phys. Chem. Minerals 43 (2016), pp. 151–159.

[72] H. Kroll and P. Ribbe, *Lattice Parameters, Composition and Al,Si Order in Alkali Feldspars*, in *Feldspar Mineralogy*, P. Ribbe, ed., Mineralogical Society of America (1983), pp. 57–99.

[73] F. Berkemeier, *Ionentransport in Alkali-Boratgläsern*, Diplomarbeit, University of Münster, Germany, 2003.

[74] A.W. Imre, S. Voss, and H. Mehrer, *Ionic transport in 0.2[xNa$_2$O·(1-x)Rb$_2$O]·0.8B$_2$O$_3$ mixed-alkali glasses*, Phys. Chem. Chem. Phys. 4 (2002), pp. 3219–3224.

[75] F. Wilangowski and N. Stolwijk, *Monte Carlo simulation of diffusion and ionic conductivity in a simple cubic random alloy via the interstitialcy mechanism*, J. Phys. Condens. Matter 27 (2015), p. 505401.

[76] G.E. Murch and J.C. Dyre, *Correlation effects in ionic conductivity*, Crit. Rev. Solid State Mater. Sci. 14 (1989), pp. 345–365.

[77] J.C. Dyre and G. Murch, *Correlation effects in tracer diffusion and ionic conductivity. II*, Solid State Ion. 21 (1986), pp. 139–142.

[78] C.A. Sholl, *Diffusion correlation factors and atomic displacements for the vacancy mechanism*, J. Phys. C 14 (1981), pp. 2723–2729.

[79] G.E. Murch and Z. Qin, *Tracer and collective correlation factors in solid state diffusion*, Defect Diffus. Forum 109-110 (1994), pp. 1–18.

[80] A.R. Allnatt, *Einstein and linear response formulae for the phenomenological coefficients for isothermal matter transport in solids*, J. Phys. C 15 (1982), pp. 5605–5613.

[81] A.R. Allnatt and E.L. Allnatt, *Computer simulation of phenomenological coefficients for atom transport in a random alloy*, Phil. Mag. 49 (1984), pp. 625–635.

[82] P. Franke and R. Dieckmann, *Correlation factors for diffusion in binary random alloys with fcc structure*, J. Appl. Phys. 70 (1991), pp. 787–792.

[83] F. Wilangowski and N.A. Stolwijk, *Vacancy-related diffusion correlation effects in a simple cubic random alloy and on the Na-K sublattice of alkali feldspar*, Phil. Mag. 95 (2015), pp. 2277–2293.

[84] A. Bendani, A. Dautant, and L. Bonpunt, *Diffusion tensor and molecular jump frequencies in naphthalene single crystals*, J. Phys. I France 3 (1993), pp. 887–901.

[85] R.E. Howard, *Random-Walk Method for Calculating Correlation Factors: Tracer Diffusion by Divacancy and Impurity-Vacancy Pairs in Cubic Crystals*, Phys. Rev. 144 (1966), pp. 650–661.

[86] M. Matsumoto and T. Nishimura, *Mersenne twister: a 623-dimensionally equidistributed uniform pseudo-random number generator*, ACM T. Model. Comput. S. 8 (1998), pp. 3–30.

[87] M. Salamon, A. Strohm, T. Voss, P. Laitinen, I. Riihimäki, S. Divinski, W. Frank, J. Räisänen, and H. Mehrer, *Self-diffusion of silicon in molybdenum disilicide*, Phil. Mag. 84 (2004), pp. 737–756.

[88] S. Divinski, M. Salamon, and H. Mehrer, *Silicon diffusion in molybdenum disilicide: correlation effects*, Phil. Mag. 84 (2004), pp. 757–772.

[89] R.E. Howard and M.J. R., *Kinetics of solute-enhanced diffusion in dilute face-centered- cubic alloys*, Phys. Rev. 154 (1967), pp. 561–568.

[90] Z. Qin and G.E. Murch, *Computer simulation of collective correlation effects for diffusion in a random alloy*, Phil. Mag. A 68 (1993), pp. 819–830.

[91] Z. Qin and G.E. Murch, *Decay of the tracer correlation process in solid-state diffusion*, Phil. Mag. A 67 (1993), pp. 777–788.

[92] L.K. Moleko, A.R. Allnatt, and E.L. Allnatt, *A self-consistent theory of matter transport ina random lattice gas and some simulation results*, Phil. Mag. 59 (1989), pp. 141–160.

[93] N.A. Stolwijk, *Correlation factors for diffusion in binary random alloys with short-range order*, Phys. Status Solidi B 105 (1981), pp. 223–232.

[94] I.V. Belova, H. Mehrer, and G.E. Murch, *Diffusion correlation effects of molybdenum and silicon in molybdenum disilicide*, Phil. Mag. 91 (2011), pp. 3727–3743.

[95] Y. Deng and H.W.J. Blöte, *Monte Carlo study of the site-percolation model in two and three dimensions*, Phys. Rev. E 72 (2005), p. 016126.

[96] G.E. Murch, *Diffusion in Crystalline Solids*, chap. Simulation of Diffusion Kinetics with the Monte Carlo Method, Academic Press, New York (1984).

[97] H.J. de Bruin and G.E. Murch, *Diffusion correlation effects in non-stoichiometric solids*, Phil. Mag. 27 (1973), pp. 1475–1488.

[98] K. Compaan and Y. Haven, *Correlation factors for diffusion in solids. Part 2.–Indirect interstitial mechanism*, Trans. Faraday Soc. 54 (1958), pp. 1498–1508.

[99] G.E. Murch, *The haven ratio in fast ionic conductors*, Solid State Ion. 7 (1982), pp. 177–198.

[100] W. Frank, U. Gösele, H. Mehrer, and A. Seeger, *Diffusion in Crystalline Solids*, chap. Diffusion in Silicon and Germanium, Academic Press, New York (1984).

[101] G. Bösker, N.A. Stolwijk, J.V. Thordson, U. Södervall, and T.G. Andersson, *Diffusion of nitrogen from a buried doping layer in gallium arsenide revealing the prominent role of As interstitials*, Phys. Rev. Lett. 81 (1998), pp. 3443–3446.

[102] A. Strohm, T. Voss, W. Frank, P. Laitinen, and J. Räisänen, *Self-diffusion of ^{71}Ge and ^{31}Si in Si–Ge alloys*, Z. Metallkd. 93 (2002), pp. 737–744.

[103] R. Kube, H. Bracht, J. Lundsgaard Hansen, A. Nylandsted Larsen, E.E. Haller, S. Paul, and W. Lerch, *Composition dependence of Si and Ge diffusion in relaxed $Si_{1-x}Ge_x$ alloys*, J. Appl. Phys. 107 (2010), p. 073520.

[104] K. Compaan and Y. Haven, *Correlation factors for diffusion in solids*, Trans. Faraday Soc. 52 (1956), pp. 786–801.

[105] P.C.L. Stephenson and C.A. Sholl, *Tracer correlation factor and atomic displacements due to the collinear interstitialcy mechanism*, Phil. Mag. 69 (1994), pp. 57–64.

[106] A.R. Allnatt and E.L. Allnatt, *Correlation effects in atom transport by the interstitialcy mechanism*, Phil. Mag. 64 (1991), pp. 777–786.

[107] K. Foland, *Alkali Diffusion in Orthoclase*, in *Geochemical Transport and Kinetics*, de Gruyter, Carnegie Institution, Washington (1974), pp. 77–98.

[108] C.W. McCombie and A.B. Lidiard, *Ratio of ionic conductivity to tracer diffusion in interstitialcy migration*, Phys. Rev. 101 (1956), pp. 1210–1211.

[109] M.F. Sykes and J.W. Essam, *Exact critical percolation probabilities for site and bond problems in two dimensions*, J. Math. Phys. 5 (1964), pp. 1117–1127.

[110] V.K. Shante and S. Kirkpatrick, *An introduction to percolation theory*, Adv. Phys. 20 (1971), pp. 325–357.

[111] S. Galam and A. Mauger, *Universal formulas for percolation thresholds*, Phys. Rev. E 53 (1996), pp. 2177–2181.

[112] S.C. van der Marck, *Percolation thresholds and universal formulas*, Phys. Rev. E 55 (1997), pp. 1514–1517.

[113] N.A. Stolwijk, *Atomic transport in semiconductors, diffusion mechanisms and chemical trends*, Defect Diffus. Forum 95-98 (1993), pp. 895–916.

[114] N.A. Stolwijk, B. Schuster, and J. Hölzl, *Diffusion of gold in silicon studied by means of neutron-activation analysis and spreading-resistance measurements*, Appl. Phys. A 33 (1984), pp. 133–140.

[115] R. Kikuchi and H. Sato, *Substitutional diffusion in an ordered system*, J. Chem. Phys. 51 (1969), pp. 161–181.

[116] R. Kikuchi and H. Sato, *Correlation factor in substitutional diffusion in binary alloys*, J. Chem. Phys. 53 (1970), pp. 2702–2713.

[117] R. Kikuchi and H. Sato, *Diffusion coefficient in an ordered binary alloy*, J. Chem. Phys. 57 (1972), pp. 4962–4979.

[118] H. Bakker, N.A. Stolwijk, L. van der Meij, and T.J. Zuurendonk, *Computer simulation of diffusion in concentrated binary alloys with short and long range disorder*, AIME Nuclear Metallurgy Series 20 (1976), pp. 96–108.

[119] I. Belova, M. Ivory, and G. Murch, *Diffusion in a model of an ordered alloy*, Phil. Mag. A 72 (1995), pp. 871–880.

[120] M. Phillips and P. Ribbe, *The structures of monoclinic potassium-rich feldspars*, Am. Mineral. 58 (1973), pp. 263–270.

[121] R.J. Friauf, *Diffusion of silver in silver bromide and evidence for interstitialcy migration*, Phys. Rev. 105 (1957), pp. 843–848.

[122] B.L. Phillips, R.J. Kirkpatrick, and G.L. Hovis, *27 Al, 29 Si, and 23 Na MAS NMR study of an Al, Si ordered alkali feldspar solid solution series*, Phys. Chem. Minerals 16 (1988), pp. 262–275.

[123] A. Benisek, E. Dachs, and H. Kroll, *Thermochemistry of the alkali feldspars: Calorimetric study of the entropy relations in the low albite–low microcline series*, n 99 (2014), pp. 76–83.

[124] A. Benisek, E. Dachs, and M. Grodzicki, *First-principles investigation of the lattice vibrations in the alkali feldspar solid solution*, Phys. Chem. Minerals 42 (2015), pp. 243–249.

[125] N. Metropolis, A.W. Rosenbluth, M.N. Rosenbluth, A.H. Teller, and E. Teller, *Equation of state calculations by fast computing machines*, J. Chem. Phys. 21 (1953), pp. 1087–1092.

[126] L. Guttman, *Monte carlo computations on the ising model. The body-centered cubic lattice*, J. Chem. Phys. 34 (1961), pp. 1024–1036.

[127] S.V. Divinski, S. Frank, C. Herzig, and U. Södervall, *The Ni Self-Diffusion in NiAl: An Experimental Investigation of the Temperature and Composition Dependencies and Atomistic Simulation of Diffusion Mechanisms*, in *Solid State Phenomena*, Vol. 72. Trans Tech Publ, 2000, pp. 203–208.

[128] F. Wilangowski, *Tracer diffusion of sodium in a potassium-rich feldspar*, Master's thesis, University of Münster, Germany, 2013.

Publikationen

F. Hergemöller, M. Wegner, M. Deicher, H. Wolf, F. Brenner, H. Hutter, R. Abart, and N.A. Stolwijk, *Potassium self-diffusion in a K-rich single-crystal alkali feldspar*, Phys. Chem. Minerals 44 (2017), pp. 345–351.

M. Wegner, F. Wilangowski, R. Wuerz and N.A. Stolwijk, *Radiotracer diffusion of Ag in Cu (In, Ga) Se 2 thin films*, Thin Solid Films 633 (2017), pp. 31–34.

F. Wilangowski and N.A. Stolwijk, *A Monte Carlo study of ionic transport in a simple cubic random alloy via the interstitialcy mechanism: E ects of non-collinear and direct interstitial jumps*, Phil. Mag. 97 (2017), pp. 108–127.

H. El Maanaoui, F. Wilangowski, A. Maheshwari, H.D. Wiemhöfer, R. Abart, and N.A. Stolwijk, *Ionic conductivity in gem-quality single-crystal alkali feldspar from the Eifel: temperature, orientation and composition dependence*, Phys. Chem. Minerals 43 (2016), pp. 327–340.

F. Wilangowski and N. Stolwijk, *Monte Carlo simulation of diffusion and ionic conductivity in a simple cubic random alloy via the interstitialcy mechanism*, J. Phys. Condens. Matter 27 (2015), p. 505401.

F. Wilangowski and N.A. Stolwijk, *Vacancy-related diffusion correlation effects in a simple cubic random alloy and on the Na-K sublattice of alkali feldspar*, Phil. Mag. 95 (2015), pp. 2277–2293.

F. Wilangowski, S. Divinski, R. Abart, and N.A. Stolwijk, *Radiotracer experiments and Monte Carlo simulation of sodium diffusion in alkali feldspar: Evidence against the vacancy mechanism*, Defect Diffus. Forum 363 (2015), pp. 79–84.